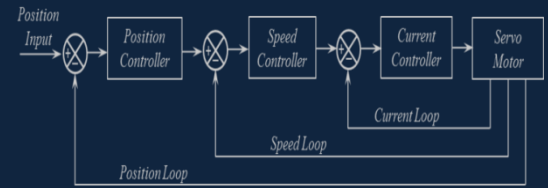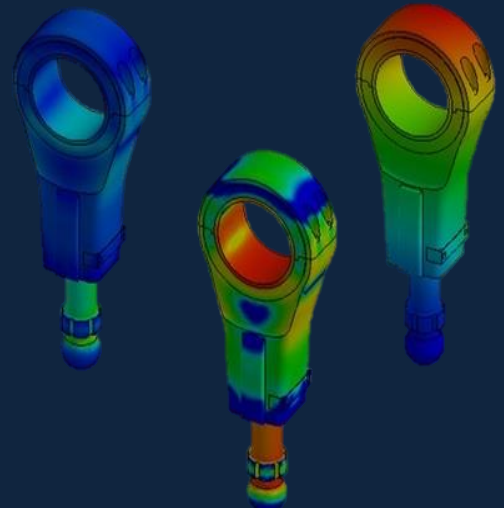# International Advanced Researches and Engineering Journal

Aerospace Engineering,
Aquaculture and Fisheries Engineering,
Architecture,
Bioengineering,
Chemical Engineering,
Civil Engineering,
Computer Engineering,
Electrical and Electronics,
Energy,
Environmental Engineering,
Food Engineering,
Geomatics Engineering,
Industrial Engineering,
Industrial Applications,
Machine Theory and Dynamics,
Manufacturing,
Mechanical Engineering,
Mechanics,
Mechatronics,
Medical,
Modeling and Simulation,
Physics Engineering,
Robotics,
Textile Engineering
Health in Engineering

$F=ma$

$E=mc^2$

$\int \frac{dy}{dx} dt$

International Advanced Researches and Engineering Journal (IAREJ) is a double-blind peer-reviewed and publicly available online journal that has Editorial Board. The editor in chief of IAREJ welcomes the submissions that cover theoretical and/or applied researches on engineering and related sciences. IAREJ publishes **original papers** that are research papers and technical review papers.

IAREJ publication, which is open access, is free of charge. There is no article submission and processing charges (APCs).

IAREJ is indexed by:

Directory of Open Access Scholarly Researches (ROAD)
Directory of Research Journals Indexing (DRJI)
Google Scholar
Journal Factor
J-Gate
Index Copernicus
Rootindexing
Scientific Indexing Services (SIS)

Authors are responsible from the copyrights of the figures and the contents of the manuscripts, accuracy of the references, quotations and proposed ideas and the Publication Ethics.

Table of Contents

Research Article

Seismic performance of steel moment frames with variable friction pendulum systems under real ground motions

Ahmet Hilmi Deringöl [a],*

[a]*Department of Civil Engineering, Gaziantep University, Gaziantep, 27310, Turkey*

ARTICLE INFO	ABSTRACT
	Many researchers have already acknowledged that the base isolation system as the most feasible and economical method for civil engineering structures exposed to the seismic excitation. The Friction Pendulum Systems (FPS) have steel concave surface connected with articulated friction slider and utilized the concept of pendulum for lengthening the period of the superstructure so as to dissipate the seismic energy. The present study investigates on various design approaches for the evaluation of the seismic response of steel frames equipped with FPS. The response of isolated frames is simply adjusted by several parameters such as the friction coefficient (μ), the radius of curvature (R), the isolation period (T) and the axial load and so 2D, three bay 3 and 7-storey steel moment resisting frames (SMRF) are designated as isolated frames in order to examine the effect of variation of the R and the friction coefficient on the seismic response of the isolated frames. The R and μ are predefined as 1, 1.55, 2.25 and 0.025, 0.05, 0.1, respectively. The seismic response of the modelled isolation systems has been evaluated through nonlinear time history analyses, a set of ground motions using SAP2000 software. The local and global deformations are employed to compare the seismic performance of different isolation frames through nonlinear analysis. The results showed that the isolated frames having greatest radius of curvature with lowest friction coefficient exhibited better seismic performance than other models in terms of the local and global deformations.

1. Introduction

In last decades, numerous researchers have developed several methods as to enhance the energy dissipation capacity of civil engineering structures. Among these methods, base isolation system (BIS) can be accepted the most popular seismic protective system that is extensively used [1-5]. BIS has been utilized for mitigating the destructive effects of the earthquakes on the structure that initially considered as one of the most effective approaches both in the design of the new buildings and in seismic retrofit of the existing buildings. The concept and theory of the base isolation is depended on decoupling the building from the ground and inserted the BIS in order to mitigate the catastrophic effect of the earthquakes. Commonly two type of base isolation systems; such as sliding systems and elastomeric bearings are available. The sliding systems are designed to dissipate the seismic

forces by providing frictional sliding and limiting the transfer of shear while the elastomeric bearings are designed to eliminate horizontal earthquake forces by providing a layer with low horizontal stiffness [6]. Recently, many analytical and experimental studies have been presented with the aim of finding out the seismic response of the FPS. For example, in the study of Landi et al. [7], several time history analyses were performed with near field records for different models of FPS, constructed by the predefined friction coefficient, sliding velocity and vertical force. The analysis results enabled to compare the models considering the influence of the earthquake component with the constant friction coefficient. Similarly, another numerical study was performed to examine the seismic response of elastically isolated frames with FPS designed by three different soil conditions corresponded to various frequency content under a set of 100 artificial earthquakes. It was obtained that greater friction coefficient was supposed in

* Corresponding author. Tel.: +90-0342-582-1111; Fax: +90-342-582-1011.
E-mail address: aderingol@gmail.com

case of soft soil with lower isolation period [8]. In the study of Castaldo et al. [9], the seismic reliability of a 3D 4-storey reinforced concrete frame equipped with FPS was evaluated and designed in compliance with the FEMA 274 [10] code. The seismic performance of the frame with FPS satisfied the requirements of corresponding seismic codes by modified lower friction coefficient adjusted with lower uncertainty. In the analytical study of the Jangid [11] multi-storey frames isolated with FPS and analyzed under near fault records in order to find out the optimal design parameters of the FPS. The analysis results showed that the optimum friction coefficient of FPS has less acceleration demand with respect to the non-isolated frames. The optimal friction coefficient changed with the values of the bearing acceleration that is ranged from 5 to 15%.

The main aims of the study are to (i) examine the seismic performance of the steel frames isolated by FPS, (ii) compare the effectiveness of the base isolation systems against seismic excitation, (iii) show the variation of the isolation parameters of the FPS for 3 and 7-storey SMRFs with different isolation systems, and (iv) offer the optimum parameters of the FPS for minimum seismic response of the isolated system under earthquake records. In the light of the previous researchers, 3 and 7-storey SMRF equipped with FPS having wide range of the radius of curvatures (from 1 m to 2.25 m), isolation period (2 s to 3 s) and friction coefficients (from 0.025 to 0.10), these isolated frames were analyzed using three natural accelerograms compatible with seismic hazard levels of 2% probability of exceedance in 50 years. The organization of the present study is as follows: the analytical modeling details of the frames including the original frames and base-isolated frames (namely FPS) are given in Section 2. Additionally, the design parameters of the base isolation systems were given. The information on the earthquake records that are representatives of 2% probability of exceedance in 50 years was described. Then, the results of the nonlinear analysis were comprehensively discussed in Section 3. Finally, the results inferred from the analysis results are presented in a comparative manner in Section 4.

2. Modelling and Analysis of SMRF with FPS

Two different SMRF are designated as bare frames those have firstly designed by Ferraioli et al. [12] according to the Italian Code [13]. These frames have 2D, three bay 3 and 7-storey and the cross sections of the examined frames are given in Table 1. The more information about those fixed base frame can be found concerned paper. In this study, 3 and 7-storey SMRF are modified as base isolated frame with FPB.

Among the BIS, FPS has come into prominence by virtue of its supremacy behavior such as non-ageing, durability, maintenance, thermal condition; thus, it can be accepted as mostly used BIS [14]. It has an articulated and slider surface in contact with the curved frictional area is made of

composite material. The other side of the slider is attached to stainless steel concave, spherical surface and covered with moderate frictional materials [15]. The mechanism of FPS depend on the movement of the bearing along the curved surface and the supported mass is moved upward, thus the movement will provide the restoring force to the system. During a seismic excitation, the bearing goes along with curved surface hereby it moves in small arcs like a pendulum. The bearings decrease the transmission of the seismic forces to the structure by the movement of pendulum and also by frictional pad. The effective stiffness and the isolation period can be easily tuned by the radius of the concave surface.

2.1 Analytical models of frames

Analytical models of the fixed base and isolated frames were provided using nonlinear finite element program Sap2000 that is capable of performing nonlinear static and dynamic analyses [16]. To depict the hysteretic behavior of the isolators of the FPS a nonlinear finite element NLlink called as friction pendulum isolator has been selected and the mechanical model of the FPS is rooted in the classic Coulomb theory.

Table 1. The details of 3 and 7-storey frames. [12]

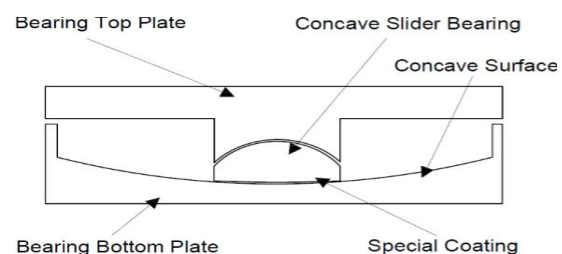| Frames	Storey Level	Beams	Outer Column	Inner Column
3-storey	1	IPE270	HE160B	HE220B
	2	IPE270	HE160B	HE200B
	3	IPE270	HE160B	HE200B
7-storey	1	IPE270	HE180B	HE240B
	2	IPE270	HE180B	HE240B
	3	IPE270	HE180B	HE220B
	4	IPE270	HE160B	HE220B
	5	IPE270	HE160B	HE220B
	6	IPE270	HE160B	HE200B
	7	IPE270	HE160B	HE200B

Figure 1. The Cross-section of FPS [14]

The cross-section and hysteretic behavior is plotted in Figures 1 and 2, respectively. For the base isolated models, two different bearings (inner and outer) were designed according to the vertical loads on the column. Designed FPS were replaced under each column of all evaluated models that include rubber isolator as a nonlinear link

element employed by Park et al. [17]. Thus, a total of 9 different cases were considered in this study. The design parameter of the FPS was computed by an iterative solution in compliance with Naeim and Kelly [5]. In the iterative procedure the following equations were employed. The load exerted on the isolator of the FPS is W, the horizontal displacement is D, and the friction coefficient is μ, then the resisting force F is given by

$$F = \frac{W}{R}D + \mu W(sgnD) \qquad (1)$$

where R is the radius of curvature of the dish. The first term is the restoring force due to rise of the mass, providing a horizontal stiffness

$$k_2 = \frac{W}{R} \qquad (2)$$

which produces an isolated structure period T given by

$$T = 2\pi\sqrt{\frac{R}{g}} \qquad (3)$$

The equivalent stiffness is given by

$$k_{eff} = \frac{W}{R} + \frac{\mu W}{D} \qquad (4)$$

effective damping, β_{eff};

$$\beta_{eff} = \frac{2\mu}{\pi x\left(\frac{D}{R}\right) + \mu} \qquad (5)$$

In this study, each isolation systems were labelled based on assumed isolation periods, T, radius of curvature, R and friction coefficient (μ) as to use in figures and throughout the rest of the text. For example, R1.55μ5 denotes an isolation system with R = 1.55 m, T = 2.5 s and μ = 0.05. The isolation system parameters for 7-storey frame with FPS were presented in Table 2, where R ranges from 1 to 2.25 m, T from 2 to 3 s and μ from 2.5 to 10 %. Moreover, the isolation periods of 2, 2.5 and 3 s are corresponded to the radius of curvatures 1, 1.55 and 2.25 m, respectively (see Eqn 3). To determine the seismic performance of the frames with and without FPS, the nonlinear time history analysis was performed using the finite element program of SAP 2000 non-linear version 14 [16] in which FPS was assigned as Nllink (Friction Isolator) components located under the bottom columns of the superstructure, the view of 3-storey SMRF with FPS in SAP2000 was given in Figure 2. The design parameters of FPS calculated using Eqs (1-5) and put into SAP2000 as follows for R1.55μ5. Nonlinear Link Type: Friction Isolator, U1 Non/Linear Effective Stiffness: 200000 kN/m, U2 and U3 Linear and Nonlinear Effective Stiffness: 190, 4102 kN/m, U2 and U3 Friction Coefficient: 0,05, U2 and U3 Radius of Sliding Surface: 1.55.

Table 2. The outer (O) and inner (I) design values of 7-storey isolated frame with FPB

R (m)	T (s)	μ (%)	k_2 (kN/m)	D (m)	k_{eff} (kN/m)	β_{eff}	Side
1.0	2.0	2.5	232.2	0.17	265.1	0.08	O
		5	232.2	0.17	297.8	0.16	
		10	232.2	0.17	363.5	0.30	
	2.0	2.5	504.4	0.22	575.7	0.10	I
		5	504.4	0.22	646.9	0.20	
		10	504.4	0.22	789.5	0.36	
1.55	2.5	2.5	149.8	0.27	176.1	0.12	O
		5	149.8	0.27	202.3	0.27	
		10	149.8	0.27	254.8	0.42	
	2.5	2.5	325.4	0.17	382.4	0.08	I
		5	325.4	0.17	439.5	0.16	
		10	325.4	0.17	553.5	0.30	
2.25	3.0	2.5	103.2	0.22	125.1	0.10	O
		5	103.2	0.22	146.9	0.20	
		10	103.2	0.22	190.7	0.36	
	3.0	2.5	224.2	0.27	271.7	0.12	I
		5	224.2	0.27	319.2	0.23	
		10	224.2	0.27	414.3	0.42	

Furthermore, the frames were exposed to three real ground motion records. These time history records data of the earthquake force obtained from the Pacific Earthquake Engineering Research Center (PEER) [18] used as seismic input, called from text file to carry out the time history analysis. The details of the time history of the earthquake records were presented in Table 3. It should be considered that in the scaling process the mean code spectra or a set of earthquakes should be as close as possible to the mean spectrum. The aim of this is to have the accelerograms of the three earthquakes scaled to approximately the same intensity level such that the responses can be represented. Analyses were carried out using the ground motion records occurring 100% along x direction. The Newmark method with integration parameters γ = 0.5 and β = 0.25 and critical damping ratio of 5% were also assumed in the time history analysis.

Table 3. The details of the earthquake records

Earthquake Record	Hills	Cape	Northridge
Year	1978	1992	1994
Magnitude (Mw)	7.35	7.01	6.69
Mechanism	Strike-Slip	Reverse	Reverse
PGA (g)	0.418	0.615	0.795
R_{jb} (km)	0.9	0	0
R_{rup} (km)	0.9	8.2	5.3
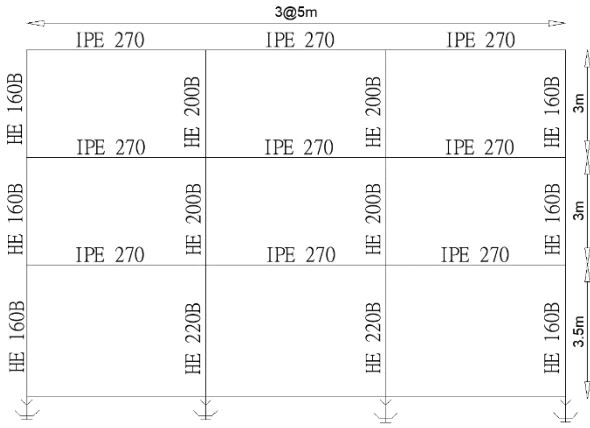
Figure 2. The view of 3-storey SMRF with FPS in SAP2000

3. Results and Discussion

This paper assessed the seismic response of SMRF with different FPS. The inelastic response of the frames with and without FPS are discussed concerning the roof displacement, relative displacement, interstorey drift ratio, absolute acceleration and hysteretic curves by means of the time history analyses. The analysis results showed that the response of frames with FPS changed with the radius of curvature R, friction coefficient μ, number of the storey and also the ground motion records. The analysis results are evaluated by series deformation parameters in Figures 3-17.

3.1 Displacement

The variation of the storey displacement of 3 and 7-storey frame exposed to three real ground motions are given in Figures 3 and 4, respectively. Further, the frames with FPS accommodated three different radiuses of curvature and friction coefficient are plotted in Figures 5 and 6 under Cape earthquake. It was clearly observed that decrease of the radius of curvature R (corresponding T) and friction coefficient μ are culminated in reduction on the roof displacement for 3 and 7-storey frames with FPS.
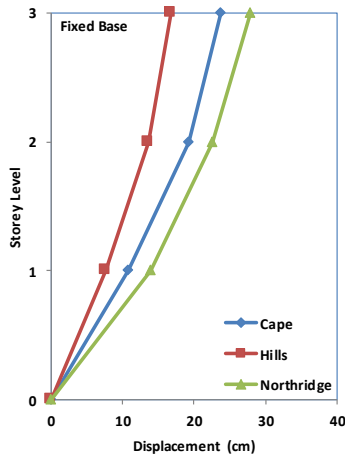
Figure 3. The displacement of 3-storey fixed base frame
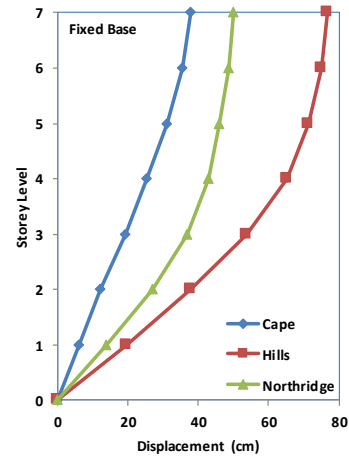
Figure 4. The displacement of 7-storey fixed base frame

The variation of the roof displacement demand for 3 and 7-storey frames was differentiated with the radius of curvature and friction coefficient due to assumption on the design parameters of FPS as shown in Table 2. Among the examined models, two lowest roof displacement of frames with the FPS was experienced in case of R2.25μ2.5 when hit Cape earthquake as shown in Figures 5 and 6. For example, it was observed that the roof displacements of 3 and 7-storey frame with FPS were 23.73 and 37.05 cm, respectively.
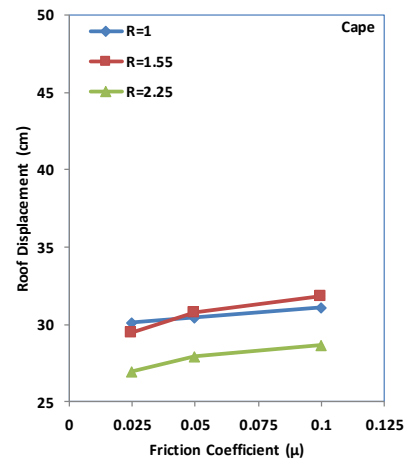
Figure 5. The roof displacement of 3-storey frames with FPS

Further, it was observed that when the friction coefficient was fixed and the radius of curvature was shifted from 1 m to 2.55 m (see Figure 5 and 6) the roof displacement demand of isolated frames was generally decreased parallel to descending trend of the isolators' horizontal and equivalent stiffness (namely, k_2 and k_{eff}) as shown in Table 2. Since increment of the radius of curvature led to enhancement of the isolation period and mitigation of the isolator stiffness, the isolated frames behave more ductile and the demand of the displacement increased as well. Similarly, the roof displacement demand of 3 and 7-storey frame with FPS was generally reduced when the radius of curvature was constant, and the friction coefficient was changed from 0.10 to 0.025 as shown in Figure 5 and 6, respectively.
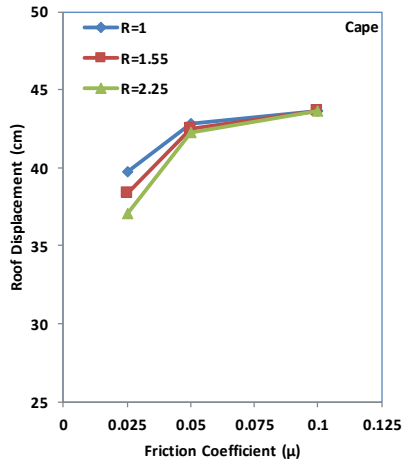
Figure 6. The roof displacement of 7-storey frame with FPS

Figure 8. The relative displacement of 3-storey isolated frames against storey height under Northridge earthquakes

3.2 Relative Displacement

The relative displacement is computed by subtracting the value of the roof displacement from the base displacement. The relative displacement with storey height of the frames with and without FPS under Northridge earthquake is generated for 9 various models and presented in Figures 7-9. The radius of 2.25 m (correspond to the isolation period of 3 s) with the friction coefficient of 2.5% is produced the lowest relative displacement for 3 and 7-storey isolated frames as shown in Figures 8 and 9. For example, when 3 and 7-storey fixed base frame equipped with R2.25μ2.5 model, the relative displacement reduced from 27.89 cm to 6.83 cm, 50 cm to 19.55 cm respectively.

Figure 9. The relative displacement of 7-storey isolated frames against storey height under Northridge earthquakes

Figure 7. The relative displacement of 3 and 7-storey fixed base frames

3.3 Interstorey drift ratio

The interstorey drift ratio can be admitted as significant benchmark for the seismic performance evaluation and also it can be used for the predicting the structural damage level. The variation of the interstorey drift ratio against storey height of the frames with and without under Hills earthquake is depicted in Figures 10 and 11. The interstorey drift ratio of the fixed base frames is regulated by means of the utilization of the FPS especially in case of R2.25μ2.5. It tended to uniform distribution against other models and fixed base frames. Further, it was observed that the isolation system of R2.25μ2.5 reduced the interstorey drift ratio from 2.2 to 1.4 % and from 6.1 to 1.8 % for 3 and 7-storey fixed base frames, respectively (see Figures 10(a) and 11(a)).

The results proved that the use of FPS is very effective in reduction of the relative displacement. Moreover, R2.25μ2.5 is significantly exhibited the most uniform distribution as shown in Figures 6 and 7. Similar to the observed trend on the variation of the displacement, greater radius of curvature R (corresponding T) and lower friction coefficient μ are caused to decrease the relative displacement for 3 and 7-storey frames with FPS under Northridge earthquake.

The maximum interstorey drift ratio of the frames equipped with FPS subjected to Cape earthquake obtained for 9 different models and plotted in Figures 12 and 13.
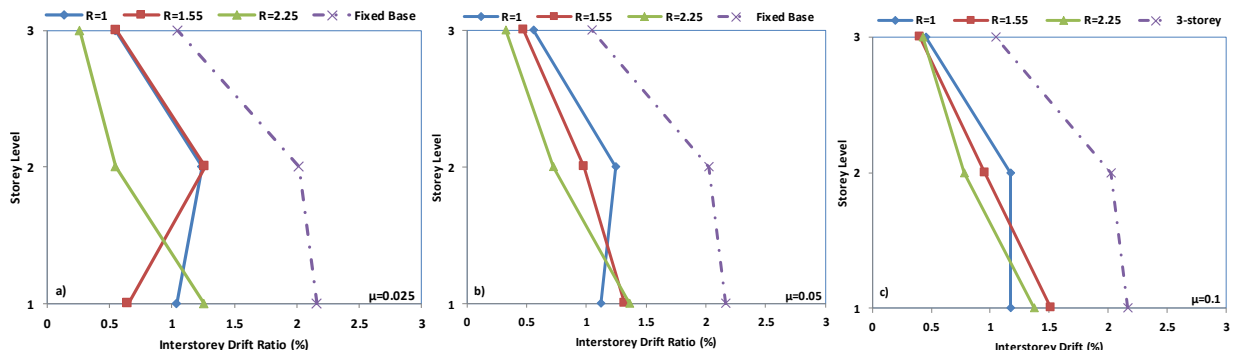
Figure 10. The variation of the interstorey drift ratio of 3-storey against storey height under Hills earthquakes
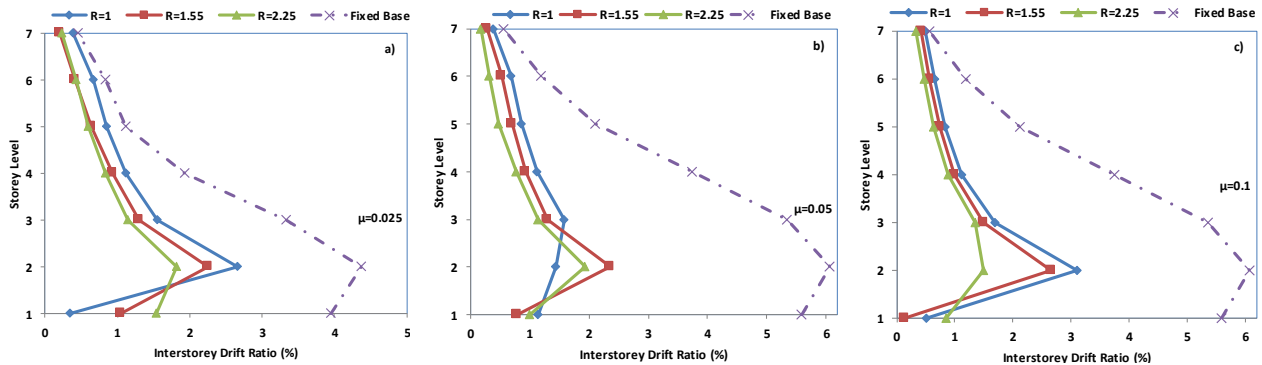
Figure 11. The variation of the interstorey drift ratio of 7-storey against storey height under Hills earthquakes
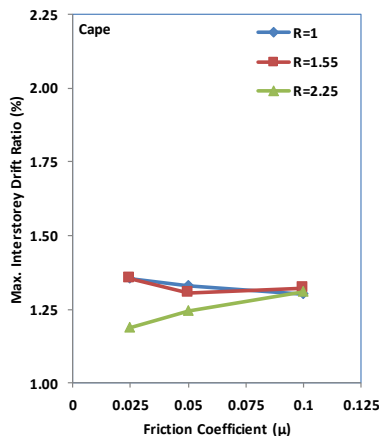
Figure 12. The maximum interstorey drift ratio of 3-storey frame
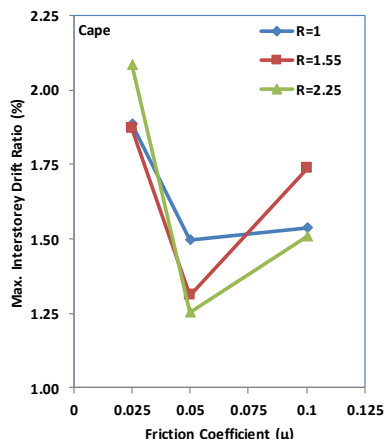
Figure 13. The maximum interstorey drift ratio of 7-storey frame

The the lowest maximum interstorey drift ratio of 1.18 % is experienced in case of R2.25μ5 for 3-storey frame with FPS as shown in Figure 12. Further the variation of the radius of curvature, friction coefficient and number of storey visibly fluctuated the drift ratios. However, an amplification trend is observed on the interstorey of 7-storey isolated frames when the friction coefficient varied from 2.5 to 5%. The utilization of optimum FPS in case of lower friction coefficient with greater radius of curvature testified the lower interstorey drift demand than other models as shown in Figures 12 and 13.

3.4 Absolute Acceleration

The variation of the absolute accelerations of the frames with and without FPS against storey height under Northridge earthquake is given in Figures 14 and 15. It was clearly observed that the increase of the isolation period, radius of curvature and friction coefficient led to great reduction on the corresponding storeys' absolute acceleration of 3 and 7-storey frame with FPS. The acceleration initially mitigated towards mid-height and then suddenly fluctuated towards the top storey. It is clearly observed that R2.25μ5 presented lowest absolute acceleration for 3 and 7-storey frame. For example, in case of R2.25μ2.5 that is caused to mitigate the absolute acceleration of 3 and 7-storey frame with FPS from 12 to 5.7 m/s^2 and 11.7 to 4.2 m/s^2, respectively. Further it assisted to tend more uniform distribution than other cases height of the storey especially for 7-storey frame with FPS.
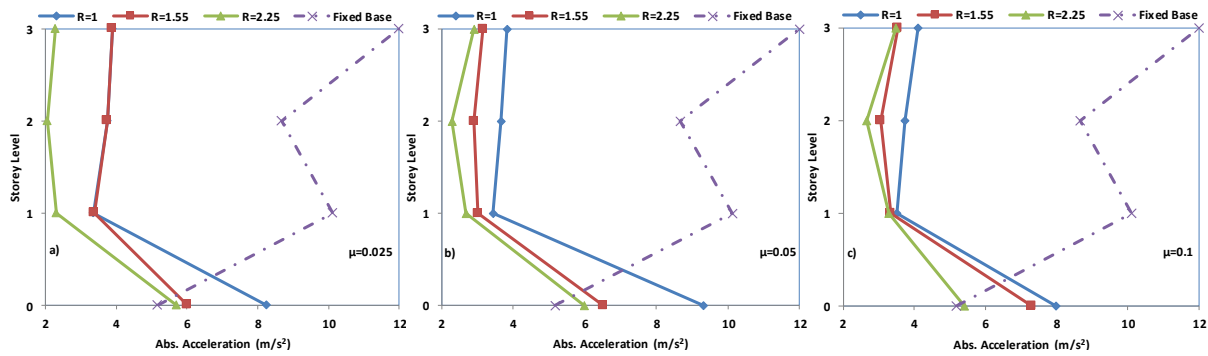
Figure 14. The variation of the absolute acceleration of 3-storey against storey height under Northridge earthquakes
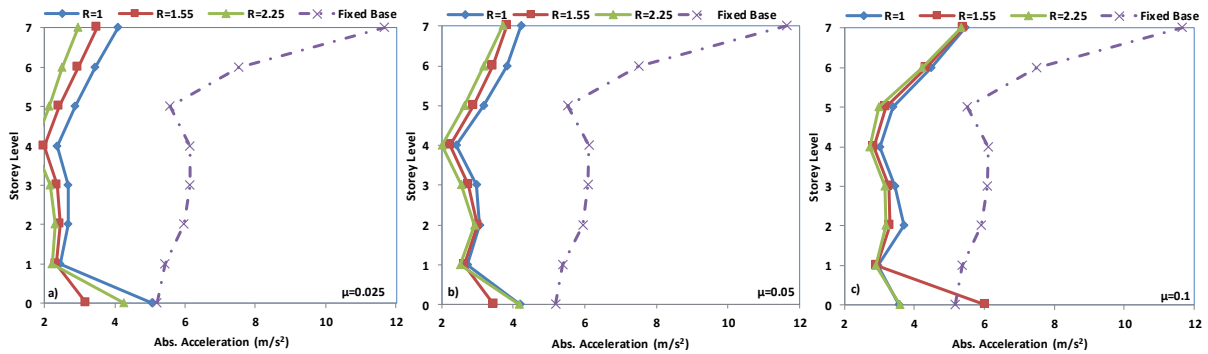
Figure 15. The variation of the absolute acceleration of 7-storey against storey height under Northridge earthquakes

3.5 Base Shear

The base shear demands of the fixed base 3 and 7-storey frames subjected to Cape earthquake are 461.7 and 506.2 kN, respectively. When each of the isolated frames subjected to the ground motions their responses are obtained. For example, the examined isolated frames subjected to Cape earthquake that is depicted in Figures 16 and 17. The use of FPS remarkably reduced the base shear especially 3-storey isolated frames. Besides the variation of the friction coefficient from 0.01 to 0.025, shifting the isolation period from 2.0 s to 3 s (corresponding the radius of curvature is 1m to 2.25 m) also caused steady reduction on the base shear. Additionally, almost similar responses are valid for 7-storey isolated frames as well (see Figure 17). When R2.25µ2.5 was implemented for 3 and 7-storey frames as isolation system that ensured the lowest base shear demand with respect to the other isolation systems as depicted in Figures 16 and 17.

The most remarkable behavior is observed under Cape earthquake, 3 and 7-storey frame with the isolation system of R2.25µ2.5 introduced the lowest base shear of 82.3kN and 164 kN, respectively. It is also noted that the aforementioned nonlinear analysis results on the base shear demand of the examined frames did not differentiate with the earthquake characteristics, similar trend is observed as well.
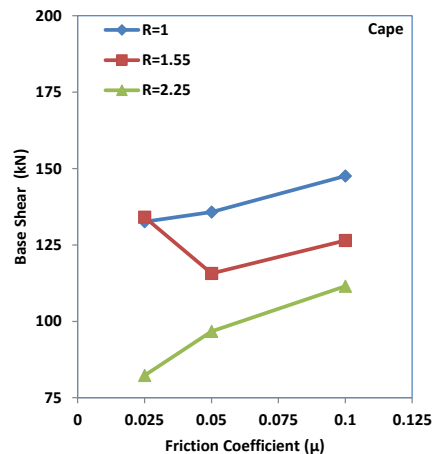
Figure 16. The base shear of 3-storey isolated frame with isolation period and Q/W ratio
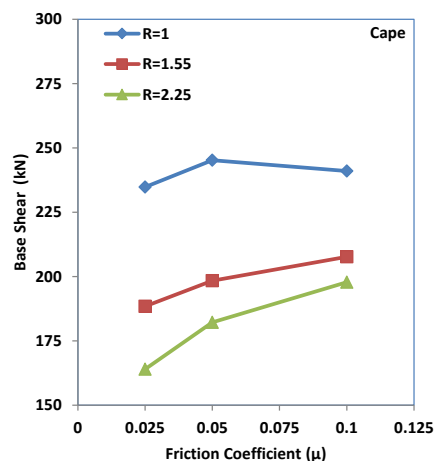
Figure 17. The base shear of 7-storey isolated frame with isolation period and Q/W ratio

3.6 Hysteretic Curve

The hysteretic curves of the 9 isolation models including different radius of curvature and friction coefficient for 3 and 7-storey frames under Hills earthquake is plotted in Figures 18 and 19. These obtained curves were similar to the bi-linear force-deformation as characteristic hysteretic curve of FPS. When the isolation parameters were computed in the light of the Equations (1-6) 9 different isolation systems were acquired and also the positions of the hysteretic curve shifted while it abided by the original force-deformation curve. Because of limited number of pages only the friction coefficient of 0.1 is plotted for 3 and 7-storey frames with FPS. Among the isolation systems, the smallest and largest hysteresis curves was performed for the radius of curvature of 1 m and 2.25 m, respectively and the other model was remained between them. Further, the effectiveness of SMRF with FPS can be very easily tuned by managing the appropriate radius of curvature and friction coefficient.
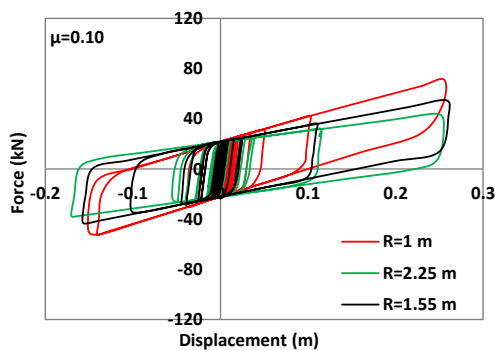
Figure 18. The hysteretic curve of 3-storey frame with FPS under Hills earthquake
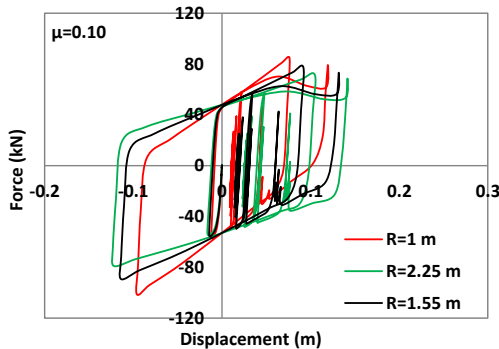
Figure 19. The hysteretic curve of 7-storey frame with FPS under Hills earthquake

4. Conclusions

In this study, it is showed that the radius of curvature, R and friction coefficient, μ on the design of base-isolated frame subjected to three natural accelerograms compatible with seismic hazard levels of 2% probability of exceedance in 50 years were considered. The response of FPS was remarkably changed by the radius of curvature

and friction coefficient. For all models, the amplification of the radius of curvature (the isolation period, T) and reduction of the friction coefficient remarkably led to great reduction in the roof displacement. For the R2.25μ2.5, it was experienced the most uniform relative displacement, interstorey drift ratio and absolute acceleration height of storey with respect to the both fixed base frame. To rehabilitate the 3 and 7-storey frames in terms of the local and global deformations R2.25μ2.5 obviously seemed to be the most favourable model when the seismic performance of the frames with and without FPS compared. According to the result of the analysis, it can be predicted that the larger radius of curvature and lower friction of coefficient for SMRF with FPS provided better seismic performance than other models and fixed base in real life.

Nomenclature

F	: The resisting force
k_2	: The horizontal stiffness
T	: The period of isolated structure
k_{eff}	: Effective stiffness
β_{eff}	: Effective damping
W	: Total weight on the isolator
g	: gravitational force
R	: The radius of curvature
D	: The horizontal displacement
μ	: The friction coefficient

References

1. Matsagar, V.A., and R.S., Jangid, *Influence of isolator characteristics on the response of base-isolated structures.* Engineering Structures, 2004. **266**: p. 1735-49.

2. Xu, C., J.G. Chase, and G.W. Rodgers, *Physical parameter identification of nonlinear base-isolated buildings using seismic response data.* Computers and Structures, 2014. 14**5**: p. 47-57.

3. Alhan, C. and S. Öncü-Davas, *Performance limits of seismically isolated buildings under near-field earthquakes.* Engineering Structures, 2016. **116**: p. 83-94.

4. Cancellara, D. and F.D., Angelis, *Assessment and dynamic nonlinear analysis of different base isolation systems for a multi-storey RC building irregular in plan.* Computers and Structures, 2017. **180**: p. 74-88.

5. Naeim, F. and J.M. Kelly. 1999, *Design of Seismic Isolated Structures.* John Wiley & Sons, New York, NY, USA, 1st edition.

6. Bhuiyan, A.VR., Y., Okui, H., Mitamura, and, T., Imai, *A rheology model of high damping rubber bearings for seismic analysis: Identification of nonlinear viscosity,* International Journal of Solids and Structures, 2009. **46:** 1778–1792.

7. Landi, L., G. Grazi, P.P., Diotallevi, *Comparison of different models for friction pendulum isolators in structures subjected to horizontal and vertical ground motions.* Soil Dynamics and Earthquake Engineering, 2016. **81**:p. 75-83.

8. Castaldo, P. and M. Ripani, *Optimal design of friction*

pendulum system properties for isolated structures considering different soil conditions. Soil Dynamics and Earthquake Engineering, 2016. **90**:p. 74-87.

9. Castaldo, P., B. Palazzo, and P.D., Vecchia, *Seismic reliability of base-isolated structures with friction pendulum bearings.* Engineering Structures, 2015. **95**: p. 80-93.

10. FEMA, *NEHRP commentary on the guidelines for the seismic rehabilitation of buildings,* 1997, Federal Emergency Management Agency, Report No. 274. Washington, DC.

11. Jangid, R.S., *Optimum friction pendulum system for near-fault motions.* Engineering Structures, 2005. **27**: p. 349-359.

12. M. Ferraioli, M., A. Lavino, and A. Mandara, *Behaviour Factor of Code-Designed Steel Moment-Resisting Frames.* International Journal of Steel Structures, 2014. 14 (2): p. 243-254.

13. Italian Code NTC08, *Norme tecniche per le costruzioni in zone sismiche,* **2008.** Ministerial Decree D.M. 14.01.08, G.U. No.9-04.02.08 (in Italian).

14. Tsai, C.S., T.C. Chiang, and B.J. Chen, *Finite element formulations and theoretical study for variable curvature friction pendulum systems.* Engineering Structures, 2003. **25**. p:1719-30.

15. Mazza, F. and M, Mazza, *Nonlinear seismic analysis of irregular r.c. framed buildings base isolated with friction pendulum system under near-fault excitations.* Soil Dynamics and Earthquake Engineering, 2016. **90**: p. 299-312.

16. Computers and Structures, Inc., SAP 2000 Advanced 14.0.0. *Structural Analysis Program*, 2011, Berkeley, CA

17. Park, Y.J., Y.K., Wen, and A.H., Ang, *Random Vibration of Hysteretic Systems under bi-directional ground motions*, Earthquake Engineering and Structural Dynamics, 1986. **14**, p. 543-557.

18. PEER, The Pacific Earthquake Engineering Research Center". *User's Manual for the PEER Ground Motion Database Application*, 2011, University of California, Berkeley.

Research Article

Investigation of the usability to nut shell ash as a mineral additive in concrete

Korkmaz Yıldırım [a],*, Mensur Sümer [b], Yüksel Furkan Yıldırım [c]

[a] *Adnan Menderes Üniversitesi Aydın Meslek Yüksekokulu, Efeler/Aydın, Türkiye.*
[b] *Sakarya Üniversitesi, Mühendislik Fakültesi İnşaat Mühendisliği, Serdivan/Sakarya.*
[c] *Sakarya Üniversitesi, Mühendislik Fakültesi İnşaat Mühendisliği, Serdivan/Sakarya.*

ARTICLE INFO	ABSTRACT
	Experimental studies are being carried out to obtain puzzolan materials from agricultural wastes. The aim of this study was to minimize environmental damage of nut shells, which are discarded as waste material after the harvesting of crops. Puzzolanic activity test conducted in experimental study showed that nut shell ash provided compressive strength at 0.59 level. An analysis of compressive strength results revealed that compressive strength increases in 28-90 and 180 day values of the specimens containing nut ash additive. Reference compressive strength results showed that compressive strength increased by approximately 57% when water/cement ratio increases and that compressive strength decreased to 50% level with the increase of additive amount in both groups of concretes with nut shell additives. ASR test results showed that ash additive used in mortar types used in 5%-10%-15%-20%-25%-30% ratios had an effect and that it reduced ASR in mortar type containing 20% additive below 0.20 maximum value which is the standard value. Improvement of ash preparation conditions will enable the use of nut shell ash as a mineral additive.

1. Introduction

Increasing types of concrete structures requires the development and use of new technologies. Thus types of cements and concrete production continue to increase. Puzzolanic mineral materials have been used together with cement in production of concrete to improve the qualities of cement and concrete, to enhance their resistance and to save money. To this end, industrial by-products apart from puzzolans are used. Industrial puzzolanic materials used in concrete contain volatile ash, silica fume and ground granulated blast furnace slag.

Puzzolanic materials are natural materials consisting of silica, aluminum or the combination of these two. When mixed with water, puzzolanic materials do not naturally harden; however, when they are fine ground, they react to form calcium silicate and calcium silicate compounds that enhance resistance with dissolved calcium hydroxide ($CaOH_2$) at normal environmental temperature in the presence of water.

Puzzolans are in fact composed of reactive silicium dioxide (SiO_2) and aluminum oxide (Al_2O_2). The remaining part contains iron oxide (Fe_2O_2) and other oxides. Puzzolanic materials should be properly prepared, homogenized, dried, exposed to heat processing in production and should be fine ground [1].

Furthermore, experimental studies are being carried out to obtain puzzolan materials from agricultural wastes. Rice husk ash, wheat stem etc can are examples of these experimental studies.

Plants intake various minerals and silicates from the soil by their roots. Inorganic substances, especially silicates are known to be found in higher amounts in annual plants when compared to other types of trees. Annual agricultural productions such as rice, wheat, sunflower, tobacco, nut etc. are rich in silica and silicate due to their stem, leaves and protective layers. Inorganic compounds are found in plant in the form of free salts or particles or in the form of cations that are partially attached to anionic groups [2].

Burning of organic substances in agricultural wastes, formation of crystal phases or crystallization of amorphous substances are exothermic reactions. Weight

* Corresponding author. Tel.: *+90 5324067725*; Fax: *+ 0 256 2125714*.
E-mail addresses: *korkmazy54@gmail.com (K. Yıldırım), msumer@sakarya.edu.tr (M. Sümer), furkan5448@gmail.com (Y.F. Yıldırım).*

decreases and ash is produced as a result of this reaction. Degradation of the structure of organic substances as a result of burning is called thermal decomposition [3].

When this ash, which is thinned by grinding into powder, is mixed with lime, material with a bonding property is obtained. The quality of this material varies largely depending on burning temperature, burning duration, sudden cooling and grinding conditions [4-6].

75% of the world's nut is produced in Turkey and approximately 85% of the world's nut export takes place in Turkey. Turkey is the most important determiner country in both production and exports of nut. According to 2004 data, Turkey produced 400.000 tons of nuts [7].

In a master's thesis, titled "Identification of Thermal Value of Organic Substances in Municipal Rubbish Composition", Halisdemir (2001) found that nut shell constitutes approximately 15% of the mass of nuts. In light of this information, it can be stated by a rough calculation that a total of 16.830 tons of shell is produced from the nuts that were exported in 2004.

Nut shell is an easily available and convenient potential source as it is produced in nut processing facilities. However, nut shell is usually used as a fuel, while it can be used as raw material in various industrial branches (plywood, chipboard, floor linoleum, plastic, dye, polishing oil etc.) [8].

Concrete elements are known to gain strength in the long term. Rheological behavior of concrete samples produced with nut ash additives remains unknown. In this respect, studies have concentrated on the usability of nut ash as a suitable additive when ash production conditions are improved.

In the present study, the coats on nut shell were subjected to pre-washing and the obtained ash was ground to 0-200μ. Puzzolanic activity test, compressive strength test and ASR test that affects strength were carried out using this ash.

2. Some Studies Conducted on Nut Shell

The literature contains studies on the use of nut shell ash as biogas and on nut cultivars that are grown in terms of the diversity geographical origin.

In a previous study on the removal of cadmium ions from aqueous solutions, it was found that obtaining nut shell and nut shell ash is more advantageous using absorption method [9] In another study which aimed to determine the effect of different carbonization conditions on solid crop yield nut shell (Corylus Avellana) was carbonized and the effect of temperature, heating rate and particle size on carbonization solid crop yield was analyzed. In conclusion, it was found that the solid product that was obtained as a result of carbonization can

be used as an environmentally friendly, solid fuel with high energy content [10].

Another study studied the effects of particle size and mini reactor internal pressure and liquefaction yield in conversion of nut shell, which is a potential waste, under high pressure and high temperature (HP/HT). The study reached the following results:

Potential benefits can be achieved by converting nut shell which has a great potential especially for Turkey using liquid products.

• CO_2 production is zero,
• Prevention of climate change and conservation of the environment
• Conservation of resources,
• Conservation of energy,
• Reduced need for petroleum by the use of the obtained oil.
• Product composition can be used as a source of chemical substance instead of petroleum [11].

3. Materials Used in the Experimental Process

3.1 CEN Standard Sand

Rilem-Cembureau standard sand compatible with TS EN 196-1was used to prepare cement mortar specimens. Granulometric properties of the sand are presented in Table 1. Unit weight of the sand was found to be 2.01 gr/cm^3 [12].

Table 1.Granulometry values of rilem sand

Sieve Mesh Size (mm)	Material retained on the sieve (%)
0.08	98 ±2
0.16	87 ±2
0.50	67 ±2
1.00	33 ±2
1.60	9 ±2
2.00	0

3.2 Aggregate

The aggregate we used in experimental study was supplied from a sand gravel quarry near Sakarya River– Geyve town. The aggregate had a thickness of 0-7 mm. Firstly, amount of active silica on the aggregate was determined using chemical analysis method in accordance with ASTM C289, TS 2517 standard. It is presented in Table 2 that it is on harmful zone [16, 17].

Table 2. Chemical ASR report conducted in accordance with TS 2517

NaOH (Consumed)	350 (mmol/L)
SiO$_2$ (Solved)	700 (mmol/L)
Result	III. Zone (Hazardousaggregate)

Analysis values of cement and nut shell ash used in ASR test are presented in Table 3.

3.3 Cement and Nut Shell Ash

In this study CEM I 42.5 R cement was used. Chemical properties of this cement are presented in Table 2 [13].

Ash was obtained by burning the nutshells that were collected after harvesting season in heating boiler. The ash was ground in mill. Chemical analysis of the ash presented in Table 2 was conducted in laboratory of Oyak Bolu Cement Factory.

Nut shell, which is an organic waste, was converted to ash by burning. The ash was ground to power form. When this ash is mixed with lime, a material with bonding quality is obtained. The quality of this material largely varies depends on burning duration, shock cooling and grinding conditions. Chemical analysis results of the ash revealed excessive potassium oxide (K_2O) CaO_2 calcium oxide amount was found to be very low.

According to ACI 221, cement equivalent alkali amount ($Na_2O+0.658K_2O$) should be maximum 0.6% and it is recommended that this limit be 0.4%. Ratio of alkali amount of cement used in the test was ($Na_2O+0.658(K_2O)$) = $0.22*0.658*0.46=0.52$ (Na_2O), which is below the value of 0.6%.[14] Chemical analyses of nut shell ash and cement are presented in table 3. SEM and microscope images are presented in Figure 1.

Table 3. Chemical analysis values of cement and nut shell ash

	CEM I 42.5 R	Nut Shell Ash
SiO_2	19.95	17.36
Al_2O_3	5.12	2.38
Fe_2O_3	3.75	3. 34
CaO	63.82	12.73
MgO	1.64	5.56
SO_3	3.36	2.77
Na_2O	0.22	0.33
K_2O	0.46	45.04
Na_2O Equivalent	0.52	-----
Loss on ignition	1.11	-----
sCaO	1.23	-----
45 Micron	1.90	57. 2
90 Micron	---	---
Specific Weight	3.13	2.62
Blaine	3971	2837

4. Experimental study

4.1 Puzzolanic Activity Test

The activity of pozzolansis determined by mechanical and chemical tests [15]. Mixture ratios of mortar specimens produced for puzzolan activity test is presented in table 4. The ash that was used as puzzolan was prepared by replacing 20% cement. In this mixture ratio, 6 pieces were prepared from each group of size 40 * 40 * 160 mm.

SEM İmage

SEM Chemical Analysis

Steriomicroscope İmage
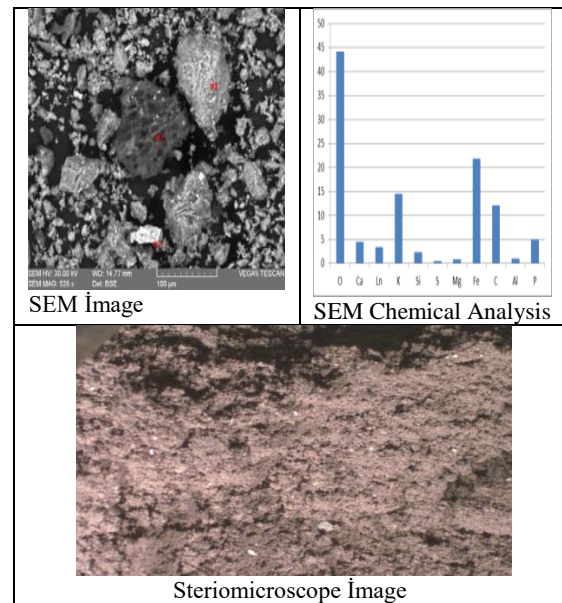
Figure 1. Sterio Microscope and SEM İmages of Nut Shell Ash

Table 4. Puzzolanic activity mortar mixture amount

	Pozzolan Additive (20%) (g)	Cement (g)	Standard Sand (g)	S/C=0.5 Water (g)
Reference Specimen	---	500	1320	250
Nut Shell Ash	100	400	1320	250

7 day and 28 day compression strength tests were carried out with these specimens. Test results are presented in table 5 and Figure 2.

Table 5. Puzzolanic activity compressive strength results of nut shell ash

	7-day results		28-day results	
	Compressive Strength (N/mm^2)	Percentage of Compressive Strength	Compressive Strength (N/mm^2)	Percentage of Compressive Strength
Reference Specimen	26.7	1.00	46.8	1.00
Concrete with nut shell ash additive	18.5	0.69	27.4	0.59
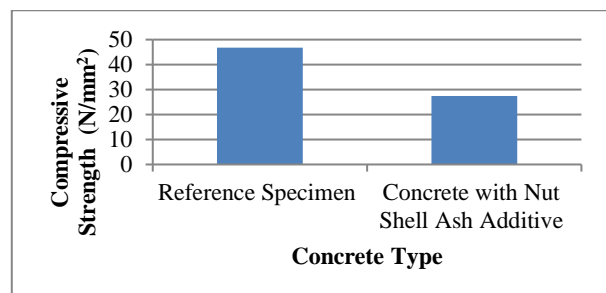
Figure 2. Nut Shell Ash Puzzolanic Activity Test 28-day Compressive Strength

As a standard, ash should have a value of 70% (0.70) in order to be used as puzzolan. Results of puzzolan activity test revealed a compressive strength of 59% (0.59) in 28-day test. This was believed to stem from the fact that nut shells were not burned in appropriate furnace and temperature in laboratory conditions. It was observed that puzzolanic property would be better if ash preparation conditions are improved.

4.2 Test Method for Potential Alkali Reactivity Aggregates (Accelerated Mortar Bar Test)

4.2.1 Preparation of Specimen Groups

Appropriate aggregate was prepared by sieving the aggregate according to mixture ratios in ASTM-C 227. In our tests, while preparing 5%-10%-15%-20%-25%-30% mortar bars in accordance with ASTM-C 227 standard using nut shell ash replacing cement, mortar mixture was prepared in such a way to have an aggregate/cement ratio of 2.25; a spread value of 120-150 mm and W/C ratio of 0.47. Minimum four mortar specimens were prepared from each group in 25×25×285 mm prismatic molds [18]. Material mixture ratios of the control mixture and of the specimens produced by 5%-10%-15%-20%-25%-30% nut shell ash replacing cement are presented in table 6.

Table 6.   Material mixture values of test specimens

Additive Ratios	Aggregate (g)	Cement (g)	Mineral Additive (g)	Water (g)
Reference Specimen	1320	587	---	276
5% Nut Shell Ash	1320	557.65	29.35	276
%10 Nut Shell Ash	1320	528.3	29.35	276
%15 Nut Shell Ash	1320	498.95	58.7	276
%20 Nut Shell Ash	1320	469.6	88.05	276
%25 Nut Shell Ash	1320	440.25	117.4	276
%30 Nut Shell Ash	1320	410.9	146.75	276

Standard values of this method which is known as ASTM-C 1260 accelerated mortar bar test are presented below [19]. Expansion percentages at the end of 16-day test are evaluated as follows:

* If the expansions at the end of 16 days are below 0.10%, the aggregates show harmless behavior.

* If the expansions at the end of 16 days are above 0.20%, the aggregates show potentially harmful expansion.

* If the expansions at the end of 16 days are between 0.10%, and 0.20%, the aggregates can show both harmful

and harmless behavior at construction site conditions. If the expansions at the end of 16 days are between the values of 0.10% and 0.20%, test duration for the aggregates had better be continued for 28 days [19]. Expansion results of control mixture and specimens with nut shell ash are presented in table 7. ASR formation graph is presented in Figure 3.

Table 7. Expansion values of accelerated mortar bar test

	Reference Specimen	Nut shell ash additive ratios					
		5%	10%	15%	20%	25%	30%
9 Day	0.60	0.24	0.20	0.17	0.15	0.21	0.17
16 Day	0.83	0.31	0.25	0.19	0.16	0.22	0.18
28 Day	0.92	0.37	0.37	0.29	0.23	0.19	0.22
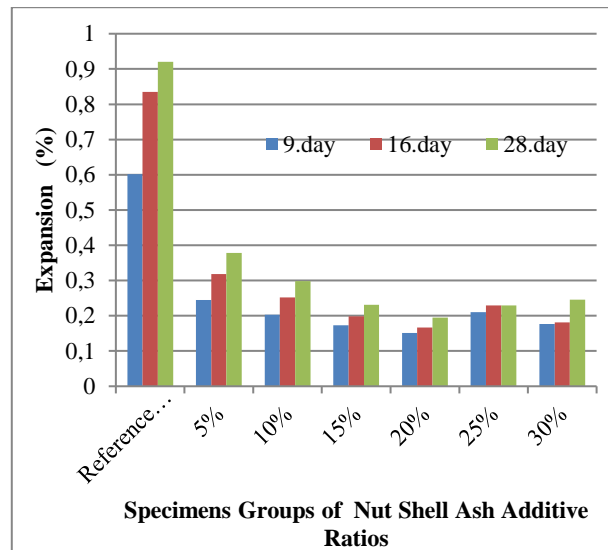
Figure 3. ASR Formation in Mortar Groups with Nut Shell Ash Additive

Results of ASTM-C 1260 accelerated mortar bar test revealed that when maximum standard value was taken as 0.20, it reduced below the standard value in the product with 20% additives. In other groups it was observed that;
* It reduced expansion at a ratio of approximately 0.59 in mortar type with 5% additive, when compared to the control mixture,
* It reduced expansion at a ratio of approximately 0.68 and 0.75 in mortar types with 10% and 15% additive respectively,
* It reduced expansion at a ratio of 0.79 and 0.75 in mortar types with 20% and 25% additive respectively,
* It reduced expansion at a ratio of 0.73 in mortar type with 30% additives.
It can be stated that this fluctuation in determination of ASR results from excessive amount of potassium oxide in the ash.

4.3 Determination of Compressive Strength of Test Specimens

Concrete compressive strength is expressed as $f_{c\ cube}$ if cube shaped specimens in compliance with the standard are produced for compressive strength. Compressive strength is determined in specimens of 7 and 28 days [20]. Fine aggregates exposed to 60% ASR, 40% fine chips and cement and nut ash, whose analysis values are explained above, were used in compressive strength tests. Concrete mixture groups were prepared in 10×10×10 cm test cubes. Six groups of concrete with a W/C ratio of 0.45 and 0.60; nut ash additive ratio of 10% and 20% were prepared for compressive strength test.

Material ratios of concrete mixture are presented in table 8 in unit of m^3. Compressive strength values are presented in table 9 and figure 4.

Table 8. Material mixture ratios of concrete prepared for compressive strength

Additive Ratios	0-8 mm Sand (kg) %60	8-13 mm Gravel (kg) %40	Cement (kg)	Mineral Additive (Nut Shell Ash)	Water (kg)
Reference Specimen 1	1040	714	420	----	189
FK 1 % 10	1040	714	378	42	189
FK 2 % 20	1040	714	336	84	189
Reference Specimen 2	1040	714	250	----	150
FK 3 % 10	1040	714	225	25	150
FK4 % 20	1040	714	200	50	150

Setting time of concrete specimens was approximately 10 hours in witness sample, while setting occurred in approximately 44-48 hours in specimens no FK3 and FK4 containing nut shell ash.

Table 9. Compressive strength values of the prepared concrete groups

	28 day (MPa)	90 day (MPa)	180 day (MPa)
ReferenceSpecimen 1	56.62	58.3	59.9
FK 1 %10	31.64	33.3	36
FK 2 %20	27.88	30.37	32.6
Reference Specimen 2	32.28	36.22	37.6
FK3 %10	20.54	25.2	27.8
FK4 %20	20.92	22.89	24
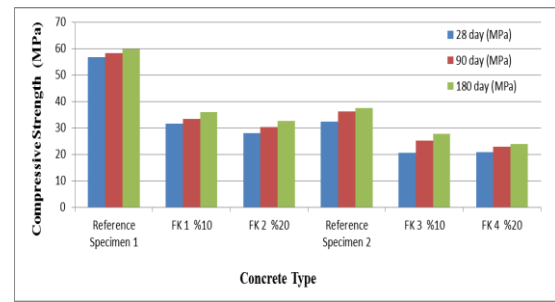
Figure 4. Compressive Strength Results of Concrete Groups with Nut Ash Additive

According to compressive strength test results,
* In reference specimen 1, in concrete group with a water/cement ratio of 0.45, compressive strength decreased by 56% in specimen with 10% nut ash additive and by 49% in specimen with 20% nut ash additive when compared to the reference specimen.
* In reference specimen 2, compressive strength decreased by 63% in concrete group with a water/cement ratio of 0.6 in specimens with 10%nut ash additive and by 65% in the group with 20% additives.
* In reference specimen 1 and reference specimen 2, strength decreased by 57% when water/cement ratio increased.
*According to the results of 90 and 180 day compressive strength test it was observed that strength increased, however it decreased by increasing at the same ratios.

Figure 5. Image of Concrete Specimen containing 10% Nut Shell Ash Additive

In specimen groups with a water/cement ratio of 0.45, setting occurred normally.

It was understood from Figure 5 that hardening of the concrete groups with a water/cement ratio of 0.60 was delayed. This delay in setting time is believed to be caused by excessive amount of potassium oxide in the ash.

5. Results and Discussion

Nut ash puzzolanic activity test, concrete compressive strength test and alkali silica reaction test affecting strength were carried out in this study, which analyzed the usability of nut shell ash in concrete products.

Results of puzzolanic activity test showed that the specimens showed a strength ratio of 0.59 when compared to the control specimen. According to test

result, although it has lost the property of being a puzzolan at the level of 0.11, it was observed that it will give a better result when it is produced in a better environment.

ASR test was carried out to determine reduction level of alkali silica reaction, which affects concrete strength. An analysis of ASR test results revealed that ash additive used in mortar types containing additives at the ratios of 5%-10%-15%-20%-25%-30% had an effect and that it reduced ASR below the standard level of maximum 0.20 in mortar type containing 20% additive.

High potassium oxide (K_2O) observed in nut culture analysis was thought to cause fluctuation of expansion values.

According to compressive strength test results;

* In Reference specimen 1, in concrete group with a water/cement ratio of 0.45, compressive strength decreased by 56% in specimen with 10% nut ash additive and by 49% in specimen with 20% nut ash additive when compared to the reference specimen.

* In Reference specimen 2, in concrete group with a water/cement ratio of 0.60, compressive strength decreased by 63% in specimens with 10% nut ash additive and by 65% in specimens with 20% nut ash additive when compared to the control specimen.

* In Reference specimen 1 and References specimen 2, strength decreased by 57% when water/cement ratio increased.

* According to 90 and 180-day compressive test results, it was observed that strength increased however strength decreased by increasing at the same ratios.

Based on these results, this material can be used in filling works on roads. Diversification of the content of studies will enable the use of nut shell ash in economy instead of a waste material.

References

1. Nagataki, S.,Ohga, H., andInoue, T., *Evaluation of Fly Ash for Controlling Alkali-Aggregate Reaction*, 955-972, Proc. 2nd International Conference on Durability of Concrete, Montreal, Canada, 1991, p. 955-972.

2. Rydjolm, SA., *Pulpin Processen* İnter Science Publishers, Newyork,1965, p. 1269.

3. Cook,J., *Using Rice Husk Formaking Cement like Materials*, Approproite Technology 1980, **6**(4): p. 9-11.

4. James, J., Rao,S., *Silica from Rice Husk through Thermal de Compositioon*, Termochimica Acta, 1986. **97:** p. 329-336.

5. R., Ngee, C.C., Yeoh, A.K., Ping, C.B., *Rice Husk Cement,* Standarts Industrial Research Institute of Malaysia, 1984.

6. Dass, A., *Puzzolanic behaviour of Rice Husk Ash*, Building Research and Practice, 1984. **12**(5): p. 307-311.

7. Mızrak, G., *Nut Specialization Commodity Exchange*, 2005, Ordu, p. 49.

8. Halisdemir, B., *Identification of Thermal Value of Organic Substances in Municipal Rubbish Composition*, Master's Thesis, Institute of Science, Department of Environmental Engineering, Mersin, 2001, p: 65.

9. Jamali,H.A, Mahvi,A.H, and Nazmara Shanrookh, *Removal of Cadmium from Aqueous Solutions by Hazel Nut Shell*, World Applied Sciences Journal, 2009, **5**: p. 16-20.

10. Özçimen, D. Ersoy, M., *Statistical Evaluation of the Carbonization Results of Hazelnut Shell*, Istanbul Technical University Journal, 2009. **8**(1): p.116-124.

11. Pehlivan, E. Taner, F., *Determination of Particle Size and Inner Pressure on Liquefaction Performance of Hazelnut Shell in HP/HT Small Reactor,* Selçuk University, Journal of the Faculty of Engineering and Architecture, 2006. **21** n.1-2.

12. TS EN 196-1, *Methods of Testing Cement-Part 1: Determination of Strength*, Turkish Standards Institute, Ankara, 2002.

13. TS-EN 197-1, *General Cements-Composition and Conformity Criteria*, Turkish Standards Institute, Ankara, 2002.

14. Yıldırım, K., Sumer, M., (2014), Comparative Analysis of Fly Ash Effect with three Different Method in Mortars that are Exposed to Alkali Silica Reaction, Composites: Part B, 2014, **61**: 110–115.

15. ASTM C618 - *12a Standard Specification for Coal Fly Ash and Raw or Calcined Natural Pozzolan for Use in Concrete,* ASTM Internatıonal, West Conshohocken PA, 2012, Available from: www.astm.org

16. ASTM C-289-94 *Standard Test Method for Potential Reactivity of Aggregates (Chemical Method),* Annual Book of ASTM Standards, Annual Book of ASTM Standards, Concrete and Aggregates, Philadelphia, PA, USA, American Society for Testing and Materials, 1994. **4**(2): p. 157-163.

17. TS 2517, *Chemical Test for Potential Reactivity of Alkali Aggregates*, Turkish Standards Institute, Ankara,1977.

18. ASTM C-227-97*, Standard Test Method for Potential Alkali Reactivity of Cement-Aggregate Combinations (Mortar-Bar Method),* Annual Book of ASTM Standards, Concrete and Mineral Aggregates, Philadelphia, PA, USA, American Society for Testing and Materials, 1994. **4**(2): p. 126-130.

19. ASTM C-1260-94, *Standard Test Method for Potential Alkali Reactivity of Aggregates (Mortar-Bar Method),* Annual Book of ASTM Standards, Concrete and Aggregates, Philadelphia, PA, USA, American Society for Testing and Materials, 1994. **4**(2): p 650-653.

20. TS EN 12390-3, Testing Hardened Concrete - Part 3: Compressive Strength of Test Specimens, Turkish Standards Institute, Ankara, 2002

Research Article

Investigation on limitation of reduced relative storey drifts according to TEC 2007

Muhammet Musab Erdem [a], Murat Bikçe [a],*

[a] *Department of Civil Engineering, Iskenderun Technical University, Hatay, Turkey*

ARTICLE INFO	ABSTRACT
	During the earthquake motion, limitation of storey drifts of is important. Maximum storey drifts for the structures to be constructed in our country has been restricted by Turkish Earthquake Code (TEC) which is in force since 2007, according to the provision of relative storey drift and A1, A2 irregularity factors. In the earthquake code which is published as draft in 2016 and is not in force yet, it has been planning to restrict the storey drifts for with and without gap conditions of infill wall - frame connections. First of all, it is aimed to investigate the limits of maximum reduced relative storey drift under specified conditions according to TEC 2007. In this study, the maximum values of allowable reduced storey drifts were specified separately for reinforced concrete buildings which have 2.75m – 4.25m storey height interval, according to limitations specified in section of TEC 2007 that is "Calculation and Limitation of Effective Relative Storey Drifts" for each of the Structural System Behavior Factors (R). Additionally, as an example, maximum relative story drifts have calculated according to "A1- Torsional Irregularity" section of TEC 2007 by using the relative storey drifts which belongs to a building from literature, and for this building, maximum relative storey drifts has calculated according to "B2- Interstorey Stiffness Irregularity" section of TEC 2007 for variable interstorey heights. At the end of the study, maximum values of relative storey drifts in the floor have revealed according to average storey drifts and storey height ratios.

1. Introduction

Due to the fact that a most part of Turkey is located in the earthquake zone, earthquake resistant structural design is very important for our country. The regulations regarding the earthquake resistant structural design are determined by standards and regulations. During the earthquake motion, the drifts that occur in the buildings have an importance in terms of building safety. The relative storey drifts is limited by TEC 2007 which is still in force, and TEC 2016 draft according to some certain conditions. In these two regulations, the limitation rules for relative storey drifts are given separately. However, in this study, it is aimed that first of all the maximum reduced storey drift limits, which will not cause A1 and B2 irregularities, mentioned in the current TEC 2007 will be revealed by ignoring the second order effects.

The relative storey drifts of structures can be calculated by various commercial softwares. In addition, studies that calculate the relative storey drifts by various methods are

available in the literature [1-5]. However, in this study, the largest relative reduced storey drifts allowed by the following sections of the TEC 2007 are calculated.

Limitation on relative storey drifts are found in sections *"2.10.1. Calculation and Limitation of Effective Relative Storey Drifts"*, *"A1-Torsional Irregularity"* and *"B2- Interstorey Stiffness Irregularity (Soft Storey)"* in TEC 2007. In addition, second order effects are excluded from this study, since it is preferred to specify drift limits independent of storey weight and shear force, although there is a restriction on relative storey drifts in the section of *"2.10.2.1 Second Order Effects"*.

In this study, it is aimed to reveal the largest reduced relative storey drifts permitted in cast-in-site reinforced concrete buildings according to TEC 2007. Also in the second section of this study, the calculations for the relative storey drift limitations specified in the TEC 2007 are compared with the TEC 2016. In this context, firstly, according to *"2.10.1. Calculation and Limitation of*

* Corresponding author. Tel.: +90 (326) 613 56 00; Fax: +90 (326) 613 56 13.
E-mail address: *murat.bikce@iste.edu.tr*

Effective Relative Storey Drifts" section in TEC 2007, the maximum reduced relative storey drifts were calculated in the range of 2.75 - 4.25 m storey height for each of the structural system behavior factors for the cast-in-site reinforced concrete buildings. Then, using the relative storey drifts of a reinforced concrete building which is in the literature [7], the largest relative storey drifts without forming "*A1-Torsional Irregularity*" are calculated. Finally, the maximum average relative storey drifts which do not cause "*B2- Interstorey Stiffness Irregularity* " were calculated for the storey height ratios (h_i/h_{i-1}) between neighboring floors of 0.65 - 1 by using the largest average relative storey drifts in this structure. The largest reduced relative storey drifts which have not caused "A1-Torsional Irregularity" in the storey are calculated according to the average relative storey drifts obtained.

Table 1. Structural system behavior factor, R (TEC 2007 -Table 2.5)

BUILDING STRUCTURAL SYSTEM (Cast-in-site reinforced concrete buildings)	Systems of Normal Ductility Level	Systems of High Ductility Level
Buildings in which seismic loads are fully resisted by frames	4	8
Buildings in which seismic loads are fully resisted by coupled structural walls	4	7
Buildings in which seismic loads are fully resisted by solid structural walls	4	6
Buildings in which seismic loads are jointly resisted by frames and solid and / or coupled structural walls	4	7

2. Limitations on Relative Storey Drifts

Restrictions on Relative storey drifts are found in sections of *"A1-Torsional irregularity"*, "*B2- Interstorey stiffness irregularity*" and "Calculation and limitation of effective relative storey drifts" in TEC 2007. In this section, criteria limiting the relative storey drifts according to the TEC 2007 and the corresponding criteria in TEC 2016 draft are presented.

2.1 Torsional Irregularity

Torsional irregularity in TEC 2007 is expressed as the *Torsional Irregularity Factor* which is defined for any of the two orthogonal earthquake directions as the ratio of the maximum relative storey drift at any floor to the average relative storey drift at the same floor in the same direction, is greater than 1.2. To avoid torsional irregularity in a structure;

$$\eta_{bi} = \frac{(\Delta_i)_{max}}{(\Delta_i)_{ort}} \leq 1.2 \qquad (1)$$

condition must be satisfied. Here $(\Delta_i)_{max}$; the maximum reduced relative storey drift on the ith floor, $(\Delta_i)_{ort}$; refers to the average relative storey drift of the ith floor of the building. If the slabs are taken as a rigid diaphragm, the average reduced relative storey drift is calculated as $(\Delta_i)_{ort}=1/2[(\Delta_i)_{max}+(\Delta_i)_{min}]$ (Figure 1).
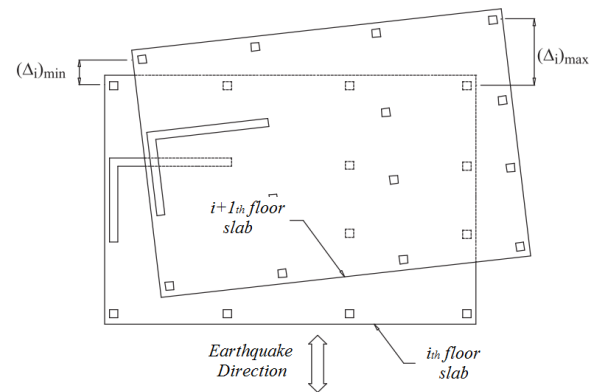
Figure 1. Floor plan in case of torsion (TEC 2007 – Fig. 2.1.)

This rule stated in the TEC 2007 was found without modification in the TEC 2016 draft.

2.2 Interstorey Stiffness Irregularity

In TEC 2007 interstorey stiffness irregularity is defined as the case where in each of the two orthogonal earthquake directions, *Stiffness Irregularity Factor* η_{ki}, which is defined as the ratio of the average relative storey drift at any i^{th} floor to the average relative storey drift at the floor adjacently above or below, is greater than 2.0. The criteria specified in Equation (2) must be satisfied in order to avoid interstorey stiffness irregularity.

$$\eta_{ki} = \frac{\left(\frac{\Delta_i}{h_i}\right)_{ort}}{\left(\frac{\Delta_{i-1}}{h_{i-1}}\right)_{ort}} \leq 2.0 \qquad (2)$$

Here, Δ_i and h_i refer to average reduced relative storey drift and storey height of ith floor; Δ_{i-1} ve h_{i-1} refer to average reduced relative storey drift and storey height of i-1th floor.

This rule is valid in the TEC 2016 draft except that basement floors are excluded from this rule.

2.3 Calculation and Limitation of Effective Relative Storey Drifts

According to TEC 2007, for each direction of earthquake, the maximum value of the effective storey drifts $((\delta_i)_{max})$ of columns or shear walls on any floor of the building must satisfy the rule given by Equation (3).

$$\frac{(\delta_i)_{max}}{h_i} \leq 0.02 \tag{3}$$

Here, the largest value of the effective relative storey drift ($(\delta_i)_{max}$) is equal to product of structural system behavior factor (R) and largest reduced relative storey drift ($(\Delta_i)_{max}$). Accordingly, Equation (3) is obtained in terms of the maximum reduced relative storey drift, in the form:

$$\frac{R(\Delta_i)_{max}}{h_i} \leq 0.02 \tag{4}$$

When $(\Delta_i)_{max}$ is taken the lead in Equation (4), the maximum value of the reduced relative storey drift is obtained as in the Equation (5).

$$(\Delta_i)_{max} \leq \frac{0.02 \cdot h_i}{R} \tag{5}$$

This part of TEC 2007 contains significant changes in the draft TEC 2016 [8]. The effective relative storey drifts of a column or a shear wall in any earthquake direction is obtained by Equation (6).

$$\delta_i^{(X)} = \frac{R}{I}\Delta_i^{(X)} \tag{6}$$

Here, the effective relative storey drift of the x - direction is $\delta_i^{(X)}$; structural system behavior factor is R; Building importance factor is I; the reduced relative storey drift in x - direction is expressed as $\Delta_i^{(X)}$. In TEC 2007, effective relative storey drift is obtained by multiplying the reduced relative storey drift by the structural system behavior factor, in the TEC 2016 draft, it is obtained by dividing the product of the structural system behavior factor and the reduced relative storey drift by the building importance factor.

In the TEC 2016 draft, two separate effective relative storey drift delimiting criteria have been defined, depending on the presence or absence of flexible joints between infill walls and frame. In Equation (7), for the cases where the flexible joint is not placed between the infill wall and frame (adjoined), Equation (8) gives the criteria to be satisfied for the cases where the flexible joints are present between the infill wall and frame.

$$\lambda \frac{\delta_{i,max}^{(X)}}{h_i} \leq 0.008 \tag{7}$$

$$\lambda \frac{\delta_{i,max}^{(X)}}{h_i} \leq 0.016 \tag{8}$$

In Equations (7) and (8), the maximum value of the effective relative storey drifts and storey height are denoted by $\delta_{i,max}^{(X)}$ and h_i respectively. The λ coefficient in these equations is expressed as the ratio of the elastic design spectral acceleration calculated according to the DD-3 earthquake to the elastic design spectral acceleration calculated according to the DD-2 earthquake.

When these limiting criteria are examined, it is seen that there are significant differences in TEC 2007 and TEC 2016. While limitation of the effective storey drifts is affected by the structural system behavior factor and storey height in TEC 2007, it is affected by the structural system behavior factor, storey height, building importance factor, natural period of the structure, joint type of infill wall and frame, the location of the structure and the distance to the active fault plane in TEC2016.

3. Calculation of Relative Storey Drifts

In this section, the largest relative storey drifts of the structure that can be obtained under the specified conditions are calculated according to TEC 2007. In the calculations, the maximum allowable relative storey drifts are calculated for each structural system behavior factor (R = 4, 6-8) in the storey height range 2.75 m - 4.25 m according to the rule given in Equation (5) (Figure 1).

According to the calculations, the maximum values of the relative storey drifts in the floor are in the range of 6.875 mm - 21.25 mm as seen in Figure 2.

The calculation of the relative drifts in the "*A1 Torsional Irregularity*" section in the TEC 2007 is made according to Equation (1). According to this rule, there is no torsional irregularity in buildings where the torsional irregularity factor η_{bi} is equal or smaller than 1.2. According to Equation (1), which determines the torsional irregularity, the average relative storey drifts of the floors must be known in order to calculate the maximum relative storey drift. For this reason, the relative storey drifts obtained in literature is used here [7]. The relative storey drifts in this structure vary between 1.5 mm and 6.5 mm.

For relative storey drifts between 1.5 mm and 6.5 mm, the maximum values ($(\Delta_i)_{max}$) of the relative storey drifts that satisfy $\eta_{bi} = 1.2$ are given in Figure 3.

As can be seen in Figure 3, the maximum values for the relative storey drifts for the average relative storey drift interval of 1.5 mm - 6.5 mm vary from 1.8 mm to 7.8 mm.

Another rule that requires the control of relative storey drifts in TEC 2007 is given in the section "*B2-Interstorey stiffness irregularity (Soft Floor)*". In order to avoid Interstorey stiffness irregularity in the structure according to this section, the Stiffness Irregularity Coefficient η_{ki}, which is obtained
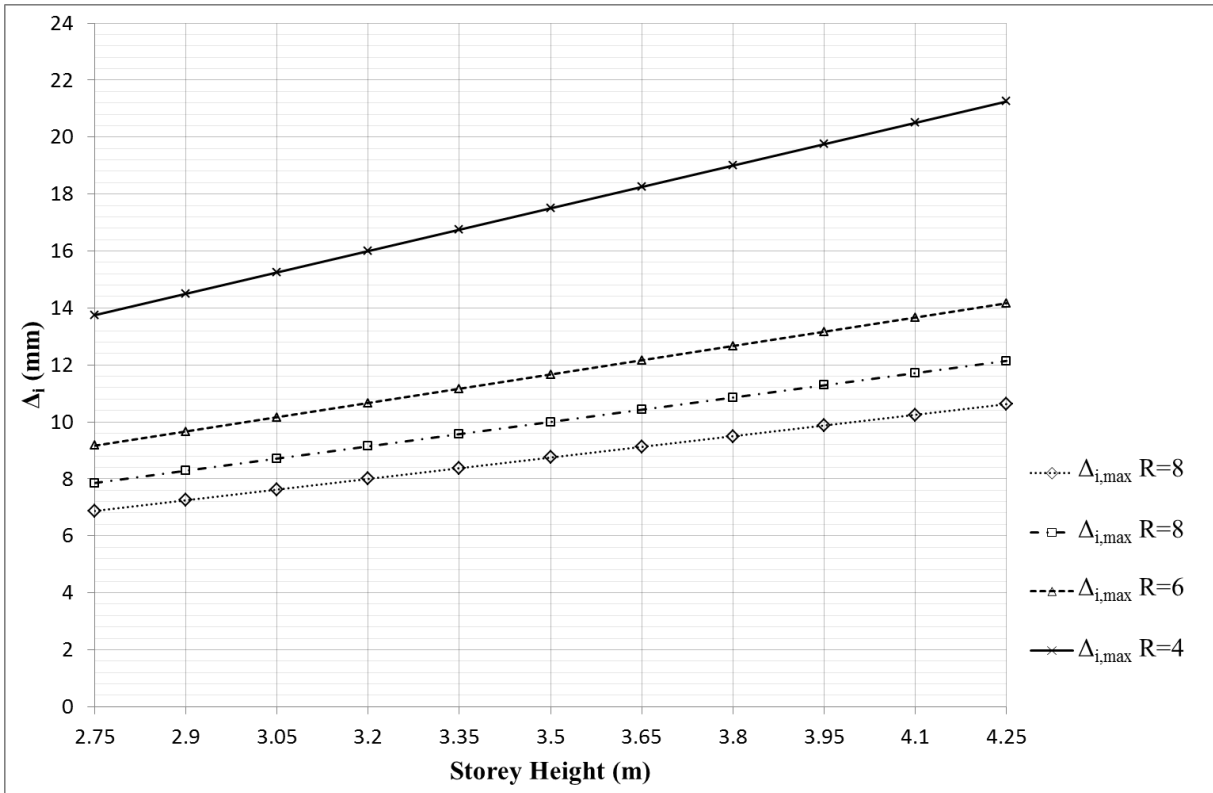
Figure 2. Change of maximum reduced relative storey drifts according to storey height and structural system behavior factor
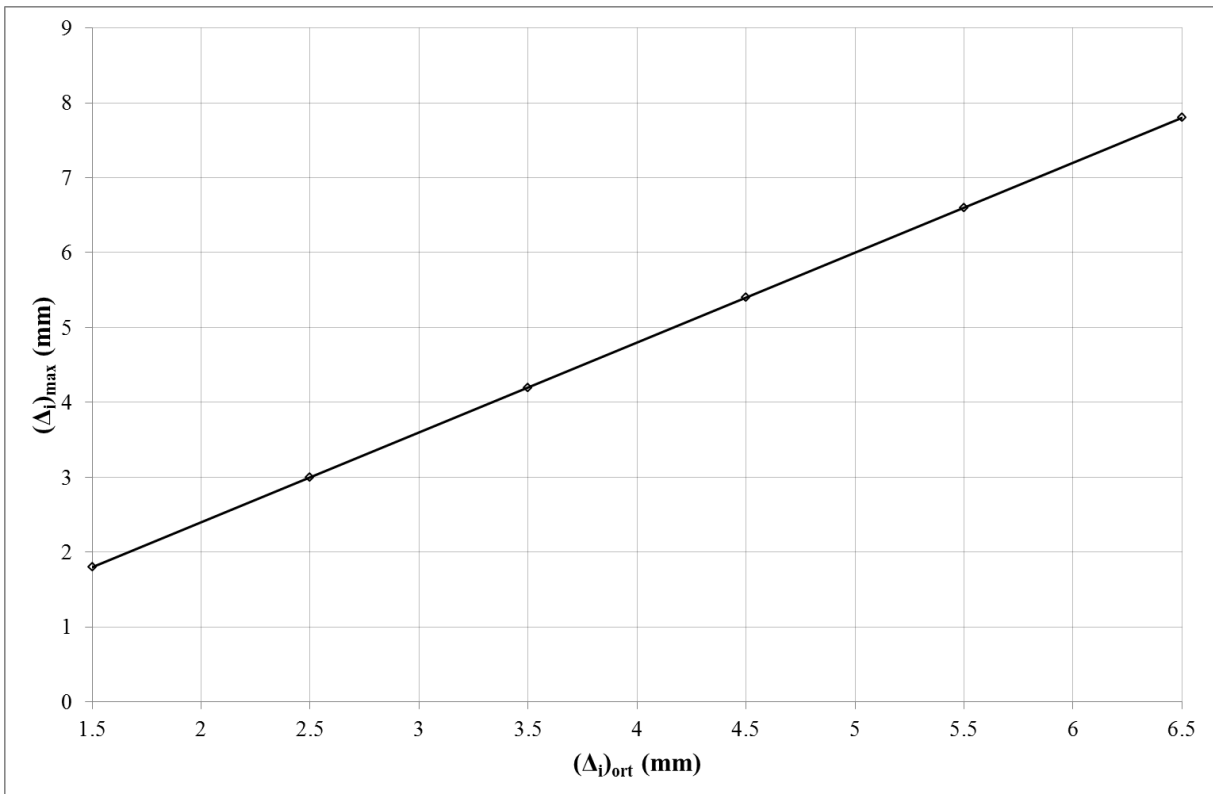
Figure 3. Change of the maximum values of the relative storey drifts relative to the average relative storey drifts

by dividing the average relative storey drift ratio by the average relative storey drift ratio of an upper or lower floors, must be less than or equal to 2 (Equation 2).

In this part of this study, a calculation was carried out according to the following assumptions in order to obtain the largest relative storey drifts which do not cause soft storey irregularity in the structure;

- In order to obtain the largest relative storey drift without causing soft storey irregularities in the construction, the largest average relative storey drift $(\Delta_{i-1})_{ort}$ of the i-1th floor in the reference structure is fixed as 6.5 mm.
- Considering that i-1 and ith storey heights may be different, the ratio of h_i/h_{i-1} was chosen to be 0.65 – 1.

- According to the specified storey height ratios and the average relative storey drifts, the largest average relative storey drifts $((\Delta_i)_{ort})$ which did not cause soft storey irregularity were obtained.
- Using the average relative storey drifts $((\Delta_i)_{ort})$ obtained for ith storey, the largest relative storey drifts $((\Delta_i)_{max})$ were found in the floor providing $\eta_{bi} = 1.2$.

In the given conditions, the largest relative storey drifts in the floor that do not cause A1 and B2 irregularities are presented in Figure 4 according to the storey height ratios.

As a result of the calculations, the maximum relative storey drifts$((\Delta_i)_{max})$ in the floor are in the range of 10.1 mm - 15.6 mm.
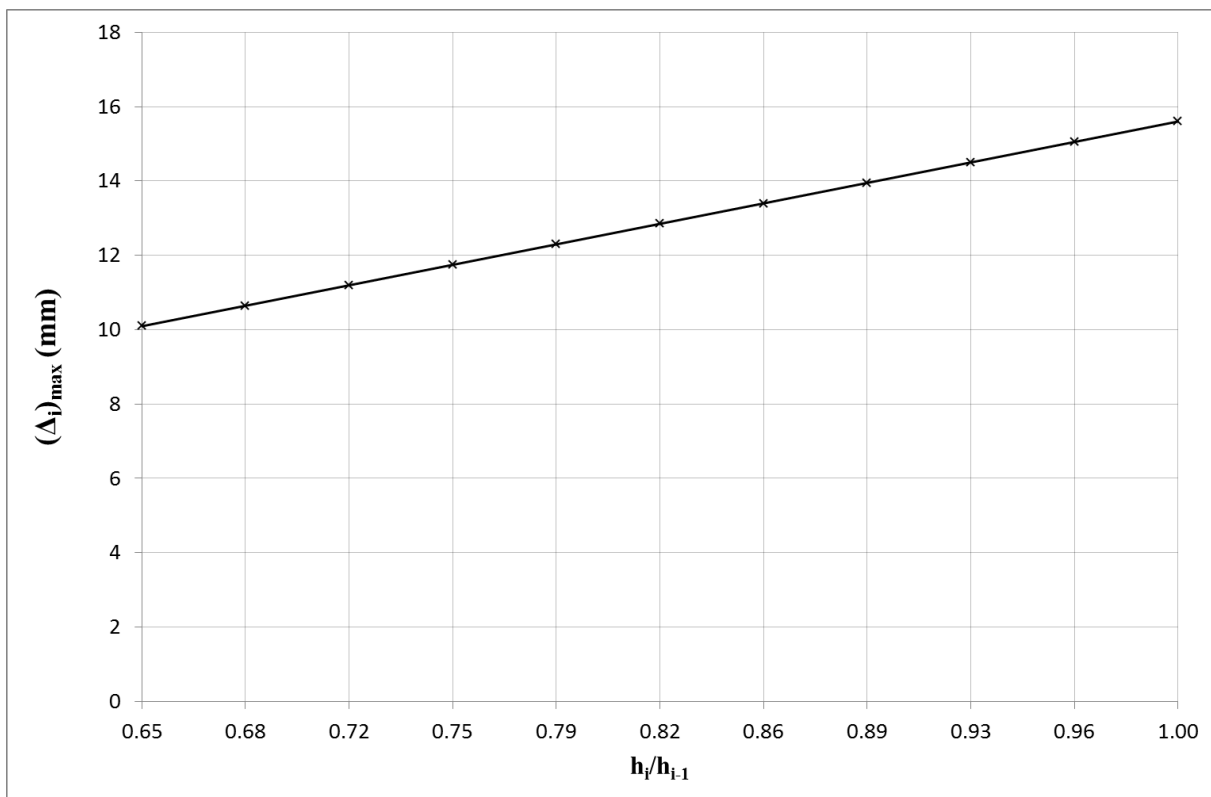
Figure 4. Change of the maximum values of the relative storey drifts according to storey height ratios

3. Conclusions

In this study, the relative storey drift limitation conditions in the sections "*A1-Torsional irregularity*", "*B2- Interstorey stiffness irregularity*" and "*calculation and limitation of effective relative storey drifts*" in TEC 2007 and TEC 2016 draft are compared. However, the relative storey drift limit of a structure to be examined according to the TEC 2016 draft will be examined within a separate study because of the changing of this limit for each point where the structure is constructed. Here, according to TEC 2007, the largest reduced relative storey drifts that frames can make in the buildings in specified parameter ranges is revealed. For this purpose, the largest relative storey drifts were found, which

would not cause torsional and interstorey stiffness irregularity for cast-in-site reinforced concrete buildings in the range of 2.75 - 4.25 m storey height, which can often be encountered in practice. In order to provide the needed parameters for the study, the relative storey drifts of a reinforced concrete structure in the literature have been used. The results obtained from the calculations are expressed below.

- According to the obtained data, the upper limit of permissible relative storey drift of a normal ductility level building is 21.25 mm according to the section "*2.10.1. Calculation and Limitation of Effective Relative Storey Drifts*" of TEC 2007.

- When the relative storey drifts of the reference RC building are checked according to the A1 torsional irregularity, the maximum relative storey drifts which is occurred in the frames is calculated as 7.8 mm in the floor reaching the maximum average relative storey drift of 6.5 mm.

- The maximum average relative storey drift that can be occurred in i^{th} floor according to the "*B2- Interstorey stiffness irregularity*" was calculated assuming that the average relative storey drift of $i-1^{th}$ floor is 6.5 mm in reference building. Since ground floors are frequently used as a workplace, it is considered that floors with different heights can be found in the buildings, and the maximum average relative storey drifs of the ith floor are calculated by assuming variable h_i/h_{i-1} ratio between 0.65 - 1. According to this, the largest relative storey drift is 13 mm when the ith and $i-1^{th}$ floor heights are equal. The maximum relative storey drifts of the frames in this floor without causing torsional irregularity is also calculated as 15.6 mm.

References

1. Saiidi, M., and M.A. Sozen, *Simple nonlinear seismic analysis of R/C structures.* Journal of Structural Engineering, 1981. **107**: 937-952.

2. Iwan, W.D., *Drift spectrum: measure of demand for earthquake ground motions.* Journal of Structural Engineering, 1997. **123**: 397–404.

3. Tekeli, H., A. Tüken, M. Türkmen, and A. Atımtay, *Depreme Maruz Yapının Ötelenmesinin Basit Hesabı: Kapalı Çözüm.* Antalya Yöresinin İnşaat Mühendisliği Sorunları Kongresi: Antalya, 2005. Vol:1, p 190-203. (in Turkish)

4. Tekeli, H., F. Demir, and E. Atımtay, *Çerçeveli ve Perdeli-Çerçeveli Betonarme Binaların Ötelenmesi: Analitik Çözümler*, Journal of the Faculty of Engineering and Architecture of Gazi University, 2008. Vol: 23, No 1, 9-19. (in Turkish)

5. Lu, Y., X. Gu, and J. Wei, *Prediction of seismic drifts in multi-storey frames with a new storey capacity factor.* Engineering Structures, 2009. **31**;345-357.

6. TEC. *Deprem Bölgelerinde Yapılacak Binalar Hakkında Esaslar*, The Ministry of Public Works and Settlement, 2007, Ankara. (in Turkish)

7. Sindel, Z., R. Akbaş, and S.S. Tezcan, *Drift control and damage in tall buildings.* Engineering Structures, 1996 **18**: 957-966.

8. TEC. *Türkiye Bina ve Deprem Yönetmeliği* (Draft), T.C. Disaster and Emergency Management Presidency, 2016, Ankara. (in Turkish)

Research Article

An approach to preparing a bill of quantities

Murat Bikçe [a],*, Süleyman Göçer [a]

[a]Department of Civil Engineering, Iskenderun Technical University, Hatay, Turkey

ABSTRACT

At the pre-design stage, it is essential for designers and property owners to have a rough idea regarding the material quantities necessary for construction as well as the building cost. To know these approximate values is of great importance in terms of the correct establishment of the financial model at the pre-design stage, the elimination of cash flow problems and the prevention of loss of national wealth. While calculating these values, approximate unit costs announced by the Ministry of Public Works and Settlement are used. In Turkey, the cost estimate at the pre-design stage is obtained by multiplying the total building construction area by the unit construction cost. However, it is generally accepted that this value is high in terms of free market costs. The purpose of this study is to prepare a program that can calculate approximate construction cost with unit workmanship prices in a specific region and approximate quantities including the minimum and maximum values of the material values by entering simple information about a planned RC building. Accurate cost estimation at the pre-design stage is proportional to the accuracy of the material metering ratios. The coefficients taken into account in this study have been checked and calibrated with a large number of projects, and it was observed that the samples containing the preliminary results of the study were compatible with the application project results.

1. Introduction

A bill of quantities (BOQ) is a detailed calculation of materials, structural elements and labor to identify the quantities by length, area, volume, weight and number of elements required to construct a building [1]. A BOQ of a reinforced concrete structure (RC) can be prepared on a project as well as on a finished structure by making certain calculations. Estimates are possible thanks to these calculations which are essential to see a general financial budget. Identifying the cost of a certain structure by looking at the architectural, RC and installation projects is called an "estimate", which is performed in two phases. The financial calculations before construction done on preliminary or final projects are called Estimate I, and the financial calculations to determine the cost of a finished structure are called Estimate II. Estimate I is approximate since it is calculated by looking at the BOQ on a project. To illustrate, although it changes depending on the country, manufacturer and specification accepted by the institution/organization, the amount of steel used for 1m³ concrete may change between 80 to 120 kilos, so it is not possible to have exact numbers during project process. On the other hand, Estimate II is certain and does not change because it is calculated by looking at purchase documents and the attachment register recorded during construction as well as construction documents. That's why, the real cost of a structure is revealed after Estimate II.

Generally, engineers are faced with the question of construction cost without the land cost even before the preliminary projects and they are expected to answer this question just with the knowledge of approximate total building area and number of storeys. However, engineers avoid this question, as construction cost depends on several parameters such as region, workmanship, the quality of structure and material. In a study regarding the cost of construction, it has been aimed to estimate the construction cost with the functional element method [2]. In order to do that, the cost of mass housing projects whose bearing systems are reinforced concrete has been calculated and the regression analysis has been performed by using the available data. As a result of the studies, it has been concluded that using hybrid methods helps to get

---

* Corresponding author. Tel.: +90 (326) 613 56 00; Fax: +90 (326) 613 56 13.
E-mail address: murat.bikce@iste.edu.tr

better estimates and similar studies are necessary for different structure types. In another study, they have aimed to determine and compare the cost estimating performance of "construction unit price method" and "unit area cost method" [3]. In a study focusing on just cost calculation, 14 different cost estimating methods and softwares developed by different institutions in the world for pre-design phase have been systematically examined in terms of the parameters defining cost data, the databanks they use and the steps they follow, and the appropriate ones for Turkey have been determined [4]. However, variables such as the construction area, the storey height of the building, the number of storeys, basement floor and the type of exterior wall are the factors that significantly affect construction cost. Therefore, the need for a calculation method necessary for an accurate cost estimating in the pre-design phase has been a serious problem in Turkey. In the preliminary design stage, the bill of material calculations based on the amount of material to be sent to Unit m^2 have not been fully realized.

The studies mentioned above focus on only cost. What matters here is the values for the BOQ presented to engineers, because it may be more realistic to get better estimates with the unit price of the materials if the BOQ of a structure is available. Since this need is quite evident in the construction sector, a lot of websites offer approximate unit quantities for masonry and framed buildings without a change in order to do a practical calculation [5]. In this list, for an RC building whose construction site is determined, the fixed values are presented as follows: reinforced concrete (0.38 m³/m²), reinforcing steel (34 kg/m²), formwork (2.6 m²/m²), supporting formwork (2.8 m²/m²), working scaffold (1.43 m²/m²), brick wall (0.15 m³/m²), interior plastering (2.4 m²/m²), exterior plastering (1.3 m²/m²), ceiling plaster (0.90 m²/m²), whitewash (3 m²/m²), tile-ceramic (0.3 m²/m²), wood (0.15 m²/m²), wooden window (0.12 m²/m²), oil painting (0.42 m²/m²), wooden roof (for 5 floors 0.25 m²/m²), metallic coating (for 5 floors 0.27 m²/m²), granolithic floor (0.90 m²/m²), glass (0.10 m²/m²). Also, the following acceptances are presented for a BOQ in this resource:

Levelling Area (A) = Granolithic Floor A.
Rubble A. = Lean Concrete A. = Mosaic A.
Roof Tiles A. = Roof Insulation A. = Wooden Roof A.
Ceiling Plaster = Ceiling Whitewash
Whitewash A. = Interior Plastering A.
Window Oil Painting A. = Window Woodwork A.
1 m³ Concrete=7-8 m² Formwork

Reinforced Concrete Volume= 70 - 90 kg Steel
Window Woodwork A. = %75 - 80 Normal Flat Glass
Door Leaf A. = %25 Frosted Glass
Of all the Steel = %40 - 45 Thin, %55 - 60 Thick

Despite being an approximate calculation, it is necessary to check and prove if this list which presents fixed values depending on the construction site matches with the real values. At least having lower and upper limits regarding the units depending on m^2 may give an idea to engineers about the limits of quantities in construction.

The purpose of this study is to prepare an excel program to calculate the approximate construction cost in the pre-design phase of III-B type buildings with a height of less than 21.50 m², IV-A apartment type with a height of less than 30.50 m² and IV-C type concrete housings with a height of 30.50 to 51.50 m². In this program, material quantities are calculated roughly by entering the values pertaining to building floor areas, number of floors and other materials that comprise the structure.

2. Cost Calculation of a Structure

In Turkey, an approximate construction cost for public and private buildings is calculated mainly with two methods as pre-design and post-design calculations.

2.1 Cost Calculation Before Architectural, RC and Installation Projects

It is possible to calculate real-like costs without the land cost with some practical formulas if the total construction area is known. These formulas, however, vary depending on the related standards and regulations, time and country.

2.1.1 Public Buildings

Unit cost per m^2 of public buildings for the previous year is regularly announced every year. For instance, "Notice regarding the approximate construction unit costs to be used in the calculation of architectural and engineering service charge" was published in the Official Gazette no. 29679 of 9 April 2016 [6]. In the notice, cost per m^2 for III-B type buildings with a height of less than 21.50 m is stated as 750 TL for the year 2016. The cost of a building whose total closed area is known can be easily calculated for the year 2016 by multiplying it with the stated value. However, the general opinion is that the cost value calculated as mentioned is higher than the real structure cost (Figure 1). That's why, in public tenders, companies bid on the discounted values that have been calculated with this method.
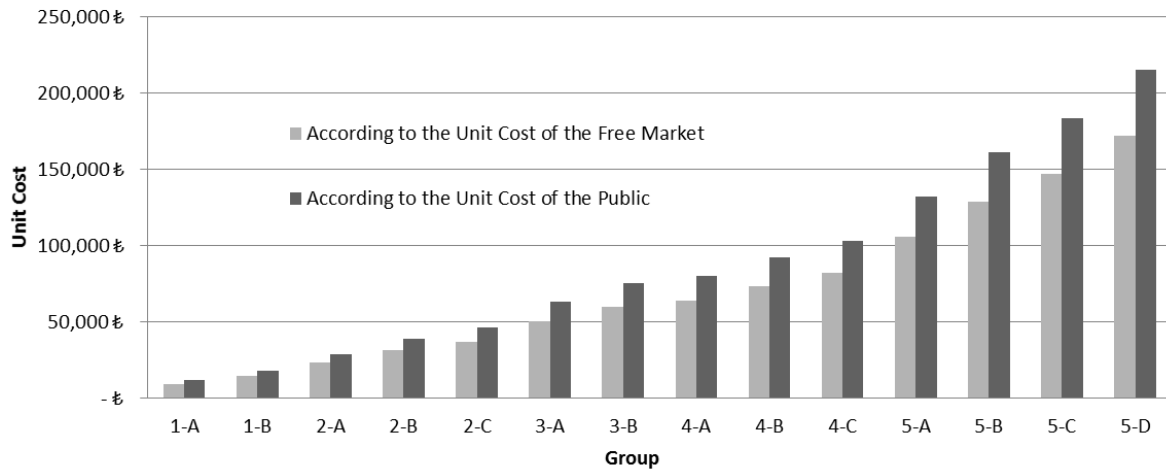
Figure 1. Sample construction cost for a 100 m² public and private building

2.1.2. Private Buildings

In the private sector, a technical worker often calculates construction cost of a projected building whose total construction area is known by using the unit cost per m² of the structures he worked on before. The exact cost of one or a few buildings in an area is calculated, and the received value is proportioned to the total construction area to get the cost for 1m² of the structure. At this point, it is possible to mention a huge gap regarding the cost of the structure.

As seen in Table 1, it is possible to get different values for 5 different buildings that were completed in 2006 with similar material and production properties in the same neighborhood [7].

Table 1. Properties and cost per m² of 5 different buildings completed in 2006 in the same neighborhood

Number of Floors	A Floor Area m²	Total Construction Area m²	Exact Construction Cost TL	Cost of 1 m² TL/m²
5	186	930	272516	293.03
8	292	2336	720843	308.58
8	326	2608	834566	320.00
5	143	715	280654	392.52
5	195	975	312478	320.49
			Total	1634.62

Engineers may defend the received values with valid reasons, yet it is a fact that results differ by a third on m² scale. In order to avoid this, construction cost can be calculated by averaging the cost per 1 m² in a specific area. According to this, the average construction cost per 1 m² is obtained as 1634.62/5=326.93 TL/m².

2.2. Cost Calculation after Architectural, RC and Installation Projects

Since the BOQ of buildings with finished projects are calculated separately in static/RC analysis programs, the only thing left to do is to multiply each item by unit cost, which has been mentioned as Estimate I above. At this stage, because project deliverables are certain, estimates, BOQs, approximate calculation and comparative estimates can be prepared with certain programs or directly on the AutoCAD project [8]. A BOQ is also prepared for progress payments during construction as well as for the calculation of the exact cost at the end of the construction period. When quantities are itemized, it is easy to receive the construction cost by multiplying them by unit cost per m² [9]. However, unit costs per m² for public and private buildings differ in cost calculation.

2.2.1. Public Buildings

Every year, a book including current unit prices for construction and installation is published for public buildings, in which each item in a BOQ is presented separately.

2.2.2. Private Buildings

For private buildings, on the other hand, the technical worker obtains the costs by multiplying the received quantities by market unit prices.

3. Preparing a Bill of Quantities at Pre-project Stage

The purpose of this study is to prepare a BOQ at the pre-project stage. At least having lower and upper limits for materials in the units depending on m² may give an idea to engineers about the limits of quantities in construction. For

practical reasons, the data wanted regarding the building has been kept minimum at the beginning (Table 2).

In this study, some practical acceptances have been made related to the ratios of the materials constituting the structural elements, because the project of the building is not ready. At the beginning of the study, in order to do a practical calculation, approximate BOQ unit values that are presented for RC buildings in the literature [5] and that match with the unit area of the building have been taken into account. It is necessary to check and prove if this list including fixed values regarding the total construction area matches with the values in real application projects. The material ratios taken into account in this study have been checked with the ones obtained from the BOQs of many projects. In this way, the coefficients used in the study have been calibrated (Table 3).

Since this study includes preliminary results of ongoing program-development studies, it contains important items of the building such as concrete, reinforcement and formwork. The previous values of the coefficients that have been used can be changed on the demand of a user. The depth and two dimensions of the foundation concrete can be obtained by multiplying them by certain coefficients depending on the basement floor area. The result of project calculation check and the comparison of error ratio are presented in Table 4.

If the BOQ of real application projects is between upper and lower limits of the values obtained in the program, it will mean that the program is close enough in reflecting the general supplies of RC buildings. In order to minimize the error ratio, calibrations have been performed by making comparisons with a lot of RC projects designed in accordance with the updated earthquake regulations. The cost results of the sample project can be seen in Table 5. The BOQ values obtained as a result of the analysis of the RC building can be counted as close enough to the upper and lower values received in the program which has been prepared in this study. It is not possible to expect the approximate results obtained in this study to match exactly because the projects of the RC buildings used here are not ready. The work on improving the unit coefficients has been going on.

Table 2. Data entry of the building

DATA TO BE ENTERED		
Constraints	**Lower Values**	**Unit**
Short Dimension	19.38	m
Long Dimension	19.38	m
Basement Floor Area	375.70	m²
Ground Floor Area	393.46	m²
Normal Floor Area	393.46	m²
Attic	393.46	m²
Number of Basement Floor	2	Number
Number of Ground Floor	1	Number
Number of Normal Floor	8	Number

Table 3. Unit material quantities for calculation and calculated values for the sample

	Material Quantity for 1 Unit			Calculated Values		
Manufacturing Type	**Lower Value**	**Upper Value**	**Unit**	**Lower Value**	**Upper Value**	**Unit**
Unreinforced Concrete	0.25	0.27	m³/m²	98.37	106.23	m³
Reinforcement Steel	24.00	27.00	kg/m²	9.44	10.62	t
Unreinforced Foundation Concrete	-	-	-	619.91	721.34	t
Foundation Steel	75.00	80.00	kg/m³	21.13	24.04	t
Unreinforced Concrete of Basement Floor	140.44	159.59	m³	140.44	159.59	m³
Basement Floor Steel	120.00	125.00	kg/m³	16.85	19.95	t
Formwork	2.80	3.00	m²/m²	1101.69	1180.38	m²

Table 4. Proportional comparison of structure material values of the real project and the results obtained in the program prepared in this study

Structural Element	Component Element	Unit	Value A	Subvalue B₁	Difference (B₁-A) / B₁	High Value B₂	Difference (B₂-A) / B₂
Foundation	*Concrete*	m^3	319.76	330.18	3%	347.56	8%
Foundation	*Reinforcement*	t	22.18	24.76	10%	27.80	20%
Basement Floor	*Concrete*	m^3	138.37	131.63	-5%	149.77	8%
Basement Floor	*Reinforcement*	t	15.29	15.80	3%	18.72	18%
Ground Floor	*Concrete*	m^3	89.19	86.89	-3%	93.84	5%
Ground Floor	*Reinforcement*	t	9.66	8.34	-16%	9.38	-3%
Typical Floor	*Concrete*	m^3	82.61	84.74	3%	91.51	10%
Typical Floor	*Reinforcement*	t	8.08	8.13	1%	9.15	12%
Loft Floor	*Concrete*	m^3	26.52	21.18	-25%	22.88	-16%
Loft Floor	*Reinforcement*	t	2.22	2.03	-9%	2.29	3%
Total Structure	*Concrete*	m^3	1544.50	1527.69	-1%	1656.08	7%
Total Structure	*Reinforcement*	t	142.08	146.04	3%	166.15	14%

Table 5. Cost including structure material results of the sample project

Component Element	Quantity			Total Budget		
	Subvalue	High Value	Value	Unit Cost (TL)	Sub Account (TL)	High Account (TL)
Concrete	1447.95	1575.84	m^3	135.00	195,473.02	212,738.90
Reinforcement	139.83	159.55	t	2,370.00	331,390.19	378,139.58

4. Conclusions

This study includes the preliminary results of the work on the calculation of BOQs for RC buildings at the pre-project stage. This program which is needed by engineers to be used in practical calculations across the country can easily calculate approximate construction costs with material quantities obtained by entering the number of floors and floor areas of a structure along with the unit prices of workmanship and material in that specific area. The previous values of the coefficients that have been used can be changed on the demand of a user. As a result of the first analyses, the values obtained in the program have been found compatible with the results received from the BOQ of the real structure analysis. When the study is completed, all engineers will be able to benefit from it.

References

1. Birecikli, B.M., *Yapı Metrajı ve Maliyeti*. Eylül 2016, Türkiye: Birsen Yayınevi. p.535. in Turkish

2. Onur, L.U. and U.N. Baykan, *Yapı maliyetinin fonksiyonel eleman yöntemi ile tahmini*. e-Journal of New World Sciences Academy, 2009. **4**(4): p. 449-458.

3. Bayram, S., M.E. Öcal, E. Laptalı Oral, ve C.D. Atış, *Yapım maliyeti tahmininde birim fiyat yöntemi – yapı yaklaşık maliyetleri kıyaslaması*, Politeknik Dergisi, 2016. **19**(2): p. 175-183. in Turkish

4. Polat D.A. ve M. Çıracı, *Türkiye'de tasarım öncesinde maliyet tahmini için veri tabanı modeli*. İtüdergisi Mimarlık Planlama Tasarım, Eylül 2005. **4**(2): p. 59-69. in Turkish

5. İMO, [cited 2017 30 August]; Available from: http://bursa.imo.org.tr/resimler/dosya_ekler/e4e313a1f589c72_ek.pdf?tipi=84&turu=X&sube=0

6. Resmi Gazete, [cited 2017 30 August]; Available from: http://www.resmigazete.gov.tr/eskiler/2016/04/20160409-22.htm. in Turkish

7. Türk, K., [cited 2017 30 August]; Available from: http://eng.harran.edu.tr/moodle/moodledata/53/Ders_Notu/Yapi_Planlama_ve_Organizasyonu.pdf. in Turkish

8. Anonim, [cited 2017 30 August]; Available from: http://www.yapi.com.tr/urunhaberleri/com-otomatik-metraj-cozumleri-ile-metraj-hesabi-1-gune-iniyor_133264.html. in Turkish

9. Çevre ve Şehircilik Bakanlığı, [cited 2017 30 August]; Available from: https://birimfiyat.csb.gov.tr

Research Article

Environmental effects on tribological behaviour of composite materials

Deniz Degirmenci [a], Murat Kisa [a], Mustafa Ozen [a], and Gokhan Demircan [a],*

[a]*Harran University, Department of Mechanical Engineering, Şanlıurfa, 63300, Turkey*

ARTICLE INFO	ABSTRACT

In recent years, developments in industrial applications has led to the demand for materials with better properties. Composite materials provide these requirements due to their high mechanical properties. Especially in the last half century, the production of composite materials used in industrial areas such as space, marine, aeronautics has increased to a great extent. This increase has led scientists to work on composite materials. One of these work areas is tribological behaviour. It is inevitable that the wear of the composite materials occurs due to surface roughness of the parts in contact with each other; therefore, they may not fulfill the functions expected from them. It is important to determine how tribological behaviour of composites used in almost all areas of the industry will be present in working conditions. In this study, wear and frictional characteristics of carbon fiber reinforced epoxy composites subjected to different environmental effects (soil, water, solar) were investigated under dry contact condition at different operating parameters. Vacuum Assisted Resin Infusion Technique (VDRIT) was used for the production of composite materials. Environmental effects, exposure times and applied loads on the friction coefficients and wear amounts were investigated. Wear tests were carried out under three different loads of 10 N, 20 N, 30 N, sliding distance of 2000 m and at a speed of 0.2 m/s. Wear rate in the experiments was calculated as weight loss. The tests were carried out on samples for each load and their average values were taken. Similar to the results found in the literature, when carbon fiber reinforced composite materials were exposed to different environmental effects, the friction coefficients decreased and the wear rate increased. The use of information and data obtained with this study will guide material selection of machine tools manufactured from composite materials in different environmental conditions.

1. Introduction

Since composite materials are used extensively today, machine parts made from composite materials must be suitable for the environment in which they work. In other words, it is necessary that the desired mechanical properties such as strength, wear resistance, corrosion are appropriate. It is essential to determine the precautions against wear especially on the surface of the materials and to apply these precautions during the use of the machine elements [1, 2].

Wear is often a mechanical strain, and in some cases, a change in shape due to the removal of small particles from the surface of the material [3]. The wear phenomenon,

however, has also been described as the deformity of the surfaces of the machine elements in use, usually resulting from the breakage of small parts that occur as a result of mechanical effects [4].

Suresha et al. [5] examined the effects of normal loading and sliding speed on friction and wear behaviors of carbon fiber reinforced epoxy composites. It was determined that the weight loss of the composite material increases with the increase of the applied load and sliding speed.

Wang et al. [6] immersed different fiber orientations (0°, 45°, 90°) carbon fiber reinforced epoxy composites into 10% sulfuric acid solution in different days and investigated their tribological behavior. As a result, 45° fiber-oriented composites had the lowest

* Corresponding author. Tel.: +90-414-318-3000
E-mail address: gdemircan@harran.edu.tr

coefficient of friction, while those with 90° fiber-oriented composites had the lowest wear rate.

Suresha et al. [7] also studied three-body abrasive wear behavior of carbon and glass fiber reinforced epoxy composites. It was determined that wear loss increased with increasing load and slip distance in both types of composite materials. In addition, they found that the abrasive wear resistance of carbon reinforced composites was higher than the abrasive wear resistance of glass reinforced composites.

Wu et al. [8] prepared silver-based composites containing WS2 in different amounts by hot pressing method and examined their tribological properties on a disk with normal load of 5 N under moist air, dry nitrogen and vacuum. It was observed that the tribological properties of silver-based composites under environmental conditions are significantly influenced. The coefficient of friction is the highest in humid air and lowest in dry nitrogen.

Sumer et al. [9] studied the tribological behavior of 30% glass fiber reinforced PEEK matrix and pure PEEK matrix materials under dry sliding and water lubricated conditions. It was observed that the friction coefficients and the wear amounts increased with the increase of the applied load and the wear resistance of the composite materials was higher in the experiments performed in water lubricated conditions.

Larsen et al. [10] examined the wear performance of CuO nanoparticle-filled carbon/aramid epoxy composites under various speed and load conditions. They found that fiber orientation in glass fiber reinforced composite materials affects the wear performance and that the addition of PTFE and CuO nanoparticles has a low effect on wear performance.

Khun et all. [11] developed short carbon fiber reinforced epoxy composite materials to investigate tribological properties. The friction coefficient and wear rates of the composites produced were examined using a steel ball at a speed of 3 cm/s and loads of 2 and 6 N. Tribological results made it clear that incorporation of SCFs was an effective way to improve the tribological properties of epoxy composites.

Özay and Hasçalık [12] investigated the effects of carbon content on the wear behavior of $Cu-C-Al_2SiO_5$ composites obtained by the powder metallurgy method with experiments carried out at loads of 10 N, 20 N and 30 N at 30 m slip distance. Microanalyses of composite test samples were observed using scanning electron microscopy (SEM) and microscope. It was also observed that the amount of wear increases by increasing the volume of reinforcing particles C and the applied external force.

Kishore et al. [13] investigated the wear surfaces with SEM microscope under dry contact condition of glass fiber reinforced composite materials. It was determined that increasing slip distance caused the separation at the interface between fiber and matrix at the wear surfaces.

Sureshkumar et al. [14] examined the friction and wear properties of epoxy resin reinforced glass/carbon hybrid composites. Tribological properties such as friction and wear rate were investigated using pin-on-disk method. Experiments were carried out at 20, 40, 60 N loads at constant speed of 5m / s and sliding times of 2, 4 and 6 min. It was observed that the wear rate increased with increasing the carbon ratio, but the friction coefficient decreased with increasing carbon ratio in the composite.

Chen et al. [15] produced carbon nanotube reinforced carbon fiber epoxy composites. The friction and wear properties of the composites were investigated using a UMT-2 friction and wear tester. The tribological properties of the composites were clearly improved after reinforcing of carbon nanotubes. The reason is that carbon nanotubes increase the mechanical interlocking and chemical bonding interactions between fiber and epoxy, so that the fibers aren't pulled easily under shear stress during friction and wear.

Srivasta et al. [16] investigated the wear and friction characteristics by adding mica to the unidirectional glass fiber reinforced epoxy resin composite material. They found that the mica particles increased the hardness and compressive strength of the composite material and exhibited better tribological properties.

The aim of this study is to experimentally determine the wear behavior of composites affected by environmental conditions (soil, water, sun). Carbon fiber reinforced epoxy composites used in this study were produced with VDRIT (Vacuum Assisted Resin Infusion Technique). Wear tests were carried out at certain periods and the differences and the tribological properties of the composite materials were investigated.

2. Materials and Methods

In this study, woven carbon fiber with a density of 300 gr/m^2 was used as reinforcing material. Aradite LY 1564 epoxy and Aradur 3487 BD hardener were selected as the thermosetting polymer matrix material. 6 layers of carbon fiber were prepared for reinforcing material in composite plate. The ratio of hardener and epoxy for matrix material was 1/3 of the mass. Prepared reinforcing fabrics were vacuumed at 1 bar pressure. After vacuum seal was established, infusion of the epoxy mixture into the reinforcing fabrics was provided. After infusing the resins into all reinforcing fabrics, the system was allowed to cure at 100 °C for 2 hours in the vacuum. For control of the wetting condition of the composite plate, samples were taken from different areas and visual inspection revealed that all plate was wetted throughout the thickness. Samples were prepared from the composite plates prior to the wear tests. The samples were cut in 18x18x10 mm dimensions with a cutting saw. Samples were tested using the TRD Wear program to retrieve the reference values before exposure to environmental effects. Then, it was exposed to water, soil and sun for 100 and 200 days. Water was used as city water. As evaporation took place, water was added every 10 days. The soil of university ground that was not used as an agricultural land was used. A 1-meter pit was opened, and the samples were buried in the soil. The sun was applied throughout the day and night. After exposures

the samples were subjected to wear tests under different load conditions (10 N, 20 N, 30 N).

3. Experiments and Results

3.1 Composite Materials without Environmental Effects

The pin-on-disc method was used for wear test of carbon fiber composite material. A 10 mm diameter high-speed tool steel was used as a wearing tool. Before composite samples were exposed to environmental effects, initial wear tests were carried out at room temperature and dry friction conditions with a sliding speed of 0.2 m/s, a sliding distance of 2000 m and loads of 10 N, 20 N and 30 N. Tests were performed for each load and the average friction coefficient and wear rate obtained are given in Table 1, Figure 1 and 2.
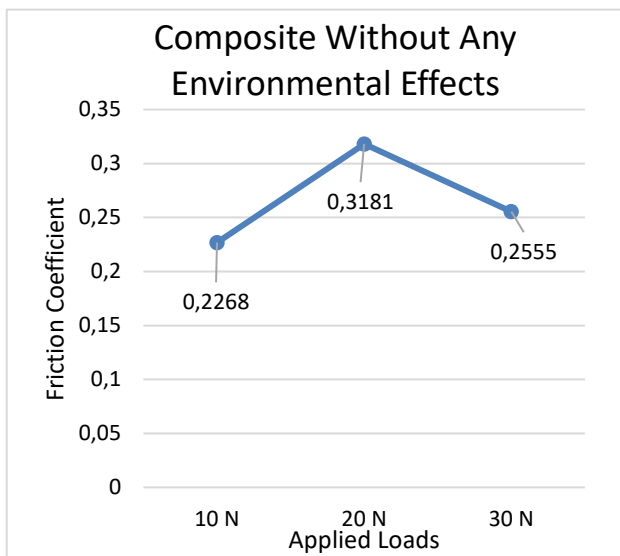
Figure 1. Average friction coefficients of carbon fiber composite samples without any environmental effects
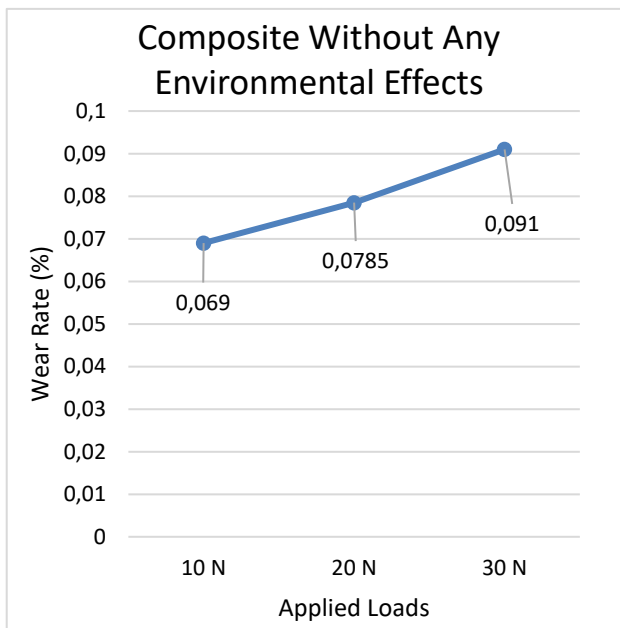
Figure 2. Average wear rate of carbon fiber composite samples without any environmental effects

The friction coefficient of carbon fiber composite without any environmental effects increased first (40,25%) and then decreased (19,67%). This result can be explained by the self-lubrication of carbon.

The wear rate of carbon fiber composite samples increased as the applied load increased. There was an increase of 13.76% from 10 N to 20 N, while an increase of 15.92% from 20 N to 30 N was observed. This change seems to be close to the linear.

Table 1. Average friction coefficients and average wear rate of carbon fiber composite samples without any environmental effects

Loads (N)	Average friction coefficients	Average wear rate (%)
10	0,2268	0,0690
20	0,3181	0,0785
30	0,2555	0,1150

3.2 Composite Materials with Environmental Effects

After exposure to environmental effects (water, soil and sun for 100 and 200 days), samples were tested using the TRD Wear program under different load conditions (10 N, 20 N, 30 N. The results are shown in figures and tables below.

3.2.1 Composite Materials with Sun Effect

The load-dependent change in average friction coefficients and wear rates of carbon-fiber composite samples exposed to the sun are given in Figure 3. The average friction coefficient for carbon fiber composite samples exposed to the sun for 100 days increased as the applied load increased, but the friction coefficient results for samples with 200 days sun effect decreased. The increase in 100 days is 9.09 % while the decrease in 200 days is 31.81%. It is known that fiber matrix interface affects the performance of the composite material [17]. It may be that the fiber matrix interface bond was weakened in the composite material exposed to the sun for 200 days. This weakening, due to the pressure at the interface, could lead to wear loss increasing while reducing the friction coefficient as the load increased. The wear rate increased as the applied load increased. It increased by 59.72% in 100 days and increased by 43.90% in 200 days. Although the rate of increase in 200 days was low, the wear rate was higher than 100 days.

3.2.2 Composite Materials with Soil Effect

The load-dependent change in average friction coefficients and wear rates of carbon-fiber composite samples exposed to the soil are given in Figure 4. The average friction coefficient for carbon fiber composite samples kept under soil for 100 days decreased (25%) at the load value of 20 N and increased (13,33%) at 30 N but on the contrary for 200 days exposure this value increased (16,66%) at the load value of 20 N and decreased (4,76%)

at 30 N. Wear debris can affect the tribological performance of composite materials [18]. It could be seen that the effect of the soil on the wear debris is not constant. This imbalance wear debris was observed as decrease and increase in results. The wear rate increased as the applied load increased. This rate is 33,33% in 100 days, while it is 30,11% in 200 days.

3.2.3 Composite Materials with Water Effect

The load-dependent change in average friction coefficients and wear rates of carbon-fiber composite samples exposed to the water are given in Figure 5. As seen in figure, the average friction coefficients under the effect of water for 100 days (71,42%) and 200 days (33,33%) were found to increase as the applied load increased. Wear rate was measured as 30.69% in 100 days and 34.58% percent in 200 days. The wear rate increased as the applied load increased. If the sample is exposed to the same load, there is an increase in wear rate during exposure to water.
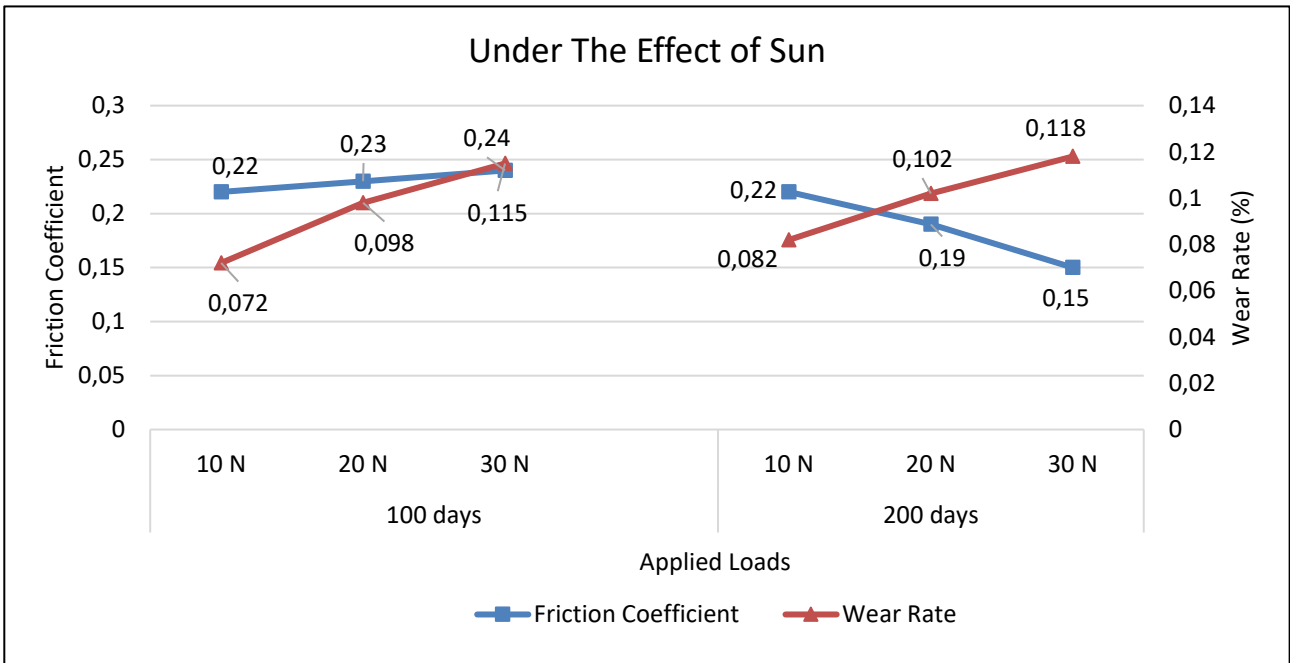
Figure 3. Average friction coefficients and average wear rate of carbon fiber composite samples with sun effect
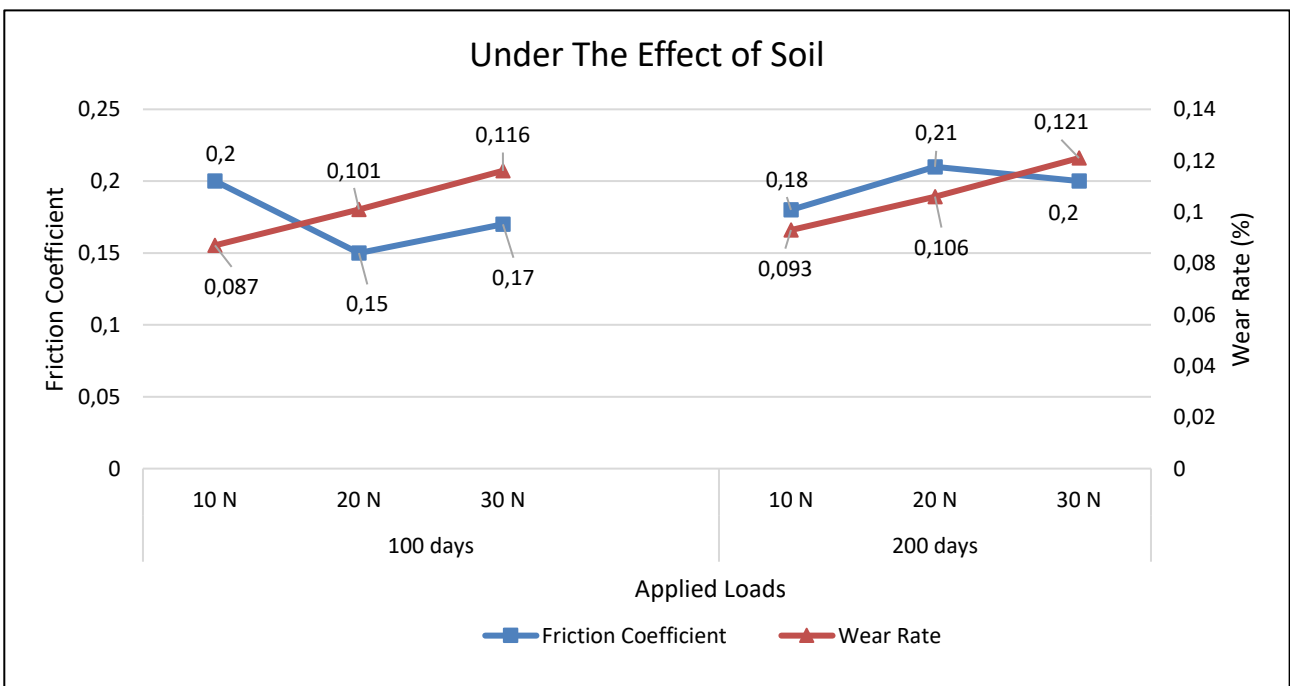
Figure 4. Average friction coefficients and average wear rate of carbon fiber composite samples with soil effect
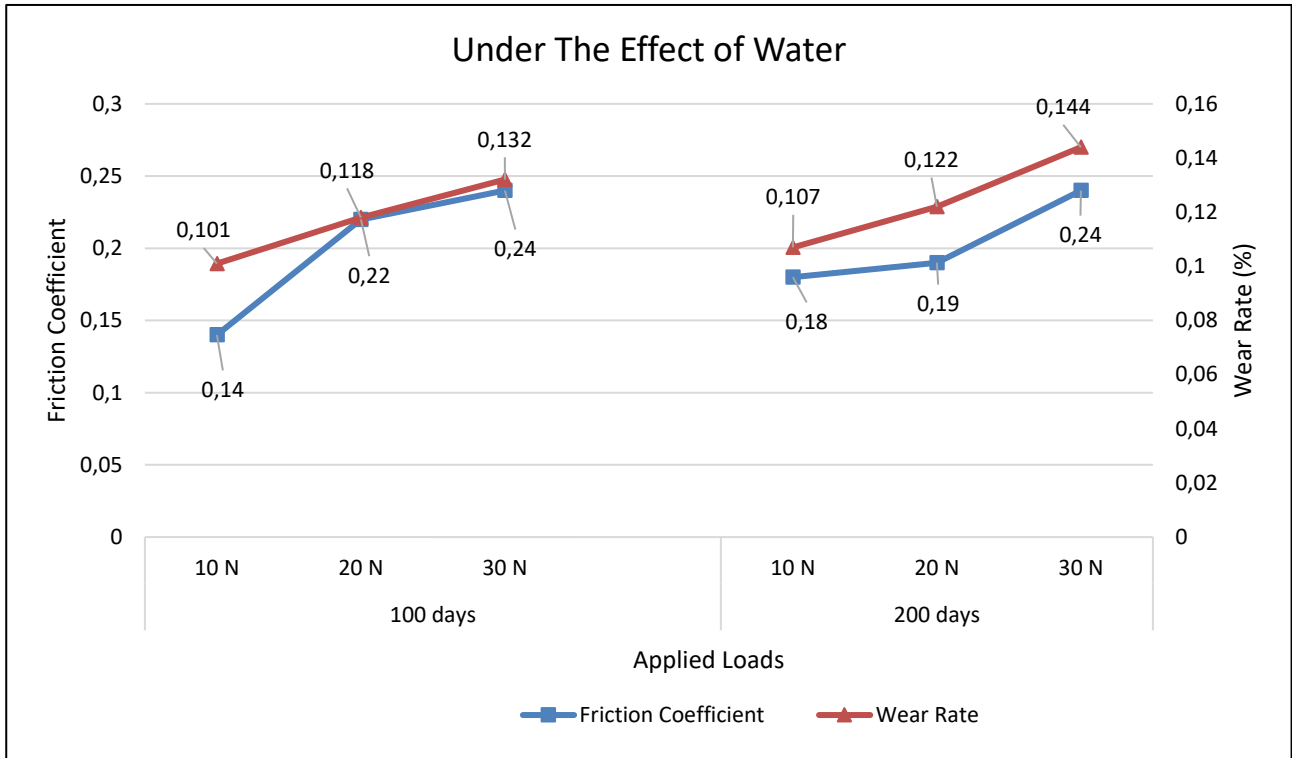
Figure 5. Average friction coefficients and average wear rate of carbon fiber composite samples with water effect

Table 2. Average friction coefficients and average wear rate of carbon fiber composite samples with sun effect

Time (Day)	Loads (N)	Average friction coefficients	Average wear rate (%)
100	10	0,22	0,072
	20	0,23	0,098
	30	0,24	0,115
200	10	0,22	0,082
	20	0,19	0,102
	30	0,15	0,118

Table 3. Average friction coefficients and average wear rate of carbon fiber composite samples with soil effect

Time (Day)	Loads (N)	Average friction coefficients	Average wear rate (%)
100	10	0,20	0,087
	20	0,15	0,101
	30	0,17	0,116
200	10	0,18	0,093
	20	0,21	0,106
	30	0,20	0,121

Table 4. Average friction coefficients and average wear rate of carbon fiber composite samples with water effect

Time (Day)	Loads	Average friction coefficients	Average wear rate (%)
100	10 N	0,14	0,101
	20 N	0,22	0,118
	30 N	0,24	0,132
200	10 N	0,18	0,107
	20 N	0,19	0,122
	30 N	0,24	0,144

4. Conclusions

In this study, tribological properties of composite materials were investigated by experimental studies on carbon fiber reinforced epoxy composites exposed to environmental effects.

The following are key observations from this study:

- As expected, as the exposure to environmental conditions increased, the composite material was more affected.
- The environmental factor that affects the composite material most often was water with an average wear rate of 51.99%, then soil with an average wear rate of 34.24% and then the sun with an average wear rate of 26.15%.
- No clear increase or decrease in friction coefficients was observed. This is because the environmental conditions affect the quantity of wear debris differently. Another effect that may be caused is the different effects of the applied loads on the transitions in the fiber matrix interfaces.

5. Suggestions

This study could be further developed within the scope of the following suggestions.

- The present work can be applied to different composite materials by changing the resin and

reinforcement elements used.

- The effects of various parameters such as wear rate, temperature, different fiber-matrix ratio on wear behaviors of composites can be examined.
- This work can be improved for different environmental conditions.
- The effects of environmental conditions, such as cracks, on the wear behaviors of composite materials can be investigated.

Acknowledgment

References

1. Nair, F., Karamiş, M.B., ve Taşdemirci, A., *Endüstriyel Uygulamalarda Borlanmış Çeliklerin Aşınma Davranışının İncelenmesi*. 8. Denizli Malzeme Sempozyumu Bildiriler Kitabı, 2000. p. 334-343.

2. Yildizli, K., *Borlamanın Çeliklerde Eroziv Aşınma Davranışına Olan Etkilerinin Deneysel Olarak İncelenmesi*. Erciyes Üniversitesi, Fen Bilimleri Enstitüsü, Makine Mühendisliği Anabilim Dalı, Yüksek Lisans Tezi, Kayseri, 2002. p. 8-154.

3. Demirci, A.H., *Ötektoidaltı Alaşımsız Çeliklerin Isıl İşlemlere Bağlı Olarak Aşınma Davranışlarının Belirlenmesi ve Optimizasyonu*. E.Ü., Makina Fakültesi, Doçentlik Tezi, Kayseri, 1982. p.8-44.

4. Gay D., Hoa, S.V.,Tsai S.W., *Composite Materials Design and Applications*. CRC Pres. USA, 2003.

5. Suresha, B., Chandramohan, G., Samaptkumaran, P., and Seetharamu, S., and Vynatheya, S., *Friction and Wear Characteristics of Carbon-epoxy and glass-epoxy Woven Roving Fiber Composites*. Journal of Reinforced Plastics and Composites, 2006. **25**(7): p. 771-782.

6. Wang, H., Wang, R., Wang, C., Li, M., & Zhu, Y., *Influence of fiber orientation on the tribological properties of unidirectional carbon fiber reinforced epoxy composites corroded by 10 wt% sulfuric acid solution*. Journal of Materials Research, 2017. **32**(4), p. 801-809.

7. Suresha, B., Chandramoha, N.G., Samaptkumara, P., and Seetharamu, S., *Three-body Abrasive Wear Behaviour of Carbon and Glass Fiber Reinforced Epoxy Composites*. Material Science and Engineering A, 2007. **443**(1-2): p. 285-291.

8. Wu, J., Li, J., Zhang, L., Qian, Z., *Effects of environment on dry sliding wear behavior of silver–copper based composites containing tungsten disulfide*. Transactions of Nonferrous Metals Society of China, 2017. **27**(10): p. 2202-2213.

9. Sumer, M., Unal, H., and Mimaroglu, A., *Evaluation of Tribological Behaviour of PEEK Composite Under Dry Sliding and Water lubricated Conditions*. Wear, 2008. **265**(7-8): p. 1061-1065.

10. Larsen, T.Ø., Andersen, T.L., Thorning, B. and Vigild M.E., *The Effect of Particle Addition and Fibrous Reinforcement on Epoxy-Matrix Composite for Severe

Sliding Conditions*. Wear, 2008. **264**(9-10): p. 857-868.

11. Khun, N.W., Zhang, H., Lim, L.H., Yue, C.Y., Hu, X., Yang, J., *Tribological properties of short carbon fibers reinforced epoxy composites*. Friction, 2014. **2**(3): p. 226-239.

12. Özay, Ç. ve Hasçalık, A,. *T/M Yöntemi ile Üretilen Cu-C-Al₂sio₅ Kompozitinin Abrasiv Aşınma Dayanımı*. DPÜ Fen Bilimleri Enstitüsü Dergisi, 2004. 6: p. 175-184.

13. Kishore, Sampathkumaran P., Seetharamu S., Murali A., and Kumar R.K. *On the SEM Features of Glass-Epoxy Composite System Subjected to Dry Sliding Wear*. Wear, 2001. **247**(2): p. 208-213.

14. Sureshkumar, P., Moorthi, R., Narayanan, B., *Experimental Investigation of Friction and Wear Properties for Glass/Carbon Hybrid Fiber Reinforced with Epoxy Resin*. Indian Journal of Science and Technology, 2016. **9**(42): p. 1-5.

15. Chen, B., Li, X., Yang, J., Huang, H., Peng, W., Li, C., Zhang. Z., *Enhancement of the tribological properties of carbon fiber/epoxy composite by grafting carbon nanotubes onto fibers*. RSC Advances, 2016. **6**: p. 49387–49394.

16. Srivastava, V.K., Pathak, J.P. and Tahzibi, K., *Wear and Friction Characteristics of Mica-Filled Fibre-Reinforced Epoxy Resin Composites*. Wear, 1992. **152**(2): p. 343-350.

17. Tiwari, S., Bijwe, J., *Various ways to strengthen the fiber–matrix interface for enhanced composite performance*. Surface and Interface Analysis, 2013. **45**, p. 1838–1848.

18. Srivastava, V.K., *Effect of CNTs on the Wear and Friction Performance of Carbon Fibre Woven Fabric Reinforced Epoxy Resin Composites*. International Journal of Composite Materials, 2016. **6**(4): p. 95-99.

Research Article

On the effect of nano particle inclusion in fiber reinforced composite tensile and flexural behavior

Nurettin Furkan Doğan [a], Ahmet Erkliğ [a,*]

[a]Department of Mechanical Engineering, Gaziantep University, Gaziantep 27310, Turkey.

ABSTRACT

This study aimed to investigate the effect of graphene nanoplatelets (GnPs) on the tensile and flexural properties of fiber reinforced composite material. For this purpose; an experimental study was conducted using composite materials which were manufactured with $[(0/90)_6]_s$ glass fiber and epoxy matrix by vacuum assisted resin transfer method. Glass fiber reinforced (GFR) epoxy composite plates were manufactured with various graphene nanoplatelets content such 0, 0.1, 0.25 and 0.5 wt% inclusion. Maximum tensile and flexural strength values were obtained in 0.1 wt% GnPs filled composites. After this weight content, decreasing trend in the strength values was observed. When fractured specimens were examined, failure modes were supported the test results also. Higher contents of GnPs were resulted as agglomeration in matrix mixture lead to impurities and stress concentrations, thus lower strength values were obtained in composite.

1. Introduction

In past few decades, fiber reinforced polymer composites (FRP) have attracted a great interest in material science and engineering applications because of their advanced strength and stiffness to weight ratios compared to conventional engineering materials. In FRP materials, material properties can be tailored by many processes like changing type of fiber/matrix material, fiber hybridization, stitching, z-pinning, adding particulate materials to matrix or fiber, etc. [1-7]. Unfortunately, poor fracture resistance of FRP composites has limited the usage area of these materials. Currently, composite modification by using inorganic nano particles has become a very popular research topic and incorporation of nano particle in matrix offers a significantly improved mechanical properties, thus has extended the limit of application area. Particularly, carbon based nano materials such as carbon nanotubes (CNTs) and graphene nano platelets (GnPs) have an important potential in this research topic. The main reason of this interest is their outstanding physical properties as large specific surface area, thermal/electrical conductivity and Young's modulus [8, 9]. In many studies, CNTs have proved their magnificent improvement in conductivity and toughness of composite material [10-15]. However, high cost of CNTs makes

GnPs more favorable for tailoring process of FRP materials. GNPs are short stacks of individual graphite layers, a newly developed, lower cost material that generally increases the composite tensile strength [16]. Large specific surface of GnPs results larger contact area with polymer matrix and increases the stress transfer from matrix to nano particle. However, agglomeration problem arises in higher content of GnPs due to strong van der Waals forces [17].

In this study, researchers produced glass reinforced/epoxy composite samples at four different rates of inclusion of GnPs with the control sample. Tensile and flexural behaviors characterized with respect to GnPs amount of inclusion.

2. Materials and Procedures

2.1 Materials

Plain woven E-glass fabric with areal density of 202 g/m2 and epoxy resin (MOMENTIVE-MGS L285) and hardener (MOMENTIVE-MGS H285) were supplied from DOST Chemical Industrial Raw Materials Industry, Turkey. GnPs with a high purity of a purity of 99.5%, bulk density of ∼ 0.05 g/cm3, 5 μm diameter, thickness of 5-8 nm and 150 m2/g surface area was obtained from Grafnano CSO, Turkey.
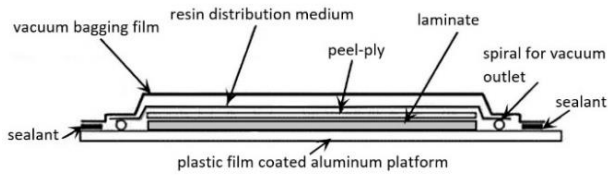
Figure 1. Schematic illustration of VARTM process.

2.2 Manufacturing process

The laminates were manufactured by vacuum assisted resin transfer method (VARTM) in Figure 1. Matrix phase was prepared by mixing the epoxy with hardener in the 100:40 weight ratio as well as different amounts of GnPs (0.1, 0.25 and 0.5 wt%). After epoxy was mixed with GnPs filler, the mixture was stirred by the help of homogenizer at 8000 rpm for 10 min to reach a good dispersity, then hardener was added, and stirred for 10 min. Twelve plies of glass fabric were cut into a certain size and laid by [0/90] lay-up sequence. During composite production, first ply was laid on to a thin release agent, and the resin mixture was distributed uniformly, the same procedure was repeated for each layer. Then peel ply and resin infusion mesh were laid on the fabrics. Finally, vacuum bag was sealed onto mesh. When the resin mixture impregnated, the composite material subjected vacuum under temperature of 45 °C for 1 h curing time and then left under vacuum for another 4-5 h under room temperature.

Table 1. Material properties

Material	Density	Thickness
Glass Fabric	202 g/m^2	0.15 mm
Graphene Nano Platelets	50 kg/m^3	5-8 nm
Epoxy Resin	1.18 g/m^3	-

2.3 Tensile Tests

To determine the effect of GnPs on the tensile behavior of glass fiber reinforced composite, uniaxial tensile tests were conducted at room temperature according to ASTM D 638 [18] standard. Shimadzu AG-x series universal testing machine with Epsilon Tech. 3542 axial extensometer was used in the experiments. Specimens in Figure 2 were prepared in the dimensions of 165 x 13 mm with a gauge length of 50 mm.
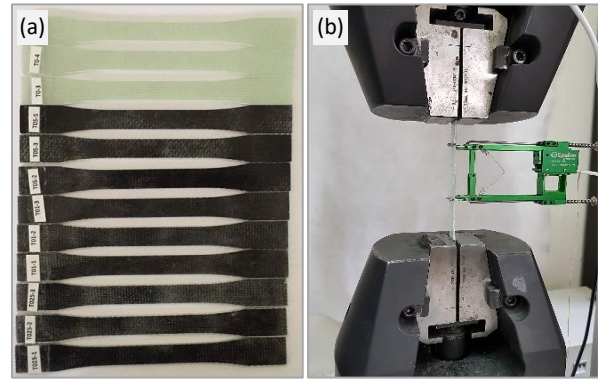
Figure 2. (a) Tensile test specimens, (b) tensile test set-up.

2.4 Flexural Tests

Three-point bending tests were performed following ASTM D 790 [19] standard using Shimadzu testing machine AG-X series (Kyoto, Japan) to determine the flexural properties of the prepared composite specimens. Specimens were cut in the size of 185 x 12.7 mm and the test was carried out at 3.6 mm/min crosshead speed according to Equation 1.

$$R = ZL^2/6d \tag{1}$$

where R is rate of crosshead motion (mm/min), L is support span (mm), d is depth of specimen (mm) and Z is rate of straining of the outer fiber (0.01).

Also, following equations [19] are adopted to calculate flexural stress (σ_f) and strain (ε_f) from test data using following equations:

$$\sigma_f = \frac{3PL}{2bd^2}\left[1 + 6\left(\frac{D}{L}\right)^2 - 4\left(\frac{D}{L}\right)\left(\frac{d}{L}\right)\right] \tag{2}$$

$$\varepsilon_f = \frac{6Dd}{L^2} \tag{3}$$

where P is the load at a given point on the load-deflection curve (N), L, b and d are the span (mm), width (mm) and depth (mm) of the specimen, respectively, D is the maximum deflection before failure (mm) and $\Delta P/\Delta x$ is the slope of the linear region of the load–deflection curve (N/m).
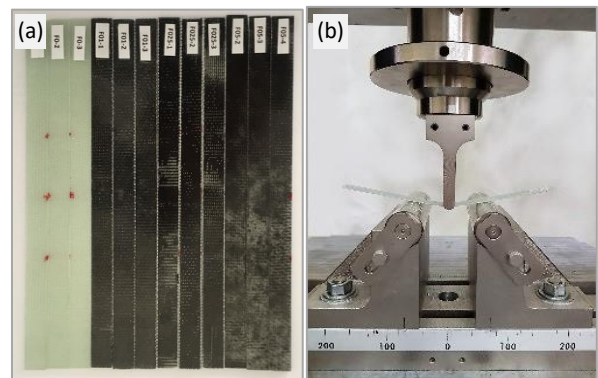
Figure 3. (a) 3-point bending test specimens, (b) 3-point bending test set-up.
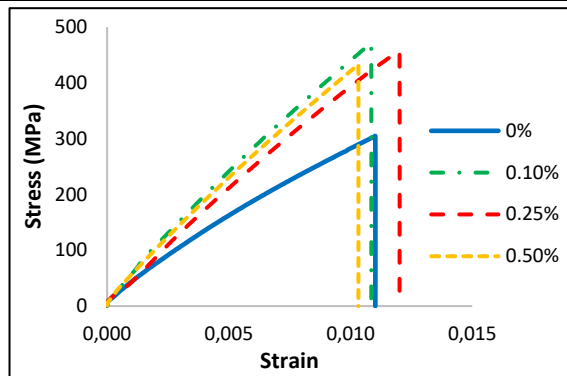
Figure 4. Stress-strain curves of test specimens.

3.   Results and Discussions

3.1 Tensile Tests

To characterize the material under tensile load the strength, modulus and strain were recorded during experiments. The variation of tensile properties with varying content of GnPs were presented in Table 2, and stress-strain curves are displayed in Figure 4.   The specimens have shown brittle behavior according to stress-strain curve and have increasing trend until 0.1 wt% in terms of strength and modulus. As seen in Table 2, tensile strength values were recorded as 304 MPa in control specimen, 471, 455 and 433 MPa for 0.1, 0.25 and 0.5 wt% specimens respectively. Enhancement in tensile strength values were measured as 54.9%, 49.67%, 42.43% in 0.1, 0.25 and 0.5wt% GnPs filled specimens respectively compared with control specimen. These considerable improvement is indicated that homogeneous dispersion of particle in matrix and successful load transfer between matrix/fiber interface. Previous studies [20-22] reported that up to a certain amount of graphene content, composite material shows better mechanical properties such as tensile strength, flexural strength and fracture toughness after that amount decreasing trend was reported.

At higher GnPs contents (0.25 and 0.5 wt%), a decreasing trend was recorded for tensile strength values compared to specimens with 0.1 wt% GnPs. These conclusions were attributed to agglomeration in graphene particles at high particle contents hence inhomogeneous particle dispersion and stress concentration in matrix material which can lead to crack initiation/propagation and consequently lower strength values in composite material [23-25].

Figure 5. Failure modes of tensile test specimens.

Fractured specimens under axial tensile loading shown in Figure 5, the failure mode was formed in the lateral mode in 0, 0.1 wt% specimens, followed by damage in the mode of fiber pull-out with the delamination failure in matrix following the increasing amount of particle content. Delamination damage proves that the matrix/fiber bonding decreases as the content of particles in the material increases.

3.2 Flexural Tests

To characterize the produced material under bending moment, 3-point bending tests were conducted, force-displacement data were recorded for varying content of GnPs. According to the different additive contents, the flexural properties of the produced material are presented on the Table 3 and force-displacement curves of test specimens are given in Figure 5. Flexural strength values were recorded as 374.7, 662.5, 613.5 and 609.2 MPa for the control, 0.1, 0.25 and 0.5 wt% specimens respectively. Maximum enhancement in flexural strength was measured as 76.8% in 0.1 wt% and 63.7% in 0.25 wt%, 62.6% in 0.5 wt% test specimens compared with control specimen. As seen in the tensile test results, after 0.1 wt% GnPs content, decreasing trend was seen in terms of flexural strength compared to specimens with 0.1 wt% GnPs.

Fractured specimens under bending loading are shown in Figure 7, the failure mode was formed as fiber breakage in lower particle content, and then delamination failure in matrix following the increasing amount of particle content. Similarly, delamination damage proves poor matrix/fiber bonding at high content of particles in the material.

Table 2. Tensile test results of test specimens

Nano Content (wt%)	Tensile Strength (MPa)	Tensile Modulus (GPa)	Tensile Strain (%)
0, control	304	13.5	0.026
0.1	471	21.56	0.0255
0.25	455	18.46	0.039
0.5	433	20.42	0.0275

Table 3. Flexural properties of test specimens.

Nano Content (wt%)	Flexural Strength (MPa)	Flexural Modulus (GPa)	Flexural Strain (%)
0, control	374.7	15.69	0.023
0.1	662.5	23.32	0.0284
0.25	613.5	21.98	0.0279
0.5	609.2	23.16	0.0263
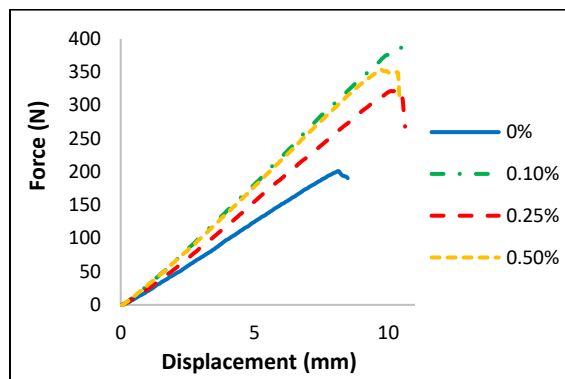
Figure 6. Force-displacement curves of test specimens.
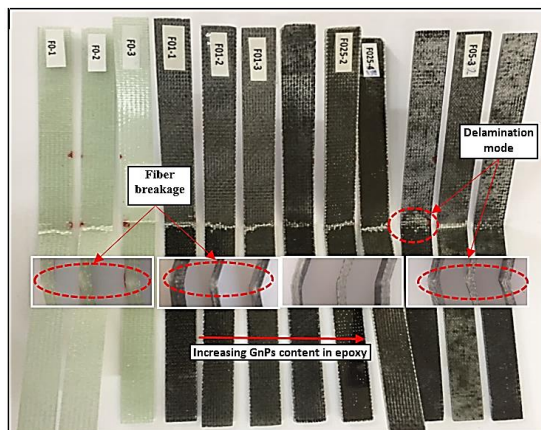
Figure 7. Failure modes of 3-point bending test specimens.

4. Conclusions

This work investigated the effect of GnPs inclusion on the mechanical properties of GFR epoxy composites. The results were revealed that addition of GnPs particles resulted as better mechanical properties in terms of tensile and flexural strength. Particularly, GnPs content of 0.1 wt% was resulted maximum enhancement in strength values compared to control material. Maximum enhancement was 54.9% in tensile strength and 76.8% in flexural strength value. After this filler content, decreasing trend was observed, but these strength values were also found to be higher than control sample values. In addition to the obtained strength values, it was evaluated that after the examination of the photographs of the fractured surface, the filler in the samples caused a decrease in fiber-matrix bonding and stress concentration in matrix due to agglomeration after 0.1 wt% of the GnPs filler content. This work has shown that a significant improvement in the tensile and flexural strengths of the glass fiber/ epoxy composite material at a certain filler content can be achieved.

Nomenclature

GnPs   : Graphene nanoplatelets
FRP   : Fiber reinforced polymer
GFR   : Glass fiber reinforced
CNTs   : Carbon nanotubes

References

1. Kostagiannakopoulou, C., Loutas, T. H., Sotiriadis, G., Markou, A., & Kostopoulos, V. (2015). On the interlaminar fracture toughness of carbon fiber composites enhanced with graphene nano-species. Composites Science and Technology, 118: 217-225.

2. S. Tsantzalis, P. Karapappas, A. Vavouliotis, P. Tsotra, V. Kostopoulos, K. Friedrich, Enhancement of the mechanical performance of an epoxy resin and fiber reinforced epoxy resin composites by the introduction of CNF and PZT particles at the microscale, Compos. A Appl. Sci. Manuf. 2007. 38: 1076-1081.

3. Jarukumjorn, K., & Suppakarn, N. Effect of glass fiber hybridization on properties of sisal fiber–polypropylene composites. Composites Part B: Engineering, 2009. 40(7): 623-627.

4. Sarasini, F., Tirillò, J., Valente, M., Valente, T., Cioffi, S., Iannace, S., & Sorrentino, L. Effect of basalt fiber hybridization on the impact behavior under low impact velocity of glass/basalt woven fabric/epoxy resin composites. Composites Part A: Applied Science and Manufacturing, 2013. 47: 109-123.

5. V. Kostopoulos, P. Karapappas, P. Tsotra, A. Paipetis, A. Vavouliotis, Enhanced fracture properties of carbon reinforced composites by the addition of multiwall carbon nanotubes, J. Compos. Mater. 2009. 43: 977-985.

6. Alsaadi, M., Erkliğ, A., & Albu-khaleefah, K. Effect of Pistachio Shell Particle Content on the Mechanical Properties of Polymer Composite. Arabian Journal for Science and Engineering, 2018: 1-8.

7. R.J. Sager, P.J. Klein, D.C. Davis, D.C. Lagoudas, G.L. Warren, H. Sue, Interlaminar fracture toughness of woven fabric composite laminates with carbon nanotube/interleaf films, J. Appl. Polym. Sci. 2011. 121(4): 2394-2405.

8. Bunch JS, van der Zande AM, Verbridge SS, Frank IW, Tanenbaum DM, Parpia JM, et al. Electromechanical resonators from graphene sheets. Science 2007. 315(5811): 490.

9. Xia, F., Mueller, T., Lin, Y. M., Valdes-Garcia, A., & Avouris, P. Ultrafast graphene photodetector. Nature nanotechnology, 2009. 4(12): 839.

10. Jeevananda, T., Kim, N. H., Lee, J. H., Basavarajaiah, S., Urs, D., & Ranganathaiah, C. Investigation of multi-walled carbon nanotube-reinforced high-density polyethylene/carbon black nanocomposites using electrical, DSC and positron lifetime spectroscopy techniques. Polymer International, 2009. 58(7): 775-780.

11. Geng, Y., Liu, M. Y., Li, J., Shi, X. M., & Kim, J. K. Effects of surfactant treatment on mechanical and electrical properties of CNT/epoxy nanocomposites. Composites Part A: Applied Science and Manufacturing, 2008. 39(12): 1876-1883.

12. Spitalsky, Z., Tasis, D., Papagelis, K., & Galiotis, C. Carbon nanotube–polymer composites: chemistry, processing, mechanical and electrical properties. Progress in polymer science, 2010. 35(3): 357-401.

13. Park, O. K., Jeevananda, T., Kim, N. H., Kim, S. I., & Lee, J. H. Effects of surface modification on the dispersion and electrical conductivity of carbon nanotube/polyaniline composites. Scripta materialia, 2009. 60(7): 551-554.

14. Li, Y., Wang, S., Wang, Q., & Xing, M. Enhancement of fracture properties of polymer composites reinforced by carbon nanotubes: A molecular dynamics study. Carbon, 2018. 129: 504-509.

15. Nguyen, V. T., Nguyen, D. K., Ngo, D. T., Tran, P., & Nguyen, D. D. Nonlinear dynamic response and vibration of functionally graded carbon nanotubes reinforced composite (FG-CNTRC) shear deformable plates with temperature dependence material properties and surrounded on elastic foundations. Journal of Thermal Stresses, 2017. 40(10): 1254-1274.

16. King, J. A., Klimek, D. R., Miskioglu, I., & Odegard, G. M. Mechanical properties of graphene nanoplatelet/epoxy composites. Journal of Applied Polymer Science, 2013. 128(6): 4217-4223.

17. Chatterjee, S., Nafezarefi, F., Tai, N. H., Schlagenhauf, L., Nüesch, F. A., & Chu, B. T. T. Size and synergy effects of nanofiller hybrids including graphene nanoplatelets and carbon nanotubes in mechanical properties of epoxy composites. Carbon, 2012. 50(15): 5380-5386.

18. ASTM, "D638-10 Standard test method for tensile properties of plastics," ASTM International, West Conshohocken, PA (2010).

19. ASTM, Inernational. "Standard test methods for flexural properties of unreinforced and reinforced plastics and electrical insulating materials." ASTM D790-07 (2007).

20. Du, J., & Cheng, H. M. The fabrication, properties, and uses of graphene/polymer composites. Macromolecular Chemistry and Physics, 2012. 213(10-11): 1060-1077.

21. Bulut, M. Mechanical characterization of Basalt/epoxy composite laminates containing graphene nanopellets. Composites Part B: Engineering, 2017. 122: 71-78.

22. Du, X., Zhou, H., Sun, W., Liu, H. Y., Zhou, G., Zhou, H., & Mai, Y. W. Graphene/epoxy interleaves for delamination toughening and monitoring of crack damage in carbon fibre/epoxy composite laminates. Composites Science and Technology, 2017. 140: 123-133.

23. Zaman I, Kuan HC, Dai JF, Kawashima N, Michelmore A, Sovi A, et al. From carbon nanotubes and silicate layers to graphene platelets for polymer nanocomposites. Nanoscale, 2012. 4(15): 4578–86.

24. Rafiee MA, Rafiee J, Wang Z, Song HH, Yu ZZ, Koratkar N. Enhanced mechanical properties of nanocomposites at lowgraphene content. ACS Nano, 2009. 3(12): 3884–90.

25. Desai T, Keblinski P, Kumar SK. Molecular dynamics simulations of polymer transport in nanocomposites. J Chem Phys 2005, 122(13): 134910.

Research Article

Biosynthesis and characterization of CaCO₃ nanoparticles from the leach solution and the aqueous extract of *Myrtus communis* plant

Deniz Uzunoğlu [a],* and Ayla Özer [a]

[a] Department of Chemical Engineering, Mersin University, Mersin, 33343, Turkey

ARTICLE INFO	ABSTRACT
	In this study, the biosynthesis and characterization of CaCO₃ nanoparticles from the leach solution and the aqueous extract of *Myrtus communis* plant were carried out. The leach solution obtained by leaching from the leaves and branches of *M. communis* growing around Mersin University Çiftlikköy Campus were analyzed by ICP-MS and it was found to be a calcium accumulator plant. Then, CaCO₃ nanoparticles were biosynthesized by adding of the leaf extract, as a biological agent, prepared by the extraction with distilled water of the leaves of same plant to the leach solution under favorable conditions. The characterization of CaCO₃ nanoparticles was performed by XRD, EDX, and SEM analyses. XRD, EDX and SEM analysis results showed that the biosynthesized nanoparticles were CaCO₃ in nano sizes and porous structures. Besides, the availability of the biosynthesized CaCO₃ nanoparticles in the color removal from different dyestuff solutions was investigated; the highest color removal yield was determined to be 90% at the end of 5 min for basic Methylene Blue (MB) dyestuff.

1. Introduction

Nanotechnology has a wide range of applications in many scientific and technological areas, such as electric-electronic, catalytic applications, optical applications, biomedicine, automotive, and chemical industry. It could be seen in the literature that various researches in the area of nanotechnology are related to the synthesis, characterization, and applications of nanoparticles due to their outstanding physical and chemical properties. Nanoparticles can be synthesized by various chemical methods such as electrochemical synthesis, reverse micelle/micro-emulsion method, chemical precipitation, hydrothermal synthesis, sono-chemical precipitation, chemical reduction. However, these methods are expensive and there are environmental and biological risks of the used harmful chemicals such as sodium borohydride, sodium citrate, hydrazine hydrate, dimethylformamide, poly- ethylene glycol and ethylene glycol [1, 2]. In recent years, the nanoparticle synthesis, in which microorganisms, enzymes, and plant extracts are used instead of the harmful chemicals, with simple, clean, non-toxic, inexpensive, and environmentally friendly approach (biosynthesis) has attracted much attention as an alternative method to the chemical methods. In the

biosynthesis method, nanoparticles are synthesized by reduction or precipitation from a synthetic metal salt solution containing a certain component, AgNO₃, FeSO₄, CaCl₂ etc., with the aid of several biological agents such as microorganism species, enzymes or plant extracts [3]. In the biosynthesis of nanoparticles, plant extracts are more preferred than microorganisms and enzymes due to their some advantages such as easy harvesting, easy and safe processing, and no need for sterilization [4]. Considering the plant diversity of our country, it is possible to transform the unused environmental friendly source into an economic value by using plant leaves as biological agents in the biosynthesis process. There are various studies in the literature about biosynthesis and characterization of different types of nanoparticles by combining various plant extracts and synthetic solutions containing a certain component [5-8]. The biosynthesis of nanoparticles is possible with the aqueous extracts prepared from the forenamed plant leaves as a biological agent and the leach solutions obtained from a plant which accumulates metals in their frame. The metals could be taken up by plants by many pathways such as soil, water, atmosphere and so on. The plants are classified as accumulator, indicator, and excluder according to the

* Corresponding author. Tel.: +90-324-361-0001/17372; Fax: +90-324-361-0073.
E-mail address: denizuzunoglu4@gmail.com

quantities that they can accumulate the metal. On the above basis, the properties the plants are as follows [9]:

- Accumulators store metals mainly in the shoot high and low metal concentration in the soils.
- Indicators grow in some specific environment, allowing an assessment of soil and other conditions in a place by simple observation of vegetation.
- Excluders restrict contaminant uptake into their frame.

In the literature, these accumulators and indicators are usually used for removing or monitoring the metals in environment. The establishment of vegetation on polluted environment helps prevent erosion and metal leaching [10].

In this work, an accumulator plant has been firstly used as both metal source and reducing agent for the metallic nanoparticle synthesis. Accordingly, our study involves the biosynthesis of $CaCO_3$ nanoparticles by combining of the extracts and the leach solutions prepared from leaves and branches of *Myrtus communis*. The comparison of nanoparticle synthesis method by plant extract and metallic salts with the biosynthesis method to be used in this study was illustrated in Scheme 1. In the biosynthesis method to be used in this study, a leach solution prepared from an accumulator plant are used instead of a synthetic metal salt solution ($AgCl$, $Fe(NO_3)_3$, $CuSO_4$, $CaCl_2$) to combine with the aqueous leaf extract under suitable conditions. It enables to synthesize of the nanoparticle by an environment friendly approach without using harmful chemicals.
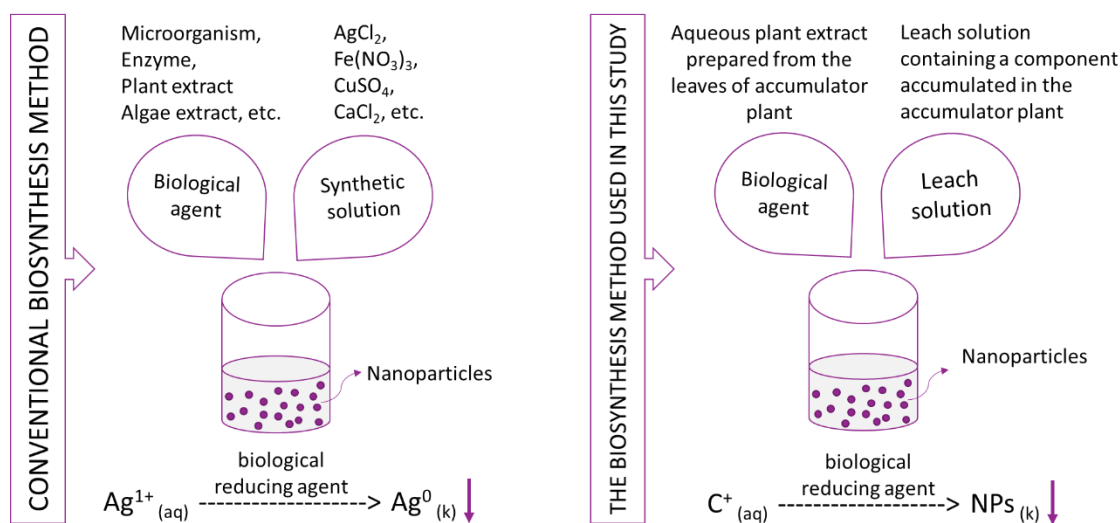
Scheme 1. The comparison of conventional biosynthesis method with the biosynthesis method used in this study
(C: component accumulated in the plant; NPs: nanoparticles)

2. Materials and Methods

2.1 Chemicals

HCl (37%, Sigma Aldrich), HNO_3 (65%, Riedel-de Haën), ethyl alcohol (≥99.8%, Sigma Aldrich), Procion Red MX-5B (Sigma Aldrich), Acid Red 97 (Sigma Aldrich), and Methylene Blue (Sigma Aldrich) were used in the experiments. All of them were of analytical grade and they were used without further purification.

2.2 Preparation of Leach and Extract Solutions from Myrtus communis

Myrtus communis is from the family of myrtaceae and also is a plant in the form of a bush from the scrub group. The plant, which does not cover its leaves in the winter season and can grow up to 2-5 meters, can be grown in places where Mediterranean climate is experienced, especially in coastal areas. *M. communis* growing around Mersin University Çiftlikköy Campus was used in this study. The leaves of *M. communis* collected for using in the experiments were separated from their branches; after that the leaves and branches were washed separately with firstly tap water and then distilled water to remove impurities. The leaves and branches removed from impurities were dried in the oven at 50 ºC for 1.0 day and they were stored in closed vessels in a refrigerator at +4 ºC for the further studies.

In the leaching process, the compounds of a solid material are taken into solution by dissolving in the solvents (usually acid or base). In order to determine of the component accumulated in *M. communis*, the leaves and branches, which were purified from impurities and dried, were firstly weighed in certain amounts separately and then they were separately burned in porcelain crucibles in a muffle furnace at 550 ºC for 10 h. Ash samples were then cooled and weighed. After that, 5.0 mL of concentrated HNO_3 solution were added to the ash samples and HNO_3 solution was evaporated by using hot-plate until the ash samples dry. The residues were re-dissolved in 5.0 mL of concentrated HCl and diluted to 25 mL by adding distilled water. The contents of the leaching solutions prepared separately from the leaves and branches were analyzed by Agilent 7500ce Octopole Reaction System model Inductively Coupled Plasma Mass Spectrometry (ICP-MS) [11].

M. communis leaf extract was prepared by boiling 5.0 g of the purified and dried leaves in 100 mL of distilled water at 100°C for 240 min. The extract was centrifuged to remove insoluble fractions and macromolecules. Lastly, the obtained

dark brown extract was stored in the refrigerator for further the synthesis experiments [12].

2.3 Biosynthesis and Characterization of the Nanoparticles

In the nanoparticle biosynthesis experiments, firstly 50 mL of the leaf extract as a biological reductant at room temperature was dropped by syringe pump to 25 mL of the leach solution prepared from the leaves of *M. communis*. The mixture was magnetically stirred for 1.0 h and then it was kept at room temperature for 2.0 days in order to complete the synthesis. The precipitated nanoparticles were separated from the aqueous mixture by a simple decantation method and then they were washed firstly with pure ethyl alcohol, after that they were washed with distilled water until the pH of wash water was neutral. Lastly, the biosynthesized nanoparticles, named MCI, were dried at 60°C in an oven for 24 h and they were then stored in closed vessels in a refrigerator for the further studies [6].

The preparation of leach solution and aqueous leaf extract as well as the biosynthesis of the nanoparticles were illustrated in Scheme 2.
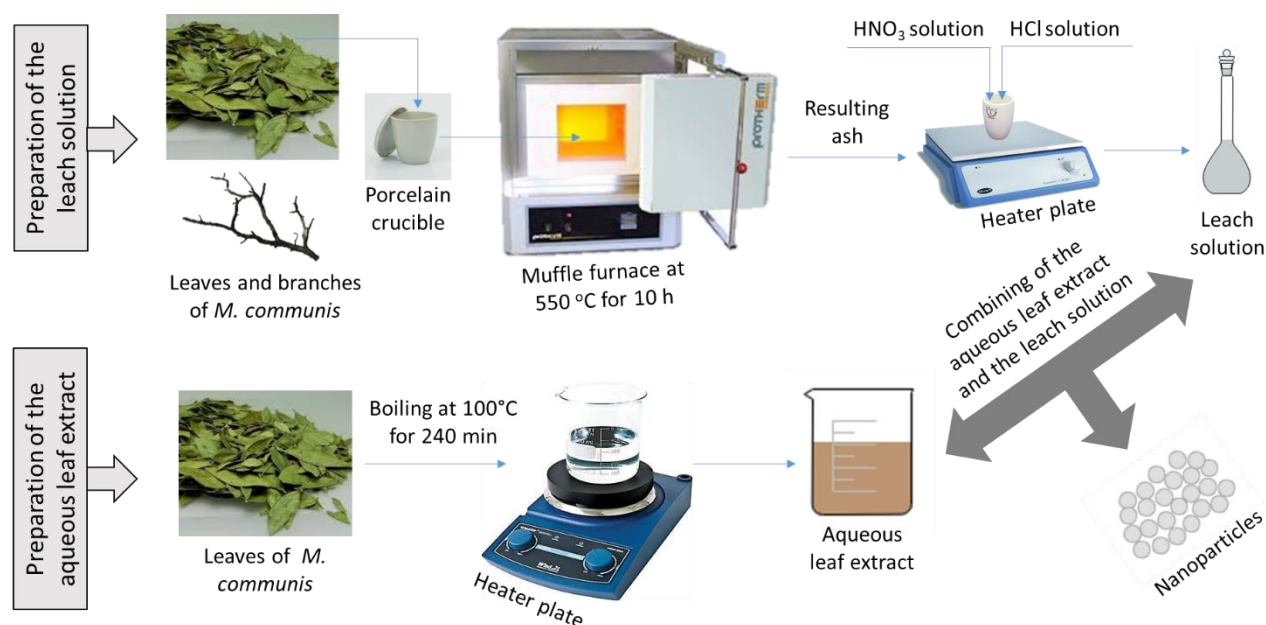
Scheme 2. The preparation of leach solution and aqueous leaf extract as well as the biosynthesis of the nanoparticles

After that, the biosynthesized nanoparticles were characterized by Philips XPert X-Ray Diffraction (XRD), Zeiss/Supra 55 Scanning Electron Microscopy (SEM) and Energy Dispersive X-Ray Analyzer (EDX) analysis methods.

The same procedure was also performed for the biosynthesis and characterization of $CaCO_3$ nanoparticles from the branches of *M. communis* and it was named as MCII.

2.4 Preparing of the Calcined Nanoparticles

The biosynthesized nanoparticles from the leaves (MCI) and branches (MCII) were calcined in a muffle furnace at 600 °C for 5.0 h and the characterization studies were also carried out by XRD, SEM, and EDX analysis methods. After calcination process, MCI and MCII were denoted as MCIII and MCIV, respectively.

2.5 Decolorisation studies

1.0 g of the dyestuff was dissolved in 1 L of distilled water in order to prepare 1.0 g/L of the stock solutions of Procion Red MX-5B, Acid Red 97, and Methylene Blue. 50 mg/L of the solutions were prepared with required dilutions from the stock solutions. The color removal studies were carried out with three different types of dyestuff that were reactive (Procion Red MX-5B), acidic (Acid Red 97), and basic (Methylene Blue). These studies were carried out in a 250 mL beakers on a shaker running at constant agitation speed and temperature. For this purpose; the experiments were initiated by mixing the desired amount of nanoparticles with the dyestuff solution at a certain initial dye concentration and initial pH value. After that, the samples were taken at predetermined time intervals during the experiment, then the solid and liquid phase were separated by centrifuging at 3000 rev/min for 5.0 min. The color removal was determined with Specord 210 Plus UV-vis spectrophotometer by recording the absorbance at 538 nm for Procion Red MX-5B, 497 nm for Acid Red 97, and 610 nm for Methylene Blue and also by spectral scanning at 200-800 nm [13].

3. Results and Discussions

The results of the synthesis and characterization of $CaCO_3$ nanoparticles [MCI, MCII, MCIII and MCIV] biosynthesized from the leaves and branches of *Myrtus communis* materials as well as the results of decolorisation studies were also presented in following the subsections:

3.1 ICP Analysis of Leach Solutions Prepared from Leaves and Branches of Myrtus communis

The leach solutions prepared separately from leaves and

branches of *M. communis* were analyzed by ICP-MS; the results were presented in Table 1. From Table 1, it was observed that the leach solutions of leaves and branches contained 1456.4 and 1502.5 mg/L calcium, respectively while it was seen that the other components were in relatively low concentrations compared to the calcium. This suggests that *M. communis* can accumulate calcium element in itself higher than the other components. Moreover, the high content of calcium in *M. communis* may be due to the calcareous nature of the soil in which it grows.

Table 1. ICP-MS analysis results of the leaching solutions prepared from the leaves and branches *M. communis*

Element	Leaf sample		Branch sample	
	Liquid base concentration (mg/L)	Solid base concentration (mg/g leaf)*	Liquid base concentration (mg/L)	Solid base concentration (mg/g branch)**
Ca	1456.4	7.28	1502.5	3.97
Na	45.46	0.2273	47.97	0.1411
Al	10.50	0.0525	11.68	0.0344
Fe	8.29	0.0415	9.33	0.0274
B	7.25	0.0363	8.43	0.0248
Mn	4.63	0.0232	5.78	0.0170
Si	4.29	0.0215	5.43	0.0160
Ti	4.03	0.0202	5.21	0.0153
Sr	3.10	0.0155	3.98	0.0117
Ba	1.93	0.00965	2.53	0.00744
Zn	1.27	0.00635	1.89	0.00556
Ni	0.967	0.00484	1.244	0.00366
Cr	0.704	0.00352	0.756	0.00222
Cu	0.671	0.00336	0.709	0.00209
As	0.304	0.00152	0.384	0.00113
Ag	0.291	0.00146	0.312	0.000918
Pb	0.100	0.000500	0.123	0.000362
Mo	0.02604	0.000130	0.02731	0.000080
Co	0.01257	0.000063	0.01352	0.000040

$$* \ 1456.4 \ \frac{mg\,Ca}{L} \cdot \frac{1\,L}{1000\,mL} \cdot \frac{25\,mL}{0.5\,g\,ash} \cdot \frac{1\,g\,ash}{10\,g\,leaf} = 7.28 \ \frac{mg\,Ca}{g\,leaf}$$

$$** \ 1502.5 \ \frac{mg\,Ca}{L} \cdot \frac{1\,L}{1000\,mL} \cdot \frac{25\,mL}{0.5\,g\,ash} \cdot \frac{1\,g\,ash}{17\,g\,branch} = 3.97 \ \frac{mg\,Ca}{g\,branch}$$

3.2 XRD Analysis of the Biosynthesized Nanoparticles

The phases and crystal structures of MCI, MCII, MCIII and MCIV were determined by using XRD at 40 kV and 30 mA in the 2θ range of 0-90°. XRD analysis showed that MCI and MCII were amorphous (XRD pattern not shown). Furthermore, XRD patterns of MCIII and MCIV were presented in Figure 1. Accordingly, the calcined nanoparticles showed the same phase and crystal structure. Similarly, Mekprasart et. al. (2015) reported that the all calcined samples have identical patterns in single phase without contaminated peaks [14].

In this work, MCIII and MCIV had the characteristic peaks of hexagonal vaterite $CaCO_3$ phase and the diffraction peaks of it were observed in the planes of (002, 100, 101, 102, 110, 104, 202) [15]. It can be concluded that the calcination process enabled the high crystallinity as reported in many studies in the literature [16-18]. It was also seen in Figure 1 that there were some peaks that did not match with the obtained phase due to some impurities in the nanoparticles.

It can be concluded that the calcination process caused the change of the crystal phases of the nanoparticles from amorphous to hexagonal vaterite $CaCO_3$ phase.

3.3 SEM Analysis of the Biosynthesized Nanoparticles

The morphologies of MCI, MCII, MCIII, and MCIV were examined by SEM; SEM images at different magnification ratios were given in Figure 2. Although Figure 2.a-d showed that the biosynthesized particles were in nanoscale and porous structure, it was also noteworthy that the agglomeration occurred resulting in growth of nanoparticles by leaguing together. Furthermore, it was seen that some lamellar structures, which were the triangular forms for leaf samples and the round forms for branch samples, occurred in SEM images of MCIII and MCIV. This may be due to the change in crystal phase by the calcination process as determined in XRD analysis. Moreover, the sizes of nanoparticles did not change after the calcination process. It was seen that the particle sizes were in the range of 20-50 nm for all of the nanoparticles.
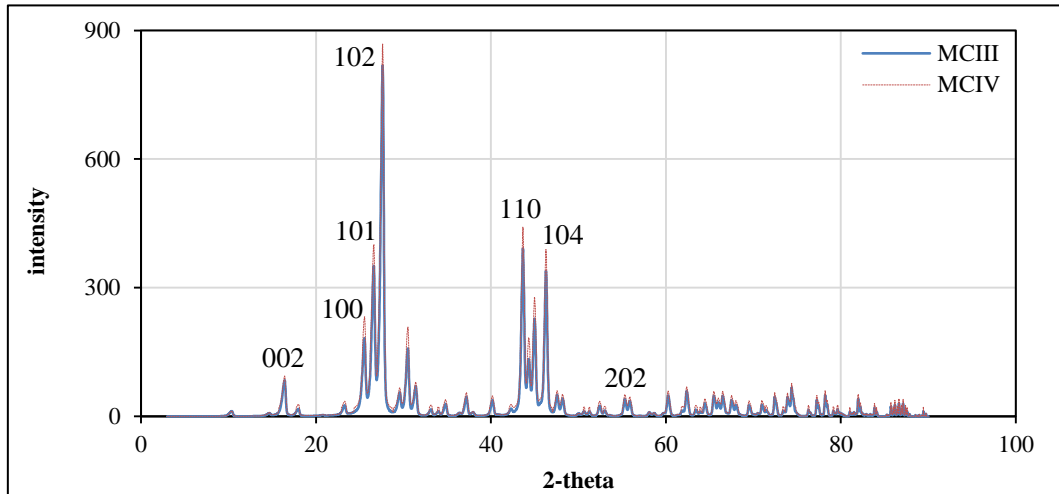
Figure 1. XRD analysis of MCIII and MCIV
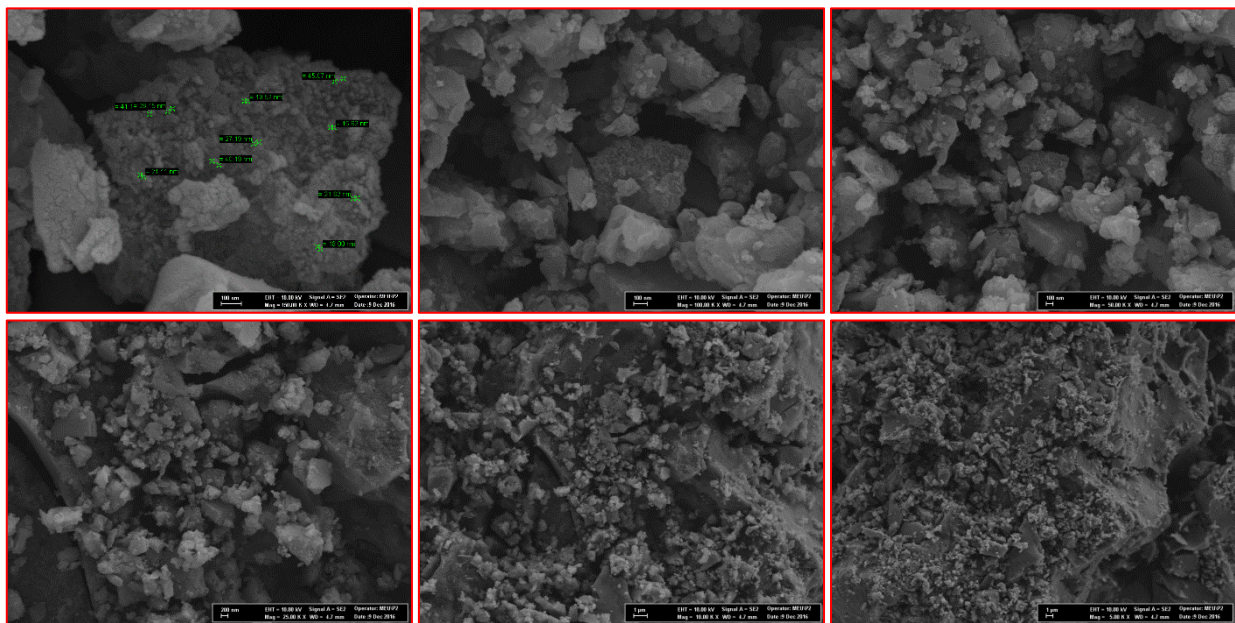
Figure 2.a. SEM images at different magnification ratios of MCI
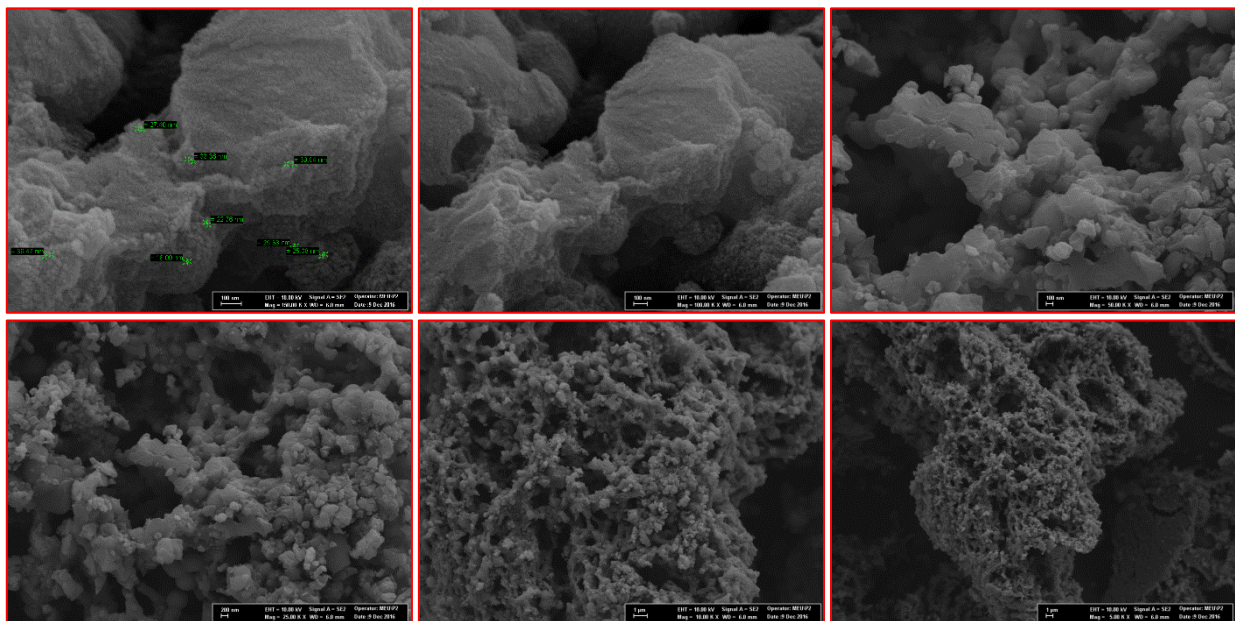
Figure 2.b. SEM images at different magnification ratios of MCII
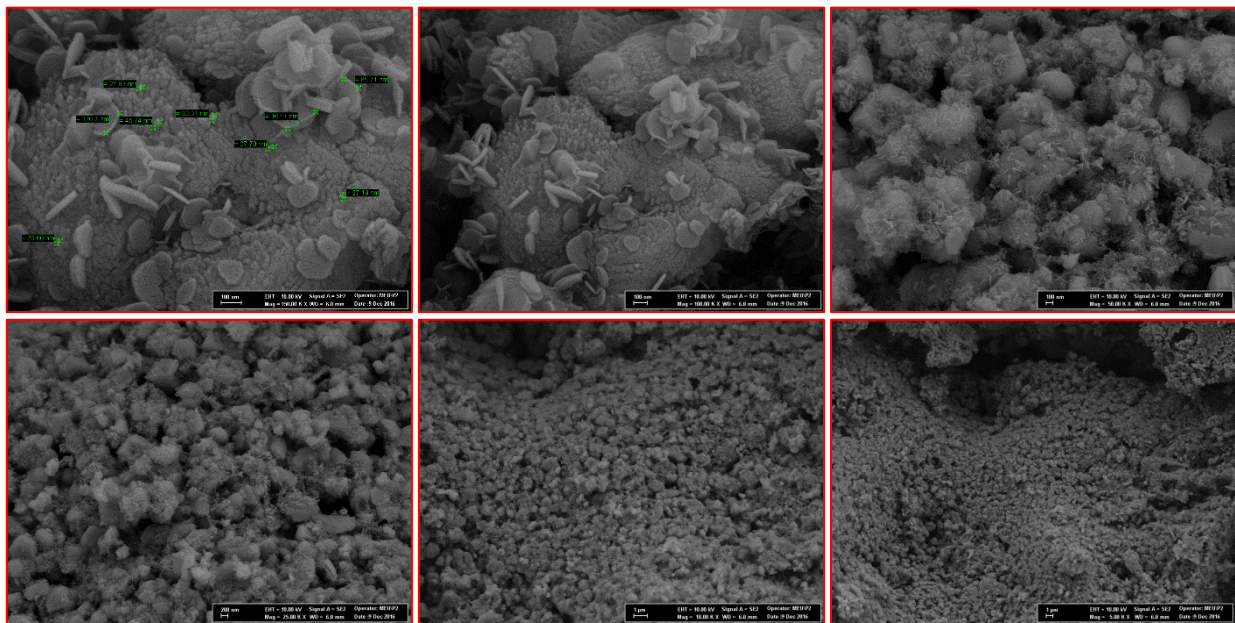
Figure 2.c. SEM images at different magnification ratios of MCIII
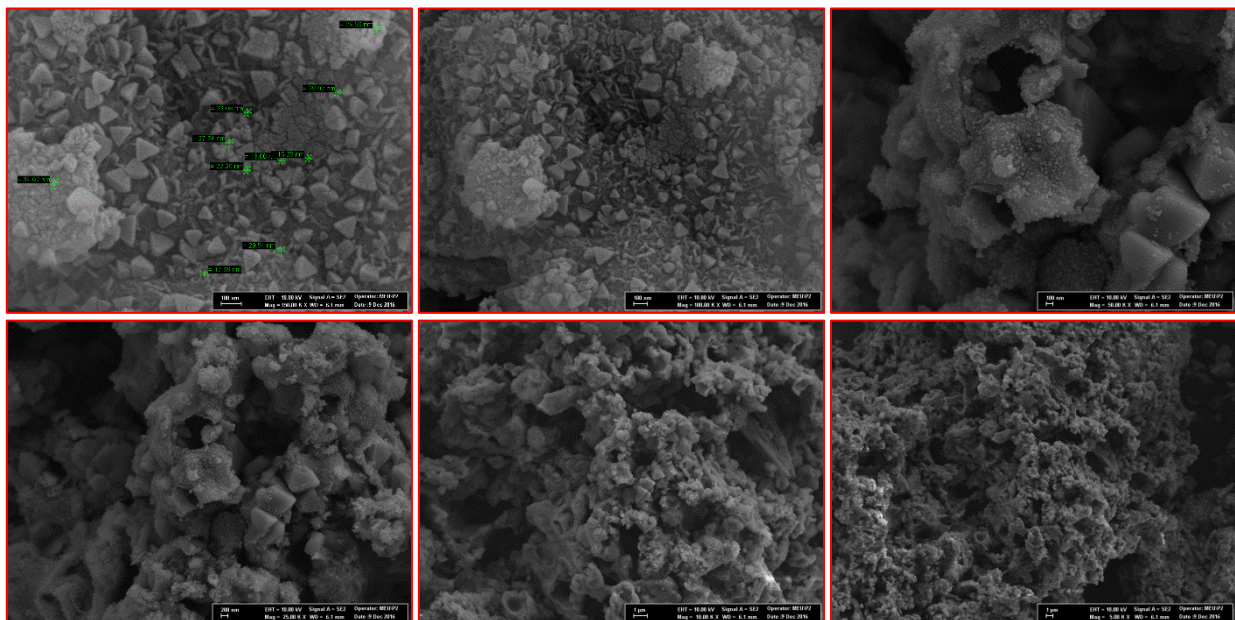
Figure 2d. SEM images at different magnification ratios of MCIV

3.4 EDX Analysis of the Biosynthesized Nanoparticles

The elemental composition of the nanoparticles were determined by EDX. The elemental analysis results of MCI, MCII, MCIII, and MCIV were presented in Table 2. Accordingly, it was obvious that all of the biosynthesized nanoparticles had almost the same elemental composition. Moreover; it could be clearly seen from Table 2 that the theoretical mass and mole percentages of elements in $CaCO_3$ composition and the mass and mole percentages of Ca, C and O elements in the nanoparticles were in agreement with each other, indicating that the biosynthesized nanoparticles were in $CaCO_3$ structure.

Furthermore, the biosynthesized nanoparticles contained trace amounts of Mg, Cl, Fe, Co, and Ni elements compared to Ca, C and O elements due to the some components in the

leaves and branches as determined by ICP-MS.

3.5 The Comparison of MCI, MCII, MCII, and MCIV Physical and Chemical Properties

The comparison of the structures, elemental compositions and morphologies of MCI, MCII, MCIII and MCIV was evaluated according to XRD, EDX and SEM analysis results. Accordingly, the similarities and differences were summarized the following below:

- XRD analysis showed that the crystal phase of MCI and MCII altered from amorphous to hexagonal vaterite $CaCO_3$ phase after the calcination process.

- It was obtained by SEM images that the sizes of the all biosynthesized $CaCO_3$ nanoparticles were in the range of 20-50 nm. Moreover, it was observed by SEM

analysis that the morphologies of MCI and MCII changed depending upon the change of the crystal phase by the calcination process whilst the calcination process did not affect the particle sizes.

- It was determined by EDX analysis that all of the biosynthesized $CaCO_3$ nanoparticles had the same elemental composition notwithstanding the particle type. Thus, it can be concluded that the nanoparticles could be biosynthesized in the same elemental composition without the need to separate branches and leaves. In addition, it just can be indicated that it is possible to obtain the leach solution at higher calcium concentration by using the branches of *M. communis.*

Consequently, it could be said that the calcination process did not cause any change in the elemental composition and particle size while it changed the crystal phase and the morphology of the nanoparticles.

After evaluating the chemical and physical properties of the biosynthesized nanoparticles, the usability of the nanoparticles as an adsorbent was tested. It was thought that the color removal capabilities of MCI, MCII, MCIII, and MCIV do not change (it may be possible to change of only removal capacities) since there is not any difference in the elemental compositions and particle sizes of them. For this reason, MCI was chosen as a model adsorbent for the dye decolorisation studies because MCI have some advantages such as being synthesized under mild conditions (no needing of calcination process) and using leaves that are more abundant than branches.

Table 2. EDX analysis results of MCI, MCII, MCIII, and MCIV

Element	MCI		MCII		MCII		MCIV		CaCO$_3$ (theoretical)	
	Weight %	Atom %	Weight %	Atom %	Weight %	Atom %	Weight %	Atom %	Weight %	Atom %
Ca	39.02	20.03	39.63	19.73	39.89	20.07	40.03	19.98	40	20
C	12.22	19.78	12.41	19.62	12.05	19.66	12.16	19.87	12	20
O	46.93	59.95	46.05	60.03	47.11	59.79	46.87	59.75	48	60
Mg	0.79	0.15	0.88	0.31	0.58	0.29	0.61	0.22	-	-
Cl	0.30	0.05	0.31	0.12	0.19	0.10	0.19	0.09	-	-
Fe	0.28	0.015	0.29	0.09	0.062	0.034	0.048	0.032	-	-
Co	0.26	0.013	0.26	0.06	0.060	0.030	0.047	0.030	-	-
Ni	0.20	0.010	0.24	0.04	0.058	0.026	0.045	0.028	-	-

3.6 Decolorization with MCI

The usability of MCI was investigated for color removal from aqueous solutions containing three different types of dyestuffs, which were reactive (Procion Red MX-5B), acidic (Acid Red 97), and basic (Methylene Blue). The color removal yields for Procion Red MX-5B, Acid Red 97, and Methylene Blue (MB) were observed as 3.35%, 2.70%, and 90%, respectively. According to these decolorisation yields, the decolorisation results of MB dyestuff by MCI was evaluated in this section. The time-varying UV-vis spectra of MB dyestuff solution were presented in Figure 3. Accordingly, the characteristic peaks of MB were observed at 665, 610, and 292 nm; and the intensities of these characteristic peaks decreased over time in the presence of MCI. In addition, as a result of the overlapped peaks belonging to 5.0 and 60 min, the optimum contact time was determined to be 5.0 min. Consequently, the color removal efficiency for 50 mg/L of initial MB concentration was determined to be 90% in 5 min.

The application areas of $CaCO_3$ nanoparticles in the literature were presented in Table 3. Accordingly; it can be seen that there are many studies in the literature where $CaCO_3$ nanoparticles synthesized by different methods have been used as additives and antibacterial agents; however it is the first time to evaluate biosynthesized $CaCO_3$ nanoparticles for color removal from aqueous solution.
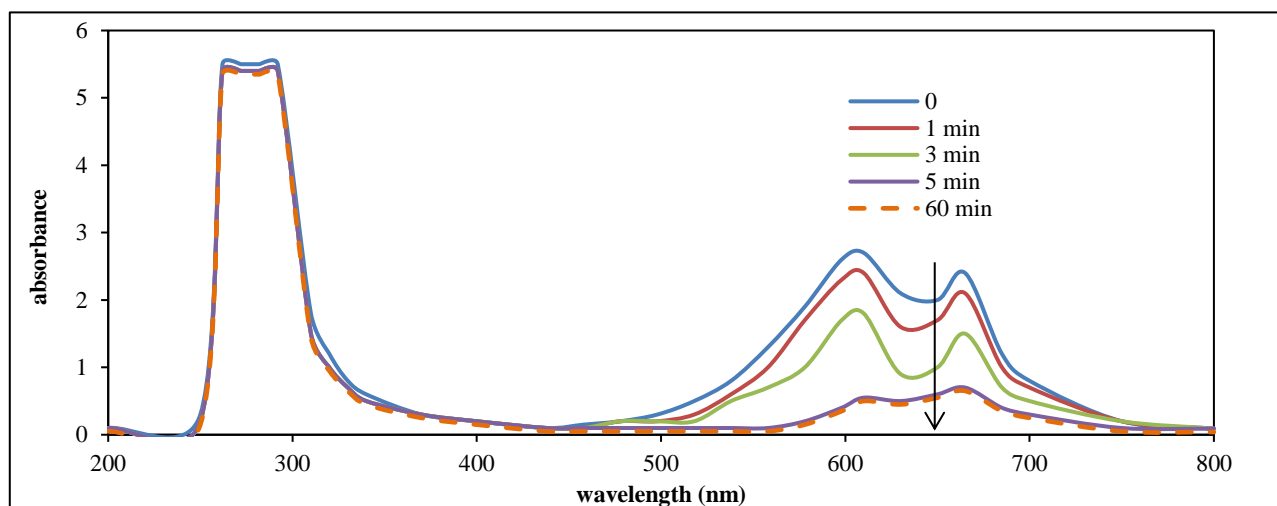
Figure 3. UV-vis spectra of MB dyestuff solution (experimental conditions: initial pH: 9.0, initial MB concentration: 50 mg/L, temperature: 30 °C, MCI concentration: 0.5 g/L)

Table 3. The studies with $CaCO_3$ nanoparticles in the literature

Nanoparticle	Synthesis method	Particle size	Application area	Reference
$CaCO_3$/Ag nanocomposite	Reduction with PPG	5-20 nm	Antibacterial agent against *Escherichia coli*	[19]
$CaCO_3$ nanoparticles	Reverse micro-emulsion method	90 nm	Antibacterial agent against *Staphylococcus aureus*	[20]
$CaCO_3$ nanoparticles	Wet carbonation	40 nm	Additive for epoxy resin	[21]
$CaCO_3$ nanoparticles	Commercial	50-120 nm	Additive in accelerating the hydration of Portland cement	[22]
$CaCO_3$ nanoparticles	Wet carbonation	< 100 nm	Paper coating for the hydrophobic character of the paper surface	[23]
$CaCO_3$ nanoparticles	Biosynthesis	< 100 nm	Color removal from aqueous Methylene Blue dyestuff solution	This work

4. Conclusion

This study has demonstrated that $CaCO_3$ nanoparticles, which are frequently used in nanotechnology applications, could be successfully synthesized with a completely environmental-friendly approach (without using harmful chemicals to the environment and human health) by using only the solutions, which are the leach and aqueous extract solutions, prepared from a bioaccumulator plant. Furthermore, this study has also showed that the biosynthesized $CaCO_3$ nanoparticles could be effectively used for color removal from aqueous solutions containing basic dyestuffs.

Acknowledgment

References

1. Iravani, S., *Green synthesis of metal nanoparticles using plants.* Green Chemistry, 2011. **13** (10): pp. 2638-2650.

2. Haiza, H., A. Azizan, A. H. Mohidin, and D. S. C. Halin, *Green synthesis of silver nanoparticles using local honey.* In Nano Hybrids. Trans Tech Publications, 2013. **4:** pp. 87-98.

3. Jagtap, U.B. and V.A. Bapat, *Green synthesis of silver nanoparticles using Artocarpus heterophyllus Lam. seed extract and its antibacterial activity.* Industrial Crops and Products, 2013. **46**: p. 132-137.

4. Veerasamy, R., T. Z. Xin, S. Gunasagaran, T. F. W. Xiang, E. F. C. Yang, N. Jeyakumar, S. A. Dhanaraj, *Biosynthesis of silver nanoparticles using mangosteen leaf extract and evaluation of their antimicrobial activities.* Journal of Saudi Chemical Society, 2011. **15**(2): pp. 113-120.

5. Abdi, V., I. Sourinejad, M. Yousefzadi, and Z. Ghasemi, *Mangrove-mediated synthesis of silver nanoparticles using native Avicennia marina plant extract from southern Iran.* Chemical Engineering Communications, 2018. **205** (8): p. 1069–1076.

6. Supraja, N., T. N. V. K. V. A. D. Prasad, Gandhi, D. Anbumani, P. Kavitha, and R. Babujanarthanam, *Synthesis, characterization and evaluation of antimicrobial efficacy and brine shrimp lethality assay of Alstonia scholaris stem bark extract mediated ZnONPs.* Biochemistry and biophysics reports, 2018. **14**: p. 69-77.

7. Radini, I. A., N. Hasan, M. A. Malik, and Z. Khan, *Biosynthesis of iron nanoparticles using Trigonella foenum-graecum seed extract for photocatalytic methyl orange dye degradation and antibacterial applications.* Journal of Photochemistry and Photobiology B: Biology, 2018. **183:** p. 154-163.

8. Naghdi, S., M. Sajjadi, M. Nasrollahzadeh, K. Y. Rhee, S. M. Sajadi, and B. Jaleh, *Cuscuta reflexa leaf extract mediated green synthesis of the Cu nanoparticles on*

graphene oxide/manganese dioxide nanocomposite and its catalytic activity toward reduction of nitroarenes and organic dyes. Journal of the Taiwan Institute of Chemical Engineers, 2018. **86**, p. 158-173.

9. Verma, D. K., A. P. Gupta, R. Dhakeray, *Removal of heavy metals from whole sphere by plants working as bioindicators–a review,* Basic Research Journal of Pharmaceutical Science, 2011. **1**: p. 1-7.

10. Ali, H., E. Khan, M. A. Sajad, *Phytoremediation of heavy metals—concepts and applications.* Chemosphere, 2013. **91** (7): p. 869-881.

11. Özdemir, Z. and E. Demir, *Nickel Accumlating species of Alyssum murale Waldst.&Kit from Fındıkpınarı-Erdemli/Mersin area.* Journal of Geological Engineering, 2010. **34** (1): p. 57-70.

12. Kouvaris, P., A. Delimitis, V. Zaspalis, D. Papadopoulos, S.A. Tsipas, and N. Michailidis, *Green synthesis and characterization of silver nanoparticles produced using Arbutus Unedo leaf extract.* Materials Letters, 2012. **76**: p. 18-20.

13. Weng, X., L. Huang, Z. Chen, M. Megharaj, and R. Naidu, *Synthesis of iron-based nanoparticles by green tea extract and their degradation of malachite.* Industrial Crops and Products, 2013. **51**: p. 342-347.

14. Mekprasart W., S. Worasawat, T. Tangcharoen, W. Pecharapa, *Characterization and effect of calcination temperature on structural properties of spinel zinc aluminate synthesized via Co-precipitation process.* Physica Status Solidi (c), 2015. **12**(6): p. 624-627.

15. Zhang, Z., D. Gao, H. Zhao, C. Xie, G. Guan, D. Wang, and S.H. Yu, *Biomimetic assembly of polypeptide-stabilized CaCO₃ nanoparticles.* The Journal of Physical Chemistry B, 2006. **110**(17): p. 8613-8618.

16. Suganthi, K. S., K. S. Rajan, *Effect of calcination temperature on the transport properties and colloidal stability of ZnO–water nanofluids.* Asian Journal of Scientific Research, 2012. **5**: p. 207-217.

17. Pang, Y. X., X. Bao, *Influence of temperature, ripening time and calcination on the morphology and crystallinity of hydroxyapatite nanoparticles.* Journal of the European Ceramic Society, 2003. **23**(10): p. 1697-1704.

18. Gupta, S. M., M. Tripathi, *A review of TiO₂ nanoparticles.* Chinese Science Bulletin, 2011. **56**(16): p. 1639-1657.

19. Apalangya, V., V. Rangari, B. Tiimob, S. Jeelani, and T. Samuel, *Development of antimicrobial water filtration hybrid material from bio source calcium carbonate and silver nanoparticles.* Applied Surface Science, 2014. **295**: p. 108-114.

20. Maleki Dizaj, S., F. Lotfipour, M. Barzegar-Jalali, M.H. Zarrintan, and K. Adibkia, *Ciprofloxacin HCl-loaded calcium carbonate nanoparticles: preparation, solid state characterization, and evaluation of antimicrobial effect against Staphylococcus aureus.* Artificial cells, nanomedicine, and biotechnology, 2017. **45**(3): p. 535-543.

21. Li, L., H. Zou, L. Shao, G. Wang, and J. Chen, *Study on mechanical property of epoxy composite filled with nano-sized calcium carbonate particles.* Journal of materials science, 2005. **40**(5): p. 1297-1299.

22. Sato, T., and J.J. Beaudoin, *Effect of nano-CaCO₃ on hydration of cement containing supplementary cementitious materials.* Advances in Cement Research, 2011. **23**(1): p. 33-43.

23. Barhoum A., H. Rahier, R.E. Abou-Zaied, M. Rehan, T. Dufour, G. Hill, and A. Dufresne, *Effect of cationic and anionic surfactants on the application of calcium carbonate nanoparticles in paper coating.* ACS applied materials & interfaces, 2014. **6**(4): p. 2734-2744.

Research Article

Prediction of calorific value of biomass based on elemental analysis

Ayşe Özyuğuran [a],*, Serdar Yaman [a], Sadriye Küçükbayrak [a]

[a]*ITU, Chemical&Metallurgical Engineering Faculty, Chemical Engineering Department, Istanbul-34469, Turkey*

ARTICLE INFO	ABSTRACT
	Thirty nine different biomass samples ranging from various herbaceous/woody materials to juice pulps were used to develop linear as well as non-linear empirical equations that predict the lower heating value (LHV) and the higher heating value (HHV) based on the elemental analysis (C, H, N, O, and S) results of the biomass species. These equations were interpreted with respect to their prediction performance considering the predicted values and the experimental data. Several criteria such as mean absolute error (MAE), average absolute error (AAE), average bias error (ABE), and root mean square deviation (RMSD) were regarded. For the linear equations, it was found that the lowest values of MAE were 0.3119 MJ/kg and 0.2906 MJ/kg for HHV and LHV, respectively, and AAE(%) changed in the ranges of (1.6659-4.5917) for HHV and (1.8216-5.5039) for LHV. Besides, it was determined that ABE(%) varies in the intervals of (0.0549-0.2976) for HHV and (0.0519-0.4177) for LHV when linear equations were tested. The best results of RMSD (0.4230 and 0.3607 for HHV and LHV, respectively) were obtained for Equation#1 where all of the linear terms were considered. Also, the addition of the non-linear terms to the linear equations was also studied to check whether any further improvement can be achieved in predictions. However, the improvements created by non-linear equations were negligible and it was concluded that the linear empirical equations provide satisfactory prediction performance and they may be tried to estimate the calorific value of very wide range of biomasses.

1. Introduction

There is a growing consensus that the fossil energy sources should be gradually withdrawn from the power technology since they lead complicated global concerns such as greenhouse gases, political instability, dependence on other countries, etc. Besides, environmental pollution that takes place during exploitation, drilling, transportation, and usage of fossil fuels cannot be ignored. On the contrary, biomass is a CO_2-neutral fuel that does not influence the concentration of atmospheric CO_2 negatively. In addition, biomass can be easily found almost everywhere, and therefore it is cheap, abundant, and very easy to access [1]. Actually, biomass energy has been used in energy and power technologies with increasing shares day by day.

Biomass that is defined as any type of carbonaceous material except fossil fuels takes a significant part in green energy technologies since it is easy to find, renewable, and

sustainable energy source [1]. According to this description woody/herbaceous crops and residues, agricultural leftovers, industrial and domestic wastes, municipal solid wastes (MSW), aquatic materials, forest by-products and residues are regarded as biomass energy resources. Despite this considerable variety in nature and properties of samples, they are mainly comprised of C, H, and O accompanied by some presence of N and S. Conversely, several different macromolecular ingredients including cellulose, hemicellulose, and lignin form the large portion of the molecular structure. Meanwhile, the amount of inorganics that form ash upon burning of biomass changes depending on type of the sample. That is, woody samples are poor in inorganics, while very large contents of inorganics may exist in waste materials. These varying characteristics of biomass also affect the "calorific value" in other words the "heating value" that is really the most important parameter to evaluate its fuel quality. That is why the calorific value of biomass cannot be forecasted

in most cases without measuring this property experimentally. Particularly in case of waste materials and herbaceous samples, the complexity of biomass makes it highly difficult to estimate the calorific value. The calorific value (heating value) is usually specified through burning of a specimen in calorimeter under well-controlled conditions, and in this way, higher heating value (HHV) is determined. Besides, lower heating value (LHV) is calculated via elimination of condensation heat of the forming water during combustion of H and moisture contents.

Calorific value estimation based on analysis results of biomass may be alternatively used provided that the analysis results have high accuracy and precision. The satisfactory prediction of HHV or LHV based on the elemental composition of biomass is a promising way since this approach does not deal with the type and distribution of the above mentioned macromolecules, and instead it only considers extents of the main elemental constituents of biomass. Actually, this approach has long been used to estimate the HHV or LHV of various coal samples globally. However, this approach was not so commonly applied yet for biomass. In this context, Channiwala and Parikh [2] complied the results of many investigations where HHV calculations were implemented considering both elemental analysis and proximate analysis results. In contrast to this, the literature that directly focus on the estimation of the HHV or LHV from the analysis results of biomass is scarce, and there have been only a few studies in this topic. Also, the existing literature on the assessment of HHV or LHV of biomass through such calculation-based approach was rather related to woody biomass types [2-9]. Motghare et al. [10] estimated the biomass calorific value upon the results of elemental analysis particularly for some waste species, and found that this approach is beneficial and gives highly reliable results.

This study attempts to apply the calculation-based method to predict HHV/LHV for miscellaneous waste biomasses, taking linear equations that contain elemental analysis results into consideration. Particularly, the most of the renewable fuel materials used in this study have not so far been chosen in investigations that target to describe the HHV/LHV prediction. For instance, some unusual samples including stems, fruit juice pulps, stalks, distinct agricultural leftovers, etc. have not been used in previous papers yet because they often show serious handling problems and tend to be easily decomposed.

2. Materials and Methods

2.1 Biomass Characterization

All of the biomasses used in the present paper are Turkish origin and provided from food/beverage industries and agricultural/forestry sector. They were kept in open container in laboratory to obtain air-dried (ad) specimens, and chopping and grinding operations were applied to reduce the particle size smaller than 250 μm. The proximate analysis was done according to ASTM standards, while Leco TruSpec® CHN model equipment with Leco TruSpec® S module was used to determine the elemental results. Determination of HHV was performed by adiabatic bomb calorimeter test using IKA C2000 model calorimeter operated under oxygen pressure of 30 atm. For this, 0.5 g of powdered (< 250 μm) biomass was placed into the sample holder and ignited by electricity current. This equipment is calibrated using benzoic acid and the measured results don't deviate more than 1-2% from the mean values. Calculation of LHV based on HHV was implemented by simplified equation given as follows:

$$LHV = HHV - \left[\left(\frac{18.015*H}{2} \right) + \%moisture \right] * 5.85 \quad (1)$$

where, H is the hydrogen content of the sample.

Experiments were checked three times to assure the reproducibility and accuracy of the results, and they were used in predictions as long as they differ within ±0.5%.

2.2 Error Analyses for Prediction Performance

Four different forms of prediction error such as MAE (mean absolute error), AAE (average absolute error), ABE (average bias error), and RMSD (root mean square deviation) were established using following equations, and from which prediction performances could be evaluated.

$$MAE = \frac{1}{n} \sum_{i=1}^{n} \left| HHV_{(p)_i} - HHV_{(e)_i} \right| \quad (2)$$

$$AAE = \frac{1}{n} \sum_{i=1}^{n} \left| \frac{HHV_{(p)_i} - HHV_{(e)_i}}{HHV_{(e)_i}} \right| \times 100 \quad (3)$$

$$ABE = \frac{1}{n} \sum_{i=1}^{n} \left(\frac{HHV_{(p)_i} - HHV_{(e)_i}}{HHV_{(e)_i}} \right) \times 100 \quad (4)$$

$$RMSD = \sqrt{\frac{\left(HHV_{(e)_i} - HHV_{(p)_i} \right)^2}{n}} \quad (5)$$

where, the indices of e and p represent the experimental and the predicted values of higher heating value. Likewise, the total number of the biomasses and any of the distinct biomass were represented by n and i, respectively. Of which, MAE shows the intimacy of the predicted HHV and the experimental HHV. From this point of view, low values of MAE indicate high prediction accuracy. Besides, the average absolute error (%) is estimated by AAE. Positive ABE means over-estimation whereas negative ABE means under-estimation

3. Results and Discussion

3.1 Sample Characterization

Results of the characterization tests are given in Table 1, and it is clear from this table that the samples differ seriously in terms of properties and the fuel characteristics. Although woody species have promising fuel properties such as low ash content and high calorific value, waste biomasses have relatively poor fuel characteristics.

Table 1. Analysis results of samples (on dry basis) [11]

Samples	C	H	N	S	O	VM	FC	Ash	HHV	LHV
	(%)					(%)			(MJ/kg)	
Elaeagnus	44.26	6.19	1.37	0.41	46.86	76.43	22.67	0.90	19.80	16.46
Tea caffeine	48.59	6.43	2.59	0.46	34.78	76.32	16.52	7.16	20.83	18.02
Ash tree wood	46.72	5.95	0.00	0.32	45.32	87.84	10.46	1.70	19.02	16.24
Green bean stem and husk	41.26	5.62	0.78	0.39	42.35	77.88	12.52	9.60	16.86	13.97
Red lentil hull	43.90	6.31	1.54	0.37	42.63	74.73	20.03	5.24	18.27	15.15
Chickpea husk	43.80	5.81	0.38	0.35	45.67	79.70	16.32	3.98	18.26	15.62
Tea waste	45.04	6.07	3.48	0.50	40.21	73.36	21.93	4.71	19.87	16.96
Cornstalk	42.02	5.58	1.24	0.43	43.53	76.79	16.02	7.19	16.55	14.19
Tobacco waste	37.02	5.01	2.20	0.45	39.95	72.85	11.78	15.36	14.51	12.26
Broad bean husk	40.11	5.52	1.35	0.33	44.98	74.97	17.33	7.70	16.24	13.50
Apricot stone	48.07	5.99	0.05	0.39	43.89	82.03	16.26	1.61	19.79	17.33
Apricot pulp	44.37	5.87	0.95	0.32	47.42	78.80	20.12	1.08	18.52	15.72
Peach pulp	43.84	6.51	1.04	0.37	42.80	71.21	23.34	5.44	18.23	15.11
Damson plum stone	50.81	6.36	1.07	0.36	40.39	82.33	16.67	1.00	21.23	18.81
Coconut shell	50.34	6.26	0.00	0.31	42.08	83.01	15.97	1.02	20.24	17.54
Cornelian cherry stone	49.03	5.86	0.05	0.34	42.67	79.27	18.67	2.06	19.84	17.44
Cacao husk	43.00	5.69	2.10	0.41	44.38	75.03	20.56	4.41	17.85	15.07
Peanut husk	46.89	5.90	0.61	0.37	46.07	79.32	20.53	0.15	19.16	16.53
Broad bean husk	41.33	5.90	0.39	0.34	46.32	74.88	19.40	5.73	16.80	13.90
Sunflower stem and stalk	37.94	5.19	0.31	0.35	46.15	77.37	12.58	10.05	15.08	12.55
Almond shell	47.70	5.88	0.05	0.31	42.58	81.70	14.82	3.48	19.53	16.81
Robinia pseudoacacia wood	46.30	6.08	0.05	0.35	46.20	86.19	12.80	1.01	18.31	15.59
Daphne	49.03	6.40	0.94	0.42	35.90	77.76	14.93	7.31	20.44	17.87
Thyme	44.53	6.01	0.81	0.36	39.34	75.04	16.00	8.96	18.16	15.27
Walnut shell	48.23	6.00	0.12	0.34	44.42	82.98	16.12	0.90	20.03	17.17
Locust bean	44.31	5.70	0.92	0.42	43.10	70.29	24.16	5.54	18.04	15.29
Flos lavandulae romanae	45.28	5.89	0.94	0.42	36.42	74.13	14.82	11.06	18.84	16.01
Apple pulp	47.05	6.70	0.86	0.35	42.73	82.56	15.13	2.31	19.85	17.15
Artichoke husk and waste	42.08	5.92	0.83	0.36	45.88	79.66	15.43	4.91	16.38	13.61
Sunflower stem	39.90	5.38	0.42	0.40	42.80	75.09	13.81	11.10	16.18	13.65
Sour cherry stem	44.78	5.75	0.50	0.40	43.22	77.48	17.16	5.36	18.27	15.62
Soybean residue	42.96	6.21	8.02	0.57	35.80	80.01	13.54	6.45	19.26	16.35
Black sesame residue	45.93	6.79	6.32	0.66	32.01	78.78	12.94	8.28	21.04	18.22
Cotton residue	45.24	6.46	6.37	0.65	33.41	74.97	17.16	7.87	19.90	17.02
Pea stem	38.97	5.45	1.79	0.42	40.31	74.67	12.27	13.06	16.31	13.57
Grape seed	50.47	6.20	2.42	0.47	35.83	74.26	21.12	4.62	21.70	18.73
Pine cone	48.28	5.73	0.10	0.40	43.89	80.92	17.48	1.60	20.07	16.96
Peach stone	51.98	6.13	0.02	0.48	40.41	86.42	12.61	0.97	20.31	17.85
Sour cherry stone	53.30	6.69	1.58	0.39	37.33	81.66	17.62	0.72	21.95	19.45

VM: volatile matter   FC: fixed carbon

3.2 Calorific Value Prediction

Table 2 presents the linear equations used to calculate HHV and LHV, r^2 values, and the results of performance criteria. Equation#1 considers five parameters, while the other equations consider less parameters. For instance, the number of the parameters in the Equations #2-6 is four.

Equation#1 that includes all of the parameters of elemental analysis gave the best prediction with respect to the coefficients of determination (r^2) as expected.

Table 2. Linear Equations and the prediction performances [11]

Eq. No	Linear Equations	r^2	SD	MAE	AAE (%)	ABE (%)	RMSD
1	$HHV = -4,914\,0 + 0,2611\,N + 0,4114\,C + 0,6114\,H + 0,3888\,S + 0,02097\,O$	0.9441	1.7379	0.3178	1.6978	0.0549	0.4230
	$LHV = -5,5232 + 0,2373\,N + 0,4334\,C + 0,2360H + 0,3732\,S + 0,000838\,O$	0.9582	1.7272	0.2915	1.8304	0.0654	0.3607
2	$HHV = -3,4643 + 0,2492\,N + 0,4045\,C + 0,6072\,H - 0,1618\,S$	0.9434	1.7373	0.3119	1.6659	0.0571	0.4256
	$LHV = -5,4653 + 0,2368N + 0,4331C + 0,2358H + 0,3511S$	0.9582	1.7271	0.2915	1.8304	0.0562	0.3607
3	$HHV = -4,6246 + 0,2732\,N + 0,4120\,C + 0,5992\,H + 0,01841\,O$	0.9440	1.7379	0.3186	1.7020	0.0562	0.4232
	$LHV = -5.2454 + 0.2489N + 0.4340C + 0.2243H - 0.00162O$	0.9581	1.7270	0.2925	1.8367	0.0519	0.3610
4	$HHV = -3.17334 + 0.3474\,N + 0.4593\,C - 0.4021\,S + 0.01972\,O$	0.9378	1.7321	0.3387	1.8134	0.0645	0.4461
	$LHV = -4.8513 + 0.2706\,N + 0.4519\,C + 0.06784\,S + 0.000356\,O$	0.9572	1.7264	0.2906	1.8216	0.0663	0.3649
5	$HHV = 1.5348 - 0.3434\,N + 3.4740\,H + 2.9958\,S - 0.1028\,O$	0.6916	1.4875	0.8524	4.5917	0.2976	0.9933
	$LHV = 1.2705 - 0.3996\,N + 3.2517\,H + 3.1196\,S - 0.1296\,O$	0.6702	1.4444	0.8698	5.5039	0.4177	1.0132
6	$HHV = -5.6318 + 0.3630\,C + 1.0237\,H + 4.1453\,S + 0.00389\,O$	0.9313	1.7261	0.3470	1.8483	0.0691	0.4689
	$LHV = -6.1755 + 0.3894\,C + 0.6107\,H + 3.7869\,S - 0.01468\,O$	0.9473	1.7173	0.3174	1.9923	0.0673	0.4049

Equations (#2- #6) ignore only one parameter compared to Equation#1. Among these equations, the best performance in HHV prediction belongs to Equation#3 that neglects effect of the content of S. Namely, Equation#3 yielded acceptable predictions for HHVs (r^2=0.9440). Moreover, LHV prediction performance of Equation#2 (r^2=0.9582) is exactly the same with those of Equation#1 that reveals the fact that oxygen content can be safely removed from the equation. Besides, the lowest r^2 was found if C content is removed from Equation#5. On the contrary, Setyawati et al. [12] correlated HHV of tropical peat based on its elemental analysis that ignores the C content and uses H, N, S, O, and ash contents.

The standard deviations (SD) of linear empirical equations varied within (1.4875-1.7379) for HHV and (1.4444-1.7272) for LHV. Concerning the error functions, MAE values indicate that the estimations of HHV and LHV can be made with a minimum mean absolute errors of 0.3119 MJ/kg and 0.2906 MJ/kg, respectively. Besides,

AAE(%) values varied in the intervals of (1.6659-4.5917) for HHV and (1.8216-5.5039) for LHV. Although the upper limits of AAE(%) results may be thought as a bit high, these values are roughly consistent with the values reported in literature for this criterion. In their paper, Nhuchen and Abdul Salam [13] compiled the results of various studies about HHV prediction for lignocellulosic residues and wastes, chars, and coals that makes it possible to compare the error analysis and prediction performances for different types of fuels. They concluded that the maximum values of AAE(%) values are calculated in the case of the lignocellulosic residues as well as the other biomasses. On the other hand, coal samples showed generally better results. Chen et al. [6] also estimated the higher heating value of the torrefied (mildly pyrolyzed) biomass using its ultimate analysis, and revealed that the relative errors of raw biomasses reached 9.03%. Alternatively, Choi at al. [14] reported 8.57% of AAE value for prediction of HHV of the mixture of animal

wastes for the equation where C, N, S, and O are incorporated. Similarly, Bousdira et al. [15] highlighted the importance of having low ash yield on prediction performance of calorific value prediction based on elementary composition. Unfortunately, the biomass species we used in this paper are very rich in inorganics, and accordingly they produce high yields of ash. Therefore, this is a significant concern originating from any unforeseen effects of the complicated nature of the inorganics. Also, the ABE(%) values altered within (0.0549-0.2976) for HHV and (0.0519-0.4177) for LHV, which can comparable with the results reported in literature [16]. The most promising values of RMSD (0.4230 and 0.3607 for HHV and LHV, respectively) were calculated if all parameters were involved (Equation#1).

Furthermore, in order to investigate the effects of non-linear terms in the form of squares of the parameters, new equations (#7-#11) were established. That is, Equation#7 excludes oxygen contents and the squares of the other ingredients (N^2, C^2, H^2, S^2) were added to their linear parameters. Likewise, Equations#8, 9, 10, and 11 exclude sulphur, hydrogen, carbon, and nitrogen contents, respectively. In this way, the new equations include squares of the related four, three, and two parameters. Table 3 presents these equations and the calculated r^2, SD, MAE, AAE, ABE, and RMSD results. These results revealed that the combination of non-linear terms did not improve so significantly the r^2 values calculated for the linear equations. The best r^2 values determined in the case of Equation#1 increased from 0.9441 to 0.9566 for HHV and from 0.9582 to 0.9668 for LHV when the sulphur content was ignored and the squares of the other four parameters were considered (Equation#8). Besides, a bit improvement took place in the prediction performance indicators. All in all, it can be concluded that the addition of the non-linear terms can not be recommended as a reliable approach to increase the prediction performance of the linear equations investigated in this paper.

4. Conclusions

This study revealed that the calorific values of the highly different biomass species can be safely predicted from their elemental analysis results. The thirty-nine different biomass species used in this study represent highly dissimilar structures in terms of the elemental analysis. Comparison of the experimental calorific values with the predicted calorific values, and the error analyses via MAE, AAE, ABE, and RMSD calculations showed that quite simple linear equations can be safely used to get the calorific value. Among the equations used, the equation that contains all of the parameters of elemental analysis provided the greatest prediction performance. Elimination of any parameter from this equation resulted in decrease in the prediction performance. However, addition of non-

linear (squared) terms of the elemental analysis results did not provide improvement in performance of the linear equations. Thus, the use of linear equations of ultimate analysis results are recommended.

References

1. Klass D.L., *Biomass for renewable energy, fuels, and chemicals*. 1998, San Diego: Academic Press.

2. Channiwala S.A., and P.P. Parikh, *A unified correlation for estimating HHV of solid, liquid and gaseous fuels*. Fuel, 2002. **181**: p. 1051-1063.

3. Gillespie G.D., C.D. Everard, C.C. Fagan, and K.P. McDonnell, *Prediction of quality parameters of biomass pellets from proximate and ultimate analysis*. Fuel, 2013. **111**: p. 771-777.

4. Yin C.Y., *Prediction of higher heating values of biomass from proximate and ultimate analyses*. Fuel, 2011. **90**: p. 1128-1132.

5. Friedl A., E. Padouvas, H. Rotter, and K. Varmuza, *Prediction of heating values of biomass from elemental composition*. Analytica Chimica Acta, 2005. **544**: p.191-198.

6. Chen W.H., W.Y. Cheng, K.M. Lu, and Y.P. Huang, *An evaluation on improvement of pulverized biomass property for solid fuel through torrefaction.*. Applied Energy, 2011. **88**: p. 3636-3644.

7. Titiloye J.O., M.S. Abu Bakar, and T.E. Odetoye, *Thermochemical characterization of agricultural wastes from West Africa*. Industrial Crops and Products, 2013. **47**: p. 199-203.

8. Maddi B., S. Viamajala, and S. Varanasi, *Comparative study of pyrolysis of algal biomass from natural lake blooms with lignocellulosic biomass*. Bioresource Technology, 2011. **102**: p. 11018-11026.

9. Chiou B.S., D. Vaenzuela-Medina, C. Bilbao-Sainz, A.K. Klamczynski, R.J. Avena-Bustillos, R.R Milczarek, W.X. Du, G.M. Glenn, and W.J. Orts, *Torrefaction of pomaces and nut shells*. Bioresource Technology, 2015.**177**: p. 58-65.

10. Motghare K.A., A.P. Rathod, K.L. Wasewar, and N.K. Labhsetwar, *Comparative study of different waste biomass for energy application*. Waste Management, 2016. **47**: p. 40-45.

11. Ozyuguran A., A. Akturk, and S. Yaman, *Optimal use of condensed parameters of ultimate analysis to predict the calorific value of biomass*. Fuel, 2018. **214**: p.640-646.

12. Setyawati W., E. Damanhuri, P. Lestari, and K. Dewi, *Correlation equation to predict HHV of tropical peat based on its ultimate analysis*. Procedia Engİneerİng, 2015. **125**: p. 298-303.

13. Nhuchhen D.R., and P. Abdul Salam, *Estimation of higher heating value of biomass from proximate analysis: A new approach*. Fuel, 2012. **99**: p. 55-63.

14. Choi H., S.I.A. Sudiarto, and A. Renggaman, *Prediction of livestock manure and mixture higher heating value based on fundamental analysis*. Fuel, 2014. **116**: p. 772-780.

15. Bousdira K., L. Nouri, and J. Legrand, *Chemical characterization of phoenicicole biomass fuel in Algerian oasis: Deglet nour and ghars cultivars case*. Energy Fuels, 2014. **28**: p. 7483-7493.

16. Garcia R., C. Pizarro, A.G. Lavin, and J.L. Bueno, *Spanish biofuels heating value estimation. Part I: Ultimate analysis data*. Fuel, 2014. **117**: p. 1130-1138.

Table 3. Non-linear Equations used and the prediction performances

Eq. No	Non-linear Equations	r^2	SD	MAE	AAE (%)	ABE (%)	RMSD
7	$HHV = -15.8566 + 0.4951\,N + 1.7601\,C + 5.4604\,H + 1.4769\,S - 0.02812\,N^2 - 0.01447\,C^2 + 0.4671\,H^2 - 2.6691\,S^2$	0.9556	1.7500	0.2885	1.5870	0.0942	0.3771
	$HHV = -16.1264 + 0.5064\,N + 1.7144\,C - 4.8484\,H - 0.8586\,S - 0.03065\,N^2 - 0.01398\,C^2 + 0.4153\,H^2$	0.9555	1.7475	0.2862	1.5735	0.0085	0.3774
	$HHV = -23.9224 + 0.5028\,N + 1.3785\,C + 0.2528\,H - 0.5169\,S - 0.03158\,N^2 - 0.01045\,C^2$	0.9546	1.7698	0.3832	2.0927	1.5776	0.4781
7	$LHV = 2.4879 + 0.4271\,N + 1.6322\,C - 11.4438\,H + 1.0062\,S - 0.0200\,N^2 - 0.01267\,C^2 + 0.9370\,H^2 - 1.9815\,S^2$	0.9662	1.7326	0.2617	1.6875	-0.0304	0.3245
	$LHV = 2.2876 + 0.4355\,N + 1.5983\,C - 10.9894\,H - 0.7277\,S - 0.02188\,N^2 - 0.0123\,C^2 + 0.8985\,H^2$	0.9662	1.7327	0.2514	1.6848	-0.0256	0.3248
	$LHV = 5.4060 + 0.2624\,N + 1.5159\,C - 11.4293\,H - 0.3867\,S - 0.01148\,C^2 + 0.9420\,H^2$	0.9639	1.7338	0.2696	1.7157	0.1103	0.3354
8	$HHV = -9.5129 + 0.4900\,N + 1.5545\,C - 3.9058\,H - 0.3211\,O - 0.03242\,N^2 - 0.01219\,C^2 + 0.3372\,H^2 + 0.00409\,O^2$	0.9566	1.7502	0.2839	1.5573	0.0449	0.3729
	$HHV = -14.7175 + 0.4883\,N + 1.2926\,C + 0.2188\,H - 0.3729\,O - 0.03307\,N^2 - 0.00945\,C^2 + 0.00467\,O^2$	0.9560	1.7481	0.2831	1.5468	0.0287	0.3753
	$HHV = -23.8290 + 0.5064\,N + 1.3355\,C + 0.2735\,H + 0.01165\,O - 0.03248\,N^2 - 0.00995\,C^2$	0.9547	1.7465	0.2895	1.5852	0.0018	0.3808
8	$LHV = 7.3723 + 0.4130\,N + 1.4676\,C - 10.0585\,H - 0.2655\,O - 0.02286\,N^2 - 0.01086\,C^2 + 0.8217\,H^2 + 0.00335\,O^2$	0.9668	1.7339	0.2605	1.6717	0.0229	0.3217
	$LHV = 2.0693 + 0.4259\,N + 1.5481\,C - 10.8196\,H + 0.0109\,O - 0.02233\,N^2 - 0.01173\,C^2 + 0.8870\,H^2$	0.9661	1.7358	0.2651	1.7083	0.1068	0.3251
	$LHV = 4.8380 + 0.2490\,N + 1.4924\,C - 11.1362\,H + 0.00164\,O - 0.01125\,C^2 + 0.9193\,H^2$	0.9638	1.7315	0.2680	1.7030	0.0025	0.3356
9	$HHV = -11.9276 + 0.5322\,N + 1.4068\,C + 3.4329\,S - 0.6077\,O - 0.03177\,N^2 - 0.01054\,C^2 - 5.2651\,S^2 + 0.00742\,O^2$	0.9561	1.7479	0.2862	1.5662	0.0035	0.3747
	$HHV = -13.4885 + 0.5504\,N + 1.3978\,C - 1.0829\,S - 0.4764\,O - 0.03589\,N^2 - 0.01044\,C^2 + 0.00584\,O^2$	0.9558	1.7485	0.2887	1.5803	0.0493	0.3762
	$HHV = -25.6364 + 0.5722\,N + 1.4851\,C - 0.6605\,S + 0.00709\,O - 0.03587\,N^2 - 0.01137\,C^2$	0.9538	1.7481	0.2921	1.6049	0.0792	0.3847

Table 3. Continue…

Eq. No	Non-linear Equations	r^2	SD	MAE	AAE (%)	ABE (%)	RMSD
9	$LHV = -4.1399 + 0.4129\,N + 0.8277\,C + 1.0241\,S - 0.4525\,O - 0.02311\,N^2 - 0.00416\,C^2 - 1.6864\,S^2 + 0.00545\,O^2$	0.9634	1.7322	0.2696	1.7130	0.0476	0.3376
	$LHV = -4.6399 + 0.4188\,N + 0.8248\,C - 0.4223\,S - 0.4104\,O - 0.02443\,N^2 - 0.00413\,C^2 + 0.00494\,O^2$	0.9634	1.7317	0.2684	1.7070	0.0464	0.3378
	$LHV = 4.7003 + 0.4250\,N + 0.4557\,C - 0.4251\,S - 0.4776\,O - 0.02321\,N^2 + 0.00587\,O^2$	0.9619	1.7303	0.2755	1.7390	0.0457	0.3444
10	$HHV = -63.3676 - 0.4996\,N + 27.2370\,H + 7.9872\,S - 0.3397\,O + 0.02661\,N^2 - 2.0138\,H^2 - 5.7886\,S^2 + 0.00232\,O^2$	0.7516	1.5506	0.7267	3.8914	0.2360	0.8914
	$HHV = -67.4014 - 0.4871\,N + 27.3544\,H + 6.2519\,S - 0.1473\,O + 0.02497\,N^2 - 2.0225\,H^2 - 3.5968\,S^2$	0.7514	1.5505	0.7304	3.9115	0.2178	0.8918
	$HHV = -67.7552 - 0.4730\,N + 27.7527\,H + 3.0500\,S - 0.1489\,O + 0.02160\,N^2 - 2.0581\,H^2$	0.7512	1.5500	0.7283	3.9011	0.2249	0.8922
10	$LHV = -52.6526 - 0.6553\,N + 22.2289\,H + 7.1848\,S - 0.2097\,O + 0.03954\,N^2 - 1.6085\,H^2 - 4.5180\,S^2 + 0.00048\,O^2$	0.7185	1.4955	0.7520	4.7456	0.3248	0.9362
	$LHV = -53.4812 - 0.6527\,N + 22.2530\,H + 6.8283\,S - 0.1701\,O + 0.0392\,N^2 - 1.6103\,H^2 - 4.0677\,S^2$	0.7185	1.4953	0.7527	4.7502	0.3273	0.9362
	$LHV = -53.8812 - 0.6368\,N + 22.7035\,H + 3.2072\,S - 0.1720\,O + 0.03539\,N^2 - 1.6505\,H^2$	0.7182	1.4953	0.7511	4.7418	0.3313	0.9367
11	$HHV = -5.6668 + 1.3547\,C - 1.4834\,H + 8.3792\,S - 0.6870\,O - 0.01075\,C^2 + 0.1770\,H^2 - 6.3435\,S^2 + 0.00806\,O^2$	0.9413	1.7351	0.3207	1.7197	0.0613	0.4334
	$HHV = -8.6907 + 1.2124\,C + 0.6759\,H + 7.8601\,S - 0.6898\,O - 0.00925\,C^2 - 5.7498\,S^2 + 0.00808\,O^2$	0.9411	1.7341	0.3236	1.7317	-0.0016	0.4341
	$HHV = -10.1398 + 1.1979\,C + 0.6475\,H + 2.7380\,S - 0.5422\,O - 0.00907\,C^2 + 0.00629\,O^2$	0.9406	1.7349	0.3181	1.7024	0.0566	0.4360
11	$LHV = 8.7097 + 1.2497\,C - 7.0316\,H + 5.1349\,S - 0.5485\,O - 0.00916\,C^2 + 0.6075\,H^2 - 2.7369\,S^2 + 0.00635\,O^2$	0.9531	1.7233	0.3004	1.8920	0.0691	0.3823
	$LHV = 7.5243 + 1.2185\,C - 6.6722\,H + 2.6985\,S - 0.4813\,O - 0.00882\,C^2 + 0.5770\,H^2 + 0.00553\,O^2$	0.9529	1.7232	0.2982	1.8783	0.0971	0.3828
	$LHV = -1.8445 + 0.7597\,C + 0.3757\,H + 2.7304\,S - 0.5398\,O - 0.00398\,C^2 + 0.00619\,O^2$	0.9512	1.7224	0.3034	1.9039	0.1061	0.3899

Research Article

Mersin province water projections and water information and management system: Erdemli district model

Halil Kumbur [a], Volkan Yamaçlı [b], Abdulkadir Küçükbahar [a],*

[a]Faculty of Engineering, Department of Environmental Engineering, Mersin University, 33343 Yenisehir / Mersin, Turkey
[b]Faculty of Engineering, Department of Electrical and Electronics Engineering, Mersin University, 33343 Yenisehir / Mersin, Turkey

ARTICLE INFO	ABSTRACT
	Mersin is one of the most important cities of the Middle East and Mediterranean Region as well as Turkey thanks to its intensive sectorial and commercial activities along with developing population. These progresses necessitate many urban needs such as drinking water, irrigation water, wastewater treatment, infrastructure planning for sewage-drinking water networks. In this study; medium and long term investments by 2050 (2015 + 35 years) for Erdemli, which is the third largest district of Mersin, are suggested and Water Information and Management System (WIMS) is formed in order to monitor all the activities and needs aforementioned above from a single center. WIMS can be considered as functional software thanks to being suitable for development, being modular software which can minimize the operating and investment costs, provide information in a short period of time and prepare electronic output of information transferred to the computer through the online database system. So far, 26606 data entries have been made in order to bring the functionality to the software. The WIMS software provided Mersin Water and Sewerage Administration with the ability to manage all data from a single center and monitor the current status of urban centers and rural settlements related to drinking water and wastewater.

1. Introduction

Water is one of the most important element for life. It is basically limited resource, contrary to what is believed. Though two-thirds of our world is covered with water, the amount of water that can be used by both living things and human population is extremely limited. Especially, in country and regional development projects; the role of water and land resources in the promotion and development initiative is inevitable.

There are serious discrepancies between places where water is found on the earth and areas where water is in demand. There are similar situations in our country and Mersin [1].

In non-water-rich countries such as Turkey, the best way to improve the water supply is managing and maintaining in optimal way. Along with the increasing population, public and private sector institutions need to use developing technology in order to use water more efficiently which has become the most important resource in the world [1, 2].

In the efficient evaluation of water resources; the economic situation of the countries, rapid population growth and urbanization, sectorial developments, water demands and projections related to all of them are done well and laws, regulations and regulations are applied correctly. However, the disadvantages encountered are more prevalent in metropolitan cities where rapid urbanization and sectorial activities are intensive. These problems are experienced more intensely in fast developing cities like Mersin. Drinking water and wastewater needs varies depending on urban centers and rural areas [1, 2].

With the Law No. 6360 entering into force at the end of March 30, 2014 Local Elections, the General Directorates of Metropolitan Municipalities, Water and Sewerage Administrations, expanded to the provincial boundaries of service area, will include new service areas; the drinking water and the wastewater in provinces, districts and rural areas should identify the current service conditions and

deficiencies of their infrastructures [2]. In the direction of feasibility studies to be made for short, medium and long term investment needs should be determined for future years and plans should be established for realizing those plans. In this context, software's such as "Water Information Management System" which will enable related institutions to do their work more quickly and systematically are preferred.

By the law aforementioned above, the borders of the Metropolitan Municipality were extended to the provincial borders. Intensive sectorial activities, as well as Mersin in Turkey with growing population and commercial activity in the Middle East and the Mediterranean region is one of the most important centers. All these intensive activities; drinking water, irrigation water, wastewater treatment, infrastructure planning (sewage-drinking water networks) and so on as well as many urban needs.

In this study, short, medium and long term investments were determined for Erdemli which is the third largest city of Mersin and 2050 target year, and Water Information Management System (WIMS), in which all these activities can be monitored online from a single center, has been prepared. For this purpose, analysis of the existing infrastructure situation of the district center, coastal area and rural areas related to drinking water and wastewater, determination of problems, determination of possible problems, examination of investments directed to the region, calculation of population projections of continuous- as well as many other field researches.

2. Material and Method

The study has started in 2015 and is projected for 35 years through year 2050. In this context; current situation analysis of water resources of Erdemli, Mersin is done. Data on drinking water and wastewater infrastructure have been collected and evaluated. Population, drinking water and wastewater formation projections are calculated. According to these results; basin-based economic and sustainable projects have been established and alternative proposals for solving problems have been introduced by 2050 target years [2]. The geographical coordinates of drinking water reservoirs located in the district, WTPs, promotion centers and other important places were determined by GPS device and so the satellite map drawings are carried out. All these studies were prepared with the software program which was designed to cover the data, and WIMS which can be continuously monitored and updated is created on this basis.

The data used in the study is obtained by collaboration of Faculty of Engineering Department of Environmental Engineering, Mersin University, Mersin Metropolitan Municipality General Directorate of Water (MESKİ) and Sewerage Administration, State Hydraulic Works (DSİ) 6th Regional Directorate, State Water Works Mersin 67. Branch Directorate, Turkey Statistical Institute Regional Directorate

of Adana, Mersin Provincial Directorate of Environment and Urban Planning, Erdemli Municipality and neighborhood headmen.

2.1 Erdemli

Erdemli has 1 municipality and 71 districts, the district map is given in Figure 1. From these neighborhoods, 23 are in the district center and the coastal zone between Çeşmeli-Kızkalesi and 48 are rural areas [5, 6]. Sectorial activities in the district; agriculture, tourism, service sectors and agriculture and animal husbandry activities are mostly performed in rural areas [8].

Figure 1. Map of Erdemli [7]

The main water sources of the province are Alata Stream, Lemas Stream, Kargıcak Stream, Kocahasanlı Stream Stream, Gökgübet Stream, Arpaçbahşiş Stream, Tömük Stream, Gilindires Stream, Karakız Stream, Karacaoğlan Stream, Sarıyer Stream, Dedekavak Stream, Madenler Stream, Kodoman Stream and Evliya Stream [2]. Water content of these rivers and streams is variable. Especially in summer months, most of the streams are not watered. The construction of Aksifat and Sorgun Dam is continuing to meet the water needs of the district [9].

2.2 Calculation of population projections

Estimated population values of 71 localities in Erdemli for the years 2015-2020-2030-2040-2050; population projections are calculated by five different methods (Iller Bank, Arithmetic Population Increase, Geometric Increase, Exponential Method and Compound Interest Methods) and is given in Table 1 [2, 14]. Turkey Statistical Institute of Population (TUİK) projection calculation population data are used [10, 11, 13].

Table 1. Erdemli District population projections [2 - 4].

Year	Iller Bank (person)	Arithmetic Increase (person)	Geometric Increase (person)	Exponential Method (person)	Compound interest (person)
2015	135181	132939	135705	135705	135677
2020	147154	132947	150428	150428	150239
2030	175467	132961	184839	184839	184221
2040	211039	132976	227121	227121	225888
2050	256080	132991	279076	279076	276981

2.3 Drinking Water and Wastewater Formation Calculations

According to the population projections calculated for Erdemli, the projections of drinking water demand and wastewater formation are calculated and given in Table 2-3. The settlement areas where drinking water and wastewater problems are most experienced are shown in Figure 4.

Table 2. Continuous population projections, drinking water demand and wastewater amount of Erdemli [2, 3].

Year	Continuous Population (person)	Water Demand (m³/d)	Amount of Wastewater (m³/d)
2015	135181	27071	21657
2020	147154	29619	23695
2030	175467	35453	28363
2040	211039	42514	34012
2050	256080	51229	40983

Table 3. Estimated drinking water demand and wastewater formation due to summer population projections in Erdemli [2, 3].

Year	Summer Population (person)	Water Demand (m³/d)	Amount of Wastewater Formation (m³/d)
2015	300159	60032	48025
2020	325735	65147	52118
2030	387355	77471	61977
2040	470322	94064	75252
2050	593300	118660	94928

The calculations of drinking water projections are based on the assumption that water consumption is 200 L / person-day and 80% of the water used is converted to wastewater (160 L / person-day) [14].

2.4 Creating satellite map drawings for the data

In Erdemli, transportation to the location of drinking water reservoirs, especially in winter, is very difficult. For this reason, locations of potable water reservoirs, promotion centers, WTP's and discharge points are processed on the internet based interactive satellite map in order to easily access information such as deposits, coordination, distance to the settlement units and network [2, 4].

In this direction; 129 drinking water reservoirs, 4 wastewater treatment plants and 5 promotion center coordinates in Erdemli are determined by Magellan

eXplorist 610 handheld GPS device. Coordinates; NetCad 5.2 and Corel Draw X6 are processed on the satellite map using computer programs. Schematic drawings of facilities, warehouses and promotion centers were made using the AutoCAD 2016 program. Facility and warehouse locations are processed on Google Earth program with html web coding on online satellite map and satellite map is used interactively.

Figure 3 shows the schematic drawing of Erdemli Aksıfat water source and drinking water tanks connected to this source as Figure 4 shows the locations of drinking water warehouses processed on the satellite map. Also the area where Erdemli Municipality WTP is marked on the satellite map indicated in Figure 5 [2, 3, 4, 15-19].
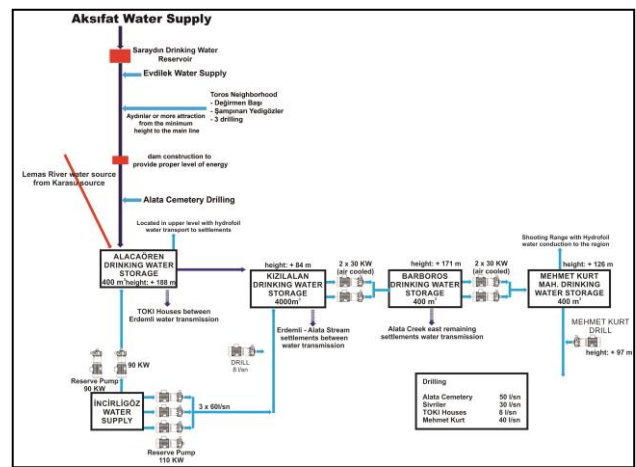

Figure 3. Schematic drawing showing Aksıfat water supply and drinking water reservoirs [2]

2.5 Design of Water Information Management System Software (WIMS)

Water Information Management System software is created by making approximately 26606 data entries for Erdemli, including continuous and seasonal population projections, water demand and wastewater formation projections, warehouse-center for interactive satellite mapping-WTP drawings and visuals, pump maintenance-repair, identification and schematic information [2, 4].

The WIMS software program is designed within the scope of the study; The C language is encoded in the C# interface. With the MySQL database connection, all collected data is easily accessible. The aim of the designed software program is to make the user interface simple, easy and understandable [4].

When the software program and the system are designed and coded, the data security is kept on the front panel and the user information is processed in encrypted form in the database. It is also aimed to ensure that each user's login time and IP address are registered and that the system operates at maximum security level [4].

Figure 4. Demonstration of locations of drinking water tanks on satellite map [2, 4]

The WIMS software aims to manage all data from a single center, to monitor the current status of urban centers and rural settlements related to drinking water and wastewater, and to provide detailed management and control capability from a single center [4]. In addition, designed software can be developed in modular manner and so can reduce the software, business and investment costs to minimum, uploaded information in a short period of time to provide transportation and computerized information is the main advantages of obtaining electronic output [4]. The user interface general view of the WIMS software program designed in this context is given in Figure 6.

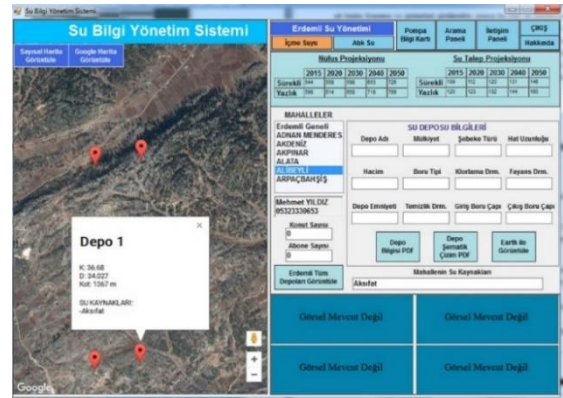Figure 5. Display of Erdemli Municipality WTP on satellite map [3].

Figure 6. Water Information Management System user interface image [4].

3. Results and Discussion

When population projections for the 2015 TUİK population are compared to the population projections for the 2050 target year, it is expected to increase by about 90% for the permanent population and about 80% for the summer population [2].

It is predicted that Erdemli drinking water projections calculated for 2015 and 2050 will increase by about 80% of the demand and wastewater formation. The water resources in the district seem to be sufficient when compared to the projections calculated according to the year 2050. In the treatment of wastewater, the existing facilities need to be upgraded, revised and adapted to new treatment technologies [2, 3, 17].

Potential hazards for water resources; wastewater and sewage network projects of Kayacı, Sorgun, Koramşalı, Fakılı, Çamlı, Karahıdırlı, Karayakup, Sinap, Çiftepınar and Pınarbaşı neighborhoods should be done. This will not contaminate the source of drinking water and reduce chlorination costs [2].

In the summer months when the water demand is very high, there are water problems in Aydınlar - Sarıkaya, Arslanlı, Hacıalanı and Esenpınar districts, which are considered to be particularly springy. This is because the water is unplanned and used in the water. Development plans of residential areas can be solved by making drinking and wastewater projects and recording and using water [19].

Since water consumption in the rural areas decreases in winter, Aksıfat Drinking Water Supply can be integrated with Erdemli Drinking Water Network between October and June (about 9 months) for better quality and economical water usage. The corresponding connection is given by
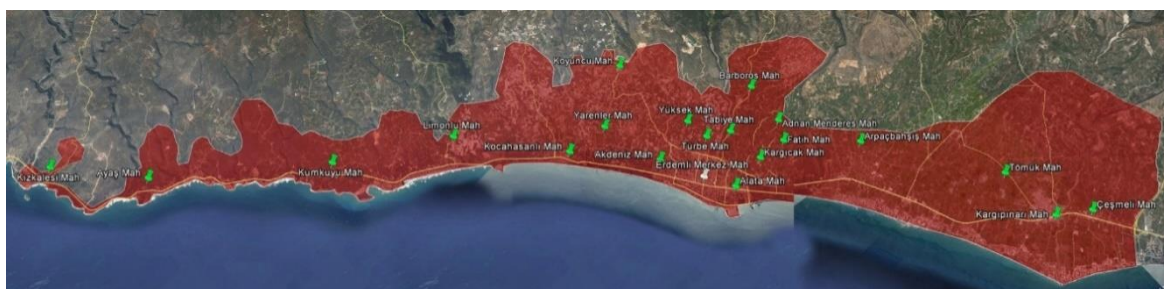

Figure 2. Settlements where drinking water and wastewater problems are most experienced in Erdemli District [2,4]

Figure 2 [2].

It is necessary to revise the insufficient drinking water reservoirs in the district. Automatic disinfection should be done by installing the storage chlorine automatic device. All these operations can easily be performed with the WIMS program designed for the study [2, 4].

Efforts should be made to reduce the rate of loss-fugitives. Subscriber registration system should be continuously updated. The number of subscribers should be compared with water consumption and water collection, and the cause of water leaks should be investigated by determining the difference between the two. There are water shortages during the summer months when there is a lot of water demand, especially in areas where water is unplanned and is considered as a springboard due to illegal use in the water. For this reason, it is extremely important to record and control the use of water [12-19].

4. Conclusions

Waste water generated in the rural areas where there is not enough infrastructure system may cause danger to water resources in the district. For this reason, wastewater problems (zoning plans, sewerage network, package treatment facilities, etc.) of these areas must be resolved permanently and economically [2, 3]

In Erdemli, the distance between the rural and the district centers is far away each other, the topography is rough and the transportation is quite difficult during the winter months. In the case of possible problems with these remote areas, technical service centers to be able to serve 24/7, and mobile support teams who can work continuously on their control, should be placed in central locations in the countryside. Any faults that may occur on this site will be eliminated in a short period of time to prevent water loss and infrastructure problems [2, 3].

Universities, non-governmental organizations, written and visual press should give information about saving of water, importance of water and irrigation techniques to the people of urban centers and rural areas [2, 3].

Acknowledgment

Nomenclature

WIMS	: Water Information Management System
WTP	: Wastewater treatment plant
GPS	: Global Positioning System
MySQL	: Structured Query Language

References

1. Kumbur H., Koyuncu G., Gülşen H.E. MESKİ Mersin İli Erdemli İlçesi İçmesuyu Atıksu Yağmursuyu Master Planı 2013, Mersin.

2. Mersin İli Erdemli İlçesi İçme Suyu Altyapısı Mevcut Durumu ve Geleceğe Yönelik Yatırım İhtiyaçlarının Belirlenmesi Projesi.

3. Mersin İli Erdemli ve Silifke İlçeleri Atıksu Altyapısı Mevcut Durumu ve Geleceğe Yönelik Yatırım İhtiyaçlarının Belirlenmesi Projesi.

4. Mersin İli Erdemli ve Silifke İlçeleri MESKİ Su Bilgi Yönetim Sistemi

5. Available from: http://www.erdemli.bel.tr/tarihcee, [cited 15.08.2017].

6. Available from: http://www.erdemli.bel.tr/ekonomi, [cited 15.08.2017].

7. Available from: http://www.erdemli.gov.tr/ilce-haritasi, [cited 15.08.2017].

8. Available from: http://www.mersin.gov.tr/erdemli-ilcesi, [cited 15.08.2017].

9. Available from: http://bolge06.dsi.gov.tr/insa-halindeki-tesisler/baraj-ve-goletler , [cited 17.08.2017].

10. Türkiye İstatistik Kurumu (TUİK) Mersin İli Belde ve Köyleri Nüfus, Konut ve İş yeri Projeksiyonları, 2014.

11. Türkiye İstatistik Kurumu (TUİK) Seçilmiş Göstergelerle Mersin, 2013.

12. MESKİ Genel Müdürlüğü 2015 - 2019 Yılı Stratejik Planı Available from: http://www.meski.gov.tr/files_upload/belgemenu/1465565 277.pdf , [cited 20.08.2017].

13. Türkiye İstatistik Kurumu (TUİK) Adrese Dayalı Nüfus Kayıt Sistemi Sonuçları, 2014.

14. Şehir ve Kasaba İçmesuyu Projelerinin Hazırlanmasına Ait Yönetmelik (18733 / 22.04.1985) Available from: http://www.mevzuat.gov.tr/Metin.Aspx?MevzuatKod=7.5. 4754&MevzuatIliski=0&sourceXmlSearch=iller%20banka s%FD.

15. Mersin İli Erdemli-Silifke İlçeleri Aksıfat Grubu İçmesuyu Birliği Verileri, 2013.

16. Gulsen Akbay, H, Akarsu, C, Kumbur, H., Treatment of fruit juice concentrate wastewater by electrocoagulation: Optimization of COD removal, International Advanced Researches and Engineering Journal, 2018. 2(1): 53-57.

17. Akarsu, C., Kıdeyş, A. E., Kumbur, H., Microplastic threat to aquatic ecosystems of the municipal wastewater treatment plant, Turkish Bulletin of Hygiene and Experimental Biology, 2017. 73-78.

18. Dogan-saglamtimur, N., Kumbur, H., Metal (Hg, Pb, Cuand Zn) Bioaccümülation in Sediment,Fish and Human Sculp Hair: A case study from The City of Mersin Along The Southern Coast of Türkey, Biol.Trace Elem Res .DOI 10,1007/s 12011-009-8516-5. 2010. 136(1): 55-70.

19. Kumbur, H., Arslan, H., Ünal, E.D., Özer, Z., Koyuncu

Türkay, G., Investigation of organochlorine pesticide residues in the well-water of Göksu Delta (Göksu Deltası Kuyu Sularında Organoklorlu Pestisit Kalıntılarının Araştırılması), Kastomunu University Journal of Engineering and Sciences (Kastamonu Üniversitesi Mühendislik ve Fen Bilimleri Dergisi), 2016. 2(1): 1-13.

Research Article

A comparative study of raspberry dehydration by lyophilisation or conventional drying

Otília Gonçalves [a,b], Marco Alves [b], Joana Grácio [b] and Valentim Nunes [a,c,]*

[a]*Escola Superior de Tecnologia, Instituto Politécnico de Tomar, Campus da Quinta do Contador, 2300-313 Tomar, Portugal*
[b]*Inov'Linea, Tagusvalley - Tecnopolo do Vale do Tejo, Rua José Dias Simão, 2200-062 Abrantes, Portugal*
[c]*Centro de Química Estrutural, Faculdade de Ciências da Universidade de Lisboa, Campo Grande, 1749-016, Lisboa, Portugal*

ARTICLE INFO	ABSTRACT

Dehydration is a food preservation process that allows to increase the availability of products on the market, as well as the introduction of new products. The objective of this work was to perform a comparative study of processes of dehydration of raspberry by freeze-drying (lyophilisation) or conventional drying. Raspberry is a perishable fruit, with about 85% (w/w) water content, and there is a need for preservation processes that generate new products with long term availability. Raw materials were subjected, or not, to blanching pre-treatments. It was analysed the effect of these treatments on physical parameters, such as water activity, colour and moisture content as well in the drying kinetics. It was found that conventional drying allowed to reduce water content to 20.7 to 35.8% while lyophilisation permitted to achieve values from 11.6 to 14%. It was also observed that lyophilisation process correspond to higher colour difference indexes, ranging from 5.30 to 11.8 values.

1. Introduction

Dehydration is a food preservation process that allows to increase the availability of the products in the market, as well as the introduction of new products. In 2015 it was estimated that the production of raspberry in Portugal reached the 7500 tons, being 90% for exportation. The raspberry is the second most exported fruit in Portugal, with sales of about 64 M€. Besides conventional drying, lyophilisation is an alternative way to remove excess water from food [1-3]. It is a drying process based on water sublimation from the material caused by application of low pressure on frozen material. This technique results in high-quality dehydrated products [4-6]. Also freeze drying processing of this fruit permits the extraction of oils that can be used as by-products reducing losses and increasing the development of new products [7]. It was also been proofed that even after long-term storage and despite exposure to atmospheric oxygen, freeze dried berries retain the antioxidant properties of the raw material to a very high degree [8]. Physical and chemical pre-treatments are also of great importance, as they allow to improve the quality of

products or change their nutritional characteristics [9,10]. In this work a study of the physical parameters and the drying kinetics of untreated and pre-treated samples of raspberry, a different raw material from the previously studied in cited literature, was performed, using lyophilisation or conventional drying.

2. Materials and methods

2.1 Raw materials and pre-treatments

The selection of the raw material is of great importance as it will interfere with the dehydration process. Raspberries are classified as fruits with high respiratory rate, that is, the higher the respiratory rate of the fruit, the lower its lifespan and the lower their ability to be conserved. Therefore the importance in developing alternative ways of fruit conservation [11]. The fruit must have good quality and with a state of maturity that allows a good quality of the final product because those aspects will influence the step of freezing and the drying kinetics [12]. Raw materials were bought from local producers and washed with deionized water. Samples were dried either untreated or subjected to blanching processes with

---

sodium hydroxide (NaOH), calcium chloride (CaCl$_2$) and ascorbic acid (C$_6$H$_8$O$_6$). For blanching with NaOH it was used an aqueous solution with 10 to 20 g/L of boiling water that was finally neutralized with ascorbic acid. For the blanching process with CaCl$_2$ it was used a 0.5% concentration aqueous solution at 95 °C. Finally for the blanching process with ascorbic acid, to inactivate the enzymatic activity [13], it was used a solution of 10 g/L. At the end of each pre-treatment the samples were passed through a cryogenic solution and finally closed in a plastic bag.

2.2. Dehydration processes

Both blanched and untreated samples were subjected to dehydration processes either by freeze drying (lyophilisation) or conventional drying. The equipment for the lyophilisation process was a Labconco liophylizer, model Freezone 6 Plus. The drying chamber has bottles where the raw material is hermetically closed under vacuum. The operating conditions were $p = 0.14$ mbar and $T = -89$ °C. During freeze-drying weightings of samples were made in an analytical balance, with an accuracy of 0.0001 g, in order to assess the loss of mass. For the conventional drying it was utilized an industrial oven, from Zanussi, Italy, with programmed temperature at $T = 40$ °C. At this temperature the blanching can have significant effect on drying kinetics [14]. Once again, samples were periodically weighted to access the loss of mass.

2.3. Analytical methods

Water activity, aw, was measured at 25 ºC using a water activity meter (Aqualab Series meter 4TE), with an accuracy of $\pm$ 0.003, by detecting the dew point of the samples. At least three iterations were made for each sample.

Water content (%) was measured by weighing the samples, in an analytical balance with accuracy of 0.0001g, before and after the drying processes. At least three repetitions were made for each type of samples.

Colour measurement is very important to the consumer, at first impact with the product, and could lead him to accept or reject it [15]. The measurement of the colour was made with a Konica Minolta colorimeter. The parameters that were evaluated, accordingly with the l*, a*, b* system, are the lightness coefficient, l*, the red colour coefficient, a* and the yellow colour coefficient, b*. Then the relative colour difference index, ΔE, is calculated from the following equation

$$\Delta E = \left[\left(l^{*,0} - l^* \right)^2 + \left(a^{*,0} - a^* \right)^2 + \left(b^{*,0} - b^* \right)^2 \right]^{1/2} \quad (1)$$

where the superscripts *,0 refers to the colour coefficients of raw (undried) materials. For $\Delta E < 2.3$ samples are equal in terms of colour and if $\Delta E > 2.3$ then samples are different in colour [16].

2.4. Statistical analysis

The statistical analysis of the results of dryings was made with the statistical software Action (Software Action. http://www.portalaction.com.br/), integrated in the Microsoft Excel 2010. The Tukey test was used for multiple comparisons tests to study the magnitude of differences between two means of parameters at a significance level of 5% (or 0.05). If we have means followed by equal letters the difference between the two means do not differ significantly by the Tukey test, otherwise they will be statistically significant.

3. Results and Discussion

3.1. Influence of the pre-treatments in evaluated parameters

In table 1, there are summarized the results obtained for the evaluated parameters, and described in the previous section, for freeze-drying and conventional drying. Control samples correspond to the undried raw materials. Comparing the two control samples they are a little different due to the fact that we have used for both tests different batches of raspberry. An observation of the results for the water activity parameter shows that there is a clear reduction of aw from conventional drying to freeze-drying, being more pronounced for the samples with pre-treatment with CaCl$_2$. For the water content parameter there are also differences between the control samples and the remaining samples, with a decrease of water content from conventional drying to freeze drying. The lyophilised samples with blanching pre-treatment have shown the lower values. The analysis of the relative colour difference index shows that conventional drying presents less colour change than freeze-drying. The sample of conventional drying with ascorbic acid pre-treatment has a $\Delta E \leq 2.3$ so the difference is not significant. In freeze-drying the sample with the pre-treatment of ascorbic acid have shown the lower colour change as for the conventional drying.

3.2. Analysis of the drying kinetics

There are several methods for modelling the drying kinetics, including theoretical, empirical and semi-empirical models. The theoretical models consider the external conditions as the process unfolds and the internal mechanisms of transfer of energy and mass. Empirical models are based on experimental data and the dimensionless analysis. These models follow a relationship between the average moisture content and drying time [17]. They omit the basics of drying process and the parameters have no physical meaning. Semi-empirical models based on the Newton's law of cooling or Fick's second law for diffusion include the Henderson and Pabis model, Lewis model and the Page model [18-20].

Table 1. Obtained parameters for the lyophilization or conventional drying of raspberry. Samples with different letters in the same column are significantly different.

Drying Process	Sample	Water activity	Water content (%)	ΔE
Lyophilisation	Control	0.9882 [a]	87.6 [a]	-
	Without treatment	0.2376 [de]	14.0 [d]	8.10
	Blanching NaOH	0.2915 [d]	11.7 [d]	6.50
	Blanching CaCl$_2$	0.0958 [e]	11.6 [d]	11.8
	Blanching ascorbic acid	0.2750 [d]	11.8 [d]	5.30
Conventional Drying	Control	0.9949 [a]	85.5 [a]	-
	Without treatment	0.7027 [b]	35.8 [b]	5.12
	Blanching NaOH	0.4839 [c]	21.1 [cd]	3.82
	Blanching CaCl$_2$	0.5997 [bc]	20.7 [cd]	2.42
	Blanching ascorbic acid	0.6151 [bc]	27.4 [bc]	2.07

In this work, and due to its simplicity, the experimental drying curves were modelled with the Page model, given by the equation:

$$MR = \frac{x - x_e}{x_i - x_e} = \exp(-kt^n) \qquad (2)$$

where *MR* represents the moisture ratio (dimensionless), x is the moisture content at any time, x_i the initial moisture content, x_e the equilibrium moisture content, k is the drying rate constant and n it's a constant (dimensionless). Experimental data was adjusted to equation 2. Data is summarized in table 2.

Figures 1 and 2 show the modelled curves for the drying kinetics of raspberry samples by lyophilisation or conventional drying, respectively. Figure 3 summarises all the curves in order to compare the different behaviours. Analysing the kinetics of freeze-drying of raspberry (Figure 1), we can see that the pre-treatments influence the drying curves. In the case of drying pre-treatments with NaOH and ascorbic acid they follow the same drying kinetic. The drying with pre-treatment with CaCl$_2$ is more efficient. For the oven-drying kinetics (Figure 2), initially all samples with pre-treatment have the same behaviour and are more efficient than the drying without pre-treatment. Once again, raspberry drying is faster with pre-treatment with CaCl$_2$.

Table 2. Parameters of the Page model (equation 2) for the drying processes, and correspondent correlation coefficient, r^2.

Drying Process	k/h^{-1}	n	r^2
Lyophilisation, without treat.	0.08083	1.0380	0.9995
Lyophilisation, NaOH	0.10651	1.0002	0.9993
Lyophilisation, CaCl$_2$	0.09256	1.0880	0.9995
Lyophilisation, Ascorbic acid	0.09731	1.0276	0.9993
Conventional, without treat.	0.14769	0.68852	0.9664
Conventional, NaOH	0.35358	0.56435	0.9852
Conventional, CaCl$_2$	0.37479	0.54676	0.9790
Conventional, Ascorbic acid	0.26842	0.57730	0.9766

Comparing the drying kinetics for freeze-drying and conventional drying (Figure 3) for all the pre-treatments, it is noted that initially the sample curves for conventional drying with CaCl$_2$ and NaOH pre-treatments are the fastest. In general, conventional drying is faster at the beginning but over time freeze-drying reaches higher levels of dehydration.

4. Conclusions

Experimental dryings of raspberry samples by conventional drying in oven at T = 40 ºC and by lyophilisation at p = 0.14 mbar and T = - 89 ºC were performed. Several pre–treatments were applied, in order to evaluate the effect in the final product physicochemical characteristics. It can be concluded that the pre-treatments affect the final product characteristics in terms of the evaluated parameters. The pre-treatments with NaOH and CaCl$_2$ of freeze-drying are the most efficient in lowering the humidity of raspberry. The dryings that change less the colour of samples are the conventional ones without treatment and with pre-treatment with NaOH. With the results obtained along the dryings, data was mathematical adjusted to the experimental data with the Page model to describe the kinetics of drying. The
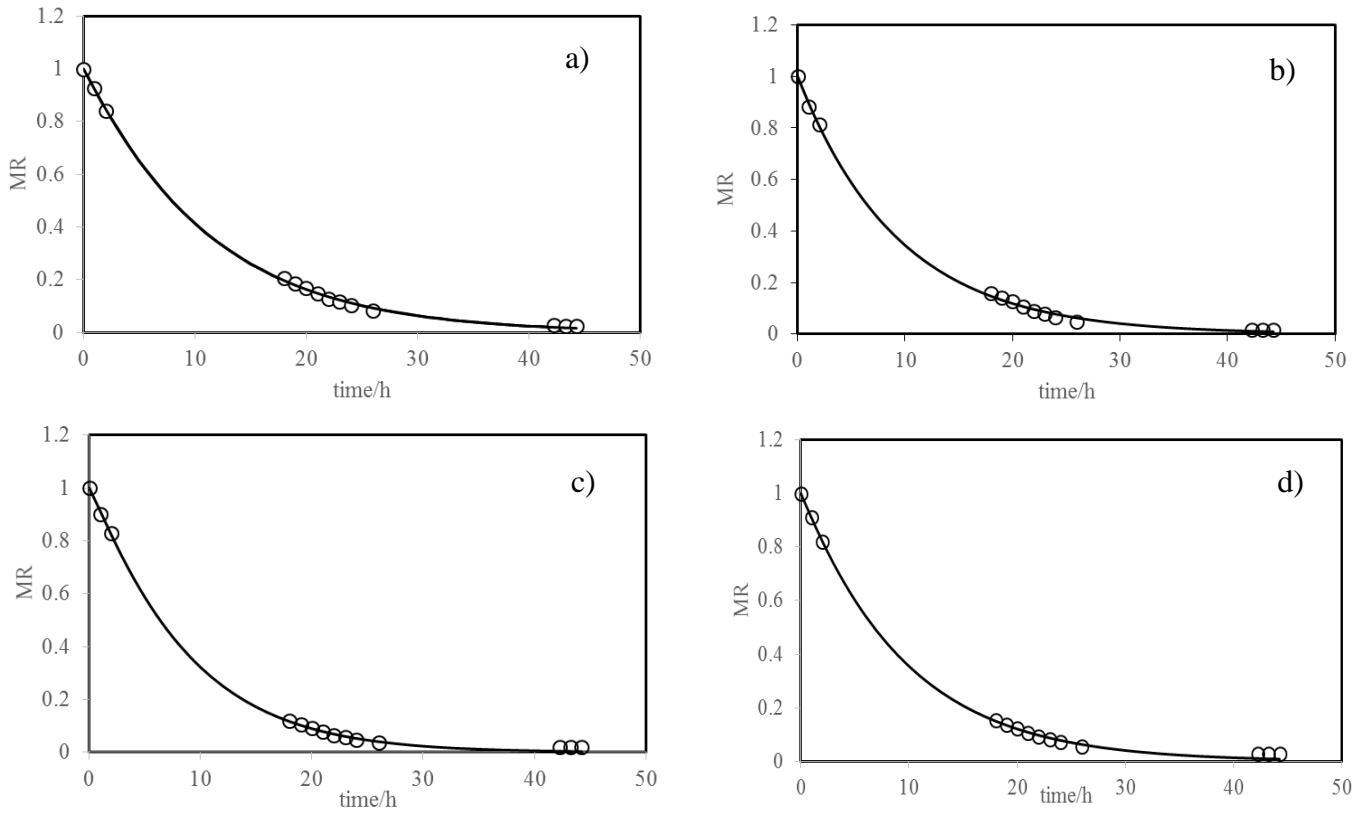
Figure 1. Drying kinetics for freeze drying: ○ exp.; ━ Page model. a) without treatment; b) blanching with NaOH; c) blanching with CaCl$_2$; d) blanching with ascorbic acid
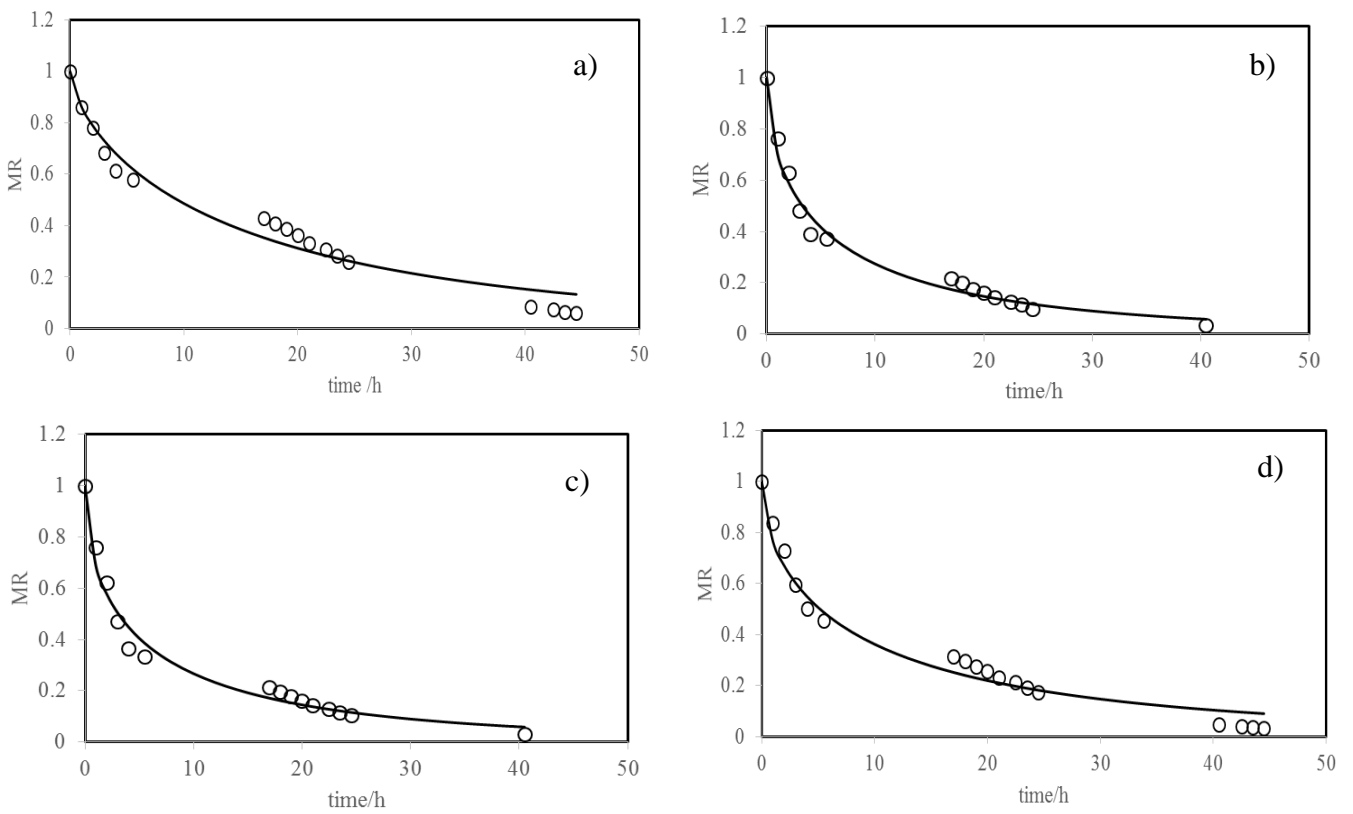

Figure 2. Drying kinetics for conventional drying: ○ exp; ━ Page model. a) without treatment; b) blanching with NaOH; c) blanching with CaCl$_2$; d) blanching with ascorbic acid
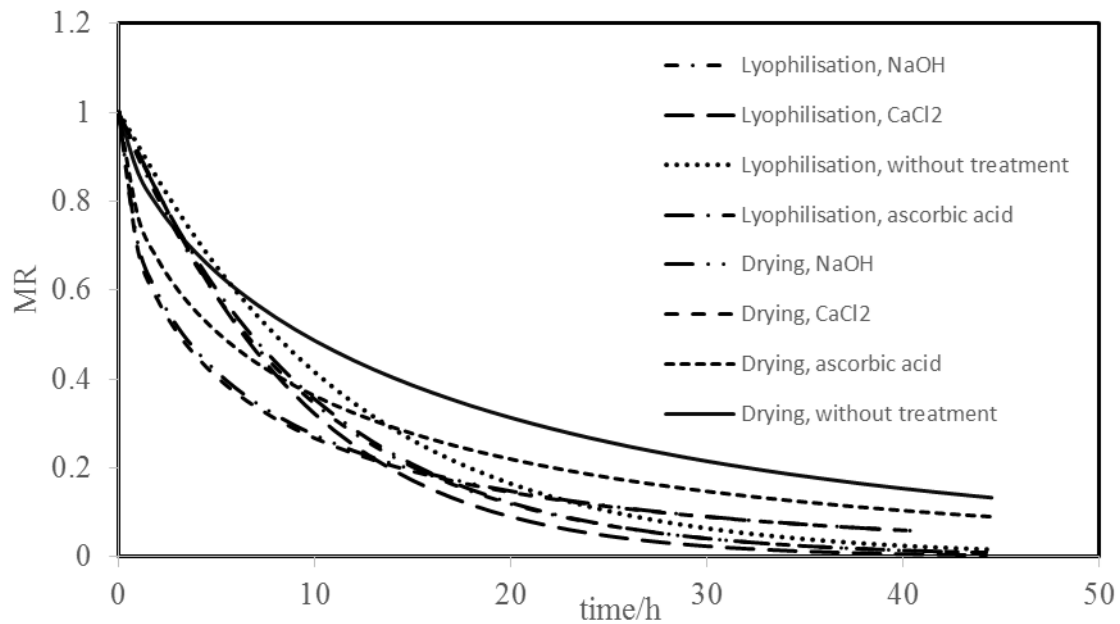
Figure 3. Comparison between the different curves for the drying kinetics

drying kinetics of raspberry for freeze-drying and conventional drying show that the samples with CaCl$_2$ pre-treatment improve the drying rate. Comparing the two technologies, freeze-drying and conventional drying, it was noted that conventional drying is faster initially although the freeze-drying allows achieving higher levels of dehydration. The water contents for conventional drying ranged from 20.7 to 35.8% while for lyophilization values from 11.6 and 14.0% were obtained. Drying kinetics are very different what is reflected in the kinetic parameters. The *k* parameters of the Page model change from 0.08083 to 0.10651 h^{-1} for lyophilisation and from 0.14769 to 0.37479 h^{-1} for conventional drying, while the *n* parameters are much higher for lyophilization ranging from 1.0002 to 1.0880 values. Since there are other factor that are also important, like the difference colour indexes, the choice of technology and pre-treatments applied to the raw material should be chosen accordingly with the final purpose for market application. This work showed that the dehydration processes are effective for long term storage of this fruit, what is very important for the producer's economy.

Nomenclature

a*	: red colour coefficient
aw	: water activity
b*	: yellow colour coefficient
k	: drying rate constant (Page model)
l*	: lightness coefficient
MR	: moisture ratio
n	: dimensionless constant of the page model
p	: pressure

t	: time
T	: temperature
ΔE	: relative colour difference index

References

1. Ratti, C. *Hot air and freeze-drying of high-values foods: A review*, Journal of Food Engineering, 2001, **49**: p. 311–319

2. Marques, L.G.; Freire, J.T. *Analysis of Freeze-Drying of Tropical Fruits,* Drying Technology, 2005, **23**: p. 2169–2184

3. Sánchez-Sáenz, C.M., Oliveira, R.A., Park, K.J., *HTST Pre-drying Influence on Vacuum Drying Kinetics and Carrot Slices Quality Parameter Evaluation*, J. Food. Process Preserv., 2015, **39**: p.1636-1646

4. Amrani, M., Brigui, J., *The impact of freeze-drying on strawberry quality*, Revista Ingenieria e Investigacion, 2007, **27**(2): p. 51-55

5. Veras, A.O.M., Béttega, R., Freire F.B., Barrozo, M.A.S., Freire, J.T., *Drying kinetics, structural characteristics and vitamin C retention of dedo-de-moça pepper (Capsicum baccatum) during convective and freeze drying*. Brazilian Journal of Chemical Engineering, 2012, **29**(4): p.741-750

6. Adhami, S., Rahimi, A., Hatamipour, M.S., *Freeze drying of quince (Cydonia oblonga): Modelling of drying kinetics and characteristics*, Korean Journal of Chemical Engineering, 2013, **30**(6): p. 1201-1206

7. Sucurovic, A., Vukelic, N., Ignjatovic, L., Brceski, I., Jovanovic, D., *Physical-chemical characteristics and oxidative stability of oil obtained from lyophilized raspberry seed ,* European Journal of Lipid Science Technolology, 2009, **111**: p. 1133–1141

8. Michalczyk, M., Macura, R., Matwzak, J., *The effect of air-drying freeze-drying and storage on the quality and antioxidant activity of some selected berries*, J. Food Process. Preserv., 2009, **33**: p. 11-21

9. Arévalo-Pinedo, A., Murr, F.E.X., *Influence of pre-treatments on the drying kinetics during vacuum drying of carrot and pumpkin*, Journal of Food Engineering, 2007, **80**: p. 152-156

10. Genevois, C., Flores, S., de Escalada Pla, M., *Effect of iron and ascorbic acid addition on dry infusion process and final color of pumpkin tissue*, LWT - Food Science and Technology, 2014, **58**: p. 563-570

11. Sette, P.A., Franceschinis, L.E., Schebor, C., Salvatori, D. *Osmotic Dehydrated Raspberries: Changes in Physical Aspects and Bioactive Compounds*, Drying Technology, 2015, **33**: p. 659–670

12. Vieira, A.P., Nicoleti, J.F., Telis, V.R.N., *Liofilização de fatias de abacaxi: avaliação da cinética de secagem e da qualidade do produto*, Brazilian Journal of Food Technology, 2012, **15**(1): p. 50-58

13. Toledo R.T., *Fundamentals of Food Process Engineering*, Chapman & Hall: New York, 1991

14. Borges, S.V., Mancini, M.C., Corrêa, J.L.G., Leite, J.B., *Drying kinetics of bananas by natural convection: Influence of temperature, shape, blanching and cultivar*, Ciência e Agrotecnologia, 2011, **35**: p. 368-376

15. Ciurzynska, A., Lenart, A., Greda, K.J., *Effect of pre-treatment conditions on content and activity of water and colour of freeze-dried pumpkin* , LWT - Food Science and Technology 2014, **59**: p. 1075-1081

16. Mahy, M., Eycken, L.V., Oosterlinck, A., *Evaluation of Uniform Color Spaces Developed after the Adoption of CIELAB and CIELUV*, Color Research & Application, 1994,**19**(2): p. 105-121

17. Park, K.J., Vohnikoza, Z., Brod, F.P.R.,*Evaluation of drying parameters and desorption isotherms of garden mint leaves (Mentha crispa L.)*, Journal of Food Engineering 2002, **51**(3): p. 193-199

18. Panchariya, P.C., Popovic, D., Sharma, A.L., *Thin-layer modeling of black tea drying process*, Journal of Food Engineering, 2002, **52**(4). p. 349-357

19. Rosa, D.P., Cantú-Lozano, D., Luna-Solano, G., Polachini, T.C., Telis-Romero, *J. Mathematical modelling of orange seed drying kinetics*, Ciência e Agrotecnologia 2015, **39**(3): p. 291-300

20. Castro, L. M. M. N., Pinheiro, M. N. C., *A Simple Data Processing Approach for Drying Kinetics Experiments*, Chemical Engineering Communications, 2016, **203**(2): p. 258-269

Research Article

Aspergillus niger may improve nutritional quality of grape seed and its usability in animal nutrition through solid-state fermentation

Aydın Altop, Emrah Güngör* and Güray Erener

Ondokuz Mayis University, Faculty of Agriculture, Department of Animal Science, Samsun, Turkey

ARTICLE INFO	ABSTRACT

Effects of different *Aspergillus niger* strains on main nutritional components of grape seed in solid-state fermentation were investigated in this study. Grape seeds were fermented with three different *A. niger* strains which are ATCC 9142, ATCC 200345 and ATCC 52172. Fermented and unfermented grape seeds were analyzed for crude protein, ether extract, ash, crude fiber, neutral detergent fiber (NDF), and acid detergent fiber (ADF). Unfermented grape seeds (control group) and fermented groups: FG1 (ATCC 9142), FG2 (ATCC 200345) and FG3 (ATCC 52172) were compared each other depending on the results of chemical analyses. Crude protein increased ($p < 0.001$) with fermentation in all groups and the highest increases were observed in FG2 and FG3 groups. Ether extract was similar with control in FG1 group but decreased ($p < 0.001$) in FG2 and FG3 groups. Ash content increased ($p < 0.001$) through fermentation in all groups, the highest increases were noted in FG2 and FG3 groups. Crude fiber, ADF, NDF and nitrogen-free extracts (NFE) were decreased with fermentation in all groups ($p < 0.001$). Whereas the highest decreases of NFE were observed in FG1 and FG2 groups, the highest reduction in crude fiber, ADF and NDF were ocurred in FG2 group. These results showed that nutritional quality of grape seeds can be improved by *A. niger* solid-state fermentation and the best results were taken from ATCC 52172.

1. Introduction

Grape is one of the most produced fruits in the world with 77 million tons of annual production [1]. Grape seed is a by-product emerges by processing of grapes in fruit juices and wine factories [2]. It is rich in polyphenols such as proanthocyanidins (catechin, epicatechin, epicatechin-3-O-gallate; [3]). These polyphenols have antimicrobial, antioxidant and anticarcinogenic properties [4].

Positive results have been obtained from animal experiments on grape seed. Grape seed has antioxidant effects on lamb meat [5] sheep milk [6], poultry meat [2, 7] and egg [8]. Besides, it enhanced growth performance in *Eimeria tenella* infected broilers [9], increased antibody titer against Newcastle Disease Virus [2] and inhibit the deterioration of jejunal epithelial cells in the bulls exposed to heat stress [10].

Grape seed can increase milk production [11, 12], milk calcium, iron [12] and fatty acid content [6] in sheep. It

has been also reported to increase the fatty acid levels in egg yolk [13] and chicken meat [14].

Grape seed can reduce methane emission from ruminants. Studies showed that grape seed can diminish methane production by 20% without affecting microbial fermentation in rumen [15, 16]. Condensed tannins in grape seed can increase the efficiency of feed protein by preventing proteins from ruminal digestion [17] and reduce blood urea level hereby [18].

Grape seed having positive effects on animals with its active components has been reported to be used at limited level in animal feed because of having less digestibility due to high crude fiber content [19, 20]. Fermentation is a method that can be used to improve digestibility of agricultural by-products [21]. Enzymes produced by microorganisms during fermentation can break down cellular structure of the substrate and thus increase its digestibility [22]. Besides microorganisms can increase protein, amino acid, ether extract, mineral and vitamin

---

* Corresponding author. Tel: +90-362-312-1919
E-mail address: *emrah.gungor@omu.edu.tr*

content of substrate with fermentation [23]. Fermentation is divided into liquid-state and solid-state fermentation. Solid-state fermentation is preferred method due to low cost, suitability for working with agricultural by-products and less risk of bacterial contamination [24]. Solid-state fermentation refers to microbial reproduction in moist substrates without free water [25]. *Aspergillus niger* is a filamentous fungus that can grow rapidly in low-water environments [26] and, therefore, used widely in solid-state fermentation of agricultural by-products [27]. In this study, it was aimed to enhance the nutritional composition of grape seed by *A. niger* solid-state fermentation for making available to be used in animal nutrition.

2. Material and Methods

2.1 Microorganisms and substrate

A. niger strains were obtained from the American Type Culture Collection (ATCC). The strains were ATCC 9142 (FG1), ATCC 200345 (FG2) and ATCC 52172 (FG3).

Grape seeds were provided from a grape juice factory in Turkey and stored at -20 °C till fermentation.

2.2 Solid-state fermentation

Grape seeds were milled to a size of 2 mm before being sterilized by autoclaving at 121 °C for 15 min. The nutritional salt (glucose:urea:(NH4)2SO4:peptone: KH2PO4:MgSO4.7H2O=4:2:6:1:4:1) were mixed to the substrate to encourage microorganism to grow after sterilizing phase. Each *A. niger* strain cultured in Potato-Dextrose-Agar (PDA) was added to grape seed substrate at 10^4 spores and uninoculated grape seeds were assigned as control. Samples were incubated at 60 °C for 48 hours. Afterwards, samples were dried at room temperature for 6 days in which samples reached approximately 90% dry matter. Three replicates were prepared for each treatment.

2.3 Main nutritional components analysis

Ash (method, 942.05), crude protein (method, 976.06), ether extract (method, 920.29), crude fiber (method, 973.18) analyses of grape seeds before and after solid-state fermentation were conducted [28]. Neutral detergent fiber (NDF) and acid detergent fiber (ADF) analyses were conducted according to Van Soest et al. [29] using the ANKOM^{2000} fiber analyzer (ANKOM corporation® Technology Fairport, NY). Measurement for each sample was conducted three times.

2.4 Statistical analysis

All of the experiments were carried out in triplicate, and results were expressed as means with pooled standard error of means (SEM). Differences between treatments were tested using ANOVA and Duncan's multiple range test (SPSS 21.0 Statistics). p values $\leq$ 0.05 were considered statistically significant.

3. Results and Discussion

Nutritional changes in grape seed by *A. niger* solid-state fermentation are given in Table 1 and photos before, during and after fermentation are shown in Figure 1. Nutritional composition of grape seeds changed with *A. niger* solid-state fermentation. Crude protein content increased ($p < 0.001$) in all groups whereas the higher increases were obtained in FG2 and FG3. Crude fiber content was decreased ($p < 0.001$) in all groups and the highest reduction was observed in FG2. Ether extract content was decreased in FG2 and FG3 but remained the same in FG1. Ash content was increased in all groups with the higher increases in FG2 and FG3. Nitrogen-free extract (NFE) was decreased in all groups with the higher decreases in FG1 and FG3. NDF and ADF were decreased in all groups, and the higher decreases occurred in FG2 and FG3.
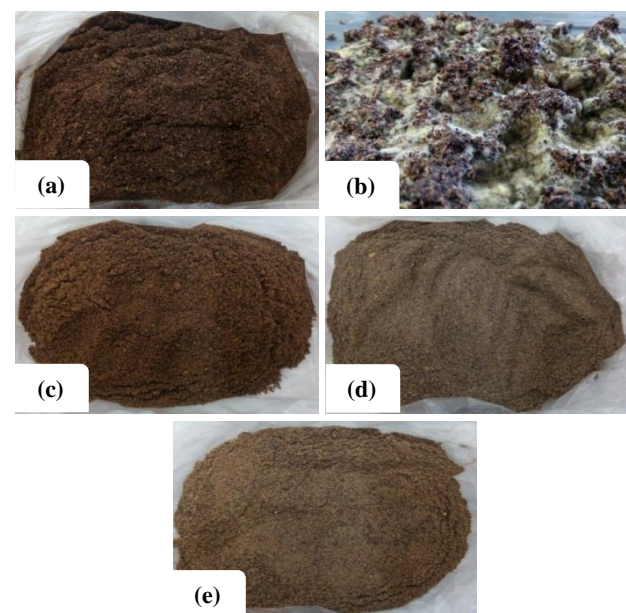

Figure 1. Photos before, during and after fermentation, a) unfermented grape seed, b) fermentation stage, c) grape seed fermented by ATCC 9142 (FG1), d) grape seed fermented by ATCC 200345 (FG2), e) grape seed by fermented ATCC 52172 (FG3)

Table 1. Nutritional changes in grape seed by *Aspergillus niger* solid-state fermentation

Composition (%)	G	FG1	FG2	FG3	SEM	P
Crude Protein	10.13^c	25.94^b	29.50^a	29.49^a	2.415	***
Ether Extract	12.50^a	13.21^a	9.82^c	11.68^b	0.394	***
Ash	3.88^c	7.99^b	8.72^a	8.84^a	0.614	***
NFE	26.06^a	13.17^c	15.72^b	12.71^c	1.632	***
Crude Fiber	47.43^a	39.69^b	36.25^d	37.30^c	1.325	***
NDF	64.01^a	52.30^b	48.98^c	49.13^c	1.857	***
ADF	57.14^a	47.85^b	43.21^c	43.34^c	1.708	***

***: <0.001; a,b,c: Means having different superscripts differ ($p < 0.05$)
G: unfermented grape seed, FG1: grape seed fermented by ATCC 9142, FG2: grape seed fermented by ATCC 200345, FG3: grape seed fermented by ATCC 52172

Nutritional composition of agricultural by-products can be enhanced with solid-state fermentation [30]. Aderemi and Nworgu [31] reported that cassava root and peels' crude protein content increased while crude fiber, NDF, and hemicellulose content decreased with fermentation. Similarly, cassava starch residues' crude protein, ether extract, ash content increased and crude fiber, NDF, ADF content decreased with fermentation [21]. Similar findings were reported in the studies on olive leaves [30] and *Gingko biloba* leaves [23, 27]. In this study, nutritional composition of grape seed was improved by *A. niger* solid-state fermentation with increases in crude protein, ether extract and ash content, decreases in crude fiber, NDF, ADF and NFE content.

Protein content of feed is an important factor affecting growth and yield of animals. Productivity losses are seen in animals when their protein requirement is not supplied by diet [32]. However, protein sources used in animal feeding are costly, therefore, increasing feed costs. In this study, crude protein content of grape seed was increased by fermentation. This increase may be due to mycelia and/or enzymes produced by *A. niger* [26]. Similar findings were reported in the studies on cassava [21, 31, 33-35], shea nut [36], *Ginkgo biloba* leaves [23, 27], pine needle [37], olive leaf [30] and sour cherry kernel [38].

Structural carbohydrates such as cellulose, hemicellulose, and lignin reduce digestibility of feeds because they are difficult to digest by animals [39]. For this reason, structural carbohydrate content is an important sign for estimating the feed's digestibility [30]. In this study, structural carbohydrate content of grape seeds such as crude fiber, NDF, and ADF decreased by fermentation. *A. niger* has been reported to produce cellulase in solid-state fermentation [30] It is thought that cellulase degraded the structural carbohydrates and it caused reduction in crude fiber, NDF and ADF content. Similar results were obtained from the studies on cassava pulp and peels [31], cassava starch residues [21] and shea nut [36]. However, these results are different from the results of the studies on cassava peels [35] and sour cherry kernel [38]. Differences in the results may be due to the fact that different strains were used in the studies or fermentation conditions were different. Indeed, Güngör et al. [38] reported that different strains had different effects on the same substrate.

Increase in ash content is line with the studies on cassava peels [35], cassava starch residues [21], shea nut [36] and sour cherry kernel [38] but not in line with the study that cassava pells' ash content was not changed with fermentation [21].

It has been reported that different *A. niger* strains affect substrate differently with regard to ether extract content [38]. Similarly, grape seed was affected differently by different *A. niger* strains in this study. Ether extract was decreased in FG2 and FG3 while remained at the same level in FG1. These results are consistent with the studies on cassava [35], pomegranate peel and creosote bush leaves [40] and sour cherry kernel [38]. However it was reported that the ether extract content was increased with fermentation of shea nut [36] and cassava [21], unlike our study.

Soluble carbohydrates are firstly preferred to other nutrients for carbon sources by fungi [41]. In fact, NFE level of grape seed decreased with fermentation in this study. This result is in an agreement with the studies on cassava peels [21, 35] and cassava bagasse [33].

4. Conclusion

Nutrient enrichment in the grape seed was achieved by fermentation. Crude protein and ash contents were increased with fermentation, and higher increases were obtained from ATCC 200345 and ATCC 52172. Crude fiber, ADF, and NDF contents were reduced in all groups and the highest reduction was obtained by ATCC 200345. Ether extract level remained at the same level in ATCC 9142 used group but decreased by ATCC 200345 and ATCC 52172. NFE level decreased in all groups; the higher decreases occurred by ATCC 9142 and ATCC 200345. These results showed that *A. niger* can improve nutritional composition of grape seed. Also, different *A. niger* strains (ATCC 9142, ATCC 200345, ATCC 52172) had different effects on grape seed, suggesting that ATCC 200345 may be used for nutritional enrichment of grape seed.

References

1. FAO. Food and Agriculture Organization, 2016. Access date: 25.04.2018. Available from: http://www.fao.org/faostat.

2. Farahat, M., F. Abdallah, H. Ali, and A. Hernandez-Santana, *Effect of dietary supplementation of grape seed extract on the growth performance, lipid profile, antioxidant status and immune response of broiler chickens.* Animal, 2017. **11**(5): p. 771-777.

3. Perumalla, A. and N.S. Hettiarachchy, *Green tea and grape seed extracts—Potential applications in food safety and quality.* Food Research International, 2011. **44**(4): p. 827-839.

4. Garavaglia, J., M.M. Markoski, A. Oliveira, and A. Marcadenti, *Grape seed oil compounds: Biological and chemical actions for health.* Nutrition and Metabolic Insights, 2016. **9**: p. 59-64.

5. Jerónimo, E., C.M. Alfaia, S.P. Alves, M.T. Dentinho, J.A. Prates, V. Vasta, J. Santos-Silva, and R.J. Bessa, *Effect of dietary grape seed extract and Cistus ladanifer L. in combination with vegetable oil supplementation on lamb meat quality.* Meat Science, 2012. **92**(4): p. 841-847.

6. Correddu, F., A. Nudda, G. Battacone, R. Boe, A.H.D. Francesconi, and G. Pulina, *Effects of grape seed supplementation, alone or associated with linseed, on ruminal metabolism in Sarda dairy sheep.* Animal Feed Science and Technology, 2015. **199**: p. 61-72.

7. Brenes, A., A. Viveros, I. Goni, C. Centeno, S. Sáyago-Ayerdy, I. Arija, and F. Saura-Calixto, *Effect of grape pomace concentrate and vitamin E on digestibility of polyphenols and antioxidant activity in chickens.* Poultry Science, 2008. **87**(2): p. 307-316.

8. Hou, F., M. Xiao, J. Li, D.W. Cook, W. Zeng, C. Zhang, and Y. Mi, *Ameliorative effect of grape seed proanthocyanidin extract on cadmium-induced meiosis inhibition during oogenesis in chicken embryos.* The Anatomical Record, 2016. **299**(4): p. 450-460.

9. Wang, M., X. Suo, J. Gu, W. Zhang, Q. Fang, and X. Wang, *Influence of grape seed proanthocyanidin extract in broiler chickens: effect on chicken coccidiosis and antioxidant status.* Poultry Science, 2008. **87**(11): p. 2273-2280.

10. Li, X., Y. Yang, S. Liu, J. Yang, C. Chen, and Z. Sun, *Grape seed extract supplementation attenuates the heat stress-induced responses of jejunum epithelial cells in simmental×qinchuan steers.* British Journal of Nutrition, 2014. **112**(3): p. 347-357.

11. Gessner, D., C. Koch, F.-J. Romberg, A. Winkler, G. Dusel, E. Herzog, E. Most, and K. Eder, *The effect of grape seed and grape marc meal extract on milk performance and the expression of genes of endoplasmic reticulum stress and inflammation in the liver of dairy cows in early lactation.* Journal of Dairy Science, 2015. **98**(12): p. 8856-8868.

12. Mokni, M., M. Amri, F. Limam, and E. Aouani, *Effect of grape seed and skin supplement on milk yield and composition of dairy ewes.* Tropical Animal Health and Production, 2017. **49**(1): p. 131-137.

13. Omidi, M., S. Rahimi, and M.A.K. Torshizi. *Modification of egg yolk fatty acids profile by using different oil sources.* in *Veterinary Research Forum.* 2015. Faculty of Veterinary Medicine, Urmia University, Urmia, Iran.

14. Francesch, A. and M. Cartañà, *The effects of grape seed in the diet of the Penedes chicken, on growth and on the chemical composition and sensory profile of meat.* British Poultry Science, 2015. **56**(4): p. 477-485.

15. Wischer, G., J. Boguhn, H. Steingaß, M. Schollenberger, and M. Rodehutscord, *Effects of different tannin-rich extracts and rapeseed tannin monomers on methane formation and microbial protein synthesis in vitro.* Animal, 2013. **7**(11): p. 1796-1805.

16. Moate, P., S. Williams, V. Torok, M. Hannah, B. Ribaux, M. Tavendale, R. Eckard, J. Jacobs, M. Auldist, and W. Wales, *Grape marc reduces methane emissions when fed to dairy cows.* Journal of Dairy Science, 2014. **97**(8): p. 5073-5087.

17. Bruno-Soares, A., A. Soares-Pereira, T. Matos, and J. Ricardo-da-Silva, *Preliminary results on the effects of grape (Vitis vinifera) seed condensed tannins on in vitro intestinal digestibility of the lupin (Lupinus angustifolius) seed protein fraction in small ruminants.* Journal of Animal Physiology and Animal Nutrition, 2011. **95**(4): p. 456-460.

18. Kronberg, S. and C. Schauer, *Cattle and sheep develop preference for drinking water containing grape seed tannin.* Animal, 2013. **7**(10): p. 1714-1720.

19. Spanghero, M., A. Salem, and P. Robinson, *Chemical composition, including secondary metabolites, and rumen fermentability of seeds and pulp of Californian (USA) and Italian grape pomaces.* Animal Feed Science and Technology, 2009. **152**(3-4): p. 243-255.

20. Baumgärtel, T., H. Kluth, K. Epperlein, and M. Rodehutscord, *A note on digestibility and energy value for sheep of different grape pomace.* Small Ruminant Research, 2007. **67**(2): p. 302-306.

21. Aro, S., *Improvement in the nutritive quality of cassava and its by-products through microbial fermentation.* African Journal of Biotechnology, 2008. **7**(25): p. 4789-4797.

22. Couri, S., S. da Costa Terzi, G.A.S. Pinto, S.P. Freitas, and A.C.A. da Costa, *Hydrolytic enzyme production in solid-state fermentation by Aspergillus niger 3T5B8.* Process Biochemistry, 2000. **36**(3): p. 255-261.

23. Zhang, X., L. Zhao, F. Cao, H. Ahmad, G. Wang, and T. Wang, *Effects of feeding fermented Ginkgo biloba leaves on small intestinal morphology, absorption, and immunomodulation of early lipopolysaccharide-challenged chicks.* Poultry Science, 2013. **92**(1): p. 119-130.

24. Pérez-Guerra, N., A. Torrado-Agrasar, C. López-Macias, and L. Pastrana, *Main characteristics and applications of solid substrate fermentation.* Electronic Journal of Environmental, Agricultural and Food Chemistry, 2003. **2**(3): p. 343-350.

25. Osma, J.F., J.L.T. Herrera, and S.R. Couto, *Banana skin: A novel waste for laccase production by Trametes pubescens under solid-state conditions. Application to synthetic dye decolouration.* Dyes and Pigments, 2007. **75**(1): p. 32-37.

26. Raimbault, M., *General and microbiological aspects of solid substrate fermentation.* Electronic Journal of Biotechnology, 1998. **1**(3): p. 26-27.

27. Cao, F., X. Zhang, W. Yu, L. Zhao, and T. Wang, *Effect of feeding fermented Ginkgo biloba leaves on growth performance, meat quality, and lipid metabolism in broilers.* Poultry Science, 2012. **91**(5): p. 1210-1221.

28. AOAC, *Official Methods of Analysis of AOAC International (17. Edition).* 2000, AOAC International: ABD.

29. Van Soest, P.v., J. Robertson, and B. Lewis, *Methods for dietary fiber, neutral detergent fiber, and nonstarch polysaccharides in relation to animal nutrition.* Journal of Dairy Science, 1991. **74**(10): p. 3583-3597.

30. Xie, P., L. Huang, C. Zhang, and Y.-l. Zhang, *Nutrient assessment of olive leaf residues processed by solid-state fermentation as an innovative feedstuff additive.* Journal of Applied Microbiology, 2016. **121**(1): p. 28-40.

31. Aderemi, F. and F. Nworgu, *Nutritional status of cassava peels and root sieviate biodegraded with Aspergillus niger.* American-Eurasian Journal of Agricultural and Environmental Science, 2007. **2**(3): p. 308-311.

32. Bregendahl, K., J. Sell, and D. Zimmerman, *Effect of low-protein diets on growth performance and body composition of broiler chicks.* Poultry Science, 2002. **81**(8): p. 1156-1167.

33. Vandenberghe, L.P., C.R. Soccol, A. Pandey, and J.-M. Lebeault, *Solid-state fermentation for the synthesis of citric acid by Aspergillus niger.* Bioresource Technology, 2000. **74**(2): p. 175-178.

34. Iyayi, E.A. and D.M. Losel, *Protein enrichment of cassava by-products through solid state fermentation by fungi.* The Journal of Food Technology in Africa, 2001. **6**(4): p. 116-118.

35. Okpako, C., V. Ntui, A. Osuagwu, and F. Obasi, *Proximate composition and cyanide content of cassava peels fermented with Aspergillus niger and Lactobacillus*

rhamnosus. Journal of Food Agriculture & Environment, 2008. **6**(2): p. 251-255.

36. Dei, H., S. Rose, A. Mackenzie, and R. Amarowicz, *Growth performance of broiler chickens fed diets containing shea nut (Vitellaria paradoxa, Gaertn.) meal fermented with Aspergillus niger.* Poultry Science, 2008. **87**(9): p. 1773-1778.

37. Wu, Q., Z. Wang, G. Wang, Y. Li, and Y. Qi, *Effects of feed supplemented with fermented pine needles (Pinus ponderosa) on growth performance and antioxidant status in broilers.* Poultry Science, 2015. **94**(6): p. 1138-1144.

38. Güngör, E., A. Altop, E. Öztürk, and G. Erener, *Nutritional changes of sour cherry (Prunus cerasus) kernel subjected to Aspergillus niger solid-state fermentation.* Journal of Tekirdag Agricultural Faculty, 2017: p. 99-103.

39. Graminha, E., A. Gonçalves, R. Pirota, M. Balsalobre, R. Da Silva, and E. Gomes, *Enzyme production by solid-state fermentation: Application to animal nutrition.* Animal Feed Science and Technology, 2008. **144**(1): p. 1-22.

40. Aguilar, C.N., A. Aguilera-Carbo, A. Robledo, J. Ventura, R. Belmares, D. Martinez, R. Rodríguez-Herrera, and J. Contreras, *Production of antioxidant nutraceuticals by solid-state cultures of pomegranate (Punica granatum) peel and creosote bush (Larrea tridentata) leaves.* Food Technology and Biotechnology, 2008. **46**(2): p. 218-222.

41. Papagianni, M., *Advances in citric acid fermentation by Aspergillus niger: biochemical aspects, membrane transport and modeling.* Biotechnology Advances, 2007. **25**(3): p. 244-263.

Research Article

Evaluation of crosslinking type and antibacterial activities of copper oxide loaded cotton textile fabrics

Aslıhan Koruyucu [a],*

[a] *Namık Kemal University, Çorlu Faculty of Engineering, Department of Textile Engineering, 59860, Çorlu/TEKIRDAG,TURKEY*

ARTICLE INFO	ABSTRACT
	In the current study, the efficacy of Cu(I)O micro and two different cross linkers as a antibacterial metal oxides on textile substrates versus Staphylococcus aureus and Escherichia coli was examined. In particular, bacterial inhibition relationship of micro Cu (I) O with two different cross linkers needed to exhibit effective bacterial action was studied. On textile substrates such as 100%cotton, there was 89,44-94,42% rebate in bacterial counts. Effectiveness of the antibacterial action was retained after ten and twenty cycles.

1. Introduction

Cotton fabrics provide an excellent environment for microorganism proliferation because of high moisture sorption and a large surface area. Some researchers believe that in hospitals, contaminated textiles might be an important source of microbes contributing to the transmission of nosocomial-related pathogens [1,2]. There are many ways to control microbial growth on textiles, such as incorporating antibacterial agents into fibers by coating. The most important antibacterial substances used in textile finishing are quaternary ammonium salts, chloro-ether phenols, poly (hexamethylene biguamidyene), silver and its compounds, organic-silicones [3-5].

Nanoparticles are clusters of atoms in the size range 1-100 nm.

With current advances in nanotechnology, different types of metal and metal oxide nanoparticles were applied in many researches for achieving antimicrobial activity [1-9]. Currently, some noble metal NPs have been largely examined and are well known for their antibacterial effects [8].

Copper and silver are very common in use for their antimicrobial properties [10]. Example of, the Cu NPs indicated higher antibacterial effect relative to the silver NPs against E.coli [19, 20]. The production of thin coated films surfaces are based on coating solid surfaces with a thin film of metal such as copper, silver or titanium, utilized by different techniques [11].Thin coated films surfaces are in contact with human skin be accomplished by using solid copper or copper alloy equipment.

In this text, copper (Cu) and nickel (Ni) are good option materials because they are more economical than gold and silver. It has already been amounced that Cu NPs [10-13] and copper oxide NPs [14-18] have antimicrobial activity.

The purpose of this study was to evaluate micro Cu (I) O and two different cross linkers as an antibacterial agent on cotton fabrics versus *Staphylococcus aureus* and *Escherichia coli*. The durability of the antibacterial activity of the treated substrates versus laundering twenty times was also examined.

In this study, FT-IR spectroscopy and SEM were used to describe CuO NPs. The antibacterial activity of these NPs on two pathogenic species with antibacterial resistance characteristic, *Escherichia coli* ATCC 25922 and *Staphylococcus aureus* ATCC 43300, was assessed.

2. Material and Method

2.1 Materials

2.1.1 Chemicals

Copper(I)oxide (Cu$_2$O), cross-linked(blocked isocyanate, glycid methacrylate)

Bleached cotton fabrics, polyurethane binder and polysiloxane additive.

2.2 Methods

2.2.1 Copper oxides particles applied to cotton fabrics

Experiments were applied samples with size of 40cmx30cm. Cotton fabrics were coated with copper micro and nanoparticles coating bath at concentrations of 0,5% and 1%. Samples were dried at 100 °C for 2 min. Curing was done at 150 °C for 2 min.

The antibacterial activities of the untreated and treated fabrics with coating bath which including copper oxide particles were evaluated after being displayed to recast washing periods (ten and twenty washing periods). Rinsing was performed with a machine set for warm water containing, 2% sodium carbonate and soap. After each rinsing (45 min), the fabrics were plummet dried in a dryer at 70^{0}C.

2.3. Characterization techniques

Constructural and optical properties of the CuO micro and nanoparticles 1 were established by using SEM (Scanning Electron Microscopy) FTIR (Fourier Transform Infra-Red Spectroscopy) in the wavelength distance of 400-4000 cm^{-1}.

2.3.1 Antibacterial activity

Bacterial strains were acquired from the Uludag University Medical Faculty, Department of Microbiology and Infectious Diseases. The culture media; Agar-agar Type-I and chemicals; were used for the surge of bacteria.

The antibacterial behavior of the coated fabrics was tested for two bacterial strains; Gram-negative Escherichia coli and Gram-positive Staphylococcus aureus.

Roughly, 25 ml of liquefied and frigid nutrient agar media was flowed in the sterilized petri dishes. The plates were left over night at room temperature to check for any pollution one. The bacterial test organism S.aureus and E.coli were grown in nutrient chowder for 24 hours at 37^{0}C. A 100μl nutrient chowder culture of each bacterial organism was used to got ready bacterial lawns. Agar wells were got ready with the aid of a sterilized stainless steel cork borer.

In order to study the antimicrobial activity of the fabrics; the samples of 1 cm^2 fabrics were taken randomly and placed in a sterile flask. Each square fabric was placed in a sterile flask. Tryptone soy chowder (2.2 ml) was then added to each vial to obtain a total volume of 3 ml. An aliquot (10μl) of S.aureus suspension was added to each flask (1.6x10^3/ml). Control chowders with and without bacterial vaccination were also incorporated. The vials were then incubated with agitation at 35^{0}C. Aliquots of 10μl chowder were sampled at 24 h and serial dilutions for the a liquots were got ready in chowder. The bacterial activity was assessed after 24 h and appraised % rebate of the bacteria using the following equation:

$$R (\%)= [(A-B)/A]x100 \qquad (1)$$

where R is the rebate rate, A is the number of bacterial colonies from untreated fabrics, and B is the number of bacterial colonies (Duran, Marcato, De Souza, Alves&Esposito,2007).

3.Results and Discussion

3.1 FTIR Spectroscopy

FT-IR analysis was used to examine the presence of the chemical bonds in the coating path structure in the utilized cotton. The FT-IR spectra of the cotton fabrics pretreated in the formulations were given in blue color. The characteristic peaks of the cotton fabrics pretreated in the spectra are summarized in Table 1. In the FTIR spectrum (Figure 1) the peak appearing in the range 1732-1750 cm^{-1} is due to C=0 groups in the ester groups. Bands observed at 1374 and 1383 cm^{-1} are characteristic of –CH-groups. In addition, the spectrum shows at 1083-1088 cm^{-1} to C-O groups. The tensile vibrations of the -OH groups of the cotton fiber structure give wide and severe bands at 3325 cm^{-1}. Glycid methacrylate cross-linker with antibacterial coating path when the FTIR spectrum of the coated cotton fabric is examined; aliphatic esters in the structure of glycid methacrylate carbonyl groups in the isocyanate structure at 1740 cm^{-1} appears to give a sharper peak. This gives us the antibacterial Cu (I) O chemical shows better binding of cotton fiber together with the coating path.

Table1. FTIR spectrum information of pretreated cotton fabric

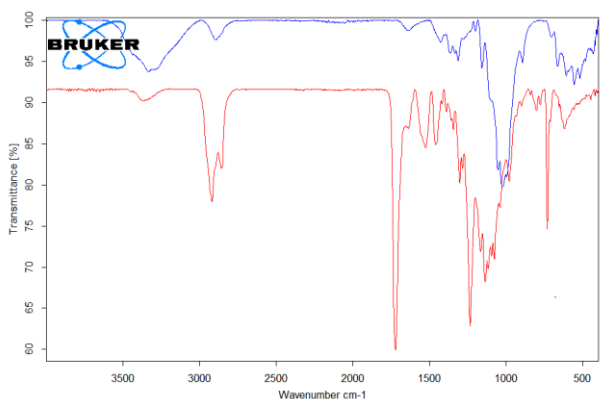| Pre-treated cotton fabric	3424 cm^{-1}-OH tension peak 2900 cm^{-1} C-H tension peak 1432 cm^{-1}-C-C strength (ringed structure) 1350-1370 C-H peak (1373-1338-1318 cm^{-1}) 1000-1300 cm^{-1} –C-O strength peak (1165- 1115-1058 cm^{-1})

Figure 1. FTIR spectra of Cu (I)O micro particles

3.2. Morphology of the coated cotton fabrics

The cotton fabrics were coated copper oxide coating bath. Samples were dried at 100^0C for 2 min tracked by curing for 2 min. at 150^0 C.

The SEM images of cotton fabrics before (untreated) and after (treated) coated with micro Cu (I)O bath are shown in figures 2a-2b.

The SEM image in Figure 2a illustrates the flat construction of the cotton fabrics before coating with Cu (I)O micro particles. After coating, the homogeneous deposition of Cu(I)O micro particles on the cotton fabrics was shown in Figure 2b. Figure 2b indicate the appearance of small particles, most probably Cu(I)O micro particles on the cotton fabric surface.
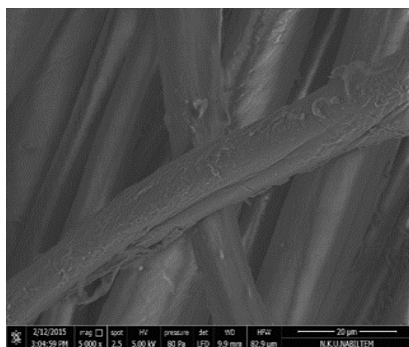

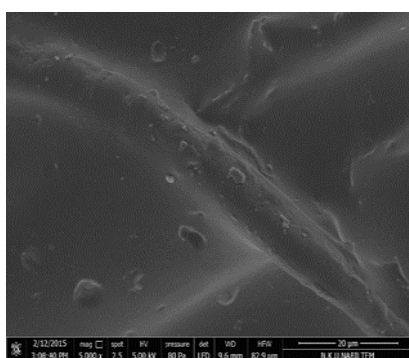
Figure 2a. SEM images of untreated cotton fabric.

Figure 2b. SEM images of Cu (I)O <5μm particles on cotton by using concentrations of 1%.

3.3. Efficiency and durability of the micro copper oxide particles with two different cross linkers-based antibacterial coating

Table 2. The effect of repeated washing periods on antibacterial coating bath with iso-cyanate cross linker

Number of washing	Bacterial reduction(%)	
	S.aureus	E.coli
Before washing	100%	97,98%
After10 periods	97,62%	93,94%
After20 periods	94,42%	89,44%

Table 3. The effect of repeated washing periods on antibacterial coating bath with glycid methacrylate crosslinker

Number of washing	Bacterial reduction(%)	
	S.aureus	E.coli
Before washing	98,81%	-203,03%
After 10periods	95,24%	-203,03%
After20 periods	92%	-203,03%

Results of Table 2 was so clear that 1% of copper oxide particles are enough to cause antibacterial properties to cotton fabric. However, approximately 94% and 89% of the communicated antibacterial properties with the isocyanate cross-linker against *S. aureus* and *E.coli* bacteria are lost under the effect on twenty washing periods, respectively.

It is apparent to the Table 3 that, in spite of the concentration of Cu(I)O <5μm particles used for treatment, the bacterial colonies decrease was always higher than 90% against *S.aureus* and the increase of bacterial colonies was 200% versus *E.coli* for Cu(I)O treated samples with washing periods.

The rebate of bacteria was noted after ten washing periods for cotton fabrics coated by knife-over coating method. Whereas the samples treated by coating method showed the bacterial colonies to values slightly higher than 90%.The treated cotton fabrics were washed for ten and twenty periods. The antibacterial efficacies were tested.The marginal rebate was obtained in antibacterial properties. Coating bath formulation containing 86,5% of the binder is given in the Table 4.

Table 4. Coating bath formulation containing 86,5% of the binder.

Cu(I)O microparticles	1%
Binder	86,5%
Coating thickness	0,1mm
Drying	100ºC/2 min
Curing	150ºC/2 min

It is observed that inclusion of copper oxide concentration in coating bath formulation increase antibacterial properties of cotton fabric even after twenty washing periods. Fabrics coated with micro copper oxide particles at concentration of 1% in the existence of binder demonstrate bacterial rebate values of 94% and 89% for *S.aureus* and *E.coli*, respectively. Cotton fabrics having excellent antibacterial properties and with washing resistant could be acquired by treating the fabrics with a bath of copper(I)oxide having particle size of 5µm in existence of a binder as defined in this work.

4. Conclusion

There is a growing body of scientific evidence with proves the antibacterial properties of Cu(I)O microparticles against various bacterial species, including *E.Coli* and *S.aureus* bacteria. Based on the literature, in some cases CuNPs denoted higher antibacterial effect relative to the silver NPs.

The disk diffusion test method of cotton fabrics described provides good antibacterial properties, as well as resistance to washing, at a concentration of Cu(I)O microparticle of about 1% (w/w).

Acknowledgment

References

1. Alt V, Bechert T,Steinrcke P, Wagener M, Seidel P, Dingeldein E, Domann U, Schnettler R, An in vitro assessment of the antibacterial propperties and cytotoxicity of nanoparticulate silver bone cement, Biomat Biomater, 2004. 25: 4383-4391.

2. Furno F, Morley KS,Wong B, Sharp BL, Arnold PL, Howdle SM, Bayston R, Brown PD, Winship PD, Reid H, Silver nanoparticles and polymeric medical devices: a new approach to prevention of infection, J Antimicrob Chemother, 2004. 54: 1019-1024.

3. Jeong,SH, Yeo SY, Yi SC, The effect of filter particle size on the antibacterial properties of compounded polymer/silver fibers, J Mater Sci, 2005. 40: 5407-5411.

4. Chou WL, Yu DG, Yang MC, The preparation and characterization of silver-loading cellulose acetate hollow fiber membrane for water treatment, Poly Adv Technol, 2005. 16: 600-607.

5. Sambhy V, Mac Bride MM, Peterson BR, Sen A, Silver bromidenanoparticle/polymer composites:dual action tunable antimicrobial materials, J Am Chem Soc, 2006. 128: 9798-9808.

6. Stoimenov PK,Klinger RL, Marchin GL, Klabunde K, Metal oxide nanoparticles as bactericidal agents,Lang, 2002. 18: 6679-6686.

7. Hsiao MT, Chen SF,Shieh DB, Yeh CS,One-pot synthesis of hollow Au 3Cu 1 spherical –like and

8. R.Garcia-Contreras, L. Argueta-Figuerona, C.Mejfa-Rubalcava,R.Jimenez-Martinez,S.Cuevas-Guajardo, P.A,Sanchez-Reyna, H.Mendieta-Zeron, Int. Dent.J., 2011. 61: 297-301.

9. Morones JR, Elechiguerra JL, Camacho A, Holt K, Kouri JB, Ramirez JT, Yacaman MJ, The bactericidal effect of silver nanoparticles, Nanotechnol, 2005. 16: 2346-2353.

10. A.Esteban-Cubillo, C.Pecharroman, E.Aguilar, J.Santaren,J.S,Moya, J.Mater.Sci.41(2006)5208-5212.

11. M.Raffi, S.Mehrwan,T.M.Bhatti,J.I.Akhter, A, Hameed, W.Yawar,M.M. ul Hasan, Ann. Microbiol, 2010. 60: 75-80.

12. N,Cioffi,L.Torsi, N.Ditaranto,G.Tantillo,L.Ghibelli, L. Sabbatini, T.Bleve-Zacheo, M. D Alessio, P.G.Zambonin, E. Traversa, Chem.Mater, 2005. 17: 5255-5262.

13. A.K.Chatterjee, R.K.Sarkar, A.P.Chattopadhyay, P.Aich , R.Chakraborty, T.Basu, A simple robust method for synthesis of metallic copper nanoparticles of high antibacterial potency against E. coli. Nanotechnology, 2012. 23(8): 085103.

14. J.Gabbay, G.Borkow,J.Mishal, E.Magen, R.Zatcoff, Y.Schemer-Avni, J Ind.Text, 2006. 35: p. 323.

15. G.Ren,D.Hu, E.W.C.Cheng, M.A.Vargas – Reus,P.Reip,R.P.Allaker, Int.J.Antimicrob Agents, 2009. 33: 587-590.

16. G.Borkow, J.Gabbay,R.Dardik, A.I.Eidelman, Y.Lavie,Y.Grunfeld,S.Ikher,M,Huszar, R.C.Zatcoff, M,Marikovsky, Wound Repair Regen, 2010. 18: 266-275.

17. G.Borkow, S.S.Zhou, T.Page, J.Gabbay, Plos One, 2010. 5: p. 11295.

18. S.Jadhav, S.Gaiikwad, M.Nimse, A.Rajbhoj, J Clust. Sci., 2011. 22: 121-129.

19. Ruparelia JR Chatterjee AK,Duttagupta SP,Mukherji S. Strain specifity in antimicrobial activity of silver and copper nanoparticles.Acta Biomater, 2008. 4: 707-716.

20. Yoon KY, Hoon Byeon J, Park JH, Hwang J. Susceptibility constants of Escherichia coli and Bacillus subtilis to silver and copper nanoparticles. Science of the Total Environment, 2007. 373(2-3): 572-575.

Research Article

Design study with height adjustable washbasin

Süleyman Çınar Çağan [a],*, Berat Barış Buldum [a] and İskender Özkul [a]

[a]*Mersin University, Engineering Faculty, Department of Mechanical Engineering, 33343, Ciftlikkoy, Yenisehir/Mersin, Turkey*

ARTICLE INFO	ABSTRACT
	According to Turkish Statistical Institute data (2011), it is known that approximately 6.6% of the population in Turkey is composed of disabled people and the highest rate of disability is from physical disabilities. It is observed that the freedom of movement of physically handicapped individuals is very limited in the environment and housing areas, and the existing regulations do not fully respond to the needs. It is difficult for people with physical disabilities to use furniture, fixtures and fixtures designed for normal people. The washbasins in bathrooms and toilets, which are the most special parts of homes and workplaces, need to be arranged for individual use without physical support for individuals with physical disabilities. In this way, disabled individuals will be able to live their lives without the need of others, at least by labor. In this study, a height adjustable washbasin was designed as a solution to minimize the difficulties caused by arrangements in the wash basin in bathrooms and toilets, one of the places where disabled people are most distressed in living spaces and public spaces. This study has been designed and manufactured not only for disabled people but also for the children and the elderly, especially those with physical competence, which will facilitate the life of each individual.

1. Introduction

According to the World Health Organization; "Disability; a deficiency or disability means a disadvantageous situation that prevents and restricts the ability to engage in activity on a particular person and which may be regarded as normal according to the age, gender, social and cultural status of that person" [1, 2]. A person with a disability is defined as a person who is in need of protection, care, rehabilitation, counseling and support services because he or she is unable to meet the requirements of normal life due to loss of physical, mental, mental, emotional and social skills after birth or afterwards [3].

Approximately 6.6% of Turkey's population is said to consist of people with disabilities [4]. Hospitals, schools, universities etc. are required to carry out studies to address the needs of individuals with disabilities [5]. The design of household appliances, furniture, etc., has a great prospect among these works so that people can live on their own without needing anyone. Urban design approaches have begun to be adopted in order to enable people to live in the street as well as to live on the street in the same way and

to be able to experience the freedom in the house in the same way and sensitive approaches to disability are planned in the planning of physical spaces such as buildings, buildings, streets, pedestrian roads, transportation networks [6]. The city plans pioneered by the European countries have become an example to other countries, and over time, "disability" has begun to take place among the city plans and strategic plans of many countries [7]. In order to reduce the difficulties of people with disabilities in their daily lives, it is of significant importance that the washbasins in bathrooms and toilets are made suitable for their use. Elevation is one of the most important parameters in the design of the washbasin. People need to go to a stand-by position in order to use the washbasin, depending on their length and the activity to be performed. The effect of height on human health is very important in this context. In addition, the height adjustable washbasin design will allow children to get cleaner education at a young age and make it easier for the elderly to use the washbasin. In this study, it was aimed to ergonomically design washbasins in bathrooms and toilets that are frequently used by children, elderly people,

* Corresponding author. Tel.: *+90-324-361-0001*.
E-mail address: *cinarcagan@mersin.edu.tr*

especially disabled people, in their living spaces. For this; height adjustable washbasin design. In this way, it has been tried to design a design that will facilitate the life of each individual who has physical disabilities, especially disabled individuals, children and the elderly.

2. Literature Research

Height adjustable washbasin design; are necessary to improve the living standards of disabled people, children and the elderly. In a study by Moon and Bae [8], a height-adjustable washbasin-based design was developed based on Korean anthropometric data. Using the human model, waist movements were examined when subjects performed hand and face washing movements. A prototype from the test results was made and a confirmation test of the guide was carried out using a height adjustable washbasin and it is reported that the height adjustable washbasin is more beneficial for people with disabilities when compared to a conventional washbasin at constant height. In a study by Goto and his colleagues [9], they conducted a study on whether the existing washbasin heights are still valid with rapid aging in Japan. During the face wash, both the tap and the cabinet were tested to examine the preferred height. Senior people were asked to wash the face without any compulsion and the preferred height was determined. According to this study, you have observed that the current height is below the acceptable level. The height of the washbasin is closely related to the moment applied to the users' pools [8]. Posture; the lower position forms a large gap between the elbow and the washbasin, so that the user has to bend the upper body forward (Figure 1). While designing the washbasin; it is very important for the health to choose the height adjustable washbasins according to the standard size washbasins which cause the increase of the applied torque. In a study by Rashid and his colleagues [10], it was designed to provide an ergonomically comfortable environment for older Malaysian people. 10 houses were taken as samples and the anthropometric studies were done according to the Malaysian living area designs.

Awang et al. [11] has been studied on medical application designs for hospitals. This study covers the design of buildings for use and care of disabled people in Malaysian hospitals. As a result of these studies, the use of washbasins and lifts of disabled people is a very critical situation.
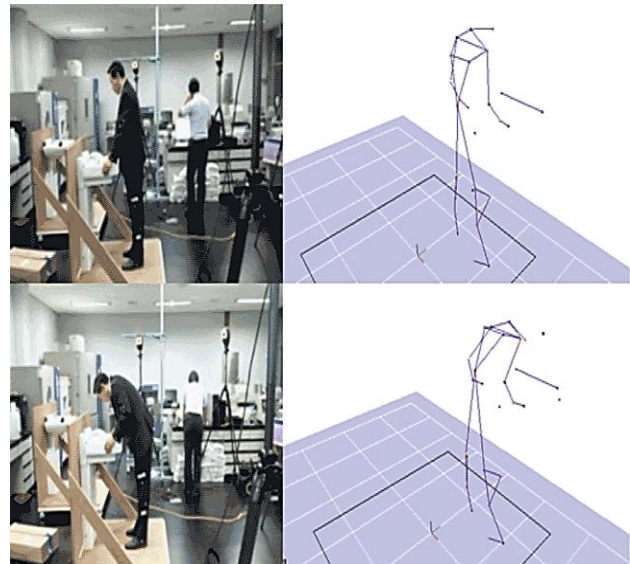

Figure 1. Data obtained by motion: standing and bending body [8].

3. Material and Method

The design of the standard washbasin was inspected and the technical drawing of the washbasin was drawn (Figure 2). The technical drawings are manufactured one by one and the assembly process is carried out and the height adjustable washbasin design is completed.

The way to follow in experimental work is:

- The initial height of the adjustable washbasin should be set to the average of the elbow height.
- The person has to show the process of washing his face in the standing position.
- 3dimensional motion capture system should measure the body and neck inclination angle.
- The moment force applied to the waist of the individual should be calculated.
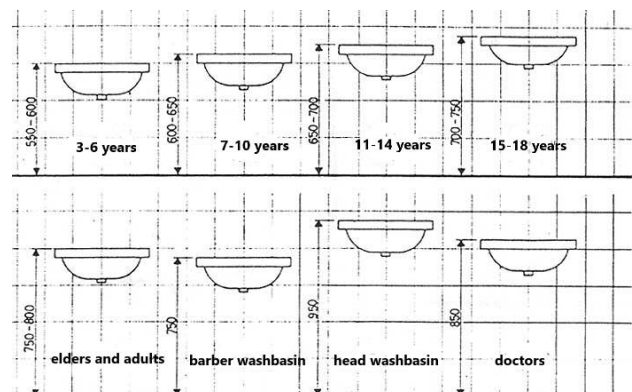

Figure 2. Standard washbasin measurements

3.1. Design Components

In this study, height adjustable washbasin design steps; drawings of technical drawings, selection of materials of

technical drawings, production of materials and assembly of manufactured parts.
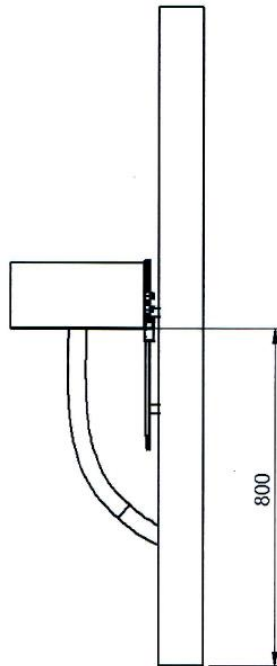

Figure 3. Technical drawing of the designed washbasin
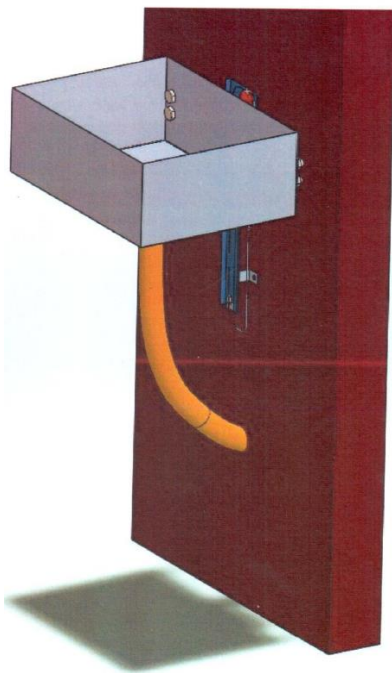

Figure 4. Installation image of the designed washbasin

In the manufacture of height adjustable washbasin design parts; 304 stainless steel was designed using washbasin as shown Figure 5. It has a design that can move up and down with 220 V. Dimensions are 750 x 590 x 700 mm and weigh about 36.1 kg (Sack weight = 19,9 kg / load-bearing construction weight = 16.2 kg).

Figure 5. General washbasin perspective view

3.2. Actuating Mechanism

In our design, the actuating mechanism was preferred as like car window pulley system as presented in Figure 6. Car window pulley system actuated with 12V DC brushed motor. The speed of the washbasin can be arranged between 0-0.3 m/s. That provides speed control for DC motors with Pulse Width Modulation (PWI) unit. That can be arranged if user demand to change the speed for washbasin. Electrical panel is managed by Central Processing Unit (CPU) which can be found cheap and easy from market as shown Figure 7. The CPU board like as Raspberry, Arduino etc. supports many auxiliary sensors and wiring options. So, that allowed us to enrich our design to make more comfortable product. We have used photocell sensor to detect a person which ready to use washbasin. Two options provided the users to define the height of the washbasin. One of this is manual height arrangement system. That can be controlled by a push button which has "0", "1" and "2" as demonstrated Figure 8. "0" indicate upside, "1" neutral and "2" downside on the button. The washbasin should be pressed on the button to reach the desired height. In this option, against to over travel for washbasin, the system was taken the safe with limit switches. In Figure 9. shows the selection button for manual and automatic option for height level. In order to prevent any electrical danger and damage we have use emergency button (Figure 10).
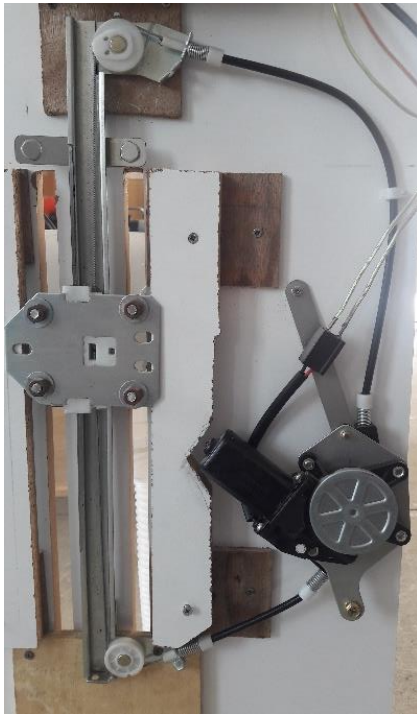
Figure 6. Actuating mechanism for washbasin

Figure 7. Electrical panel

Figure

8. Up down push button for height arrangement

Figure 9. Manual and automatic option for height level arrangement

Figure 10. Emergency button

4. Conclusions

In this study, a height adjustable washbasin was designed. A prototype has been developed considering the literature data. The height adjustable washbasin design compared to a conventional washbasin at constant height; disabled people, children and the elderly. It is regarded useful to consider anthropometric data for future designs of this topic. The system has been developed with electronic CPU platforms and supported with different sensors. The electronic components usage made the design more comfortable and ergonomic for last users. The speed of the washbasin can be arranged between 0-0.3 m/s. Users and device safety were provided emergency button limit switches. Hence, this design was prepared as user friendly and ergonomic device.

References

1. Available from: http://www.who.int/en [cited 2017 29 June].

2. Koca, C. Engelsiz Şehir Planlaması Bilgilendirme Raporu, Dünya Engelliler Vakfı, İstanbul. 2010.

3. Yılmaz, M. G. Herkes için Tasarım ve Kamusal Alan, Güney Mimarlık, 2012. 10: p.10.

4. Available from: http://www.tuik.gov.tr [cited 2017 29 June].

5. Talib, Y. A., Ghani, N. I. A., & Ismail, K. The Provision of the Disabled Facilities in Public Hospitals. Paper presented at the MATEC Web of Conferences, 2016. 66: p. 00081.

6. Chamberlain, L. Design for Everyone, Disabled or Not, The New York Times, 2007.

7. Benneth, U. Disabled by Design, Disability ans Society, 2002. 17(7): 809-823.

8. Bae, J. H., Moon, I. A guideline for height-adjustable wash basin based on bio*mechanic analysis and usability tests.* Rehabilitation Engineering & Assistive Technology Society, 2014. 110(136.3): 132-2.

9. Goto, Y., Kose, S., Tanaka, S., Nakajima, Y., Nakamura T. *Analysis of design of washbasin for use by the elderly.* Advances in Design for Inclusion, 2017. p. 195-206.

10. Rashid, S. N. S. A., Hussain, M. R., Yusuff, R. M. *Designing homes for the elderly based on the anthropometry of older Malaysians*, Asian Journal of Gerontology & Geriatrics, 2008. 3: p. 75-83.

11. Awang N. A., Chua S. J. L., Ali A. S. *Building Condition Assessment Focusing on Persons with Disabilities' Facilities at Hospital Buildings". 2017. p. 73-84.*

Research Article

Calculation of the diffusion lengths for one-speed neutrons in a slab with forward and backward scattering

Ökkeş Ege [a] and Hakan Öztürk [a],*

[a] *Department of Physics, Osmaniye Korkut Ata University, Osmaniye, 80000, Turkey*

ARTICLE INFO	ABSTRACT

The diffusion lengths for one-speed neutrons in a slab are calculated using the first kind of Chebyshev polynomials approximation (T_N) method. The scattering models are constituted in place of the scattering function with an argument of the cosine of the neutron scattering angle. Therefore, the forward-backward-isotropic (FBI) scattering model is used as the scattering function in transport equation which describes the interaction and the conservation of the neutrons throughout a system. In the solution algorithm, first the neutron angular flux is expanded in terms of the Chebyshev polynomials of first kind. After inserting this expansion in the transport equation, the coupled differential equations are derived using the properties of the Chebyshev polynomials of first kind. These equations are solved together and then the diffusion equation is obtained by applying the first order approximation ($N = 1$) which is known as the diffusion approximation. Finally, the diffusion lengths for one-speed neutrons are calculated for selected values of the collision, backward and forward scattering parameters. The calculated diffusion lengths are given in the tables together with the ones already obtained in literature in order to indicate the applicability of the present method. The convenience and rapid convergence of the present method with its easily executable equations can be observed from the derived equations and the results in tables.

1. Introduction

The neutrons are interacted with all materials inside a reactor system. The transport equation is describes their behaviors with an integro-differential form. Therefore, It is not very easy to find an exact solution for the transport equation. As well known, the neutrons are neutral particles and they are not affected by electric or magnetic fields and thus their path through the material is in zigzag. Therefore, it is difficult to determine how they interact with the materials inside the system and to guess the distribution of them through the boundaries. In order to solve this equation, some detailed knowledge about nuclear cross sections and energy dependence of the neutrons should be known. When a polynomial approximation technique is established to solve the problems stated in different fields of engineering and science especially in transport theory, first approximation of the method is tried and then its higher orders are applied to the problems. The first order approximation of these techniques is known as the diffusion approximation.

The first estimates of a nuclear reactor is still done by using diffusion approximation in which many properties about the neutrons such as transport and energy spectrum of them can be predicted convincingly. This theory works well for values close to unity in *c*, the number of secondary neutrons per collision [1].

Many stochastic and deterministic methods have been developed for the problems about particle or photon transports. Among the deterministic methods, the spherical harmonics (P_N) is one of the most commonly preferred ones because of its accepted application convenience for the problems in transport theory. The first order P_1 approximation is easy in derivation of the equations for many geometries and the results obtained from it can be accepted as accurate in many studies [1-3]. However, this does not mean that the spherical harmonics method is always true and valid for all computations. Therefore, the Chebyshev polynomials instead of Legendre polynomials are used by Aspelund, Conkie and Yabushita in series expansion of the neutron angular flux and they reported the applicability of the method for the

problems of transport theory [4-6].

In the last decade, the first kind of Chebyshev polynomials, i.e. T_N method is used effectively for the solutions of the problems related with transport theory such as criticality, eigenvalue spectrum and diffusion lengths of the neutrons in bare and reflected slabs and spheres [7-10]. However, in any of those studies, T_1 the lowest order approximation of the Chebyshev polynomials of first kind is not used for the calculation of the diffusion lengths calculations in the case of forward and backward scattering. Therefore in this study, apart from the previous studies T_1 approximation is firstly applied one-dimensional transport equation to determine diffusion lengths of neutrons in the case of forward and backward scattering. It is aimed to show that applicability and thus the accuracy of the T_1 approximation against the traditional P_1 approximation in diffusion length calculations. In other words, the present method independent from the problem under consideration is thought to be useful in the long run as an alternative method. Hence, using various values of the collision and the scattering parameters in the mathematical derivations of the method, the diffusion lengths of neutrons are calculated numerically. At the end, the numerical results are obtained from the present method and they are tabulated with ones already presented in literature to indicate the accordance of the methods.

In this study, an alternative deterministic method based on the polynomial expansion of the Chebyshev polynomials of first kind is presented other than the traditional methods. This is important for the literature since this alternative method can be applied to other problems to get better results or new results for the problems in science and engineering. This method can also be improved to solve various problems in many areas.

2. Theory

The one-dimensional linear transport equation derived with forward-backward-isotropic scattering (FBI) model for monoenergetic neutrons is given as,

$$\mu \frac{\partial \psi(x,\mu)}{\partial x} + \sigma_T (1 - \alpha c) \psi(x,\mu)$$
$$= \frac{c\sigma_T}{2} (1 - \alpha - \beta) \int_{-1}^{1} \psi(x,\mu') d\mu' + \beta c \sigma_T \psi(x,-\mu) \quad (1)$$

where $\psi(x,\mu)$ is the angular neutron flux at point x and direction μ, cosine of the scattering angel between the neutron velocity vector and the positive x-axis. α and β are the parameters of forward and backward scattering probabilities in a collision and σ_T is the total macroscopic cross section [2].

In this study, a successfully applied angular neutron flux [7] is chosen because of its easily executable derivations and advantages,

$$\psi(x,\mu) = \frac{\Phi_0(x)T_0(x)}{\pi\sqrt{1-\mu^2}} + \frac{2}{\pi\sqrt{1-\mu^2}} \sum_{n=1}^{\infty} \Phi_n(x)T_n(x) \quad (2)$$
$$-a \leq x \leq a, \qquad -1 \leq \mu \leq 1$$

Later this angular flux will be used in Eq. (1) to obtain the moment equations. But before it, the orthogonality and recurrence relations of the Chebyshev polynomials of first kind are needed to derive the equations [11],

$$\int_{-1}^{1} \frac{T_m(x)T_n(x)}{\sqrt{1-\mu^2}} d\mu = \begin{cases} 0; & m \neq n \\ \frac{\pi}{2}; & m = n \neq 0 \\ \pi; & m = n = 0 \end{cases} \quad (3)$$

$$T_{n+1}(\mu) - 2\mu T_n(\mu) + T_{n-1}(\mu) = 0. \quad (4)$$

First, Eq. (2) is inserted into Eq. (1), then the resultant equation is multiplied by $T_0(\mu)$ and $T_1(\mu)$ and integrated over $\mu \in [-1, 1]$. During these operations, Eq. (3) and Eq. (4) are auxiliary for the derivations in the integrals. At the end of this application, T_N moments of equations for $n = 0$ and $n = 1$ are obtained, respectively;

$$\frac{d\Phi_1(x)}{dx} + \sigma_T (1-c)\Phi_0(x) = 0 \quad (5)$$

$$\frac{d\Phi_2(x)}{dx} + \frac{d\Phi_0(x)}{dx} + 2\sigma_T \left[1 - c(\alpha - \beta)\right]\Phi_1(x) = 0 \quad (6)$$

These equations are known as T_1 equations. As well known, $\Phi_{N+1}(x) = 0$ and $d\Phi_{N+1}(x)/dx = 0$ are used in spherical harmonics (P_N) method [2,3]. The same approximation technique is also valid for T_N method. Therefore, for T_1 approximation, $d\Phi_2(x)/dx = 0$ is used in Eq. (6) and $\Phi_1(x)$ is obtained as,

$$\Phi_1(x) = -\frac{1}{2\sigma_T \left[1 - c(\alpha - \beta)\right]} \frac{d\Phi_0(x)}{dx} \quad (7)$$

Eq. (7) is very familiar with the equation known as Fick's law of diffusion which defines the flow of atoms from high concentration to low concentration. Then, the diffusion equation can be obtained by inserting Eq. (7) into Eq. (5),

$$\frac{d^2\Phi_0(x)}{dx^2} - 2\sigma_T^2\left[1-c(\alpha-\beta)\right](1-c)\Phi_0 = 0 \qquad (8)$$

The same procedure developed for the traditional P_1 approximation is followed to obtain Eq. (8). Then, from the definition of the diffusion length, the square root of the inverse of the coefficient of the second term of Eq. (8) can be referred as the diffusion length (L) in T_1 approximation,

$$L = \frac{1}{\sigma_T \sqrt{2\left[1-c(\alpha-\beta)\right](1-c)}} \qquad (9)$$

In addition, Eq. (8) is a homogeneous differential equation with constant coefficient. When this differential equation is solved, the scalar neutron flux for $c < 1$ can be obtained,

$$\Phi_0(x) = A e^{\sigma_T \sqrt{2\left[1-c(\alpha-\beta)\right](1-c)}\, x} + B e^{-\sigma_T \sqrt{2\left[1-c(\alpha-\beta)\right](1-c)}\, x}, \qquad (10)$$

where A and B are the constants which can be found from boundary conditions.

It is not hard to think that this process on obtaining the diffusion length can be done with other methods. The diffusion length for isotropic scattering from the method of separation of variables is given as

$$1 = cL \tanh^{-1}\frac{1}{L}, \qquad (11)$$

and it is called as the asymptotic relaxation length in that method.

The diffusion lengths of the neutrons obtained by the traditional P_1 (diffusion) approximation can be given as,

$$L = \frac{1}{\sigma_T \sqrt{3\left[1-c(\alpha-\beta)\right](1-c)}}. \qquad (12)$$

This result is derived for a slab with forward and backward scattering. Other results from various methods can also be found from the literature. However, there is no need to exceed them here. Because it is accepted as to be necessary to compare the results obtained from the present methods with ones obtained from one or two references.

These methods are discussed in detail in many references, therefore more explanations about them can be got by following them [2,3].

3. Results

An analytic study for the diffusion length of neutrons in a homogeneous slab with forward and backward scattering is studied through equations (1) to (9). In this analysis, first the angular neutron flux is expanded in terms of the first kind of Chebyshev polynomials. After applying the first order approximation of the method, the equations of moments are obtained in Eqs. (5) and (6). Then, these coupled differential equations are solved together to obtain an analytic expression for the diffusion length. Finally, the numerical results for the present study are calculated from Eq. (9). The diffusion lengths are also calculated from Eqs. (11) and (12) and they are given in the tables and figures side by side for comparison. Therefore, one can easily see the efficiency or the performance of the present method from tables and figures. These calculations are done for various values mediums related with the collision parameter c, forward scattering parameter α and backward scattering parameter β. In all cases, the calculations can be carried out using a simple calculator or a mathematical software and the normalized value of the total macroscopic cross section is taken as, $\sigma_T = 1$ cm^{-1}.

During the numerical calculations, special softwares may be used. However, since this study is a first step for further studies, there is no need to use any software to calculate the results from equations (9), (11) and (12). A simple calculator could be enough for this kind of applications.

Table 1. Diffusion lengths L obtained from T_1 approximation for ($\alpha = 0.0$ and $\beta = 0.0$) and comparison with literature values, (cm).

c	T_1(present method, Eq. (9))	P_1 (Eq. (12))	Exact
0.99	7.07107	5.77350	5.79673
0.98	5.00000	4.08248	4.11552
0.95	3.16228	2.58199	2.63515
0.90	2.23607	1.82574	1.90320
0.80	1.58114	1.29099	1.40763
0.50	1.00000	0.81650	1.04438
0	0.70711	0.57735	1.00000

Table 2. Diffusion lengths L obtained from T_1 approximation for ($\alpha = 0.3$ and $\beta = 0.0$) and comparison with literature values, (cm).

c	T_1(present method, Eq. (13))	P_1 (Eq. (12))
0.99	8.43349	6.88592
0.98	5.95069	4.85872
0.95	3.73979	3.05352
0.90	2.61712	2.13687
0.80	1.81369	1.48087
0.50	1.08465	0.88561
0	0.70711	0.57735

Table 3. Diffusion lengths L obtained from T_1 approximation for ($\alpha = 0.0$ and $\beta = 0.3$) and comparison with literature values, (cm).

c	T_1(present method, Eq. (9))	P_1 (Eq. (12))
0.99	6.20890	5.06955
0.98	4.39545	3.58887
0.95	2.78964	2.27773
0.90	1.98419	1.62008
0.80	1.41990	1.15935
0.50	0.93250	0.76139
0	0.70711	0.57735

In order to see visually the general behavior of the diffusion lengths of neutrons with respect to the collision forward and backward scattering parameters the following figures are plotted.
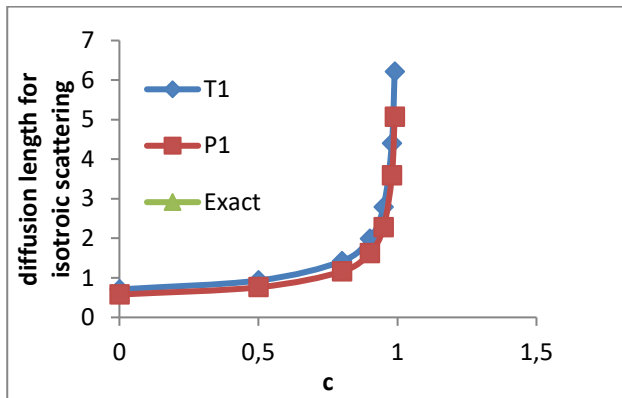

Figure 1. Diffusion lengths for isotropic scattering obtained from T_1, and P_1 approximations and exact results.
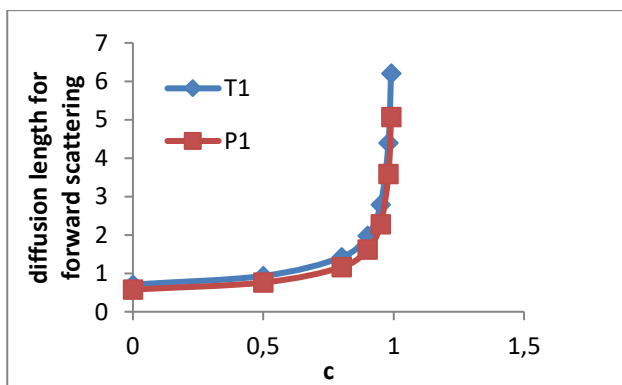

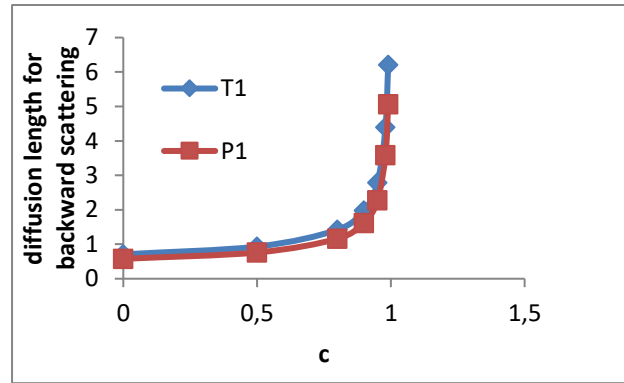Figure 2. Diffusion lengths for forward scattering obtained from T_1 and P_1 approximations.

Figure 3. Diffusion lengths for backward scattering obtained from T_1 and P_1 approximations.

4. Conclusions

An analytic expression for the diffusion length is obtained from the present method and it is given in Eq. (9). The reference results tabulated in tables are quoted from Ref. [12]. One of them is the exact results obtained by Eq. (11) from transport theory and the other is the results obtained by Eq. (12) from traditional P_1 approximation. The numerical results for the diffusion length are calculated for the c values increasing from 0 to 1 and isotropic ($\alpha = 0.0$ and $\beta = 0.0$), forward ($\alpha = 0.3$ and $\beta = 0.0$) and backward ($\alpha = 0.3$ and $\beta = 0.0$) scattering cases. While the lower values of c represents the weakly absorbing medium, the higher values of it represents highly scattering medium.

In Table 1, diffusion lengths for isotropic scattering obtained from the present method are given with the literature values. While the results obtained from the present method are given with the ones obtained from conventional P_1 approximation in the case of forward scattering in Table 2, they are given in the case of backward scattering in Table 3. By investigating the results given in the tables, one can first tend to insist on some inconsistencies between the results obtained from the present method and the ones obtained from the P_1 approximation and the exact ones. However, this assertion should not be taken into consideration since these are first order polynomial approximations. As well known, in a polynomial expansion based technique, it is not waited for good results in low order approximations. Hence, higher order approximations of the present method have been successfully practiced to related problems of the transport theory in previous studies [7-9]. However, this study should not to be evaluated with only the numerical results but also it should be evaluated with its easily executable equations and rapid convergence. It can be summarized that the present method is effective and alternative in the field of the science and engineering and it can be served to the literature as an impressive method.

In addition, in these figures given in this study, one can

easily observe how the results obtained from the present method are in good accordance with the ones obtained from the traditional P_1 approximation and the exact ones. Therefore, this study can be a sign that the present method can be accepted as an alternative method for the problems of the transport theory and other applied sciences.

References

1. Lamarsh, J.R., Baratta, A.J., *Introduction to nuclear engineering*. 2001, USA: Prentice Hall, Inc.
2. Davison, B., *Neutron transport theory*. 1958, London: Oxford University Press.
3. Case, K.M, Zweifel, P.F., *Linear transport theory*. 1967, USA: Addison-Wesley Publishing Company.
4. Aspelund, O., *On a new method for solving the (Boltzmann) equation in neutron transport theory*. PICG, 1958. **16**: p.530-534.
5. Conkie, W.R., *Polynomial approximations in neutron transport theory*. Nucl. Sci. Eng., 1959. **6**: p.260-266.
6. Yabushita, S., *Tschebyscheff polynomials approximation method of the neutron transport equation*. J. Math. Phys., 1961. **2**: p.543-549.
7. Anlı, F., Yaşa, F., Güngör, S., Öztürk, H., T_N *approximation to neutron transport equation and application to critical slab problem*. J. of Quant. Spectros. Radiat. Trans., 2006. **101**: p.129-134.
8. Öztürk, H., Anlı, F., Güngör, S., T_N *method for the critical thickness of one-speed neutrons in a slab with forward and backward scattering*. J. of Quant. Spectros. Radiat. Trans., 2007. **105**: p.211-216.
9. Tıraş, M., Öztürk, H., Bülbül, A., T_1 *and* U_1 *approximations to neutron transport equation in one-dimensional spherical geometry*. Kerntechnik, 2014. **79**: p.163-166.
10. Yıldırım, S., Öztürk, H., *Diffusion length calculations for one-speed neutrons in a slab with backward, forward and linear anisotropic scattering*. Kerntechnik, 2014. **79**: p.243-246.
11. Arfken, G., *Mathematical methods for physicists*. 1985, London: Academic Press, Inc.
12. Bell, G.I., Glasstone, S., *Nuclear reactor theory*. 1972, New York: VNR Company.

Research Article

Electricity pricing algorithm based on resource type and nodal approach

Hayri Oğurlu[a] and Nurettin Çetinkaya[b],*

[a]*Turkish Electricity Transmission Corporation, 9th Regional Directorate, Konya Turkey*
[b]*Selçuk University, Faculty of Engineering, Electrical-ElectronicsEngineering Department, Konya Turkey*

ARTICLE INFO	ABSTRACT
	The aim of the electrical system operators is to ensure that energy is delivered to the consumer in good quality and without interruption. The main purpose of the electricity market operators is to provide the electricity to the end user as adequate, continuous and low cost. Demand for energy in the world is constantly increasing due to technological developments, increasing world population and welfare of people. The lower cost of electricity will lead to a higher quality of life and a more competitive condition in the industry [1-3]. For this reason, the cost of electricity is very important for everyone. While revealing the price of electricity, many different data are taken into account. These are generation, transmission and distribution costs. Generation costs include such as initial investment, operation, and supply costs. Depending on the source used, electric energy can be generated at very different costs. Transmission costs include investment and operation costs of substation centers and transmission lines used in the transmission system. Distribution costs are the operation and investment of the distribution system and the expenditures of some ancillary services delivered to the end user. Electricity prices are offered to end users with specific tariffs. However, these tariffs are disadvantageous for some users. Because, in the calculations made, the type of production source or the geographical location of the plant are not considered [4]. Therefore; for both producers and consumers, it is thought that these calculations can be made in a more acceptable way, taking into account the location of the source of production in the system and the interconnected system.

1. Introduction

In an electrical system, it is also aimed at ensuring the continuity, safety and regeneration of energy while being economical. As much as possible, fair and realistic prices should be determined to provide electricity to the consumers economically. To achieve this realistic approach, the energy production cost and the transmission cost should be reflected separately in the prices. It should not apply the same price tariff to a consumer who is fed from a factory with a relatively low production cost and a factory with a higher production cost. Manufacturers and consumers will set their investment positions in the electrification system with these different pricing options that can be offered to them [5-8]. The system will achieve a homogeneous structure with different prices to be produced in different buses of the interconnected system. Otherwise, production facilities will be gathered in one part of the system; the

consumption facilities will be collected in another region. This will cause unnecessary financial burdens in the country's economy with long transmission lines and transformer centers that need to be set up. In the present case, in some regions of the electrification system there are transformers or installed power capacities waiting in idle, while overloading problems are encountered on the other side. In order to avoid this situation, users can be directed to more economical parts of the system with pricing algorithms. For example, for a company that wants to set up a new generation facility in an area with more generation facilities, the generation price in that area would be lower than in other regions, thus encouraging the establishment of a generation facility in other possible locations. In the same way, a user with energy demand in areas where heavily consumed (for large subscriptions such as the Organized Industrial Zone fed from the Transmission System) could plan an investment in a region where the electricity cost would be

* Corresponding author. Tel.: +90 532 206 37 44; Fax: +90 332 265 09 72
E-mail address: hayriogurlu@gmail.com

more economical because the electricity costs in this region will be higher than in other regions.

For each generation facility that is a market participant; a calculation to be made considering factors such as the type of energy source, the position of participating in the generation, the size of the installed power, etc. may result in more realistic results. The different costs that arise in different parts of the interconnection system must be reflected to the energy demand consumer [9-11]. With this approach, the cost can be calculated according to the area to be connected on the interconnected system.

There are no articles in the studied studies that are calculated according to the production source type. From this point of view, this article presents an innovative approach. Another innovation introduced in the proposed pricing algorithm is the multi-stage dynamic programming method used. This method is able to obtain multiple solution functions in a way not previously implemented in Dynamic Programming.

In the first part of the work, information on the importance of Electricity Pricing methods and the method applied is given. This method will be explained benefits in terms of users and in terms of the transmission system. Then, a brief description will be given about the structure of the electricity market in Turkey. In the third part, information about pricing algorithms will be given and details of the pricing algorithm suggested in the last section will be determined. The proposed pricing algorithm will be tested on the IEEE-30 busbar test system and the sample balanced busbar system. Benefits will be evaluated in the last section compared to other methods applied.

2. Structure of Electricity Market in Turkey

After starting in 1902, the first electricity production, electricity sector in Turkey is advancing constantly and quickly. In 1970 (Turkey Electricity Authority) was established and electricity transmission, distribution, production and trade are given tasks. In 1984 private companies were allowed to generate electricity. In 1993, TEK, TEAS and TEDAŞ were divided into two. In 2003 TEAS, TEİAŞ, EÜAŞ and TETAŞ were divided into three divisions. TEİAŞ, as a public institution (Turkey Electricity Transmission Company) engages in electricity transmission tasks. TEDAŞ (Turkey Electricity Distribution Company) is divided into 21 regions and distribution tasks are managed by private companies.

EMRA (Energy Market Regulatory Authority) was established in 2001. In 2013, transmission system operation and market operation are separated. EPIAS (Energy Market Operational Company - EXIST) was established for the market operation. As a result of these developments, the electricity energy market has become more flexible and all participants have shaped as shown in Table 1.

Table 1 The Occurrence Process of Turkish Electricity Market

Before 1993	TEK			
1993-2003	TEAŞ		TEDAŞ	EPDK
2003-2015	TEİAŞ	EÜAŞ	TETAŞ	21 Dist. Co.	
After 2015	TEİAŞ	EÜAŞ	TETAŞ	21 Dist. Co.	EPİAŞ

Resources used in electricity generation in Turkey can be listed as Natural Gas, Hydroelectric, Coal (Domestic and Import), Wind, Solar, Geothermal, Biomass and Nuclear (in the near future) energy. These sources are used in generation facilities that supply energy to the system from different points of the national interconnection system. This actually means that different costs are created in different regions. At present, the installed capacity of Turkey is 80.000 MW and annual consumption is 285.000 GWh for the year 2017. The national electricity network has approximately 800 down-center (transformer center) and more than 60,000 km energy transmission lines. The distribution of these lines and transformer centers on the interconnected system is not homogeneous in the present case. For instance in Thrace and Western Anatolia, the density of industry is high but generation is low, consumption in Eastern Anatolia is very small, but energy generation is quite high. In addition to the many different reasons underlying this situation, one of the reasons is the applied electricity pricing methods.

With the new price tariffs that are introduced, different prices can be offered to the consumers according to the regions. Consumers will be able to obtain the electric energy more economically by determining the production resource type and location [12]. This will affect prices positively. As a side benefit, the electrification system of the country will become a homogeneous structure.

3. Pricing Algorithms

As pricing approaches; it can be said that there are three main approaches, namely, Price Based Pricing (PBP), Competitive Based Pricing (CBP) and Demand Based Pricing (DBP). PBP, can be divided into "cost plus" and "target price". The method which is calculated by calculating fixed costs and variable costs and adding the targeted profit ratio is called "cost plus". The pricing that is calculated by calculating the profit to be obtained in a certain sales volume is defined as "Target Pricing" [13-16]. CBP is divided into two parts as "Market Price Based" and "Tender Procedure". The method of determining its own price on the current price in the market is called "Market Price Based". It is known as the "Tender Procedure" or the closed envelope method, and the price is estimated without knowing the price of the rival. On the other hand, DBP is based on the methods of price determination according to customer, time, time and product. Due to the characteristic of electric energy and being the only product on the market, the PBP-based pricing approach is considered as the most appropriate method. Here, the price of the product should be determined taking into consideration any of the cost value, investment value and sales value. So, in general, the

method known as "Cost Plus" is chosen.

Energy resources are divided into renewable and non-renewable energy sources according to their use. According to its convertibility, it is divided into primary and secondary energy sources. Energy that is not converted to any energy is called primary energy. The energy obtained after the transformation of the primary energy is defined as secondary energy. Primary energy sources are oil, coal, natural gas, nuclear, hydraulics, biomass, wave, tide, sun and wind. Secondary energy sources are electricity, gasoline, diesel, coke, secondary coal, petroleum coke, air gas, liquefied petroleum gas (LPG). Renewable energy sources are energy resources which cannot be consumed in a natural cycle and which do not decrease [17-20]. Hydraulics, solar, wind, biomass and wave are sources of renewable energy. Non-renewable energy sources are energy sources that cannot renew themselves once they are used. Core energy sources such as oil, coal, natural gas and uranium, thorium are non-renewable energy sources.

As mentioned in the first section, there are different calculation methods for calculating the costs of production plants. The main determining factor here is the type of resource used by the plant. The cost of each plant depends on its own fuels, operation and plant costs. The average cost of electricity production of the most important sources in Turkey and percentage of production is shown in Table 2. The values given in this table were obtained from different studies prepared by the World Energy Council (WEC).

Table 2. Resources, Costs and Generation Contribution Rates.

Type	FIC (TL/kW)	FOC (TL/kW-year)	VOC (TL/kWh)	PTP (%)
Coal	16.362	189,45	20,7	144,9
Natural Gas	4.401	49,5	15,75	161,1
Nuclear	26.752,5	451,26	10,35	-
Wind	8.446,5	178,65	-	27,9
Solar	12.019,5	105,3	-	-
Biomass	22.432,5	495	18,9	3,6
Hydro	13.212	63,59	-	104,85
Geothermal	7.038	83,7	10,8	7,65
FIC: First Investment Cost FOC: Fixed Operation Cost VOC: Variable Operation Cost PTP: Percentage of Total Production				

There are various calculation methods for calculating **the cost of the transmission system**. The costs associated with the transmission system are generally regarded as operating and maintenance costs of energy transmission lines and transformer centers. The most common pricing method that can be shown using these costs is "Investment Cost Based Pricing" (ICBP). This method is used in Turkey and many world countries [21-23]. When calculating the transmission cost, power losses are also taken into account, depending on the lengths and characteristics of the transmission lines.

4. Multi Stage Dynamic Programming

There are two main elements of the price list prepared for transmission system users. Production and transmission cost. Determination of Production Cost: Firstly, other production facilities connected to the reference bar should be identified. Then, the type and loading rates of the

resources used by these production facilities should be known (Table 3.). The load flow analysis data of the other plants in the rear will be included dynamically (with certain periods) in the calculations.

Table 3. Characteristic information of the plants in the sample bus bar system.

	Resource Type	Installed Power [MWe]	Offer Price [TL/MWh]	Production Amount [MW]	Capacity Factor (%)
1	Coal	400	216	400	88
2	HPP	1000	182	900	86
3	WPP	130	190	100	32
4	Nat. Gas	600	204	400	93
5	Coal	720	183	600	91
6	WPP	310	211	200	28
7	SPP	180	194	100	21
8	HPP	800	188	700	80
9	HPP	330	200	300	91
10	Nat. Gas	1000	199	800	96
11	Coal	550	201	300	83

Determination of transmission cost: Transmission lines and other transformer centers (lines with positive energy flow) in the transformer center to which the consumer is connected are determined. In addition to the production facilities in the bar, the costs of the loads coming from the other transformer center are included in the account like a production facility. In addition, the transmission cost is determined by considering the characteristic, cross-section, length of the connection lines (Table 4.). The transmission cost coefficient is obtained according to the loading rates of the connected energy transmission lines. In power transmission lines, the power losses to be calculated according to the load flow are also calculated. The cost of transmission lines and transformers installed by the transmission system operator will be included in the tariff locally [24-25].

Table 4. Characteristic information of energy transmission lines in the sample bus system.

Label	Conductor Cross-Section	Conductor Length	Load Flow	Constraint State
1-2	1272 MCM	43 km	200 MW	None
1-5	954 MCM	72 km	200 MW	None
1-4	1272 MCM	130 km	200 MW	None
1-6	2x1272 MCM	62 km	200 MW	None
6-5	954 MCM	29 km	100 MW	None
4-5	1000 mm^2 cable	12 km	300 MW	None
5-11	1272 MCM	64 km	100 MW	None
6-3	477 MCM	28 km	200 MW	None
3-2	1272 MCM	110 km	900 MW	None
3-7	795 MCM	96 km	500 MW	None
6-9	954 MCM	64 km	200 MW	None
9-11	477 MCM	43 km	100 MW	None
9-8	2x954 MCM	74 km	900 MW	None
8-7	1272 MCM	210 km	800 MW	None
8-10	2x1272 MCM	38 km	0 MW	Yes
9-10	954 MCM	57 km	100 MW	None

A small section of the transmission system can be considered to illustrate the operation of the design. It is seen here that the system is balanced in terms of loads and production facilities. This is because when the entire transmission system is taken into consideration, a balance state will be discussed. There are 11 bus bars and 16 energy transmission lines in the system part taken as a section here. There is 4900 MW of total production in the bus bars. The instantaneous load flow of this system also appears in Figure 1. A bus bar selected as reference and will be calculated price on this bus bar. According to the step-by-step solution technique of Dynamic Programming, stages are determined starting from the reference bus bar.
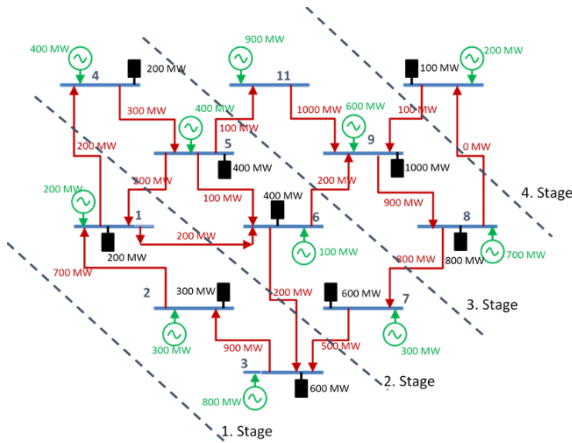

Figure 1. Balanced section of the interconnected system

The bar number 10 was chosen as the reference bar. From this point on, a four-stage calculation will be made. In the fourth stage, the reference bars own production and consumption (COPC) are calculated in Equation 1.

$$F_4(10) = COPC \ [TL/MWh]$$

$$COPC = CP_{TL} \div (TPP - TCP)_{MW} \ (per \ hour) \ [TL/MWh] \quad (1)$$

COPC: Cost of Production and Consumption

TPP: Total Production Power

TCP: Total Consumed Power

CP: Cost of Production

In the third stage; the costs of bars 9, 8 and 11 to the reference bar are calculated. Appropriate functions are written for the other bars in the generated steps. These functions are given in the equations 2,3 and 4.

$$F_3(9) = min \begin{cases} İ_{8-9} + F_3(8) \\ İ_{9-10} \ COPC \end{cases} \ [TL/MWh] \quad (2)$$

$$F_3(8) = İ_{8-10} \ COPC \ [TL/MWh] \quad (3)$$

$$F_3(11) = İ_{11-9} \ COPC + F_3(9) \ [TL/MWh] \quad (4)$$

In the second stage; costs of bars 7, 6, 5 and 4 are calculated on the way to the reference bar. These functions are given in the equations 5,6,7 and 8.

$$F_2(7) = İ_{7-8} COPC + F_3(8) \ [TL/MWh] \quad (5)$$

$$F_2(6) = min \begin{cases} İ_{6-9} \ COPC + F_3(9) \\ İ_{6-5} \ COPC + F_2(5) \end{cases} \ [TL/MWh] \quad (6)$$

$$F_2(5) = min \begin{cases} İ_{5-11} COPC + F_3(11) \\ İ_{5-6} COPC + F_2(6) \end{cases} \ [TL/MWh] \quad (7)$$

$$F_2(4) = İ_{4-5} \ COPC + F_2(5) \ [TL/MWh] \quad (8)$$

In the first stage; the costs of cars 3, 2 and 1 on the way to the reference bar are calculated. (Equations 9,10 and 11)

$$F_1(3) = min \begin{cases} İ_{3-7} \ COPC + F_3(7) \\ İ_{3-2} \ COPC + F_1(2) \\ İ_{3-6} \ COPC + F_2(6) \end{cases} \ [TL/MWh] \quad (9)$$

$$F_1(2) = min \begin{cases} İ_{2-3} COPC + F_1(3) \\ İ_{2-1} \ COPC + F_1(1) \end{cases} \ [TL/MWh] \quad (10)$$

$$F_1(1) = min \begin{cases} İ_{1-2} + F_1(2) \\ İ_{1-5} + F_2(5) \\ İ_{1-6} + F_2(6) \\ İ_{1-4} + F_2(4) \end{cases} \ [TL/MWh] \quad (11)$$

Same way, the similar functions are calculated for different stages selected towards the direction of the other bus bars to which the reference bus bar is connected. The price of the reference bus bar is determined by selecting the most economical one among the results obtained from all these functions.

A flow chart is used to create the steps shown above and to reveal the functions. The flow chart of the process followed to determine the tariff of the reference bus bar is given in Figure 2. In the flow chart, firstly the price targeted by the consumer needs to be determined. Since all the bus bars on the transmission system are numbered separately, the formulas are executed on these numbers. Then it will be determined which bus bar price to calculate (reference bar). Then production facilities and consumption facilities connected to the reference bus bar has been determined. Load Case Analysis for the total installed capacity, capacity factor, resource type and related period interval of the production facilities is revealed. Capacity information is also obtained for consumption facilities. Then, the energy transmission lines connected to this bar and the length of these lines,

cross section (if section changes), transport capacities and limit conditions of the line are determined.
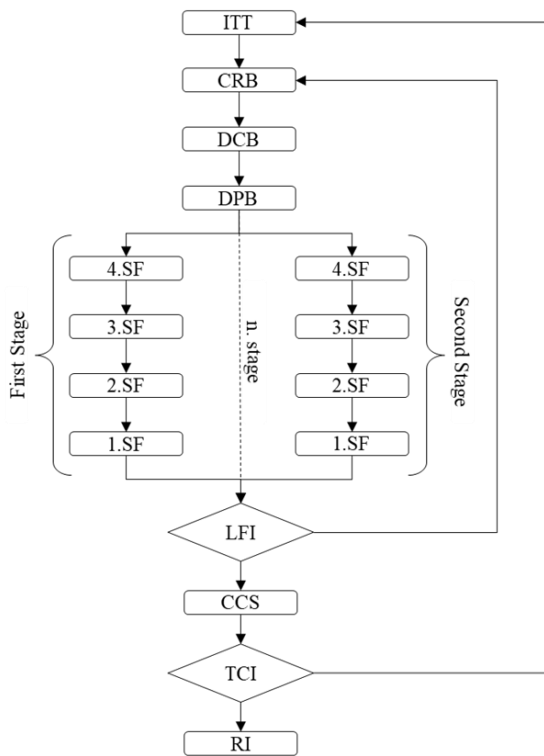

Figure 2. Multi Stage Dynamic Programming Algorithm Flowchart

After this phase, the first stage path is determined backward from the relevant bar. First, the bus bar closest to the reference bus bar, then the other bus bar connected to this bus is identified. This is continued until the fourth stage. At the same time, considering the other bar that is connected to the reference bar, it moves again to the fourth step in a different direction. After all stages are completed on all possible routes, the calculations obtained are compared. Before determining the most advantageous stage path, it is checked whether there are any restrictions on the load flow and the characteristics of the line. If there are constraints, the calculations are repeated in a way that this constraint permits. If there is no constraint or is included in the calculations, the pricing formulas are reached [26-28]. After this phase, the actual values obtained for the production facility and the values from the tariffs for the transmission lines are written in the formulas to obtain the optimum energy price for the reference bar.

The details of the process at each step of the flow chart can be explained as follows:

1. **I**dentification of **T**arget **T**ariffs: Calculation of the price the user expect to connect the system
2. **C**hoice **R**eference **B**ar: Selection of the Reference Bar
3. **D**etermination of **C**onsumers in the **B**ar: Calculation of usage capacity of other consumers in bar
4. **D**etermination of **P**roducers in the **B**ar: Calculation of installed capacity of other producers in bar
5. n. **S**tage **F**unctions: Determination of stages and obtaining functions for each stage. (For each direction)

6. **L**oad **F**low **I**nquiry: If available Y, If not available N: Checking the suitability of the connection for load flow.
7. **C**ost **C**alculation for **S**ource: Calculation of electricity cost according to source type
8. **T**arget **C**ost **I**nquiry: Comparison of targeted and obtained price: If target price is less than cost Y, target price is greater than cost N.
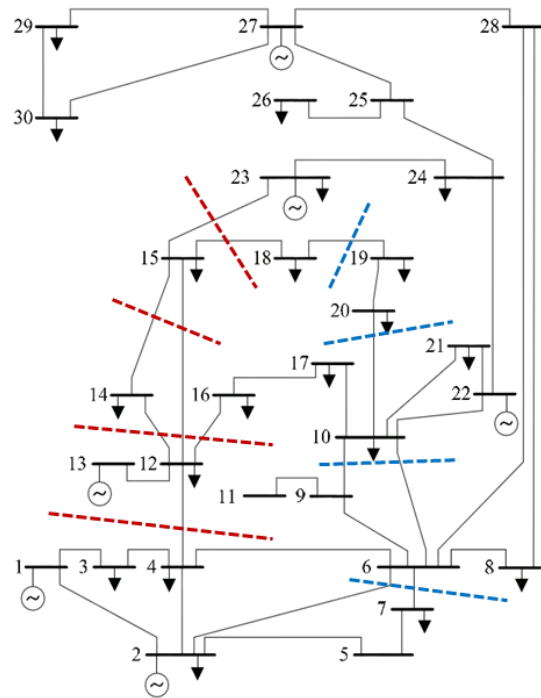9. **R**ealization of **I**nvestment

Figure 3. IEEE-30 (RTS) Bus Test System

The proposed pricing model has been tested on the IEEE-30 bar test system. Accordingly, the price function will be obtained for the bar number 18 selected as the reference bar. As shown in Figure 3, the MSDP model is run with the specified steps towards different routes. The final results of the obtained functions and the final prices are given in Table 5. There are also prices obtained from Balanced System Section (BSS) on the same Table. A comparison was made between the average price obtained from the current pricing method and the prices found. The error rate is shown in the same table. Accordingly, it can be said that the MSDP model offers more favorable prices for selected reference bus bars than the current situation.

Table 5. Comparison of the results of the MSDP model.

		MSDP [TL/MWh]	CPM [TL/MWh]	MAPE (%)
IEEE-30 RTS	First Stage	60.13		
	Second Stage	94.98		
	Third Stage	137.83		
	Fourth Stage	209.61	231.43	9.42
BSS	First Stage	53.76		
	Second Stage	86.12		
	Third Stage	138.28		
	Fourth Stage	190.54	211.91	10,08

5. Conclusions

There are many different pricing methods for transmission system users. Some of them accept the system as a whole and perform calculations accordingly. Some of them make different tariffs by dividing them into regions (Regional Pricing). Another approach is to calculate a separate price for each bus bar (Nodal Pricing). In this study, a different and new approach to the nodal pricing method has been introduced. Price calculation has been done according to production source type which was not taken into account in the literature before. Another innovation introduced is; it has been tried to achieve optimum functions by creating multiple stages in dynamic programming. The prices obtained from this new method, called Multi-Stage Dynamic Programming (MSDP), are compared with the prices obtained from the Conventional Pricing Model (CPM). For this comparison, a Balanced System Section (BSS) and IEEE-30 test system was used for the interconnected system.

According to the obtained data, the proposed method provides more realistic and economic prices for the users of the transmission system on a bus bar basis. With this new method, about 10% lower prices can be obtained for the users of the transmission system than the prices calculated by the conventional method. This new price tag, which is achieved without change in the total revenue cap, is expected to provide considerable advantages for users. The MSDP method, which is advantageous for transmission system users, will also ensure that the transmission system becomes homogeneous in the long run.

References

1. Ahmadi, H. and Akbari Foroud, A., A stochastic framework for reactive power procurement market, based on nodal price model, International Journal of Electrical Power & Energy Systems, 2013. 49: 104-113.

2. Azad-Farsani, E., Agah, S. M. M., Askarian-Abyaneh, H., Abedi, M. and Hosseinian, S. H., Stochastic LMP (Locational marginal price) calculation method in distribution systems to minimize loss and emission based on Shapley value and two-point estimate method, Energy, 2016. 107: 396-408.

3. Azad-Farsani, E., Loss minimization in distribution systems based on LMP calculation using honey bee mating optimization and point estimate method, Energy, 2017. 140: 1-9.

4. Baghayipour, M., Akbari Foroud, A. and Soofiabadi, A., A comprehensive fair nodal pricing scheme, considering participants' efficiencies and their rational shares of total cost of transmission losses, International Journal of Electrical Power & Energy Systems, 2014. 63: 30-43.

5. Bjørndal, E., Bjørndal, M., Cai, H. and Panos, E., Hybrid pricing in a coupled European power market with more wind power, European Journal of Operational Research, 2018. 264(3): 919-931.

6. Dourbois, G. A. and Biskas, P. N., A nodal-based security-constrained day-ahead market clearing model incorporating multi-period products, Electric Power Systems Research, 2016. 141: 124-136.

7. Egerer, J., Weibezahn, J. and Hermann, H., Two price zones for the German electricity market — Market implications and distributional effects, Energy Economics, 2016. 59: 365-381.

8. Ghasemi, A., Mortazavi, S. S. and Mashhour, E., Integration of nodal hourly pricing in day-ahead SDC (smart distribution company) optimization framework to effectively activate demand response, Energy, 2015. 86: 649-660.

9. Gianfreda, A. and Grossi, L., Forecasting Italian electricity zonal prices with exogenous variables, Energy Economics, 2012. 34 (6): 2228-2239.

10. Goel, L., Wu, Q. and Wang, P., Nodal price volatility reduction and reliability enhancement of restructured power systems considering demand–price elasticity, Electric Power Systems Research, 2008. 78(10): 1655-1663.

11. Gökgöz, F. and Atmaca, M. E., Financial optimization in the Turkish electricity market: Markowitz's mean-variance approach, Renewable and Sustainable Energy Reviews, 2012. 16(1): 357-368.

12. Jokić, A., Lazar, M. and van den Bosch, P. P. J., Real-time control of power systems using nodal prices, International Journal of Electrical Power & Energy Systems, 2009. 31(9): 522-530.

13. Kaleta, M., 2016, A generalized class of locational pricing mechanisms for the electricity markets, Energy Economics.

14. Kang, C. Q., Chen, Q. X., Lin, W. M., Hong, Y. R., Xia, Q., Chen, Z. X., Wu, Y. and Xin, J. B., Zonal marginal pricing approach based on sequential network partition and congestion contribution identification, International Journal of Electrical Power & Energy Systems, 2013. 51: 321-328.

15. Kia, M., Setayesh Nazar, M., Sepasian, M. S., Heidari, A. and Sharaf, A. M., Coordination of heat and power scheduling in micro-grid considering inter-zonal power exchanges, Energy, 2017. 141: 519-536.

16. Kristiansen, T., Comparison of transmission pricing models, International Journal of Electrical Power & Energy Systems, 2011. 33(4): 947-953.

17. Kumar, M., Kumar, A. and Sandhu, K. S., Impact of distributed generation on nodal prices in hybrid electricity market, Materials Today: Proceedings, 2018. 5(1): 830-840.

18. López-Lezama, J. M., Contreras, J. and Padilha-Feltrin, A., Location and contract pricing of distributed generation using a genetic algorithm, International Journal of Electrical Power & Energy Systems, 2012. 36(1): 117-126.

19. Lorca, Á. and Prina, J., Power portfolio optimization considering locational electricity prices and risk management, Electric Power Systems Research, 2014. 109: 80-89.

20. Murphy, F. H., Mudrageda, M., Soyster, A. L., Sarić, A. T. and Stanković, A. M., The effect of contingency analysis on the nodal prices in the day-ahead market, Energy Policy, 2010. 38(1): 141-150.

21. Polisetti, K. and Kumar, A., Distribution System Nodal Prices Determination for Realistic ZIP and Seasonal

Loads: An Optimal Power Flow Approach, Procedia Technology, 2016. 25: 702-709.

22. Ruiyou Zhang, Dingwei Wang and Yun, W. Y., Power-Grid-Partitioning Model and its Tabu-Search-Embedded Algorithm for Zonal Pricing. Proceedings of the 17th World Congress The International Federation of Automatic Control. Seoul, 2018. Korea,: 15928-15932.

23. Sahraei-Ardakani, M., Blumsack, S. and Kleit, A., Estimating zonal electricity supply curves in transmission-constrained electricity markets, Energy, 2015. 80: 10-19.

24. Singh, R. K. and Goswami, S. K., Optimum allocation of distributed generations based on nodal pricing for profit, loss reduction, and voltage improvement including voltage rise issue, International Journal of Electrical Power & Energy Systems, 2010. 32(6): 637-644.

25. Sleisz, Á. and Raisz, D., Integrated mathematical model for uniform purchase prices on multi-zonal power exchanges, Electric Power Systems Research, 2017. 147: 10-21.

26. Tranberg, B., Schwenk-Nebbe, L. J., Schäfer, M., Hörsch, J. and Greiner, M., Flow-based nodal cost allocation in a heterogeneous highly renewable European electricity network, Energy, 2018. 150: 122-133.

27. Weibelzahl, M. and Märtz, A., On the effects of storage facilities on optimal zonal pricing in electricity markets, Energy Policy, 2018. 113: 778-794.

28. Zenón, E. and Rosellón, J., Optimal transmission planning under the Mexican new electricity market, Energy Policy, 2017. 104: 349-360.

Research Article

Broadband Wilkinson power divider based on chebyshev impedance transform method

*Ömer Kasar [a], Mahmut Ahmet Gözel [b] and Mesud Kahriman [b],**

[a]*Artvin Çoruh University, Engineering Faculty, Electrical and Electronics Engineering, Artvin, 08100, Turkey*
[b]*Suleyman Demirel University, Engineering Faculty, Electronics and Telecommunication Engineering, Isparta, 32260, Turkey*

ARTICLE INFO	ABSTRACT
	Broadband impedance matching techniques widely used in microwave circuits. In this study, we proposed a 2-way multi-layer micro strip Wilkinson Power Divider (WPD) circuit matched by Chebyshev İmpedance matching technique. The design was chosen at 1 GHz center frequency and as four layers. The design was carried out as 3 dimensions on Advanced Design tool (ADS 2009) which is 3D microwave circuits' simulation tool. For -20 dB return loss reference level, while the reflection bandwidth was 25% in the basic quarter wave matched WPD, it could be increased up to 132% in the Chebyshev matching. Additionally, for the reference power transmission of -4.3 dB, the transmission bandwidth raised up to %160. In the range, the proposed design could transfer 75% of the input power to both output ports.

1. Introduction

Maximum power transmission problem is one of most important parameter characterizing basic circuits or systems properties in electronics [1]. In a circuit, the level of power transmission indicates the operating efficiency of the circuit [2-5].

Impedance matching is named as balancing of an electromagnetic (EM) wave propagation between load and transmission line impedance [3, 6]. At the microwave (MW) circuits, the matched situation must exist in the inter-sections of all transmission lines. Otherwise, some problems such as standing wave and unintended physical defections may occur [7-9].

Actually, the impedance matching is a maximum power transmission (MPT) problem [2]. There are various MPT technics in literature. Each of them has contributed many novelties. One of these technics is multi-layer matching. In this technic, it is possible to build broad band circuits. Contrary to lumped elements and single section (quarter wave) matching, multi-layer (section) matching can obtain wider frequency interval. That means the less reflection between source and load

[10, 11]. Thus, at microwave frequencies, a better power transmission can be achieved [12].

There are a lot of studies in the literature focusing on eliminating the impedance mismatching between the branches of WPD. There are also studies attempting to obtain broader bandwidth and less reflection over the WPDs by the impedance matching techniques [13]. Those studies have developed power transfer through different mathematical distributions and equations [14, 15]. In addition to these, studies that succeed the high power transmission with the help of Microwave circuit analysis applications are increasing day by day[16, 17].

In this study, it was aimed to eliminate mismatching between the input and output ports of the WPDs. Furthermore, four section Chebyshev polynomials matching technic was used. For 1GHz center frequency, reflection (S11) and transmission (S21 and S31) parameters were evaluated by using Chebyshev impedance matching method. As design tool, the Advanced Design System (ADS 2009) which is 3D EM simulation program was preferred.

* Corresponding author. Tel.: *+0 246 211 1371*;
E-mail address: *omerkasar@artvin.edu.tr (O. Kasar), mahmutgozel@sdu.edu.tr (M.A. Gözel), mesudkahriman@sdu.edu.tr (M. Kahriman).*

2. Power divider technic and theoretical impedance matching approach

2.1 The Power Divider Technic

In microwave circuits, the basic problem of T-junctions is that all ports do not have impedance matching [18]. Wilkinson Power Divider (WPD) was developed to eliminate this mismatching. WPD circuits split the power transmitted through the lossless transmission lines equally into two or more ports without loss [19].

In the microwave circuits, power transmission is stated as logarithmic (dB) units. Over both output ports of WPD, half of the input power is delivered [20]. Ideally, in lossless environment, transferred power in a branch is 50 percent and means -3 dB of power. In fact, real lines have minor loss. If the loss is very little, then the delivered power will be closer to -3 dB levels [21].

In WPDs, input transmission line has Z_0 and each output ports have $2Z_0$ characteristic line impedance. Therefore, a mismatching situation is observed between input and output ports. One of the solutions is a general method known as single section (quarter wave) matching. Technically, a single section line with $Z = \sqrt{2}Z_0$ of characteristic and $\theta = \beta l = \lambda/4$ line length is added between T-junction point and output port [21]. General schematic view of WPD is shown in Figure 1 where wl1=2.9 mm (50 Ω), wl2=1.55 mm (70.7 Ω). Since it was cheap and readily available, FR4 whose permittivity was $\varepsilon_r = 4.3$ and loss tangent was tand=0.025 was chosen as substrate material. The effective relative permittivity of FR4 is $\varepsilon_{eff} = 3.26$. At the center frequency of 1GHz, the quarter wave length was computed as $\lambda/4 = 41mm$.
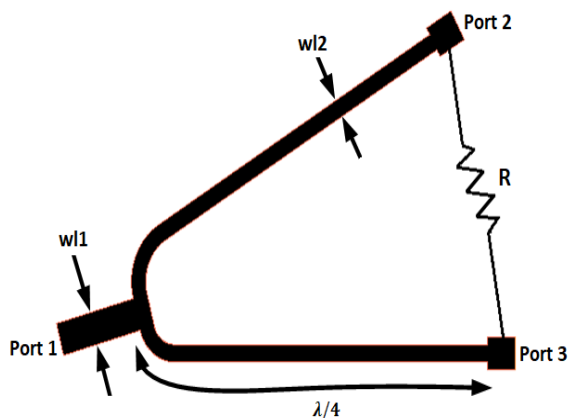

Figure 1. General schematic view of WPD

In order for the Wilkinson power divider to be able to transmit power without loss, mode analysis should be performed. In the theoretical even-odd mode calculation, the resistance at the output is determined as R=100 Ω.

Thus, 50 Ω output impedance and -3 dB of input power will be obtained at ports 2 and 3 [18,20, 22].

2.2 Chebyshev Matching Approach

In the literature, there are a lot of methods for modelling multi-layer impedance matching. One of the most used modelling techniques is Chebyshev transform [3, 4]. In this technique, while calculating each matching section, Chebyshev polynomials are used. General equations of Chebyshev Polynomials are given in equation 1 [3, 10].

$$T_n(x) = 2xT_{n-1}(x) - T_{n-2}(x) \qquad (1)$$

As in multi-layer matching, each step of the Chebyshev transform depends on previous one since all steps are calculated sequentially. One disadvantage of this technique is fluctuation on the pass band frequencies. However, comparing with single section and some other multi-layer matching methods, Chebyshev Transform is a design from which more performance can be obtained [3]. In Figure 2, there is a comparison of reflection graphic between single section (quarterwave) and four-section (N=4) Chebyshev transform. It is seen obviously that despite of fluctuations, Chebyshev Transform is better than single section matching.
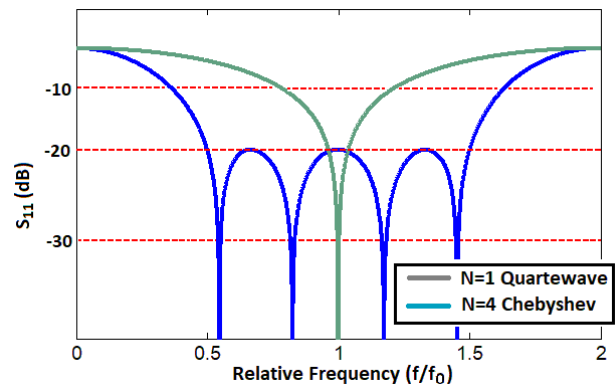

Figure 2. Comparison of reflection graphic between single section (quarter wave) and four-section (N=4) Chebyshev transform

Modelling of Chebyshev Polynomials to impedance matching is given in equation 2 [3].

$$T_N(sec\theta_m) = \frac{1}{\Gamma_m}\left|\frac{Z_L - Z_0}{Z_L + Z_0}\right| \approx \frac{1}{2\Gamma_m}\left|\ln\frac{Z_L}{Z_0}\right| \qquad (2)$$

where, θ is line angle $\beta\ell$, θ_m is an angle obtained for maximum tolerable reflection coefficient Γ_m. As shown in equation 3, generally N^{th} degree of Chebyshev polynomial($T_N(sec\theta)$) is obtained by adapting to reflection coefficient.

$$\Gamma(\theta) = A.e^{-jN\theta}T_N(\sec\theta_m\cos\theta) \qquad (3)$$

where A is design factor and calculated for each section as in equation 4 [3].

$$A = \frac{Z_1-Z_0}{Z_1+Z_0}\frac{1}{T_N(\sec\theta_m)} \qquad (4)$$

In this study, impedance mismatching of each branch of WPDs' output ports ($2Z_0 = 100\ \Omega$) was attempted to eliminate by proposed method. It was decided that the number of section was 4 (N=4) and maximum tolerable reflection coefficient was selected as $\Gamma_m = 0.01 = -20\ dB$ because of minimum mismatching loss.

3. Proposed Design

In this study, two-way WPD whose each branch was matched with Chebyshev design was proposed. The dielectric material thickness of FR4 was $d = 1.5\ mm$. Lower and upper cover of the substrate was copper where the thickness was $t = 0.035\ mm$. The upper micro strip base was the place where the design was built. The substrate dimensions were $L = 100\ mm$ and $W = 80\ mm$. In Figure 3, perspective (upper) and cross section view (under) of the design are shown.
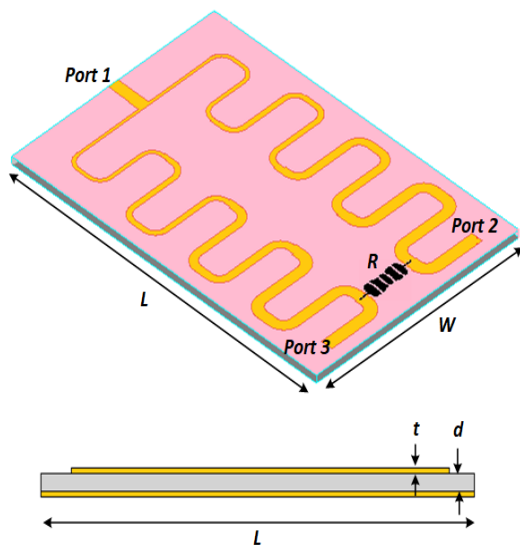

Figure 3. Perspective (upper) and cross sectional view (under) of the design

Lengths and inner dimensions of WPD are shown in Figure 4. Here, each length of sections are equal and they are $\theta = \lambda/4 = 41\ mm$. Thickness of each layer was computed according to Chebyshev method ($\Gamma_m = 0.01 = -20\ dB$). It was also calculated as $wl1 = 2.9\ mm$ (50 Ω), $wl3 = 0.89\ mm$ (90.15 Ω), $wl4 = 1.3\ mm$ (77 Ω), $wl5 = 1.93\ mm$ (63.3 Ω), $wl6 = 2.55\ mm$ (54.08 Ω). The second and third ports was

terminated at $wl1 = 2.9\ mm$ (50 Ω) thickness. Between these two ports, there was a resistor $R = 100\ \Omega$ due to theoretically analysis.

To avoid the circuit being too long, the matching lines were bended till terminals. Therefore, it was determined as $l1 = 12.6\ mm$, $l2 = 11\ mm$ and $l3 = 3\ mm$. Thus, each length of line was equalized to $\lambda/4$.
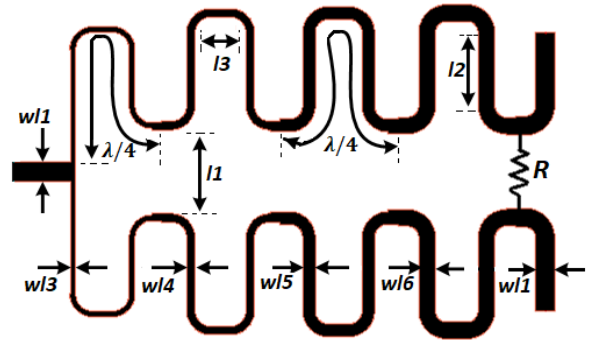

Figure 4. Lenghts and inner dimensions of power divider circuit

4. Results

The reflection in the input port of the designed power divider circuit has improved compared to the single section. In Figure 5, comparison between quarter wave and Chebyshev design of input reflection (S_{11}) graphic was seen. As chosen input reflection level was smaller than $S_{11} < -20\ dB$; while single section was 0.9-1.3 GHz band width, the Chebyshev design showed 0.350-1.67 GHz performance. The formula of percentage of bandwidth is given in equation 5 [3].

$$BW\% = \frac{f_U-f_L}{f_0} \qquad (5)$$

where, BW% is percentage of bandwidth, f_U is the upper band and f_L is the lower band and f_0 is the center frequency of 1 GHz.

While the percentage of bandwidth in the quarter wave matching is 25%, it shows 132% BW performance in the Chebyshev Design.
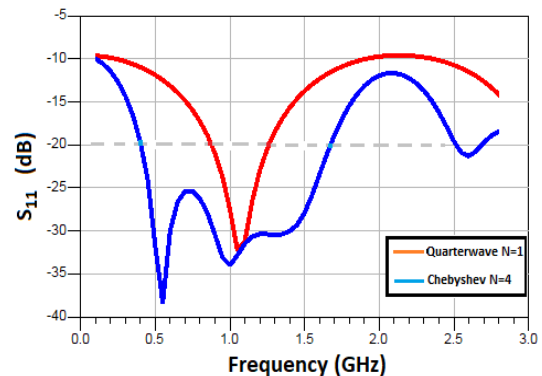

Figure 5. Comparison between quarter wave and Chebyshev design of input reflection (S$_{11}$) graphic

In a power divider circuit, one of the most important parameters is power transmission line coefficient (S_{21} and S_{31}). In Figure 6, a comparison about logarithmic power transmission characteristic between quarter wave and Chebyshev design is shown. In a symmetrical circuit with respect to the input port, output power of second and third port are identical. If the reference level is accepted as $S_{21} = S_{31} > -4.3$ dB, the transmission frequencies will be between 0.1 and 1.7 GHz. Then the percentage of transmission bandwidth would be %160 and it could be said that the method is successful on the matching. The logarithmic and percentage conversion of power transmission is given in equation (6) [3].

Ultimately, in the interval of bandwidth, 37.5% power transfer can be performed to each port. Therefore, it means that the Chebyshev matched multi-layer WPD could transfer 75% of the input power to both output ports.

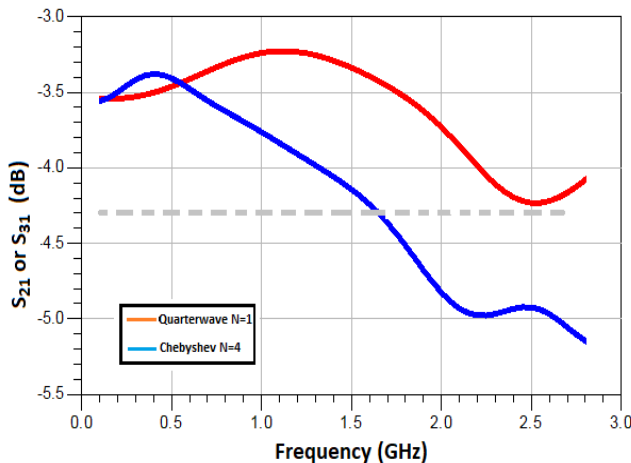$$P \% = \frac{10^{P\,(dB)}}{10} \times 100 \qquad (6)$$

Figure 6. Compared logarithmic transmission graphics of quarterwave and Chebyshev design

5. Conclusion

In the study, the impedance was matched through WPD Chebyshev Impedance matching technique. The proposed design was compared with the quarter wave technique in the literature. For -20 dB return loss reference level; while basic WPD (quarter wave matched) bandwidth was 25%, the Chebyshev matched WPD's bandwidth reached 132%. In addition, the proposed design could transfer 75% of input power to both output ports in the range where the transmission power level is -4.3 dB and the transmission bandwidth (BW) became %160. Regarding the reference studies presented in Table 1, it can be said that this study conforms to the literature and contributes to the recent studies.

Table 1. Comparison of this study with the reference studies

Ref.	Method	Freq (GHz)	S_{11} Ref. Level (dB)	S_{11} BW (%)	S_{21} Ref. Level (dB)	S_{21} BW (%)
[16]	Non Uniform Transm. Line	1.25	-10	56	-4.25	24
[13]	Stub Matching	1 - 2	-20	4	-3.5	22
[15]	Z Polinomials	0.7- 2	-20	60 66	-3.22 max	-
[17]	Gysel Power Divider	1.5	-18	92	1,92 max	-
[14]	Analytically Compensated	9	-10	160	-4.5	77
This Study	Chebyshev	1	-20	132	-4.3	160

As expected, the obtained results indicate that proposed design enables the power division/transmission in a wider frequency range. This study showed that power divider circuit can be designed with broadband Microwave impedance matching techniques. Besides, obtained results conform to the literature about Chebyshev broadband impedance transform studies.

References

1. Garg, R., *Microstrip antenna design handbook* 2001: Artech House.
2. Yarman, B.S., *Design of ultra wideband power transfer networks* 2010: John Wiley & Sons.
3. Pozar, D.M., *Microwave Engineering 3e*. 3rd ed 2005, USA: John Wiley & Sons,Inc.
4. Balanis, C.A., *Antenna theory: analysis and design*. Vol. 1. 2005: John Wiley & Sons.
5. Kumar, G. and K. Ray, *Broadband microstrip antennas* 2002: Artech House.
6. Caron, W.N., *Antenna impedance matching* 1993: American radio relay league.
7. Yarman, B.S., *Design of ultra wideband antenna matching networks: via simplified real frequency technique* 2008: Springer Science & Business Media.
8. Khan, A.S., *Microwave engineering: Concepts and fundamentals* 2014: CRC Press.
9. Guha, D. and Y.M. Antar, *Microstrip and printed antennas: new trends, techniques and applications* 2011: John Wiley & Sons.
10. Antoniades, M.A. and G.V. Eleftheriades, *A broadband series power divider using zero-degree metamaterial phase-shifting lines*. Ieee Microwave and Wireless Components Letters, 2005. **15**(11): p. 808-810.
11. Gai, C., et al., *Dual band gysel power divider with high power dividing ratio*. Microwave and Optical Technology Letters, 2017. **59**(10): p. 2428-2431.
12. Cheng, K.K.M. and C. Law, *A novel approach to the design and implementation of dual-band power*

divider. Ieee Transactions on Microwave Theory and Techniques, 2008. **56**(2): p. 487-492.

13. Cheng, K.-K.M. and C. Law, *A novel approach to the design and implementation of dual-band power divider.* IEEE Transactions on Microwave Theory and Techniques, 2008. **56**(2): p. 487-492.

14. Uchendu, I.E. and J.R. Kelly, *Ultrawide isolation bandwidth compensated power divider for UWB applications.* Microwave and Optical Technology Letters, 2017. **59**(12): p. 3177-3180.

15. Kim, J. and Y. Lee, *A ${Z} $-Transform Method for Synthesis of Unequal-Length Multisection Transmission Lines for Multiband Applications.* IEEE Transactions on Microwave Theory and Techniques, 2017. **65**(9): p. 3200-3210.

16. Hawatmeh, D., N. Dib, and K. Alshamaileh, *Microstrip Non-uniform Transmission Lines Triple Band 3-way Unequal Split Wilkinson Power Divider.* Revue Roumaine Des Sciences Techniques-Serie Electrotechnique Et Energetique, 2017. **62**(3): p. 288-293.

17. Gharehaghaji, H.S. and H. Shamsi, *Design of unequal dual band Gysel power divider with isolation bandwidth improvement.* IEEE Microw. Wireless Compon. Lett, 2017. **27**: p. 138-140.

18. Scardelletti, M.C., G.E. Ponchak, and T.M. Weller, *Miniaturized Wilkinson power dividers utilizing capacitive loading.* Ieee Microwave and Wireless Components Letters, 2002. **12**(1): p. 6-8.

19. Minin, I.V., *Microwave and Millimeter Wave Technologies Modern UWB antennas and equipment*2010: Sciyo. com.

20. Chen, W.-K. and T. Chaisrakeo, *Explicit formulas for the synthesis of optimum bandpass Butterworth and Chebyshev impedance-matching networks.* IEEE Transactions on Circuits and Systems, 1980. **27**(10): p. 928-942.

21. Lim, J.S., et al., *A 4 : 1 unequal Wilkinson power divider.* Ieee Microwave and Wireless Components Letters, 2001. **11**(3): p. 124-126.

22. Wu, L., et al., *A dual-frequency Wilkinson power divider.* Ieee Transactions on Microwave Theory and Techniques, 2006. **54**(1): p. 278-284.

Research Article

An implementation of chaotic circuits with Multisim-LabVIEW

Gülden Günay Bulut [a], M. Emin Şahin [b]*, Hasan Güler [a] [b]

[a] *Nevsehir Hacı Bektas Veli University, Nevsehir, Turkey*
[b] *Fırat University, Elazig, Turkey*

ARTICLE INFO	ABSTRACT
	In last decades, chaos phenomenon and chaotic systems are defined as a nonlinear behavior have received a plenty of attention. In many areas, a chaotic system is used due to chaotic signals depend very sensitively on initial conditions, have unpredictable features and noise like wideband spread spectrum. In literature as well as the basic chaotic systems, there are many hybrid chaotic systems. In this paper, Sprott case A chaotic system is formed by using OP-AMPS and other appropriate circuit components on Multisim environment. This model is being constructed for each chaotic system, so the results of mathematical simulations of these chaotic differential equations can be seen. Convenient chaotic behavior is observed, circuit simulation is conducted via co-simulation between Multisim and LabVIEW. The simulation results show similar behavior when it is compared with the theoretical chaotic system.

1. Introduction

Chaos word, which is the subject of academic studies, can be defined as the arrangements in non-linearity of non-linear systems. Chaotic systems can be described as systems that are very sensitive to initial conditions, exhibit non-periodic behaviors, and have complexity which cannot be measured. In addition to sensitivity to initial conditions, chaotic systems have a broadband noise-like and periodic structure

The term chaos was first used by Henri Poincaré during the dissolution of three-body problem raised in 1889. [1] Ed Lorenz who is an American mathematician and meteorologists expressed chaotic behaviour with differential equations for the first time [2]. In practice, the first real physical dynamic system similar to the Lorenz system was created by Chua [3]. The Chua's circuit is a simple autonomous third level circuit that exhibits dynamic behavior. Following these studies, scientists such as Chen, Rössler, Sprott, Van Der Pol, Rucklidge, Lü formed their own chaotic systems [4-9]. After these studies, many chaotic novels and hyper-chaotic systems which display different dynamical behaviours have took place in literature [10-16].

Chaos theory and chaotic systems have attracted the interest of academic community in the fields of theoretical research and practical application. It has been used in applications ranging from weather prediction to computer science, economics, geology, robotics, physics etc. [17]. Chaotic systems have many applications. Examples of application areas of chaotic systems in daily life include oscillation control of chemical reactions, measurement of heart rhythm, examination of brain waves, biomedical and medical applications, secure communication using chaotic signals, internet banking, increase of laser power, power electronics, image compression and transmission, turbulence controversy, chaotic masking, weather forecasts, chaotic modulation, pattern recognition, random number generators, population projection studies, polymer production, protein production of bacterial colonies, etc [18].

In this study, Sprott case A, case B and case C chaotic system is created with using OP-AMPS and appropriate circuit opponents in Multisim environment. Then the systems are designed with LabVIEW control&simulation toolbox. Chaotic behaviour is observed and real-time circuit simulation is conducted via Multisim-LabVIEW platform simulation. The results are compared with theoretical Sprott system and observed similar behaviour.

* Corresponding author.
E-mail addresses: ggunaybulut@nevsehir.edu.tr (G. G. Bulut), memnshn@gmail.com (M.E. Şahin), hasanguler@firat.edu.tr (H. Güler).

2. Method

2.1 Sprott Chaotic System

J.C Sprott, introduced nineteen simple systems with a few terms which show similar dynamical behaviour to the traditional Lorenz, Rossler and Chua systems [19-20]. Among these systems, while equations A to E have 5 terms in total, F-S equations have 6 terms.

$$\dot{X} = a + \sum_{i=1}^{3} b_i + X_i + \sum_{i=1}^{3}\sum_{j=1}^{3} c_{ij} X_i X_j \qquad (1)$$

Sprott accepted that the second-order nonlinear three-dimensional ordinary differential equations are in the form given in (1). Here, X = (x, y, z) is the real three-dimensional state variables, and a, b, and c are real three-dimensional coefficients.

A	B	C	D	E	F
$\dot{x}=y$	$\dot{x}=yz$	$\dot{x}=yz$	$\dot{x}=-y$	$\dot{x}=yz$	$\dot{x}=y+z$
$\dot{y}=-x+yz$	$\dot{y}=x-y$	$\dot{y}=x-y$	$\dot{y}=x+z$	$\dot{y}=x^2-y$	$\dot{y}=-x+0.5y$
$\dot{z}=1-y^2$	$\dot{z}=1-xy$	$\dot{z}=1-x^2$	$\dot{z}=xz+3y^2$	$\dot{z}=1-4x$	$\dot{z}=x^2-z$

G	H	I	J	K	L
$\dot{x}=0.4x+z$	$\dot{x}=-y+z^2$	$\dot{x}=-0.2y$	$\dot{x}=2z$	$\dot{x}=xy-z$	$\dot{x}=y+3.9z$
$\dot{y}=xz-y$	$\dot{y}=x+0.5y$	$\dot{y}=x+z$	$\dot{y}=-2y+z$	$\dot{y}=x-y$	$\dot{y}=0.9x^2-y$
$\dot{z}=-x+y$	$\dot{z}=x-z$	$\dot{z}=x+y^2-z$	$\dot{z}=-x+y+y^2$	$\dot{z}=x+0.3z$	$\dot{z}=1-x$

M	N	O	P	Q	
$\dot{x}=-z$	$\dot{x}=-2y$	$\dot{x}=y$	$\dot{x}=2.7y+z$	$\dot{x}=-z$	
$\dot{y}=-x^2-y$	$\dot{y}=x+z^2$	$\dot{y}=x-z$	$\dot{y}=-x+y^2$	$\dot{y}=x-y$	
$\dot{z}=1.7+1.7x+y$	$\dot{z}=1+y-2z$	$\dot{z}=x+xz+2.7y$	$\dot{z}=x+y$	$\dot{z}=3.1x+y^2+0.5z$	

R	S				
$\dot{x}=0.9-y$	$\dot{x}=-x-4y$				
$\dot{y}=0.4+z$	$\dot{y}=x+z^2$				
$\dot{z}=xy-z$	$\dot{z}=1+x$				

Figure 1. Sprott System Equations[21]

Chaotic results are obtained when X_0=0.05, Y_0=0.05, Z_0=0.05 are taken as the initial condition for the equations except for the equation A. The initial conditions for the case A are X_0=0, Y_0=0.5, Z_0=0 .If the Sprott chaotic system is examined, it appears that there are separate attractors for each equation case. Change of state variables over time and chaotic attractors for Sprott A, and B systems are shown in Fig.2, 3, 4, 5 [21].
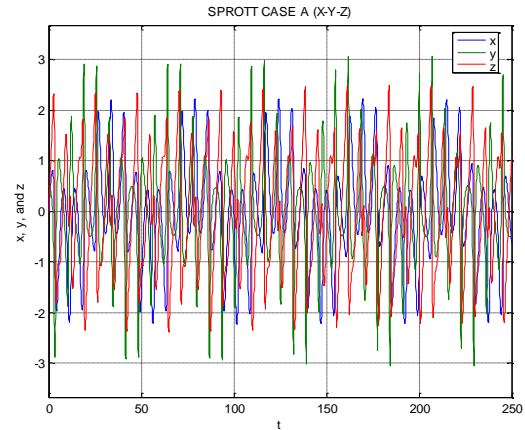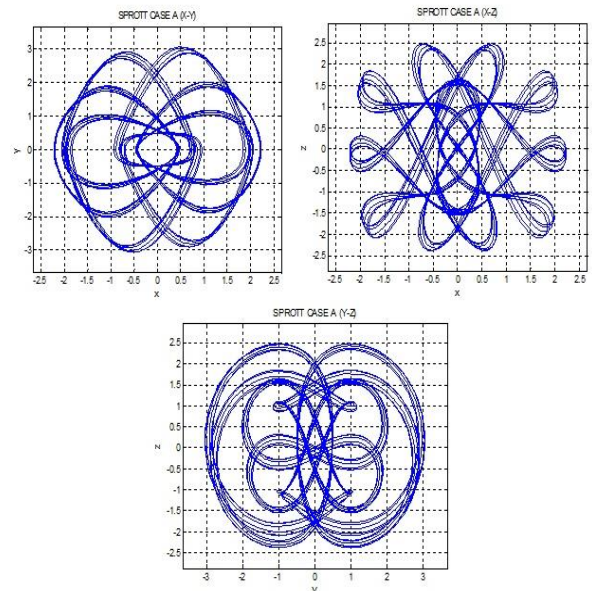

Figure 2. Sprott Case A(nose-hoover system)

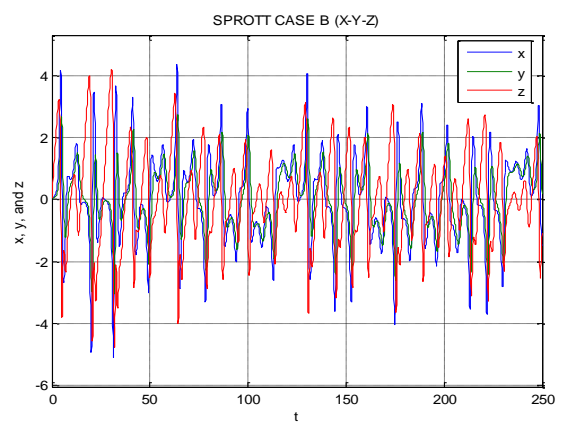Figure 3. Sprott Case A Chaotic Attractors
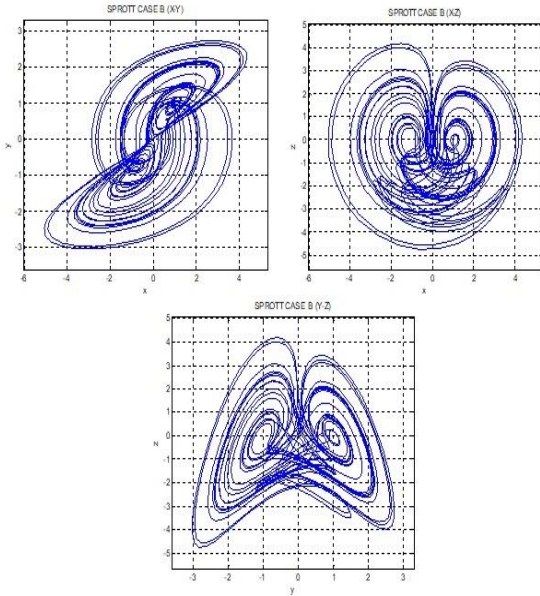

Figure 4. Sprott Case B

Figure 5. Sprott Case B Chaotic Attrattors

2.2 Circuit Simulation

The chaotic circuit for the Sprott case A system established in the Multisim program using functional elements to provide chaotic system's simulation. Sprott case B and case C chaotic systems simulated using via Labview. Initial parameters for all chaotic systems except case A , X_0, Y_0, Z_0 parameters were taken 0,05, 0.05, 0,05.The initial conditions of the case A taken as 0, 0.05, 0 [22]. It is expected that the simulation circuit which established in the Multisim and Labview environment will be similar to the theoretical system outputs. Case A, B, C chaotic system equations are given in equations (2-4).

Sprott Case A:

$$\dot{x} = y$$
$$\dot{y} = -x + z \quad\quad\quad (2)$$
$$\dot{z} = 1 - y^2$$

Sprott Case B:

$$\dot{x} = yz$$
$$\dot{y} = x - y \quad\quad\quad (3)$$
$$\dot{z} = 1 - xy$$

Sprott Case C:

$$\dot{x} = yz$$
$$\dot{y} = x - y \quad\quad\quad (4)$$
$$\dot{z} = 1 - x^2$$

Sprott case A chaotic system is established with using simple OP-AMP's and other appropriate components. Then system is designed with using Multisim program. Fig 6 shows Multisim design of Sprott model.
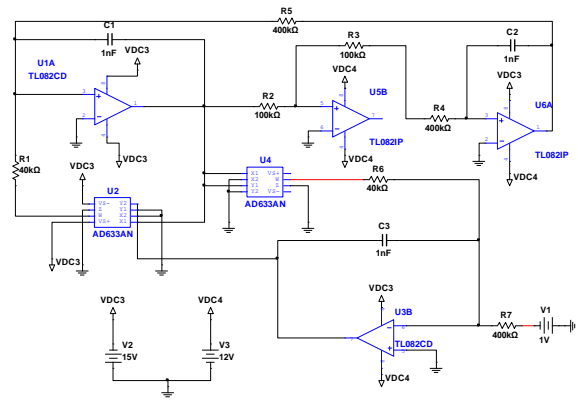

Figure 6. Multisim Design of Sprott Model

Fig. 7 and fig. 8 illustrate Sprott Case A and C chaotic models of LabVIEW. LabVIEW is a graphics-based software platform. The usage of program is increasing in engineering applications day by day[23-24]. It ensures a visual platform for the development of algorithms.
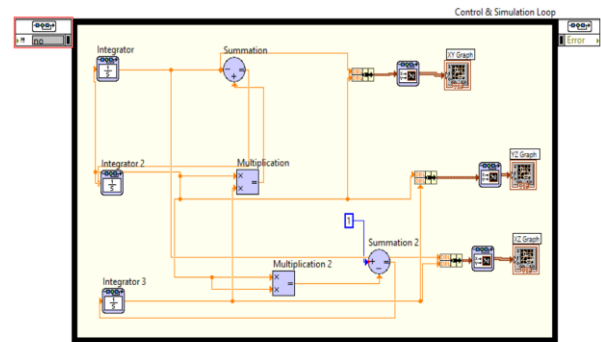
Figure 7. LabVIEW Design of Sprott Case A Chaotic Attractors

The operations required to model differential equations can be summarized by adding, multiplying, multiplying by a fixed number, analog multiplication, taking an integral, taking a derivative etc. The generated block diagrams can be modeled and simulated with electronic circuit programs using analog operational elements.
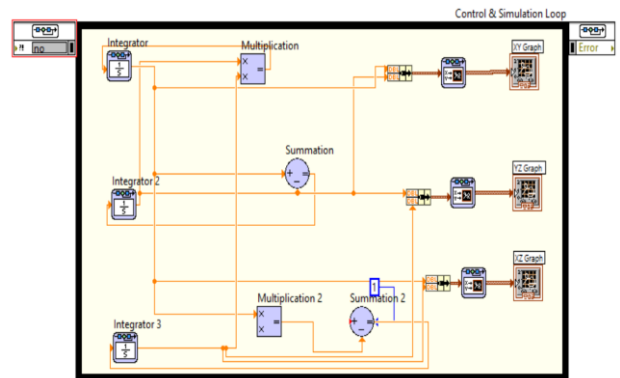

Figure 8. LabVIEW Design of Sprott Case C Chaotic Attractors

The same simulation results can also be obtained by establishing the actual electrical circuit of the systems which has also the digital modeling and simulation.

Models are created using control& simulation toolbox in LabVIEW. Sprott model's differential equations are given before section. Their LabVIEW designs are showed.

3. Results

Sprott Systems using functional elements, chaotic for state A circuits are installed in the Multisim program to provide chaotic circuit implementations. The systems are designed with the system parameters which is in the literature. For case A, initial conditions taken as $X_0 = 0$, $Y_0 = 0.5$, $Z_0 = 0$. Fig. 9 shows Sprott Case A chaotic attractors x-y, y-z and x-z phase.
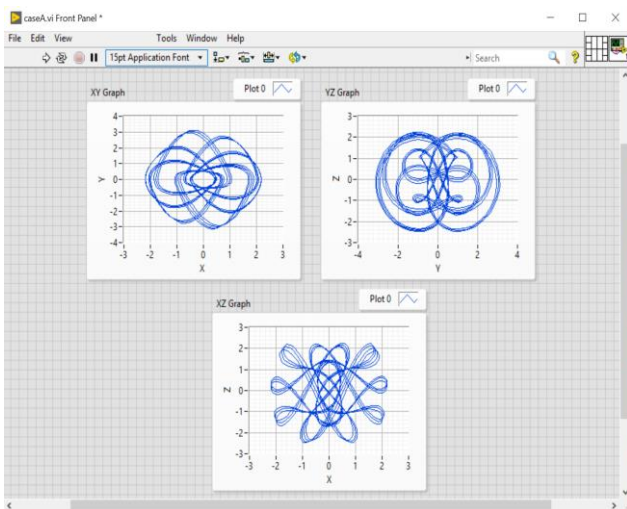

Figure 9. LabVIEW Design of Sprott Case A Chaotic Attractors

The second Sprott model Case B is also designed in the LabVIEW program to provide its chaotic behaviour. The system parameters are used as in literature. For B condition is taken as $X0 = 0.05$, $Y0 = 0.05$, $Z0 = 0.05$. Fig. 10 shows Sprott Case B chaotic attractor results in x-y, y-z and x-z phase.
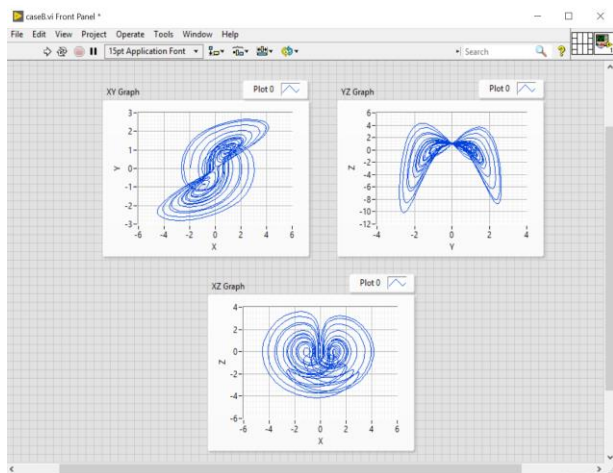

Figure 10. LabVIEW Design of Sprott Case B Chaotic Attractors

The other chaotic model is C. For C condition initial parameters are taken as $X_0 = 0.05$, $Y_0 = 0.05$, $Z_0 = 0.05$. Fig. 11 shows Sprott Case C chaotic attractors results x-y, y-z and x-z phase.
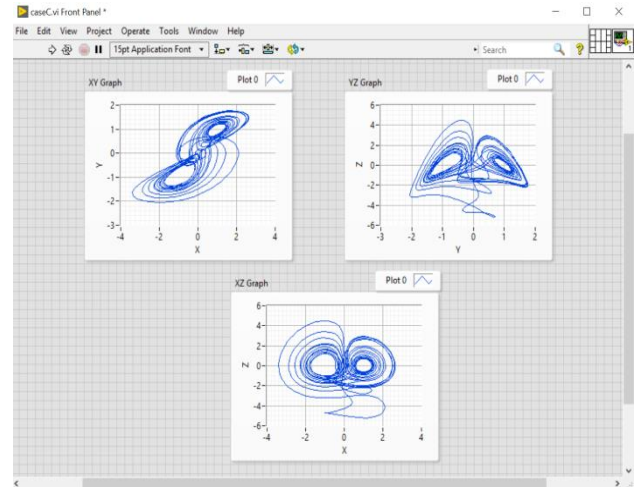
Figure 11. Sprott Case C Chaotic Attractors

Sprott chaotic system's 3D phase portrait for case A is also shown in fig. 12.
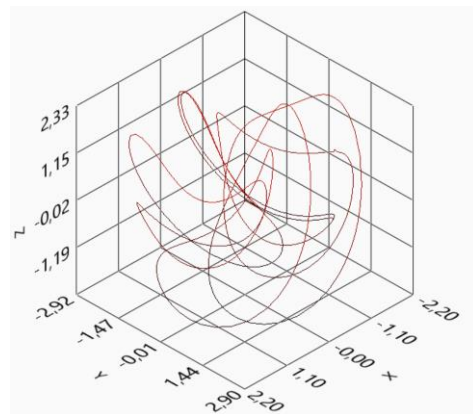
Figure 12. Sprott Chaotic Systems 3D Phase Portrait

4. Conclusion

Research on engineering related to nonlinear dynamics and chaos is generally theoretical and simulation based, and experimental studies include a single circuit model whose results are reported in the literature. In this study Sprott case A, B and C chaotic models designed with using Multisim circuit program and LabVIEW control& simulation toolbox. As a result, the simulation results of the digital model with block diagrams and electronic circuit programs and the results of the oscilloscope output of the actual electronic circuit can be the same.

References

1. Poincaré, H., 1967. New Methods of Celestial Mechanics, 3 vols. (English trans.). American Institute of Physics
2. Lorenz E.N "Deterministic Nonperiodic Flow" Journal Of Atmospheric Siences, 1963. 20:130-141.

3. Chua, L.O., Desoer, C. A., Kuh, E. S., 1987. Linear and Nonlinear Circuits", New York: McGraw Hill.

4. Chen G., Ueta T. Yet Another Chaotic Attractor, International Journal of Bifurcation and Chaos, 1999. 9(7): 1465–1466 .

5. Rössler, Otto E., An equation for continuous chaos, Physics Letters A,1976. 57(5): 397-398.

6. Sprott JC., Some Simple Chaotic Flows, Physical Review E., 1994. 50(2):647-650.

7. Van der Pol, B., "On relaxation-oscillations", The London, Edinburgh and Dublin Phil. Mag. & J. of Sci., 1926. 2(7), 978-992.

8. Rucklidge A.M "Chaos in Models of Double Convection" J. Fluid Mech., 1992. 237:209-229.

9. C. Liu, T. Liu, L. Liu, K. Liu, "A new chaotic attractor coined", Chaos Solitons Fract., 2004. 22: 1031–1038.

10. X. Wang, G. Chen, "A new system with only one stable equilibrium", Commun. Nonlinear Sci. Numer. Simulat, 2011. 17: 1264–1272.

11. Z. Wei, . Pehlivan, "Analysis, nonlinear control, and chaos generator circuitof another strange chaotic system" Turk J. Elec. Eng. & Comp. Sci., 2012. 20240: 1229–1239.

12. P. Zhou, K. Huang, "A new 4-d non-equilibrium fractional-order chaotic system and its circuit implementation", Commun. Nonlinear Sci. Numer. Simulat., 2014. 19: 2005–2011.

13. C. L. Li, J. B. Xiong, W. Li, "A new hyperchaotic system and its generalized synchronization", Optik, 2014. 125: 575–579.

14. A. M. A. El-Sayed, H. M. Nour, A. Elsaid, A. E. Matouk, A. Elsonbaty, "Circuit realization, bifurcations, chaos and hyperchaos in a new 4d system",Appl. Math. Comput., 2014. 239: 333–345.

15. A. Abooe, H. A. Yaghini-Bonabi, M. R. Jahed-Motlagh, "Analysis and circuitry realization of a novel three-dimensional chaotic system", Commun. Nonlinear Sci. Numer. Simulat., 2013. 18: 1235–1245.

16. S.Çiçek, A.Ferikoğlu, İ.Pehlivan "A new 3D chaotic system: dynamical analysis, electronic circuit design, active control synchronization and chaotic masking communication application" Optik (Accepted Manuscript)

17. Saptarshi Das , Anish Acharya, Indranil Pan, "Simulation studies on the design of optimum PID controllers to suppress chaotic oscillations in a family of Lorenz-like multi-wing attractors" Mathematics and Computers in Simulation, 2014. 100: 72–87.

18. S. Wiggins, Introduction to Applied Nonlinear Dynamical Systems and Chaos, Springer, New York, 2003.

19. Sprott JC "Some Simple Chaotic Flows" Physical Review E., 1994 50(2):647-650.

20. Olurotomi S., Abdulahi N.,N, Njah, "A 5D Hyper Chaotic Sprott B System with Coexisting Hidden Attractors" Chaos Solutions and Fractals, 2016. 87: 172-181.

21. Gözde Kargün "Secure Communication Aplication with Chaotic Systems" Master Thesis. Bilecik Seyh Edebali University Graduate School of Sience Electrical-Electronics Engineering. 1-156. Bilecik, 2014.

22. ME Sahin, H Guler, T Kaya, LabVIEW Model Of Memristor With Nonlinear Dopant Drift, European Journal of Technic, 2016. 6 (2): 124-130.

23. Guler, H., & Ata, F. The Comparison of Manual and LabVIEW Based-Fuzzy Control on Mechanical Ventilation. Journal of Engineering in Medicine, 2014. p. 916-925.

Research Article

Design and implementation of the FPGA-based chaotic van der pol oscillator

Mustafa Dursun [a] and Elif Kaşifoğlu [b,]*

[a] *Department of Electrical-Electronic Engineering, Faculty of Technology, DüzceUniversity, Düzce, 81010, Turkey*
[b] *Department of Electronic Communication Technologies Program, Düzce Vocational School, Düzce University, Düzce, 81010, Turkey*

ARTICLE INFO	ABSTRACT
	In this study, the chaotic Van der Pol system was implemented for real-time chaos applications on FPGA chip. The chaotic Van der Pol system was also modelled numerically by using the Euler algorithm ODE (Ordinary Differential Equation) solver on Matlab. Numerical structure of the chaotic Van der Pol oscillator designed on Matlab was taken as reference for the design of FPGA-based chaotic Van der Pol oscillator unit. The chaotic Van der Pol system was coded in Very High-Speed Integrated Circuits Hardware Description Language (VHDL) with 32-bit IEEE-754-1985 floating point number standard. The designed chaotic Van der Pol system was synthesized in the Xilinx ISE Project Navigator program and was implemented on the Xilinx VIRTEX-6 chip family, XC6VLX75T device, FF784 package. The maximum operating frequency of the FPGA-based chaotic Van der Pol oscillator unit obtained from Place and Route processes was 498.728 MHz. Additionally, chip statistics of the FPGA-based Van der Pol oscillator were presented.

1. Introduction

Chaos or chaotic systems are one of the fields theorized in recent years and studied extensively. Some of the research areas related to chaos or chaotic systems are oscillator design [1], biomedical [2], communication [3], optical [4], power electronics [5], robotic [6], artificial neural networks [7-9], pseudo random number generator [10], true random number generator [11], synchronization [12], image processing [13], optimization [14]. Chaotic oscillators are used in many applications because of their characteristic features, such as the fact that signals generated by them show noise-related and non-periodic behaviors, and they depend on the initial conditions and the system parameters very sensitively. Therefore, many chaotic systems with different characteristics are proposed in the literature. From these chaotic systems, the oscillators, whose system dynamics are best known, are Lorenz [15], Chua [16], Shimizu-Morioka [17], Duffing systems [18], and Chen [19]. In addition, there are some other chaotic systems presented to the literature newly with their different

characteristic features. [20-22]. Chaotic oscillators can be examined in two types: continuous-time and discrete-time chaotic oscillators. For the purpose of performing discrete-time chaotic oscillators, various hardware platforms such as digital Signal processors (DSPs) [23], Application Specific Integrated Circuits (ASICs) [24], microcontroller (μC) [25], and Field Programmable Gate Arrays (FPGAs) [26] are used. FPGA chips, which are one of the digital-based platforms, are frequently used in the literature because of their characteristics such as parallel processing and ability to be programmed repeatedly.

In the study conducted by Rajagopal et al., by using the RK5-Butcher algorithm and 32-bit IEEE-754 floating point standard, a new 3D chaotic chameleon system application on the Xilinx Virtex-6 XC6VLX240T FPGA chip was carried out [27]. In the study of Alçın et al., by using ANN structure and 32-bit IEEE-754 floating point standard, Pehlivan Uyaroglu Chaotic System on the Xilinx Virtex-6 FPGA chip was designed as hardware [8]. In another study, by using Heun algorithm and floating-point number format, on the Xilinx virtex-6

FPGA chip, design and implementation of a new 3D chaotic system with a single equilibrium point was carried out by Tuna et al. [1]. In another study, Azzaz et al. modelled the 3D hybrid chaotic system with the Virtex-II family FPGA chip of Xilinx Company in accordance with 32-bit IQ-Math format, and by using this system, they carried out an application [28]. In the study of Lai et al., using the fourth degree Runge Kutta algorithm, a multi-butterfly chaotic attractor was designed with the 32-bit IEEE-754 number standard and the Xilinx Kintex-7 FPGA chip, and engineering applications were performed by using the oscillator [29]. In the study conducted by Tlelo-Cuautle and his colleagues, the chaotic system was modelled on the Altera Cyclone IV FPGA chip by using the 32-bit fixed-point number standard. [30]. Using the RK-4 algorithm and the 32-bit IEEE-754 number Standard, the Chen Chaotic System was carried out on the Xilinx virtex-II FPGA chip in real time by Sadoudi et al. [31]. Rajagopal et al. modelled the 3D Time-Delayed Chameleon Chaotic System on the Xilinx Virtex-7 XC7-VX980tffg FPGA chip by using Matlab Xilinx system generator [32].

In the second section of this study, brief information about chaotic systems, Van der Pol oscillator, FPGA chips and numerical algorithms will be given. In the third section, the design of FPGA-based Van der Pol oscillator unit will be presented. In addition, FPGA chip statistics and simulation results obtained from the design testing will be given. In the last section, the results of the study will be interpreted.

2. Background Information

2.1 Chaotic Systems and Van der Pol Oscillator

The term Chaos was first introduced by M.I.T. scientist Edward Lorentz's work in 1963. Lorentz wanted to round down the results of the mathematical meteorological model he created with the aim of forecasting the weather, but could not get the results he wanted. In this way, the first foundations of Chaos Science Field were laid. As a definition, chaotic systems or chaos can be expressed as dynamic systems which are deterministic, non-linear, non-periodic and highly sensitive to system parameters and system startup conditions [11].

Chaotic systems are expressed by using ordinary differential equations. In the literature, there are 1st degree discrete-time chaotic systems. On the other hand, in continuous-time chaotic systems, at least a second-order differential equation set should be used. In the Equation 1, the differential equation for Van der Pol system is given. [33].

$$\frac{d^2x}{dt^2} - \mu(1-x^2)\frac{dx}{dt} + x = 0 \qquad (1)$$

The Van der Pol oscillator shows chaotic oscillator characteristics under certain conditions. In this study, while the system parameter was taken as μ=0.5, the initial conditions were taken as x_0=1.0 and u_0=-0.97.
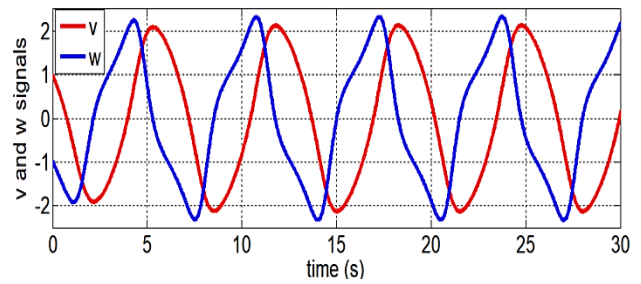

Figure 1. Time Series of the Van der Pol oscillator

2.2 FPGA Chips

FPGA chips can be defined as integrated circuit tools with repeatedly programmable properties for digital system/circuit designs. These chips, after the first silicon production process, allows the designer to make system design in the chip whenever he/she wants [34]. These chips are also called as "System On a Chip" (SOC), and they can work together with other hardware platforms as part of the larger designs when needed [35]. In recent years, FPGA chips have gained quite high capacity and high performance, but their structures have become more complex day by day. FPGA chips, which are produced for general purpose and can be programmed specifically for design, have approximately 1 GHz working frequency [36]. Compared with the platforms working sequentially such as DSP, μC and PC, very high performance can be obtained from FPGA chips due to their some advantages such as parallel processing and system-specific design. Therefore, they can perform operations much faster than personal computers. Multiple copies of the design made inside FPGA chips can also be executed inside the chip. Moreover, with a standard computer and FPGA based custom computing machines, which is connected to this computer and contain one or more FPGA chips, designs can be carried out and high-performance platforms can be obtained. Because of these and similar advantages, in recent years, FPGA hardware has been widely used from motor control to industrial imaging, from Crypto communication to electronic warfare applications in space and defense industries, from digital cameras to Satellite Receivers in consumer electronics, from computerized tomography to ultrasound imaging in biomedical and from image processing to in-car information systems in automotive industry [37, 38]. Today, FPGA chips are manufactured by many companies such as Xilinx, Altera, Atmel, SiliconBlue, Microsemi and Lattice.

In general, FPGA equipment consists of three parts: input-output blocks (I-O blocks), interconnection network, and Configurable Logic Block (CLB). All of the Input-Output blocks (I-O blocks), connection network, and CLB structures can be configured. Input-output blocks can be used as input, output, or both input and output ports. Although their structure varies according to the type of chip, CLB units are generally composed of memory, logical blocks and multipliers. On the other hand, the interconnection networks are programmable

structures that provide the connection between the input-output ports and the CLB.

In FPGA chips, designs are carried out schematically and by using HDL (Hardware Description Language). VHDL and Verilog languages are the most preferred hardware description languages [39].

2.3 Numerical Algorithms

In the literature, various algorithms were developed for numerical solutions of differential equations. Euler, Heun, fourth order Runge-Kutta (RK-4), fifth order Runge-Kutta Butcher and Dormant-Prince methods can be shown as examples of these algorithms. The Euler algorithm, one of these algorithms, is preferred because of its advantages such as being able to calculate numerical solution in a short time and easy modeling on digital processors. The Euler algorithm is given in the equation 2.

$$y_{\lambda+\Delta h} \approx y_{\lambda+1} = y_{\lambda} + f(y_{\lambda})\Delta h \quad (2)$$

In this equation, Δh refers to step range, y_{λ} refers to initial value, and $y_{\lambda}+1$ refers to the values of the system to receive an iteration sonar. In the numeric algorithms used to be able to model continuous-time systems in real time on digital processors, in order to calculate the next $y_{\lambda}+1$ value of the system, $y_{\lambda,}$ which is the previous value of it, is used.

3. FPGA-Based Van der Pol Oscillator

In this section, the Van der Pol oscillator is modelled to work on FPGA chips by using the Euler numerical algorithm and the 32-bit IEEE-754-1985 floating point number format [40]. The design was coded in VHDL, which is a hardware identification language. Units such as adders, dividers and subtractors in floating point number format, used in FPGA-based Van der Pol oscillator design, were created by using the IP Core generator presented with the Xilinx ISE Project Navigator program. In order to model the presented Van der Pol oscillator on FPGA chip, the discrete-time model of the system was created. In equation 3, using the Euler algorithm, a differentiated mathematical model of the Van der Pol system is presented.

$$w(k+1) = w(k) + \Delta h\, w(k)$$
$$v(k+1) = v(k) + \Delta h\left(-w(k) + \mu v(k) - \mu w(k)^2 v(k)\right) \quad (3)$$

In the equation, intermediate values are calculated first

by putting the w(K) and v(K) values in their place. Then, the calculated values are multiplied by Δh step range value. By summing the obtained values with the initial values of w(K) and v(K), the values of w(k+1) and v(k+1) are calculated, respectively. In this study, for the design of FPGA based Van der Pol oscillator, the Step range of Euler algorithm was taken as Δh=0.05 and μ=10.

The first-order block diagram for Modeling Van der Pol oscillator with Euler algorithm-based FPGA is given in Figure 2. One-bit Start and CLK signals at the entrance of the designed system are used to ensure the timing of all units and the synchronization between the units and the system to which the units are connected. In the design, while the initial values of the oscillator were embedded in the FPGA chip, the 32-bit initial conditions were embedded in the design to reduce resource utilization. However, when needed, the relevant signals can be taken out of the design by the designer. The FPGA-based Van der Pol oscillator unit has w_out and v_out 32-bit output signals in floating point standard and 1-bit Ready_wv signal used to indicate that these output signals are ready.

Figure 2. The first-order block diagram of FPGA-based chaotic Van der Pol oscillator

Figure 3 shows the second-order block diagram of the chaotic Van der Pol oscillator designed to operate in the FPGA chips. Designed system consists of 2 units; MUX and Euler units. The MUX unit serves as a selector for the starting conditions of the system and the signal produced by the oscillator. On the other side, the Euler unit is the unit that produces chaotic Van der Pol signals. When the '1' signal is applied to the start input of the design, the initial conditions required by the system are transferred to the Euler unit via the MUX. When the Euler unit generates its first value, the Ready_wv signal become '1', and at this time, the Van der Pol oscillator unit generates its first outputs as w_Out and v_Out. From this moment, the MUX unit sends the signals produced by the Euler unit to the system instead of the initial conditions.
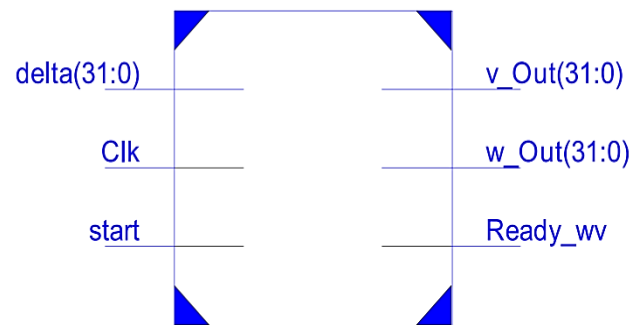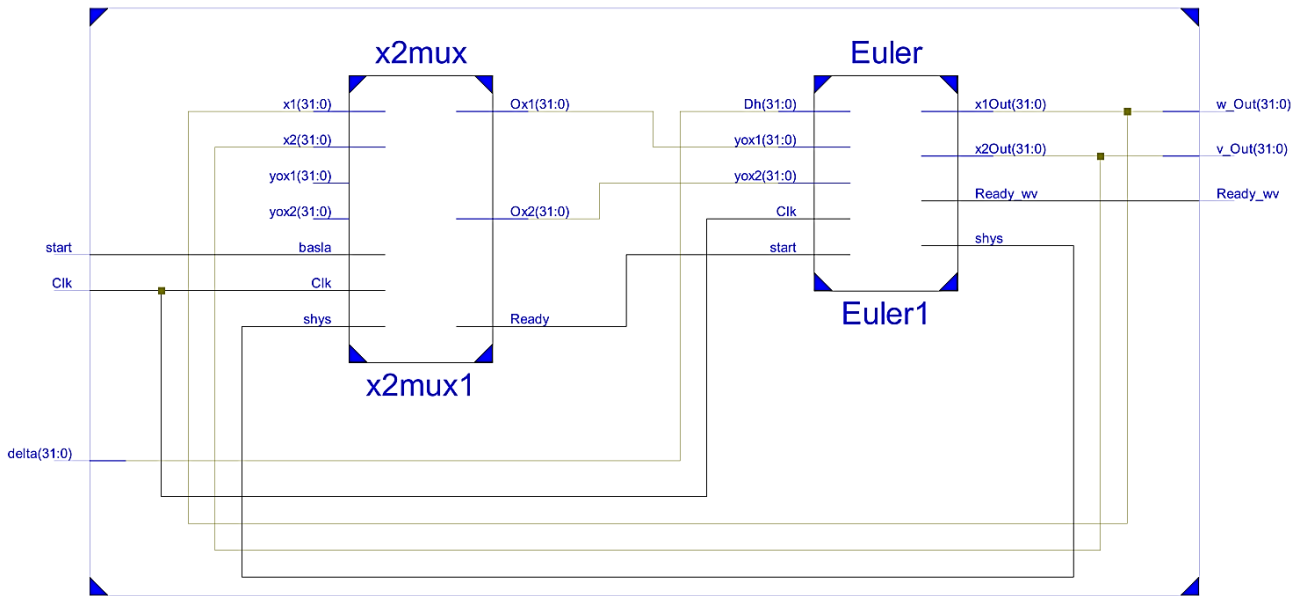
Figure 3: The second-order block diagram of FPGA-based chaotic Van der Pol oscillator

Figure 4 shows the third-order block diagram of the Euler-based chaotic Van der Pol oscillator unit. In the oscillator unit structure, there are 7 units including MUX, V, multiplication, addition and counter units. The V unit enables the calculation of w(k+1) and v(k+1) values in Van der Pol system equations with control signals coming from MUX unit. The signals obtained from the unit are summed in the addition unit with the start value signals (w(k) and v(k)), and the results are sent to the counter unit. Since the counter unit is designed as System pipeline, it is used to filter unwanted signals. The multiplication, addition, subtraction and other modules in the 32-bit floating point number format used in the Van der Pol oscillator, which was designed based on FPGA,

were created by using the IP Core Generator developed by Xilinx Company. The Euler-based oscillator unit works as a pipeline, and the designed system produces the first result at the end of 128 clock cycles. In the next each 128 clock cycles, the system continues to produce a result. The designed chaotic Oscillator unit is tested by synthesized for the xc6vlx75t-3FF784 chip of the Virtex-6 Family produced by Xilinx Company. Figure 5 shows the simulation results of the Xilinx ISE Project Navigator program obtained from the realization of the Van der Pol chaotic generator on FPGA; this Van der Pol chaotic generator was designed by using Euler algorithm.
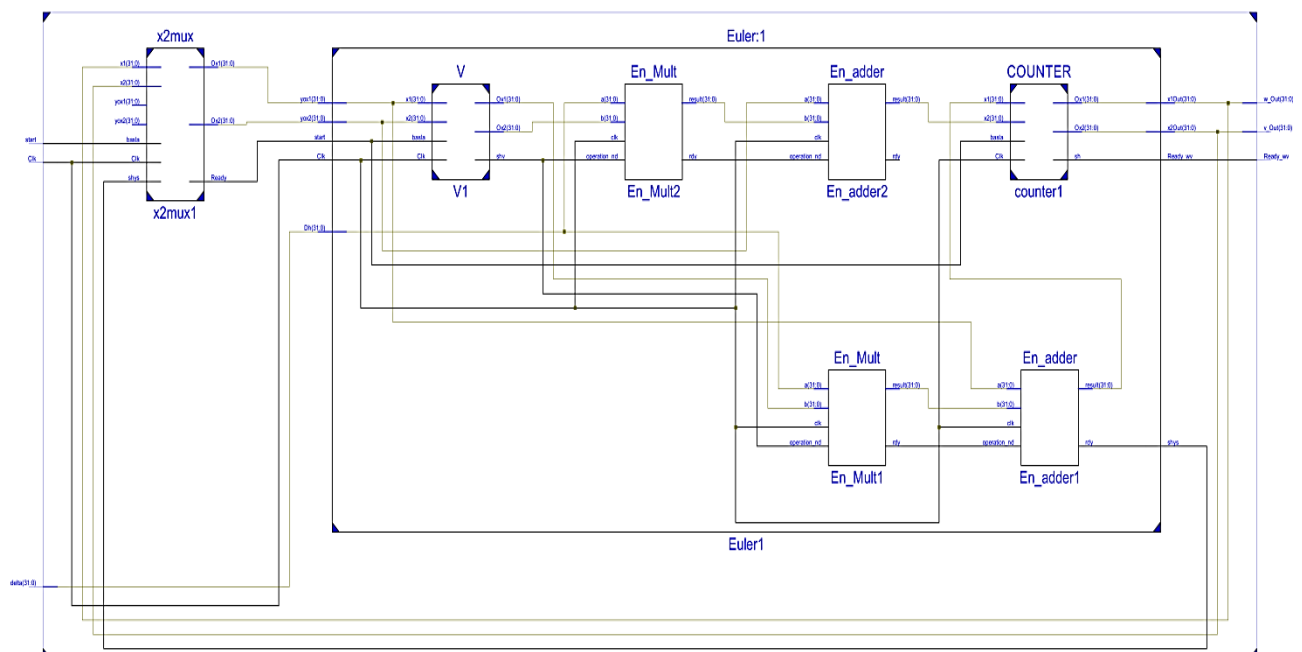

Figure 4: The third-order block diagram of FPGA-based chaotic Van der Pol oscillator
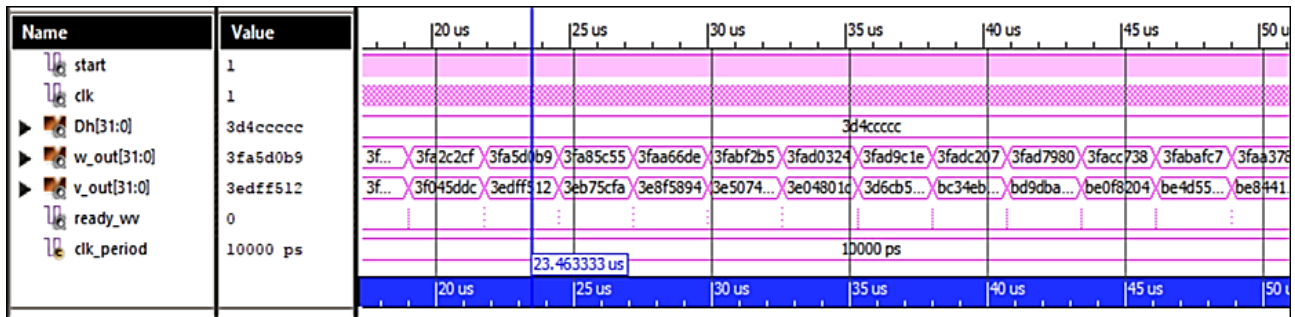
Figure 5: The simulation results of the Xilinx ISE Navigator of FPGA-Based Chaotic Van der Pol Oscillator Unit

The designed chaotic Van der Pol oscillator unit was realized using Euler algorithm on FPGA, and the FPGA chip statistics obtained from place and route process are given in Table 1. The maximum operating frequency of FPGA-based chaotic Van der Pol oscillator unit was obtained as 498.728 MHz. In other words, the minimum operating period of the designed unit is 2.005 ns.

Table 1. The usage statistics for Xilinx Virtex-6 XC6VLX75T-3FF784 chip of FPGA-based Van der Pol oscillator

Logic Utilization	Used	Available	Utilization (%)
Number of Slice Registers	4,702	93,120	5
Number of Occupied slices	1,326	11,640	11
Number of Slice LUTs	4,160	46,560	8
Number of bonded IOBs	99	360	27

4. Conclusions

In this study, for chaos-based engineering applications, Van der Pol oscillator was implemented by using the Euler algorithm on the FPGA. In the study, first the Van der Pol oscillator was numerically modelled and time-series were obtained. Then, using the numeric model, it was encoded on FPGA by using VHDL language and the Euler algorithm. In the design, 32-bit IEEE-754-1985 standard was used and it was synthesized by using the Xilinx ISE Project Navigator program. At the end of Place & Route process for Xilinx VIRTEX-6 chip family, the maximum operating frequency of FPGA-based Van der Pol oscillator unit was obtained as 498.728 MHz. The unit was tested by using Xilinx ISE Project Navigator program and test results were presented. In the future studies, random-number-generator design and synchronization applications will be able to be realized by using the FPGA-based Van der Pol oscillator presented in this study.

References

1. Tuna, M., Fidan, C.B., Electronic circuit design, implementation and FPGA-based realization of a new 3D chaotic system with single equilibrium point. Optik-International Journal for Light and Electron Optics, 2016. 127(24): p. 11786-11799.

2. Belkhouja, T., Mohamed, A., Al-Ali, A.K., Du, X., Guizani, M., Light-weight encryption of wireless communication for implantable medical devices using henon chaotic system. In Wireless Networks and Mobile Communications (WINCOM), IEEE 2017 International Conference on. p. 1-6.

3. Wang, X., Akgul, A., Cicek, S., Pham, V. T., & Hoang, D. V., A chaotic system with two stable equilibrium points: Dynamics, circuit realization and communication application. International Journal of Bifurcation and Chaos, 2017. 27(08): p. 1750130.

4. Ji Y, Zhang M, Wang Y, Wang P, Wang A, Wu Y, et al., Microwave-Photonic Sensor for Remote Water-Level Monitoring Based on Chaotic Laser. International Journal of Bifurcation and Chaos, 2014. 24: 1450032.

5. Ashita S, Uma G, Deivasundari P. Chaotic dynamics of a zero average dynamics controlled DC–DC Ćuk converter. IET Power Electronics, 2014. 7: p. 289–98.

6. Pomares J., Perea I., Torres F., Dynamic Visual Servoing With Chaos Control for Redundant Robots. IEEE/ASME Transactions on Mechatronics, 2014. 19: p. 423–31.

7. Alçın, M., The Modelling Performance Evolution of Recurrent Neural Networks Having Different Training Functions for Modelling Sprott H Chaotic System. Int. Journal on Research Innovations in Engineering Science and Technology, 2017. 2(10): p. 563–568.

8. Alçın M, Pehlivan İ, Koyuncu İ, Hardware design and implementation of a novel ANN-based chaotic generator in FPGA. Elsevier, Optik-International Journal for Light and Electron Optics, 2016. 127(13): p. 5500-5505.

9. Koyuncu İ, Şahin İ, Gloster C, Sarıtekin N.K., A Neuron Library for Rapid Realization of Artificial Neural Networks on FPGA: A Case Study of Rössler Chaotic System. Journal of Circuits, Systems and Computers, 2017. 26(01): p. 1750015.

10. Avaroğlu, E., Pseudorandom number generator based on Arnold cat map and statistical analysis. Turkish Journal of Electrical Engineering & Computer Sciences, 2017. 25(1): p. 633-643.

11. Fidan, C. B., Tuna M., A Study on the importance of chaotic oscillators based on FPGA for true random number generating (TRNG) and chaotic systems. Journal of the Faculty of Engineering and Architecture of Gazi University, 2018. 33(2): p. 469-486.

12. Shi, K., Tang, Y., Liu, X., & Zhong, S., Non-fragile sampled-data robust synchronization of uncertain delayed chaotic Lurie systems with randomly occurring controller gain fluctuation. ISA transactions, 2017. 66: p. 185-199.

13. Çavuşoğlu Ü., Kaçar S., Pehlivan İ., Zengin A., Secure image encryption algorithm design using a novel chaos based S-Box. Chaos, Solitons Fractals, 2017. 95: p. 92-101.

14. Heidari, A.A., Abbaspour, R.A., Jordehi, A.R., An efficient chaotic water cycle algorithm for optimization tasks. Neural Computing and Appl., 2017. 28(1): p. 57-85.

15. Sharma, N., Saini, I., Yadav, A. K., & Singh, P. Phase-Image Encryption Based on 3D-Lorenz Chaotic System and Double Random Phase Encoding. 3D Research, 2017. 8(4): p. 39.

16. Vaidyanathan, S., Rasappan, S., Global chaos synchronization of n-scroll Chua circuit and Lur'e system using backstepping control design with recursive feedback. Arabian Journal for Science and Engineering, 2014. 39(4): p. 3351-3364.

17. Alcın, M., Pehlivan, I., Koyuncu, I., The Performance Analysis of Artificial Neural Network Based Shimizu-Morioka Chaotic System with Respect to Sample Numbers. Balkan Journal of Electrical and Computer Engineering, 2015. 3(4), p. 252–255.

18. Yu, S.H., Kang, H.S., Kim, Y.T., Hyun, C.H., Park, M., Fuzzy adaptive modular design of uncertain chaotic duffing oscillators. International Journal of Control Automation and Systems, 2014. 12(1): 188-194.

19. Alcin, M., The Effect on Modelling Performance of Different Activation Functions for Feed Forward and Feedback Network Structures in Modeling of Chen Chaotic System. International Journal of Scientific and Technological Research, 2017. 7(3): p. 60-70.

20. Jafari, S., Ahmadi, A., Khalaf, A.J.M., Abdolmohammadi, H.R., Pham, V.T., Alsaadi, F.E., A new hidden chaotic attractor with extreme multi-stability. AEU-International Journal of Electronics and Communications, 2018. 89 (May): p. 131-135.

21. Azar, A. T., Volos, C., Gerodimos, N. A., Tombras, G. S., Pham, V. T., Radwan, A. G., Pacheco, J. M., A novel chaotic system without equilibrium: dynamics, synchronization, and circuit realization. Complexity, 2017. ID:7871467.

22. Tuna, M., Fidan, C. B., Koyuncu, İ., Pehlivan, İ., Real time hardware implementation of the 3D chaotic oscillator which having golden-section equilibra. IEEE 24 th In Signal Processing and Communication Application Conference (SIU), May 2016. p. 1309-1312.

23. Zhong Z., Guanrong C., Simin Y., Hyperchaotic signal generation via DSP for efficient perturbations to liquid mixing. Int. J. Circuit Theory Appl., 2009. 37: p. 31-41.

24. Yiwei Z., Zexiang L., Xinjian Z., A chaos-based image encryption ASIC using reconfigurable logic. IEEE Asia Pacific Conference on Circuits and Systems, Macao-China, December, 2008. p. 1782-1785.

25. Kaçar S., Analog circuit and microcontroller based RNG application of a new easy realizable 4D chaotic system. Optik, 2016. 127: p. 9551-9561.

26. Koyuncu, I., Implementation of High Speed Tangent Sigmoid Transfer Function Approximations for Artificial Neural Network Applications on FPGA. Advances in Electrical and Computer Engineering, 2018. 18(3): p. 1-8.

27. Rajagopal, K., Akgul, A., Jafari, S., Karthikeyan, A., Koyuncu, I., Chaotic chameleon: Dynamic analyses, circuit implementation, FPGA design and fractional-order form with basic analyses. Chaos, Solitons & Fractals, 2017. 103: p. 476-487.

28. Azzaz M.S., Taugast C., Sadoudi S., Fellah R., Dandache A., A new auto-switched chaotic system and its FPGA implementation. Commun. Nonlinear Sci. Numer. Simul., 2013. 18 (7): p. 1792-1804.

29. Lai, Q., Zhao, X. W., Rajagopal, K., Xu, G., Akgul, A., & Guleryuz, E., Dynamic analyses, FPGA implementation and engineering applications of multi-butterfly chaotic attractors generated from generalised Sprott C system. Pramana, 2018. 90(1), p. 6.

30. Tlelo-Cuautle E., Pa-Azucena A.D., Rangel-Magdale J.J., Carbajal-Gomez V.H., Rodriguez-Gomez G., Generating a 50-scroll chaotic attractor at 66MHz by using FPGAs. Nonlinear Dyn, 2016. 85(4): p. 1-15.

31. Sadoudi S., Mohamed SA., Mustapha D., Mustapha B. An FPGA real-time implementation of the Chen's chaotic system for securing chaotic communications. International Journal of nonlinear Science, 2009. 7(4): 467-474.

32. Rajagopal, K., Jafari, S., Laarem, G., Time-delayed chameleon: Analysis, synchronization and FPGA implementation. Pramana – J. Phys., 2017. 89: 92. https://doi.org/10.1007/s12043-017-1487-8.

33. Vaidyanathan, S., Output regulation of the forced Van der Pol chaotic oscillator via adaptive control method. International Journal of PharmTech Research, 2015. 8(6): p. 106–116.

34. Kuon, I., Tessier, R., Rose, J., FPGA architecture: survey and challenges. Foundations and Trends in Electr. Design Autom., 2017. 2(2): p. 135–253.

35. Munden, R., ASIC and FPGA verification: a guide to component modeling. 2005, San Francisco, USA: Morgan Kaufmann Publ., Elsevier.

36. Xilinx, [cited 2018 29 June]; Available from: http://www.xilinx.com/publications/prod_mktg/zynq7000/Zynq-7000-combined-product-table.pdf.

37. Sarıtaş, E., Karataş, S., Her yönüyle FPGA ve VHDL. 2013, Ankara: Palme Yayıncılık.

38. Karakaya, B., Türk, M. A., Türk, M., Gülten, A., Selection of Optimal Numerical Method for Implementation of Lorenz Chaotic System on FPGA. International Advanced Researches and Engineering Journal, IAREJ, 2018.

39. Tuna, M., Koyuncu, İ., Fidan, C. B., Pehlivan, İ., Real Time Implementation of A Novel Chaotic Generator on FPGA. 23rd IEEE Signal Processing and Communications Applications Conference, Malatya, 2015. p. 698-701.

40. Lai, Q., Zhao, X. W., Rajagopal, K., Xu, G., Akgul, A., Guleryuz, E., Dynamic analyses, FPGA implementation and engineering applications of multi-butterfly chaotic attractors generated from generalised Sprott C system. Pramana, 2018. 90(6): p. 1-12.

Research Article

The shortest path detection for unmanned aerial vehicles via genetic algorithm on aerial imaging of agricultural lands

Abdülkadir Gümüşçü [a],*, Mehmet Emin Tenekeci [b] and Ahmet Tabanlıoğlu [a]

ªHarran University, Electrical and Electronics Engineering Department, Şanlıurfa, Turkey
ᵇHarran University, Computer Engineering Department, Şanlıurfa, Turkey

ARTICLE INFO	ABSTRACT
	By using unmanned aerial vehicles (UAV) for improving fertility of large agricultural lands in the GAP region, it is aimed to guide the end users through processing of the aerial images obtained by using image processing algorithms. The productivity problem of "Agriculture" sector that has the most important role in the economic development of the region directly has been solved in an innovative way by improving the fertility of agricultural lands. Related to the UAVs used for this process, the most important problem to consider is limited battery life. Therefore, it is very important to calculate the optimum route to reduce the flight time and to scan the large agricultural lands in the shortest time. In this paper, the shortest path problem is optimized by using the genetic algorithm for scanning large agricultural lands and collecting data. In the study, the points taken by UAV according to the field of view of the images are determined. The shortest path has been calculated by using genetic algorithm so that images can be taken from these determined points within a minimum flight time.

1. Introduction

Recently, agriculture and food have become very important concepts [1]. In terms of agricultural productivity, many different technologies have begun to be used in agricultural areas [2, 3]. One of these technologies is unmanned aerial vehicle (UAV) [4, 5]. The monitoring of agricultural lands for a certain period of time is important especially in early disease detection and yield estimation. Monitoring the productivity of large agricultural areas in the GAP Region is not effective enough if it is conducted by monitoring techniques done in the ground. Also, this situation causes the problem of wasting time. Unmanned aerial vehicles are widely used today in aerial photography and imaging. Recently, it has been also begun to be used in industrial problems. UAVs are used to collect data by integrated cameras and sensors [6, 7]. Many applications such as monitoring and spraying of the agricultural lands can be achieved more easily and effectively with the widespread use of unmanned aerial vehicles. Analysis of the images of

agricultural lands taken at a certain altitude by using image processing algorithms will increase the productivity and quality. Despite all these advantages, unmanned aerial vehicles need energy provided by Lithium Polymer (Li-Po) batteries. It can be said that the 4-engine unmanned aerial vehicle with a limited energy source does not have a very long flight time. Regarding the fact that the flight time of a quadcopter is estimated as 20 minutes on average, it is unlikely to be able to take images of a large agricultural land. Thus, scanning the entire agricultural area between the coordinates digitally marked within the limited time, and collecting data with sensors and cameras have become a purpose. Scanning of the maximum agricultural land with a limited energy source can actually be considered as an optimization problem.

In this study, the flight route was optimized by using genetic algorithm and the scanned maximum area with minimum flight time was provided. For this purpose, a designated agricultural land was considered. On this agricultural land, some stop points for the unmanned

* Corresponding author. Tel.: *+90 414 318 3000-1041.*
E-mail addresses: *agumuscu@harran.edu.tr (A. Gümüşçü), etenekeci@harran.edu.tr (M.E. Tenekeci), atabanlioglu@harran.edu.tr (A. Tabanlıoğlu).*

aerial vehicle to image all of the agricultural land had been identified. After this process, when the unmanned aerial vehicle arrived at all designated stops, it would be assumed that all agricultural land had been scanned. The genetic algorithm would decide the order in which the unmanned aerial vehicle would arrive at the determined point. The fitness function of the genetic algorithm would be the length of the flight path.

The rest of the paper is organized as follows. In the 2nd section, previous studies related to subject has been summarized. In the section 3, all the algorithms used are summarized. In the 4th section, the results obtained by the proposed method are presented and the performance of the study is evaluated by examining the results.

2. Related Works

Studies for real-time road extraction of UAVs have been investigated with realistic simulations in the 3D plane [6]. In that paper, workload and affection are taken as a strong parameter and 2D plane simulation is preferred. Many studies in the literature aimed to make the energy suitable for collecting data using the most efficient level of energy.

In this context, during the more data collection process by using multiple UAVs, this problem becomes more important [7] [8]. The fact that this problem is real-time is also important because it will save time in order to be able to make online tactical plan for UAVs [9]. Regarding their ability to bring tactics to the UAVs, five different heuristic algorithms were compared. These algorithms were Search algorithm, the Dijkstra algorithm, the Bellman Ford algorithm, the Floyd-Warshall algorithm, and the Primer algorithm. As a result, the Dijkstra algorithm was found to be the fastest [10]. For the problem of finding the shortest path, there are a genetic algorithm and a search algorithm that working well for heuristic algorithms used optimally for this problem [9] [11-15].

Unlike the studies in the literature, in this study, it was assumed that the height of the unmanned aerial vehicle was constant and this problem was considered as the traveling salesman problem.

3. Material and Methods

3.1 Genetic Algorithm

The Genetic Algorithm, developed by John Holland in 1975, is a search and optimization method based on natural selection principles. Genetic algorithms are considered as effective search techniques in many areas. [16] Genetic algorithms are based on the initial populations, and they create new populations by using methods such as crossover and mutation in those populations [17]. Steps of the Genetic Algorithm process

are shown in Fig.1.

As shown in Fig.1, firstly, a population is generated. Then the fitness function is calculated. If the value of the fitness function is the desired value, the loop is terminated. If the fitness function does not reach the desired value, the selection, crossover and mutation procedures are applied, and the fitness function for the obtained new population is recalculated. This cycle is repeated until the desired fitness value is reached.
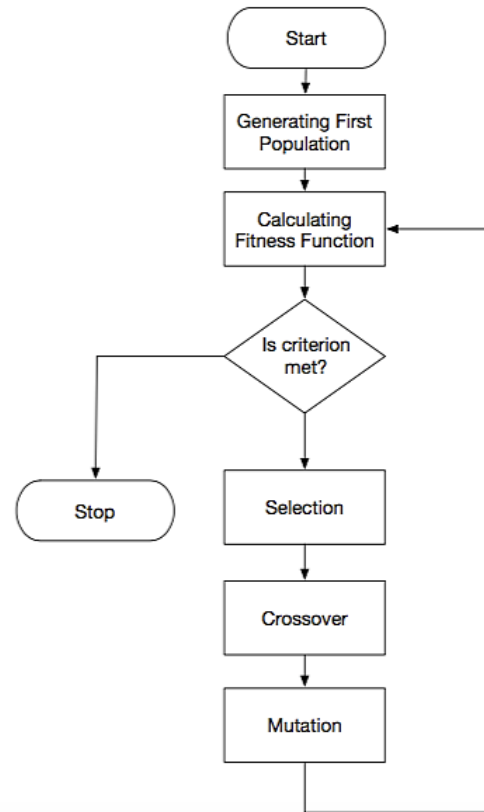
Figure 1. Genetic Algorithm Flow Chart

In this study, the genetic algorithm was used to determine the order in which the unmanned aerial vehicle was supposed to stop at the determined stop points for the shortest flight route.

$$Fitness\ Function\ = Flight\ distance(route) \quad (1)$$

$$Flight\ distance\ = \sum_{i=1}^{P}\sum_{j=1}^{P} x_{ij} \quad\quad (2)$$

The fitness function shown in Equation (1) gives the shortest route that arrives to all stop points determined in the agricultural land. Equation (2) calculates the total route distance for the fitness function. The p value in the Equation (2) refers to the number of stop points.

3.2 Travelling Salesman Problem

It is a problem that is explored in the field of operations research and theoretical computer science. It is assumed that a travelling salesman has to go through n

different towns. In this case, the travelling salesman should take its route in the shortest way, and every city must be visited once. As such, the problem addressed in this study was evaluated and interpreted in this way.

3.3 Unmanned Aerial Vehicles

Unmanned aerial vehicles are used to collect data with integrated cameras and sensors [6, 7]. As shown in Figure 2, an angle has been given to the camera by the anti-shake gimbal mechanism.

Figure 2. DJI Phantom 2 Vision

In this study, it was assumed that the unmanned aerial vehicle flew at a fixed height of 40 meters. In this case, it was also assumed that in the agricultural land, a circular area with radius of 50 meters was scanned.

3.4 Shortest Path Detection for UAVs via Genetic Algorithm on Aerial Imaging of Agricultural Lands

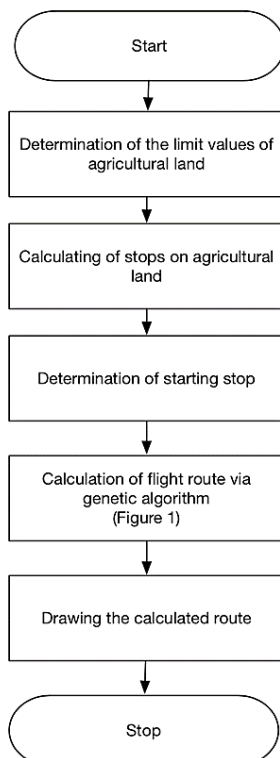The workflow of the proposed method is shown in Figure 3.

Figure 3. Proposed Method

As shown in Figure 3, in the proposed method, the boundaries of the agricultural land are primarily determined by the user. According to the determined land, the places where the unmanned aerial vehicles will stop are calculated and the starting point is selected. Then, the travelling salesman problem is set up to stop at the designated stop points once. The genetic algorithm optimizes the travelling salesman problem and provides scanning of the entire agricultural land with less flight route length. Thus, the limited battery should be used very efficiently.

In this study, the agricultural lands required to be scanned by the unmanned aerial vehicle was determined as shown in Figure 4.
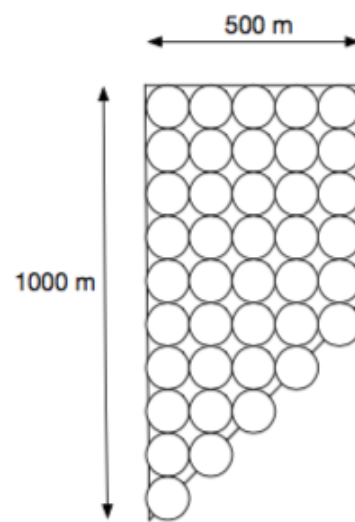
Figure 4. Agricultural Land

As seen in Figure 4, 40 stop points were identified. Therefore, it was necessary to calculate the distances between the stop points, and to determine a flight route between those points by the genetic algorithm. The genetic algorithm was applied respectively with 20, 40, 60 population sizes, and the results were compared.

The results were calculated by a computer having an Intel Core i7 processor with a frequency of 2.8 GHz, 8 GB RAM. Matlab 2016b software was also used for calculations.

4. Results and Discussion

In this study, the shortest flight route of unmanned aerial vehicles was optimized via genetic algorithm. The population size parameter of the genetic algorithm was given as 3 different values (20, 40, 60) and the results were obtained. In addition to this, in case of no optimization, the length of the flight as a result of stopping at the stop points sequentially was also calculated.

Table 1. Obtained Results

Population Size	Number of Iteration	Shortest Flight Route Length
No Optimization		4482,84
20	2132	4165,68
40	827	4082,84
60	3604	4082,84

Table 1 shows the results obtained from different population sizes. It is seen that the shortest flight route having more population size is optimized better.

(a)

(b)

(c)
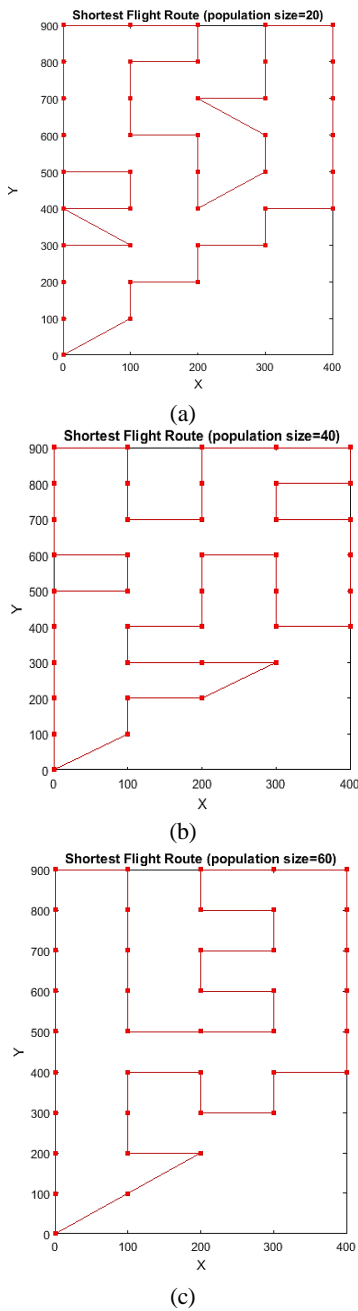
Figure 5. Shortest Flight Routes for Determined Agricultural Land

Figure 5a, 5b, 5c shows the shortest path found via genetic algorithm respectively when the number of populations of 20, 40, and 60 were selected.

(a)

(b)

(c)
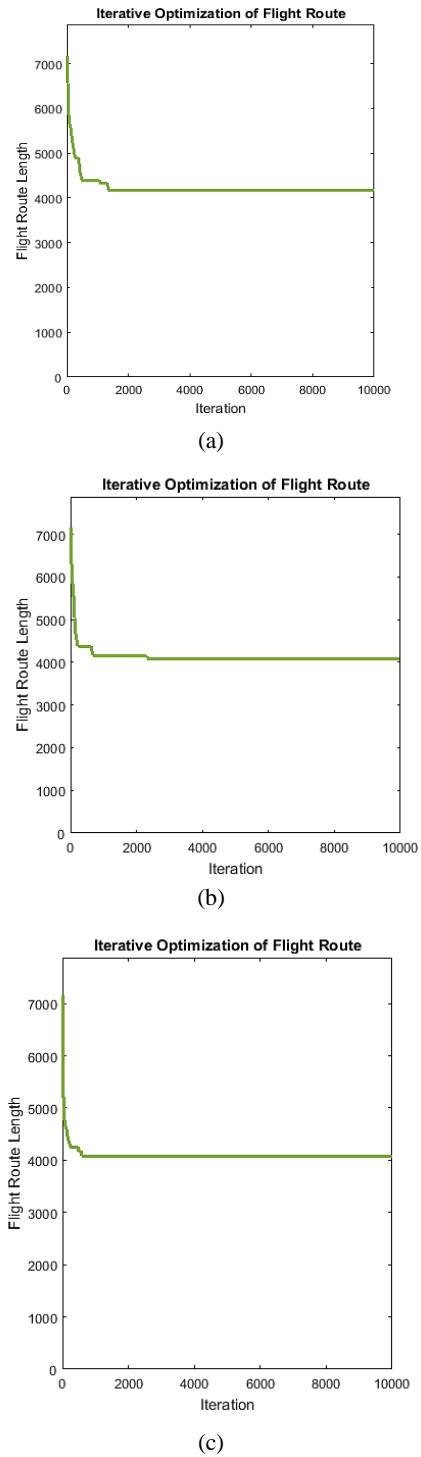
Figure 6. Optimization of Flight Route (population size=20,40,60)

Figure 6a, 6b, 6c shows the total flight length calculated in iterations respectively when the population size of 20, 40, and 60 were selected.

Examining the results of this study, it is seen that the calculated flight length was not suitable when there was no optimization. The flight route length was reduced when optimization was done by genetic algorithm. As seen in

genetic algorithm results, the fastest and best result was obtained when population of 40 was selected.

This study shows that same agriculture land can be scanned with a shorter flight length by determining the route of the unmanned aerial vehicles via the genetic algorithm. As seen in Figure 6, the scanning process, initially provided at about 7000 meters, was optimized by the genetic algorithm and reduced to 4082.84 meters. Regarding the results of this study, it can be said that with this kind of optimization in flight route, limited batteries, which are already the biggest disadvantage of unmanned aerial vehicles, will be much more efficient.

References

1. Grew, R., *Food In Global History* 2000, USA: Routledge.

2. Tan, F., Sağlam, C., *A different method of using nitrogen in agriculture; Anhydrous ammonia*. International Advanced Researches and Engineering Journal, 2018. **2** p. 43-47.

3. Halewood, M., Chiurugwi, T., Sackville Hamilton, R., Kurtz, B., Marden, E., Welch, E., Michiels, F., Mozafari, J., Sabran, M., Patron, N., Kersey, P., Bastow, R., Dorius, S., Dias, S., McCouch, S. and Powell, W., *Plant genetic resources for food and agriculture: opportunities and challenges emerging from the science and information technology revolution*. New Phytol, 2018 **217:** p. 1407-1419. doi:10.1111/nph.14993

4. Tshida, Tetsuro, et al. *A Novel Approach for Vegetation Classification Using UAV-Based Hyperspectral Imaging*. Computers and Electronics in Agriculture, 2018. 144: pp. 80–85., doi:10.1016/j.compag.2017.11.027.

5. Schut, Antonius G.t., et al. *Assessing Yield and Fertilizer Response in Heterogeneous Smallholder Fields with UAVs and Satellites*. Field Crops Research, 2018. 221: pp. 98–107., doi:10.1016/j.fcr.2018.02.018.

6. Chandler, P. R., and Meir Pachter. *Research issues in autonomous control of tactical UAVs*. American Control Conference, 1998. Proceedings of the 1998. Vol. 1. IEEE.

7. Bellingham, John S., et al. *Cooperative path planning for multiple UAVs in dynamic and uncertain environments*. Decision and Control, 2002, Proceedings of the 41st IEEE Conference on. Vol. 3. IEEE, 2002.

8. Ru, Li, Lu Ya-fei, and Hou Zhong-xi. *A model of mission planning for cooperative UAVs*. Control and Decision Conference (CCDC), 2015 27th Chinese. IEEE, 2015.

9. Nikolos, I. K., Valavanis, K. P., Tsourveloudis, N. C., & Kostaras, A. N., *Evolutionary algorithm based offline/online path planner for UAV navigation*. IEEE Transactions on Systems, Man, and Cybernetics, Part B (Cybernetics), 2003. 33(6): 898-912.

10. Sathyaraj, B. M., Jain, L. C., Finn, A., & Drake, S. *Multiple UAVs path planning algorithms: a comparative study*. Fuzzy Optimization and Decision Making, 2008. 7(3): 257-267.

11. Chen, Yong-bo, et al. *UAV path planning using artificial potential field method updated by optimal control theory*. International Journal of Systems Scienceahead-of-print 2014. p. 1-14.

12. Yang, K., & Sukkarieh, S., *An analytical continuous-curvature path-smoothing algorithm*. IEEE Transactions on Robotics, 2010. 26(3): 561-568.

13. Pierre, Djamalladine Mahamat, Nordin Zakaria, and Anindya Jyoti Pal. *Master-slave parallel vector-evaluated genetic algorithm for unmanned aerial vehicle's path planning*. Hybrid Intelligent Systems (HIS), 2011 11th International Conference on. IEEE, 2011.

14. Roberge, V., Tarbouchi, M., & Labonté, G., *Comparison of parallel genetic algorithm and particle swarm optimization for real-time UAV path planning*. IEEE Transactions on Industrial Informatics, 2013. 9(1): 132-141.

15. Sathyaraj, B. M., Jain, L. C., Finn, A., & Drake, S., *Multiple UAVs path planning algorithms: a comparative study*. Fuzzy Optimization and Decision Making, 2008. 7(3): 257-267.

16. J. H. Holland, *Adaptation in natural and artificial systems: an introductory analysis with applications to biology, control, and artificial intelligence*, 1992, England: MIT Press.

17. Marwala, S. Chakraverty, *Fault classification in structures with incomplete measured data using autoassociative neural networks and genetic algorithm*, Curr. Sci. India 90 2006, p. 542–548.

Research Article

Effect of functional group distribution on combustion characteristics of chars from Afsin Elbistan lignite and RDF

Gülşen Kurt Demir [a], Hanzade Haykırı Açma [b] and Serdar Yaman [b],*

[a]Department of Chemical Engineering, Kocaeli University, Engineering Faculty, Kocaeli, 41380,Turkey
[b]Department of Chemical Engineering, Istanbul Technical University, Istanbul, 34469, Turkey

ARTICLE INFO	ABSTRACT
	RDF (Refuse Derived Fuel) and lignite from Afsin-Elbistan region were subjected to carbonization to produce their chars. For this purpose, these samples were heated from ambient to temperatures of 400, 500, 600, 700, 800, 900°C by a heating rate of 10°C/min in a tube furnace under nitrogen flow. Then, the chars were characterized in terms of the calorific values and the functional groups were investigated using FTIR (Fourier Transform Infrared Spectroscopy) technique. Also, some fuel blends where the chars of RDF and lignite are blended in different ratios were prepared. Effects of the charring process on the fuel properties of RDF and lignite were interpreted.

1. Introduction

Future projections of Turkey in power generation show that the importance of lignites will be increased proportional to the increasing energy demand since oil and natural gas reserves in this country are seriously limited. Although, Turkey has large coal deposits in various coal ranks, low quality lignites account for the most part of the Turkish lignites. That is, low calorific value, high sulfur content, and high ash yield lignites are the most abundant natural primary energy sources. In addition to these disadvantages, fossil fuels consumption increases the CO_2 emission and triggers the greenhouse gases (GHG) formation and climate change. New technologies are actively being investigated to achieve emission reductions. Thus, the development of appropriate technologies for the evaluation of low-quality lignite potential must be one of the most important energy policies of our country [1]. For this reason, alternative energy sources must be found to meet the energy need of the industrialized world [2-4].

At the same time waste management is an important problem for the industrialized and urbanized countries.

Overpopulation and industrialization changes the consumption habits and Municipal Solid Waste (MSW) generation is increased [5-6]. When the wastes are used as alternative energy source, the energy, waste management and environmental problems can be avoided. MSWs are transformed to alternative fuel which is called Refuse Derived Fuel (RDF). RDF is the organic part of MSWs after separation of recyclable materials and its calorific value is considerably high [7].

RDF production from the MSW process starts with the separation of the recycled materials from the MSW, and then size of the separated waste is reduced by milling or shredding processes. Metal or glass particles are removed from finer wastes via air classification and magnetic separation steps. Homogenized wastes are dried to eliminate humidity in order to increase calorific value. At the end of the process wastes are packed to reduce volume. Pelletized fuels stored easily in order to their stable shapes [8-9]. RDF fuels are used in energy intensive areas such as cement, paper, chemical production industries or power generation [9-12]. Especially, RDF blends are suitable for rotary cement kiln in

* Corresponding author. Tel.: *+90 (212) 2853351*; Fax: + 90 (212) 2852925
E-mail address: *yamans@itu.edu.tr*

cement production power plants because of high flame temperatures. The use of RDF at the rotary kiln reduces the CO_2 emissions [13].

RDF fuels have high calorific values that are compatible with the lignitic coals. In this paper, RDF and Afsin-Elbistan lignite samples have been carbonized at different temperatures. In consequence of the calorific value measurements, the carbonization temperatures that produce the chars with the highest calorific value were assumed as the optimum carbonization temperatures for RDF and lignite, and the chars from these carbonization experiments were blended in different proportions to obtain the char blends. FTIR analysis of untreated RDF and lignite as well as their chars and char blends were carried out to determine the functional groups that have significant role on the fuel properties and the burning reactivities.

2. Material and Method

2.1 Materials

RDF was provided from Istanbul Metropolitan Municipality Odayeri Sanitary Landfill Area. Besides, the lignite sample was provided from Afsin-Elbistan region in Turkey. In this study, untreated main Afsin-Elbistan lignite coal sample (L) and RDF (R) were used and their chars were produced by carbonization at temperatures of 400, 500, 600, 700, 800, and 900°C.

2.2 Sample Preparation

RDF and lignite samples were dried under atmospheric conditions in open containers firstly and then these air-dried samples were put in an oven to eliminate the moisture completely. The dried samples were milled and sieved through Retsch AS200 sieve to get the particle size below 250 μm. Semicokes in other words chars which are the solid products of the carbonization experiments were produced by carbonization of the coal and RDF samples. That is, the carbonization process was performed under N_2 flow of 100 mL/min in a horizontal tube furnace by heating the sample from ambient to the final temperatures of 400, 500, 600, 700, 800, 900°C with a fixed heating rate of 10°C/min. Once the temperature reaches the final value, hold-time of 30 min at these temperatures was allowed. Then, the thermally treated samples were cooled down inside the furnace under nitrogen flow to avoid oxidation of the char. The char samples were kept in air-tight bottles to eliminate any interaction with oxygen. The chars will be hereafter named as L (lignite) or R (RDF) with the final temperature of carbonization. For an instance, L400 means the lignite char obtained at 400°C.

Figure 1. Horizontal tube furnace

2.3. Calorific Value Analysis

Considered the calorific values of these chars, the optimum carbonization temperatures were determined for lignite and RDF. Calorific values of samples were determined using IKA C2000 model calorimeter.

2.4. FTIR Analysis

Combustion characteristics of untreated samples, chars and char blends were investigated using thermal analysis method. FTIR (Fourier Transform Infrared Spectroscopy) technique was applied to untreated samples as well as the chars to specify the functional groups and interpret the effects of functional groups on the combustion behavior. FTIR analysis was conducted using Bruker Alfa-T FTIR device to determine the functional groups in the coal sample and its chars. For this purpose, the samples to be tested were mixed with potassium bromide (KBr) powders with a proportion of 1/100. Then, the specimens for FTIR were pressed between two 13 mm disks under 10 MPa pressure with KBr.

All the tests repeated several times to check the accuracy and the precision of the experimental results and the average values were taken.

3. Results and Discussion

The calorific values of char samples were determined using IKA C2000 calorimeter and the results were shown in Table 1 and indicated that the highest calorific values were obtained when the final temperature was 800°C for lignite while the corresponding temperature was 400°C for RDF. For this reason, we decided to produce char blends by simply mixing L800 and R400 chars in different proportions. Namely, the percentages of R400 changed in the interval of 10-50 wt% in these blends. This shows that the L800 was the dominant ingredient in these blends and R400 was used as an additive to increase the calorific value of the blends. Table 1 also gives the calorific values of these blends.

In this case, as the RDF char content of the blends increases, the thermal values increase. It has been thought that the RDF chars contribute to the coal chars, and as the blending ratio increases, the volatile matter content increases and the thermal values can be improved.

The FTIR spectra for Afsin-Elbistan lignite and its char samples are given in Figure 2. That is, there is evidence of O-H stretching bands at around 3000-3500 cm^{-1} in Figure 2. The strong bands between 2800-2950 cm^{-1} indicate the presence of methyl and methylene groups [14]. The bands between 1400-1600 cm^{-1} indicates the aromatic C=C vibrations [15]. The peaks between 970-1250 cm^{-1} indicate the C-O stretching vibrations and existence of alcohol or phenolic structures [16]. The peaks between 700-900 cm^{-1} shows the ester groups' existence in the lignite samples [17].

Table 1. Calorific values of samples

Sample Name	Calorific Value (cal/g)
Lignite	2536
L400	2194
L500	2208
L600	2375
L700	2603
L800	2940
L900	2826
RDF	5424
R400	6623
R500	3382
R600	3359
R700	2983
R800	2902
R900	3094
10 R400+90 L800	3178
20 R400+80 L800	3570
30 R400+70 L800	3944
40 R400+60 L800	4252
50 R400+50 L800	4577

Figure 2 also shows the FTIR spectra of the chars in order to monitor the variations of functional groups due to carbonization at different temperatures. That is, the methyl and methylene groups could not be detected until carbonization is carried out at 500°C. This can be explained by the relatively enrichment of these constituents as a result of deoxygenation through partial devolatilization. The hydroxyl groups can be attributed to the moisture content of the samples. Besides, intensities of the derivations of etheric functional groups became stronger in L600 and L700 compared to L500. On the other hand, intensities of these groups lowered again in the cases of L800 and L900.

The intensities of the peaks at around 800 and 1400 cm^{-1}, which may be resulted from the presence of aromatic C-H peaks, are highly distinctive in cases of L600 and L700. However, these peaks almost decayed in L800 that suggest the fact that aromatic structure was decomposed under high temperature effect. In addition, the intensity of aliphatic C-H peaks at around 2800 cm^{-1} started to increase from L800.

Bonds in aromatic ring structures are relatively much stronger than straight-chain aliphatic bonds and accordingly high temperature is required for their breakdown. It is well-known that high rank coals such as anthracites and bituminous coals are rich in aromatic ingredients, while low rank coals such as lignites are poor in aromatics. Instead, low rank coals are rich in aliphatic constituents. Thus, in L800 and L900, thanks to the straight-chain structures, given heat was enough to effect these bonds. In fact, two different phenomena determine the extent of the calorific values of the chars. One of them is in the favor of increase due to elimination of oxygen-rich volatiles. On the other hand, the other effect leads to decrease in the calorific value since severe disintegrations take place in the structure under elevated temperature conditions. That's why the calorific values of L600 and L700 are lower than that of L800 and L900 and the mentioned first phenomenon is more dominant at these temperatures. Besides, the calorific value of the L900 showed some decrease in comparison to L800 as carbonization temperature increased from 800°C to 900°C that predicts the fact that the second phenomenon is the governing phenomenon in the investigated temperature interval. FTIR spectra of the chars are in good agreement with the mentioned situations.

Figure 3 illustrates FTIR spectra of RDF and its chars basing on the absorbance intensities. That is, since RDF was already dried before the analyses and the chars were almost free of moisture, it is hardly difficult to detect the band at around 3500 cm^{-1} that indicates hydroxyl (O-H) groups and is the characteristic bands of water. The peaks located in the region of 2800-3000 cm^{-1} indicate the existence of C-H stretching in methyl and methylene groups. The macromolecular ingredients of biomass such as cellulose, lignin, and hemicellulose contain C-H bonds. On the other hand, plastic components found in RDF also contribute to these peaks [18]. Evaluation of HCl is indicated by peaks at 2600-3000 cm^{-1} and the source of the HCl can be attributed to PVC in the RDF blends [14]. However, it couldn't be seen any peak in this range and this can be attributed to the fact that PVC had already been eliminated from MSW and the RDF used in this study is poor in PVC.

The medium-weak multiple bands at 1400-1600 cm^{-1} indicate the aromatic C=C vibrations [19]. It is well-known that lignin that is the second most important ingredient in biomass after cellulose is the only aromatic material and these bands can be attributed to lignin found in biomass. The peaks in the range of 1200-1100 cm^{-1} are related with the ether type structures such as cellulose and hemicellulose. In fact, C-O bonds in biomass are the most abundant bonds because of large amount of oxygen in biomass. Cellulose and hemicellulose have great contribution to these bands. Also, lignin contains C-O bonds. The source of these ligno-cellulosics is woody wastes, shells, barks, and agricultural remnants. Similarly, paper and paper products are very rich in cellulosics [20].

Peak intensity of C-O bonds of about 1000 cm^{-1}, indicating cellulosic structures, decreased at R400. Because

at this approximate temperature cellulose is degraded and thus an increase in the thermal value is expected. The highest thermal value of the R400 sample in the thermal value results confirms the FTIR results. The peaks appearing at 1450-1600 cm^{-1} originate from aromatic C-H bonds. In addition, a decrease in peak intensity, which indicates C-H bonds, has been observed on the R400 sample with removal of the plastic volatile components, but as higher temperatures are reached, C-H bonds are again formed to form aromatic structures. The aromatic structures formed after R800 also degrade. Thus, the FTIR results confirm that there is a decrease in the thermal values after R400 and that the thermal value after R800 slightly increases.

Similarly, the FTIR spectra for the blends can be seen in Figure 4. It can be concluded that the FTIR spectra of the blends were closely affected from the proportions of the chars in the blends. As the content of RDF char in the blends increases, the C-H bonds, which represent aromatic structures seen around 1400 cm^{-1}, are broken and the peak shrinks. The aromatic bonds, ie ring bonds, are much stronger than aliphatic bonds in straight chain structures and require high energy to break. As the RDF char content increases, the increase in thermal values confirms the FTIR results.
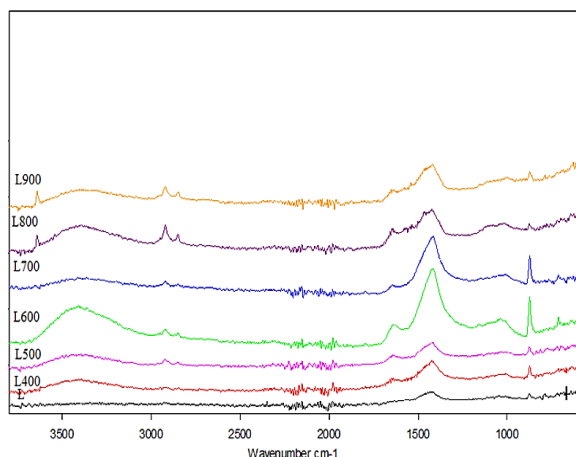

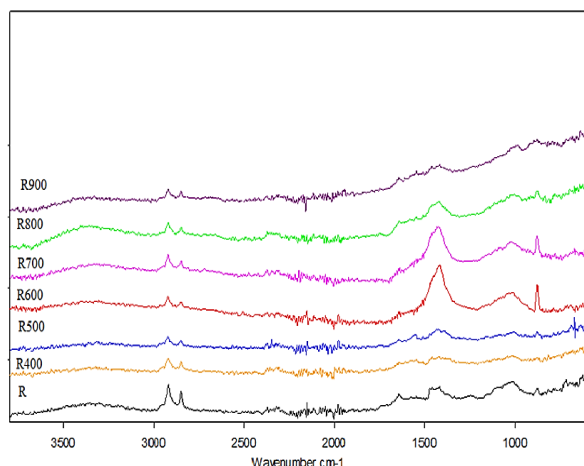Figure 2. FTIR spectra of lignite and char samples

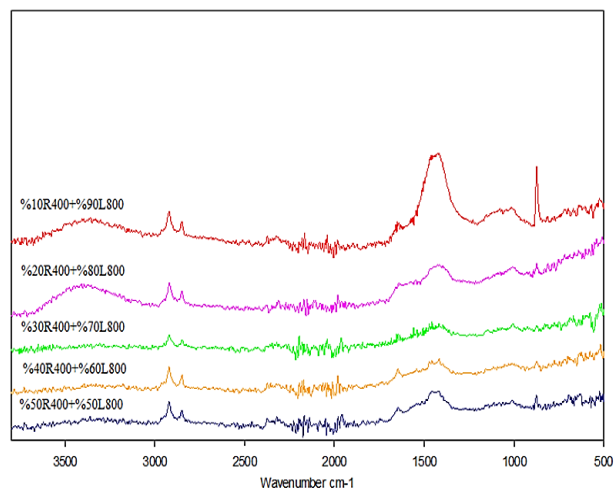Figure 3. FTIR spectra of RDF and char samples

Figure 4. FTIR spectra of char blends

4. Conclusions

RDF samples have higher calorific values than the Afsin-Elbistan lignite coal. When the RDF samples are carbonized at 400°C, the highest calorific value is reached. However, increasing the carbonization temperature beyond the 400°C has detrimental effects on structure and consequently it leads to reductions in the calorific value. Therefore, 400°C can be regarded as the optimum temperature for carbonization of RDF and the chars of RDF can be produced at this temperature. In addition, the char blend that has a composition of 50% of R400 and 50% of L800 is the optimum composition in terms of the calorific value and the sustainability of the fuel. The FTIR spectra of the untreated RDF and lignite, their chars, and the char blends showed the presence of several functional groups including O-H, C-H, C-O, C=C. The intensities of these bands are highly influenced from the carbonization temperature.

This study revealed that carbonization of lignite affected not only the calorific values of the carbonized chars but also the functional groups found in these chars are highly influenced from the carbonization temperature. Namely, the intensity of a given bond in FTIR spectrum was determined by the relative abundancy of the other bonds. That is, the stages of drying, devolatilization, and even further devolatilization of the forming char during carbonization need different temperature regions and heat requirements in such thermal treatment studies. Accordingly, some peaks on FTIR spectrum became either decayed or intensified depending on the temperature applied during the carbonization process.

As a result of the experimental studies, Afsin Elbistan lignite coal and RDF produced high thermal value fuel. It has been thought that the improvement of the thermal values can be made as the contribution of the RDF char on the coal char and the ratio is increased.

Nomenclature

L : Lignite
R : RDF
RDF : Refuse Derived Fuel

References

1. Smooth, L.D., Coal and char combustion in fossil fuel combustion. 1991, New York, Wiley-Interscience.
2. Wong, S., Ngadi, N., Abdullah, T., INuwa, I., Current state and future prospects of plastic waste as source of fuel: A review. Renewable and Sustainable Energy Reviews, 2015. **50:** p.1167-1180.
3. Ariyaratne, W., Melaaen, M., Tokheim, L., Determination of biomass fraction for partly renewable solid fuels,.Energy**,** 2014. **70**: p. 465–472,.
4. Agll, A., Hamad, Y., Hamad, T., Sheffield, J., Study of energy recovery and power generation from alternative energy source. Case Studies in Thermal Engineering, 2014. **4**: p. 92–98.
5. Hou, S., Chen, M., Lin, T., Experimental study of the combustion characteristics of densified refuse derived fuel (RDF) produced from oil sludge. Fuel, 2014. **116**: p. 201–207.
6. Gallardo, A., Carlos , M., Bovea , M., Colomer, F., Albarrán , F., Analysis of refuse-derived fuel from the municipal solid waste reject fraction and its compliance with quality standards. Journal of Cleaner Production, 2014. **83**: p. 118-125.
7. Akdağ, A., Atımtay, A., Sanin, F., Comparison of fuel value and combustion characteristics of two different RDF samples. Waste Management, 2016. **47**: p. 217-224.
8. Gendebien, A. Leavens, A., Blackmore, K., Godley, A., Lewin, K., Whiting, K, Refuse Derived Fuel, Current Practice and Perspectives, Final report, B4-3040/2000/306517/MAR/E3, Swindon, 2003.
9. *Rotter*, S., Kost, T., Winkler, J. and Bilitewski, B., Material flow analysis of RDF-production processes. Waste Management, 2004. **24**: p.1005-1021.
10. Białowiec, A., Pulka, J., Stępień, P., Manczarski, P., Gołaszewski, J., The *RDF*/SRF torrefaction: An effect of temperature on characterization of the product – Carbonized refuse derived fuel. Waste Management, 2017. **70**: p.91-100.
11. Edo, M., Skoglund, N., Gao, Q., Persson, P., Jansson S., Fate of metals and emissions of organic pollutants from torrefaction of waste wood, MSW, and *RDF*. Waste Management, 2017. **68**: p. 646-652.
12. Costa, M., Massarotti, N., Mauro, A., Arpino, F., Rocco, V., CFD modelling of a *RDF* incineration plant, Applied Thermal Engineering, 2016, **101**: p.710-719.
13. Kara, M., Günay, E., Tabak, Y., Yıldız, Ş., Perspectives for pilot scale study of RDF in Istanbul Turkey. Waste Management, 2009. **29**: p.2976–298,.
14. Singh, S., Wu, C., Williams, P., Pyrolysis of waste materials using TGA-MS and TGA-FTIR a complementary characterisation techniques. Journal of Analytical and Applied Pyrolysis, 2012. **94**: p.99-107.
15. Bilgic, E., Yaman, S., Haykiri-Acma, H., Kucukbayrak S., Limits of variations on the structure and the fuel characteristics of sunflower seed shell through torrefaction. Fuel Processing Technology, 2016. **144** : p. 197-202.
16. Fu, P., Hu, S., Xiang, J., Li, P., Huang, D., Jiang, L., Zhang, A., Zhang, J**.,** FTIR study of pyrolysis products evolving from typical agricultural residues. Journal of Analytical and Applied Pyrolysis, 2010. **88**: p.117–123.
17. [cited 2018 25 February]; Available from: https://www2.chemistry.msu.edu/faculty/reusch/virttxtjml/Spectrpy/InfraRed/infrared.htm
18. Lu, R., Purushothama, N., Yang, X., Hyatt, J., Riley, J., Lloyd, W., TG/FTIR/MS study of organic compounds evolved during the co-firing of coal and refuse-derived fuels. Fuel Processing Technology, 1999. **59**:p. 35–50.
19. [cited 2018 25 February]; Available from: http://www2.ups.edu/faculty/hanson/Spectroscopy/IR/IRfrequencies.html
20. Poletto, M., Zattera, A., Santana, R., Structural differences between wood species: Evidence from chemical composition, FTIR spectroscopy, and thermogravimetric analysis. Journal of Applied Polymer Science, 2012. **126:** p. 337-344.

Research Article

Two countries at same parellel in solar energy productions: USA and Turkey

Gülcan İner [a],* and Evren Çağlarer [b]

aKirklareli University, Vocational School of Technical Sciences, Kırklareli, 39100, Turkey
bKirklareli University, Faculty of Technology, Kırklareli, Turkey

ABSTRACT

Energy is a basic necessity after the industrial revolution in our lives. Energy demand is increasing with the development of technology from day by day. Humanity has head towards to the alternative energy sources. Therefore, alternative energy must have renewable sources. This situation can be supply a significant benefit for future energy demand. These resources play an important role in meeting the demand and provide significant benefits in terms of economic and environmental protection. Among the renewable energy sources have taken an important place like hydroelectric power plants, wind turbines, geothermal energy, wave energy, biomass energy, rock gas, etc. However, solar energy is the biggest renewable energy potential most countries in the world. Various countries around the world use renewable energies solar energy and photovoltaic panel technology to choose energy production and increasing the production potentials day by day. In this study, samples will be compared to the United States and Turkey in energy production from solar energy.

1. Introduction

Developing technologies, rapid increase in population, need for more comfortable life increase energy need each day. Studies conducted for resource supply of the energy that may fulfil such needs and use of fossil resources in production may cause global warming, increase of environmental pollution, limitation of agricultural production and the risk of extinction of animal and plant variety. According to OECD 2016 data, 6 to 9 million people in the world will encounter early death risk each year due to air pollution until 2060. Today, global warming and increase in sea levels, floods, air pollution, stress, heat stroke, diseases, agricultural losses, severe storms and drought, loss of corals and fish in oceans cost annually 2,6 billion USD globally and this amount increases day by day [1].

Lack of resources for energy production is also a significant problem for countries. Non-renewable and mostly used energy resources used today are coal, oil and natural gas. Import of such resources causes economically significant costs and foreign borrowing for countries which have insufficient own reserves such as Turkey.

There is a need for renewable, economical and sustainable resources which are not harmful to the environment and ecosystem for producing the energy required. It is possible to obtain this energy from wind, rain, sun and geothermal resources which can renew itself in the nature. There is no doubt that the most important resource in terms of reserve amongst these alternatives is the sun.

The temperature of the sun measured using various methods is 5800 ºC. The power of such a hot object, in other words the radiant energy it radiates per second is measured approximately as 4 x 1023 kW. The power falling on each square meter of the earth after this energy is absorbed in the atmosphere is approximately 1.000 watt/m^2 [2] (317 BTU-h/ft^2 in USA). Since solar energy is an environmentally clean resource, it is a strong alternative for fossil fuel. Solar radiant energy falling on earth each year is almost 160 times of the fossil fuel reservoirs on Earth determined until today, and is approximately 15.000 times more than the energy that all fossil, nuclear and hydroelectricity plants may generate in one year.

---

* Corresponding author. Tel.: +90 533 212 45 91.
  E-mail address: gulcaniner@gmail.com

Therefore, it is very significant that solar energy is transformed into an energy type that can be used accordingly in human activities [1].

2. Electricity Energy Consumption and Generation Potentials

While China, United States of America, India, Russia, Japan and Germany are respectively ranked as the countries which consume and generate energy most in the world according to 2015 data, Turkey ranks as the 19th in consumption and 17th in generation (Table 1 and 2).

Most commonly used energy resources used for energy generation are coal, oil and natural gas. These reserves are rapidly decreasing in proportion with the increasing energy need. Consumption time projected for 892 billion tons of coal reserve is 114 years, 186,9 trillion m^3 natural gas is 53 years, 250 billion tons of oil is only 51 years.

Majority of the energy is generated by nuclear plants after fossil originated resources globally. According to January 2017 data of International Atom Energy Agency (IAEA), there are 449 nuclear plants active in 31 countries in total. While Germany and many European countries chose to shut down the present nuclear plants and obtain energy from renewable resources, construction of 60 nuclear plants are in progress in 16 countries which wish to increase their energy generation capacities and do not have any nuclear plants including United Arab Emirates which has a sunshine duration more than European countries [3].

Annual electricity energy consumption of Turkey increased 3.3% in 2016 and reached to 278.3 billion kWh. Annual electricity generation increased 4.9% in 2016 and reached to 274,7 billion kWh [4]. 32,1% of electricity generation was obtained from natural gas; 33,9% thereof was obtained from coal, 24,7% thereof was obtained from hydroelectricity, 5,7% thereof was obtained from wind, 1,8% thereof was obtained from geothermal and 1,8% thereof was obtained from other resources [4].

22,3% of the electricity energy presented for consumption was used in dwellings, 1,9% thereof was used in illumination, 1,8% thereof was used in agricultural irrigation, 47,2% thereof was used in industry, 26,2% thereof was used in business organizations and public buildings.

Energy consumption in USA in 2016 is 4,303.0 TWh. 37% of this energy was obtained from oil; 29% of this energy was obtained from natural gas; 15% of this energy was obtained from coal; 9% of this energy was obtained from nuclear plants; 10% of this energy was obtained from renewable energy resources. 6% of renewable energy resources generate electricity from sun [5]. USA uses 39% of the energy it generates to generate electricity energy. 29% of the remaining energy is used in transportation; 22%

thereof is used industry; 6% thereof is used in settlements; and 4% thereof is used in commercial activities.

Energy is one of the basic inputs needed by any sector. Therefore, the most important reason of the increase in energy demand in every field is the effort to maintain or improve the present structure. The efforts to achieve better, more comfortable, more practical and more economical also support this need.

Table 1. Global Primary Energy Consumption

COUNTRY	2014 (TWh)	2015	Share (%)	Line
China	2.970,3	3.014,0	22,9	1
USA	2.300,5	2.280,6	17,3	2
India	666,2	700,5	5,3	3
Russia	689,8	666,8	5,1	4
Japan	453,9	448,5	3,4	5
Canada	335,5	329,9	2,5	6
Germany	311,9	320,6	2,4	7
Brazil	297,6	292,8	2,2	8
S. Korean	273,1	276,9	2,1	9
Iranian	260,8	267,2	2,0	10
S. Arabian	252,4	264,0	2,0	11
France	237,5	239,0	1,8	12
Indonesia	188,3	195,6	1,5	13
U.K.	188,9	191,2	1,5	14
Mexico	190,0	185,0	1,4	15
Italy	146,8	151,7	1,2	16
Spain	132,1	134,4	1,0	17
Australia	129,9	131,4	1,0	18
Turkey	**123,9**	**126,9**	**1,0**	**19**
Thailand	123,4	124,9	0,9	20
S. Africa	128,0	124,2	0,9	21
Taiwan	111,4	110,7	0,8	22
UAE	99,0	103,9	0,8	23
Poland	92,4	95,0	0,7	24
Ukraine	101,0	85,1	0,6	25
TOTAL	**13.020,6**	**13.147,3**	**100,0**	

3. Electricity Generation from Solar Energy

The sun is the resource with the highest potential amongst the renewable energy resources. USA ranks on the 4th place in electricity generation from solar energy with 36.75 TWh [7].

Turkey's annual average sunshine duration of has been determined as 2640 hours and daily total sunshine duration as 7.2 hours; average total radiant intensity has been determined as 1.311 kWh/m²-year and daily total radiant intensity as 3,6 kWh/m². Photovoltaic panels were started to be used in 2008 to generate electricity from solar energy [4]. Directorate General of Renewable Energy was established in 2011 and research & development activities were accelerated.

Table 2. Global Primary Energy Generation

COUNTRY	Generate (TWh)	Share (%)	Line
China	5.810,6	24,1	1
USA	4.303,0	17,9	2
India	1.304,8	5,4	3
Russia	1.063,4	4,4	4
Japan	1.035,5	4,3	5
Germany	647,1	2,7	6
Canada	633,3	2,6	7
Brazil	579,8	2,4	8
France	568,8	2,4	9
S. Korean	522,3	2,2	10
U.K.	337,7	1,4	11
S. Arabian	328,1	1,4	12
Mexico	306,7	1,3	13
Iranian	281,8	1,2	14
Italy	281,8	1,2	15
Spain	278,8	1,2	16
Turkey	**261,8**	**1,1**	**17**
Taiwan	258,0	1,1	18
Australia	253,6	1,1	19
S. Africa	249,7	1,0	20
Indonesia	234,7	1,0	21
Egypt	180,6	0,7	22
TOTAL	**24.097,7**	**100,0**	

While energy from solar energy is generated using photovoltaic panels in Turkey, solar and thermal (solar thermal) systems with greater capacity were developed in USA after use of photovoltaic panels for energy generation. Concentrated solar panels (CSP) or single focal solar panel systems, parabolic systems, energy tower systems are used in large scale entities for electricity generation.

Annual sunshine duration varies according to states in USA. California, Arizona, Nevada and Texas located geographically on the south of USA have large scaled generation plants in electricity generation from solar energy. USA Ministry of Energy established Solar Energy Research Institute in 1977. In 1980, studies directed towards electricity generation using photovoltaic panels started. In 1982, large scale electricity generation plants were started to be established with solar towers, and photovoltaic panel technology, thermal solar and concentrated solar technology (CSP) were started to be used [8].

Today, one million dwellings benefit from energy generated by solar panels in USA; and it is aimed to increase this number to 2 million at the end of 2018 [9].

Turkey is a country located between 36° - 42° northern latitudes and has an area of 783.562 km²; and USA is continental country which has 50 states, located between 25° - 48° northern latitudes and has an area of 9.629.091 km². The energy generated from solar energy plants as of the end of 2016 was 832,5 MWh and this amount covers 1.1% of the energy generation on resource basis. 12.700 persons work in this field [6].

Comparative chart of USA states based upon the data obtained from SEIA is presented in Table 3.

Table 3. Turkey-USA Comparative Chart for Renewable Energy

	Turkey	California	Arizona	Nevada	Texas
Area (km2-sq mi)	783.56 302.534	423.970 163.696	295.2541 13,990	286.3821 10,577	696.24 1268,581
Latitude (N)	36-42	32-42	36-37	35-42	25-36
Generate (MWh)	832,5	19.664,7	3.254,23	2.349,9	1.620,19
Gen. Per. (%)	1,1	14,2	5,43	9,06	0,39
Num. of Gener.	520	2639	428	130	565
Num. of Emp.	12.700	100.050	7310	8371	9396

California State, which has an area of 423.970 km² (163,696 sq mi.) and is located between 32°-42° northern latitudes, has the greatest plants which generate electricity from solar energy in USA. There are 2.639 individual and corporate electricity generators in total and 14,2% of annual electricity energy need is provided from the sun. The generation capacity for 2016 was 19.664,7 MWh and it is aimed to increase this capacity 14.272 MWh more within the following 5 years. 100.500 persons are employed in this sector in total.

Arizona State, which has an area of 295.254 km² (113,990 sq mi) and is located between 36°-37° northern latitudes, is ranked in the second place with an electricity generation of 3,254.23 MW. 5,43% of electricity generation is provided from the sun. There are 428 individual and corporate electricity generators. It is aimed to increase this current capacity 3.240 MWh more within the following 5 years. 7.310 persons are employed in this sector in total.

Nevada State, which has an area of 286.382 km² (110,577 sq mi) and is located between 35°-42° northern latitudes, is ranked in the third place with an electricity generation of 2.349,9 MW. 9,06% of electricity generation is provided from the sun. There are 130 individual and corporate electricity generators. It is aimed to increase this current capacity 2.632 MW more within the following 5 years. 8.371 persons are employed in this sector in total.

Texas State has an area of 696.241 km² (268,581 sq mi) and is located between 25°-36° northern latitudes. 0,39% of electricity fourth place with an electricity generation of

1.620,19 MW and 565 electricity generators. It is aimed to increase this current capacity 4.673 MW more within the following 5 years. 9.396 persons are employed in this sector in total [9].

Current solar energy plant quantity in Turkey is 1644. 520 of these plants are active. Total installed power there is of 1.362,60 MWh. In 2016, totally 1.020.000 MWh electricity was generated through solar energy plants. 0,46% of the total consumption was obtained from solar energy [4].

Turkey aims to increase photovoltaic solar panel capacity to 5 GWh and wind energy capacity to 20 GWh until 2023 with regards to increase of renewable energy capacity [7].

3. Conclusions

Electricity generation from solar energy using planar photovoltaic panels was initiated in USA in 1980 and in 2008 in Turkey. In Table 3, data relating to four states ranking in the first places in USA which generate electricity from solar energy are compared to Turkey.

Electricity generation from solar energy in these states, which is smaller than Turkey in terms of area, is much more than the current generation in Turkey. When plant quantities are taken into consideration, electricity generation in Nevada State which has the least plants with 130 plants in total is three times of the plant quantity in Turkey. The electricity generation in Arizona State, which has 428 plants, is almost four times, in Texas State, which has 565 plants, it is twice and in California State, which has 2639 plants, it is twenty-three times of the electricity generation of Turkey.

When the ratios of contribution in generation Texas State has the least contribution ratio with 0,39%. This ratio is 5,43% for Arizona State, 9,06% for Nevada State, and 14,2% for California State. This significant difference in ratios of contribution in generation arises from network connected or not network connected generation styles of states. The facts that Texas State is an important centre in oil production and that it covers the energy need from this source also affect its ratio of contribution in generation.

The reason why Nevada State has a 9,06% contribution in generation despite of 130 generation plants is the large scaled plants and parabolic solar collectors & heliostats and solar tower technologies used in energy generation.

The greatest solar energy generation plant in USA is 'Ivanpah Solar Electric Generating System' is located on the border of California and Nevada States. The size of California in terms of area, redundancy of plant quantity and high capacities increase the contribution in electricity generation.

Energy generation from renewable resources provides a significant employment opportunity. More than 260.000 persons were employed in solar energy industry in 43 states of USA in 2016. The number of persons employed in this industry in Turkey is 12.700 despite of low generation capacity. This employment number is 9.396 in Texas State, 8.371 in Nevada State, 7.310 in Arizona State and 100.050 in California State. The fact that this number is high in

Turkey shows the numerical existence of small scaled generation plants and that they use a generation system requiring workforce.

When the quantity of generation plants and the workforce employed by such plants in Turkey are taken into consideration, the generation capacities of plants in our country is quite low. Individual generators can only generate energy with limited amounts, and they have to consume the energy they generate. Therefore, the plant quantity which seems to be high in number cannot provide conditions appropriate for storage and distribution.

Turkey should start to utilize developed new technologies in solar energy generation in order to reduce foreign dependency for energy resources and to ensure resource continuity and increase the quantity of generation sites. Continuity of energy can only be achieved thus.

Acknowledgment

Nomenclature

OECD	:	Organisation for Economic Cooperation and Development
kW	:	Kilo Watt
MW	:	Mega Watt
TWh	:	Tera Watt Hour
IRENA	:	International Renewable Energy Agency
SEIA	:	Solar Energy Industries Association
REN	:	Renewable Energy Policies Network
IAEA	:	International Atom Energy Agency

References

1. OECD, Organisation for Economic Co-Operation and Development, 2016. Available from: http://www.oecd.org/turkey.

2. Ültanır, M.Ö., *Solar Energy on the Threshold of the 21. Century,* Journal of Science and Technic, March 1996, 340: p.50-55.

3. Turkish Asian Center for Strategic Studies, Available from: http://www.tasam.org/tr-TR/Icerik/1080/uluslararasi_atom_enerjisi_ajansi

4. Ministry of Energy and Natural Resources, Available from: www.enerji.gov.tr

5. U.S. Energy Information Administration, 2017, Available from:: www.eia.gov

6. IRENA Renewable Energy and Job, Annually Review 2017, Available from: http://www.irena.org/DocumentDownloads/Publications/IRENA_RE_Jobs_Annual_Review_2017.pdf

7. REN21, Renewables 2016 Global Status Report 2016, Available from: http://www.ren21.net/wp-

content/uploads/2016/06/GSR_2016_Full_Report.pdf

8. U.S. Department of Energy, Available from: https://www1.eere.energy.gov/solar/pdfs/solar_timeline.pdf

9. Solar Energy Industries Association, Available from: https://www.seia.org/solar-industry-data